EPFL

ÉCOLE POLYTECHNIQUE
FÉDÉRALE DE LAUSANNE

Institut de Physique de l'Energie et des Particules
Laboratoire de Physique des Hautes Energies

$B_s^0 \to J/\psi\ \eta$ DECAYS AND SENSITIVITY TO THE B_s^0 MIXING PHASE AT LHCb

Thèse de Doctorat

présentée à la Section de Physique de la Faculté des Sciences de Base
(Ecole Polytechnique Fédérale de Lausanne)
pour l'obtention du grade de docteur ès sciences

par

Benjamin CARRON

Ingénieur physicien diplômé
de l'Ecole Polytechnique Fédérale de Lausanne

Jury

Pr Georges **MEYLAN**, président du jury
Dr Minh-Tâm **TRAN**, directeur de thèse
Pr Ulrich **STRAUMANN**, rapporteur externe
Dr Guy **WILKINSON**, rapporteur externe
Pr Minh-Quang **TRAN**, rapporteur interne

Lausanne
2005

Abstract

𝕿ʜᴇ LHCb experiment will be installed in the proton-proton Large Hadron Collider (LHC) at CERN, Geneva. The detector is a single arm spectrometer currently under construction: LHC running and LHCb data taking will start in 2007. LHCb will then benefit from the prolific source of B-mesons provided by the LHC.

The main goals of the LHCb experiment are to measure the CP asymmetries in the B-meson sector and to study rare decays of b-hadrons. These will extend the measurements presently made with B_d^0 mesons by the Belle (Japan) and BᴀBᴀʀ (USA) experiments. The expected accuracy on the comprehensive measurements with both B_d^0 and B_s^0 mesons will allow to open new windows on physics beyond the Standard Model.

The Standard Model of particle physics (SM) provides the framework for the description of a possible violation of the CP symmetry in the neutral B-meson sector. In particular, it predicts an asymmetry due to CP violation in the time dependent rates for $B_{d,s}^0$ and $\overline{B}_{d,s}^0$ to a common CP eigenstate when this transition is dominated by the subprocess $\bar{b} \to \bar{c}c\bar{s}$: this is due to the interference between the decay and the mixing of these neutral mesons. In this case, the CP violation is directly related to $\sin(\phi_{d,s})$ where $\phi_{d,s}$ is the $B_{d,s}^0$ weak mixing phase.

The B_s^0 meson system can be used for the measurement of such an asymmetry. However it requires hadron machines and high luminosities to compensate the low branching ratio to CP eigenstates.

In contrary to the "golden channel" $B_s^0 \to J/\psi \, \phi$ which demands an angular analysis to distinguish the different CP eigenstates contributions, the $J/\psi \, \eta$ final state is a pure CP-even eigenstate. This channel can therefore provide an excellent probe to the ϕ_s phase.

The reconstruction and performances of this decay mode will be detailed in this dissertation. They are performed with a full Monte Carlo simulation. An annual yield of about 9'000 events for the $B_s^0 \to J/\psi(\mu^+ \, \mu^-) \, \eta(\gamma \, \gamma)$ channel and 3000 for the $B_s^0 \to J/\psi(\mu^+ \, \mu^-) \, \eta(\pi^+ \, \pi^- \, \pi^0)$ decay will be collected with a background-to-signal ratio smaller than 3. The mass and proper time resolutions are quite limited due to the electromagnetic calorimeter photon reconstruction low quality. Hopefully they can be improved by the application of a Kalman Filter fit.

The sensitivity of the LHCb experiment to the weak mixing phase ϕ_s has been determined with a toy Monte Carlo. This simulation uses the $B_s^0 \to J/\psi \, \eta$ decay channels enriched by the $B_s^0 \to \eta_c \, \phi$ pure CP eigenstate channel. It takes into account the event-by-event proper time error, the time-dependent selection efficiency, the B/S ratio, the tagging efficiencies and the reconstruction performances of each decay channel. The combined sensitivity to ϕ_s is found to be 0.068 rad when the SM prediction for this phase is $\phi_s \simeq -0.04$ rad.

These results have been finally compared to the $B_s^0 \to J/\psi \, \phi$ channel, whose sensitivity to ϕ_s reaches 0.031 rad with a annual yield of 125'000 events. The combined sensitivity of all these channels then increases to 0.028 rad. The contribution of the pure CP eigenstates is estimated to $\sim 17\%$.

Even with much smaller statistics, the pure CP eigenstate decay channels provide a non-negligible contribution to the determination of the B_s^0 weak mixing phase ϕ_s.

Résumé

$\mathcal{L}$'EXPERIENCE LHCb sera construite sur le futur grand collisionneur de hadrons (LHC) au CERN, à Genève. Le détecteur est un spectromètre à un seul bras actuellement en construction : la mise en route du LHC et la prise de données de LHCb débutera en 2007. LHCb profitera alors de l'abondante source de mésons beaux produits par le LHC.

Les principaux objectifs de l'expérience LHCb sont de mesurer précisément les asymétries CP dans le secteur des mésons B et d'étudier les désintégrations rares des hadrons beaux. Cela étoffera les mesures déjà collectées par les expériences Belle (au Japon) et BABAR (aux Etats-Unis) à partir de mésons B_d^0. Les précisions attendues sur les mesures complètes des B_d^0 et B_s^0 permettront d'ouvrir de nouvelles perspectives concernant la physique au-delà du Modèle Standard.

Le Modèle Standard de la physique des particules fournit le cadre à une description de la violation de la symétrie CP dans le secteur des mésons B. Une propriété remarquable de ce système est sa capacité à apparier le méson neutre à son anti-particule. Ce mélange $B_{d,s}^0 - \overline{B}_{d,s}^0$ est à l'origine de la violation de CP autour de laquelle est construite cette thèse.

La violation de CP vient d'une phase irréductible dans la matrice de mélange des quarks de l'interaction faible (matrice de Cabibbo-Kobayashi-Maskawa (CKM)). Le Modèle Standard prédit en particulier une violation de la symétrie CP dans les taux de désintégration dépendants du temps des $B_{d,s}^0$ et $\overline{B}_{d,s}^0$ en un état final commun état propre de CP. Quand la transition est dominée par le processus $\bar{b} \rightarrow \bar{c}c\bar{s}$, la violation de CP est directement liée à $\sin(\phi_{d,s})$ où $\phi_{d,s}$ est la phase faible de mélange des $B_{d,s}^0$.

Le système de mésons B_s^0 est particulièrement sensible à ces effets mais nécessite de hautes énergies (collisionneurs hadroniques) et une grande luminosité pour récolter un nombre suffisant de données pour les canaux de désintégration étudiés. Le LHC fournira ces deux éléments essentiels.

Contrairement au $B_s^0 \rightarrow J/\psi \ \phi$, le "canal doré", qui a besoin d'une analyse angulaire pour permettre la distinction des composantes de différents états propres de CP, l'état final $J/\psi \ \eta$ est un état propre de CP. C'est pourquoi ce canal peut permettre une excellente estimation de la phase ϕ_s.

La reconstruction et les performances de ce mode de désintégration seront détaillées dans ce mémoire. Elles ont été calculées grâce à une simulation de Monte-Carlo complète du détecteur et des interactions des particules avec la matière. Environ 9'000 événements pour la désintégration $B_s^0 \rightarrow J/\psi(\mu^+ \ \mu^-) \ \eta(\gamma \ \gamma)$ et 3000 événements pour le canal $B_s^0 \rightarrow J/\psi(\mu^+ \ \mu^-) \ \eta(\pi^+ \ \pi^- \ \pi^0)$ seront collectés chaque année avec un rapport bruit-sur-signal plus petit que 3. La résolution en masse et en temps propre est plutôt limitée à cause de la faible qualité de reconstruction des photons du calorimètre électromagnétique. Heureusement les déterminations de la masse et du temps propre peuvent être améliorées à l'aide

d'un ajustement du genre "filtre de Kalman".

La sensibilité de l'expérience LHCb à la phase de mélange faible ϕ_s a ensuite été déterminée avec un Monte-Carlo simplifié. Cette simulation utilise les canaux décrits plus haut en y ajoutant le $B_s^0 \to \eta_c \, \phi$, une désintégration en un état propre de CP. Elle prend en compte l'erreur en temps propre événement par événement, l'efficacité de sélection dépendante du temps, le rapport B/S, les efficacités d'étiquetage et les performances de reconstruction de chaque canal de désintégration. La sensibilité combinée à ϕ_s a été estimée à 0.068 rad, alors que la prédiction du Modèle Standard pour ϕ_s est de $\phi_s \simeq -0.04$ rad.

Ces résultats ont finalement été comparés avec ceux du canal $B_s^0 \to J/\psi \, \phi$, pour qui la sensibilité à ϕ_s atteint 0.031 rad avec un taux annuel de 125'000 événements. Tous ces canaux mis ensemble permettent d'augmenter la sensibilité à 0.028 rad. La contribution des désintégrations en un état propre de CP est estimée $\sim 17\%$.

Même avec une statistique plus faible, les désintégrations en un état propre de CP apportent une contribution non négligeable à la détermination de la phase faible de mélange ϕ_s des mésons B_s^0.

Remerciements

URANT les cinq années de mon doctorat, j'ai eu le privilège de rencontrer et découvrir de nombreuses personnes qui, par leur aide ou leur soutien, ont contribué à la réussite de ce travail de longue haleine. Cette page leur est dédiée.

J'aimerais commencer par exprimer ma profonde gratitude envers le Docteur Minh Tâm Tran, mon directeur de thèse, pour m'avoir suivi et accompagné dans mon travail pendant ces cinq années. En plus de son aide précieuse et de ses encouragements, j'ai beaucoup apprécié le rituel thé vert au jasmin de quatre heures, qui m'apportait la dose d'excitant nécessaire aux longues soirées de labeur.

Mes remerciements vont aussi au Professeur Aurelio Bay pour m'avoir permis de débuter dans le domaine à l'occasion de mon travail de diplôme, et pour m'avoir donné la possibilité de réaliser cette thèse. Son aide fut très appréciable pendant mes mesures de bruit sur le système d'acquisition de l'"Inner Tracker".

Je tiens également à remercier le Professeur Olivier Schneider qui m'a judicieusement conseillé et motivé tout au long de mon analyse.

Mon travail dans la collaboration LHCb a été un grand plaisir. Le développement du détecteur et les analyses physiques se sont déroulés dans un esprit de motivation respective. Notre porte-parole, le Professeur Tatsuya Nakada, y a contribué pour beaucoup.

Je tiens donc à remercier tous les membres de la collaboration LHCb qui de près ou de loin ont participé à la réalisation de ce travail, en particulier Luis Fernández, Patrick Koppenburg, Yvan Belyaev, Jeroen Van Hunen, Gloria Corti et Gerhard Raven.

Un grand merci aussi à toute l'équipe de l'"Inner Tracker" et du VELO ainsi qu'aux électriciens du 5ème étage et à l'atelier mécanique du Cubotron, en particulier Paula Collins, Olivier Dormond, José Hernando, Raymond Frei, Guy Masson et Jean-Philippe Hertig pour leur serviabilité et leur efficacité.

Je souhaite remercier encore tous les membres du Laboratoire de Physique des Hautes Energies de l'EPFL, à Lausanne, pour l'atmosphère chaleureuse et stimulante qu'ils y mettent. Tout particulièrement, je remercie nos charmantes secrétaires Mesdames Erika Lüthi, Monique Romaniszin et Esther Hofman qui contribuent grandement à sa merveilleuse ambiance ainsi qu'à son bon fonctionnement.

Un immense merci à mon collègue Charles Currat avec qui j'ai partagé le bureau pendant de nombreuses années et qui m'a initié à la programmation, non sans quelques difficultés. J'ai apprécié sa patience et son humour incisif. Je tiens aussi à remercier Hubert, Odie et Christian, nos "gourous" informaticiens, qui ont su m'empêcher de sombrer corps et âme dans les méandres de l'informatique.

Merci beaucoup à Luis Fernández pour notre fructueuse collaboration, ses conseils avisés et sa lecture critique de mon mémoire. Mes remerciements vont aussi à tous mes

collègues pour leur camaraderie et les moments de détentes nécessaires au bon rendement de mes neurones.

Et je n'oublie pas toutes mes amies et amis qui m'ont permis de garder les pieds sur terre et de sortir le nez de mon bureau, que ce soit à travers le sport, la salsa ou toute autre revigorante et sympatique occasion, fRED, DKI&, Alexandre, les "Gen" de Fully, Conga Cao, Salsa Factory et bien d'autres.

Enfin, je remercie du fond du coeur toute ma grande famille. Ma gratitude va tout d'abord à mes parents qui ont su m'encourager et me soutenir durant tout mon parcours. Un grand merci ensuite à mes frères et leurs compagnes pour les agréables moments de détente et les discussions animées que nous avons partagés. Mon grand-père mérite aussi un clin d'oeil dans cette page pour sa constante curiosité à l'égard de mon travail ainsi que Nicolas pour ses délicieux vins rouges qui m'ont si bien désaltéré. Finalement merci à tous ceux que je ne mentionne pas ici mais qui ont leur place dans mon coeur.

C'est à mon amour, Leslie, que j'adresse enfin mille mercis. Merci tout d'abord pour sa patience - la thèse étant parfois une "amante" très possessive; merci aussi pour ses encouragements - il y eu des périodes "légèrement" stressantes ces dernières années; et les 998 mercis qui restent je les consacre à sa douce présence chaque jour à mes côtés.

Lausanne, le 7 novembre 2005.

Contents

Introduction

$\mathcal{D}$URING the last thirty years, the Standard Model of particle physics has been developed and the various particles of this model have been discovered. Almost all experimental tests of the three forces described by the Standard Model have agreed with its predictions. However it has two important weaknesses:

- The model contains 19 free parameters which cannot be independently calculated;

- The model does not describe the gravitational interaction.

One can think of the Standard Model as a low-energy realization of a more general theory.

The most important challenge for particle physicists in the next decade will be to constrain the Standard Model and eventually find a theory which goes beyond it. In this perspective, experiments related to CP violation will play an important role. In the Standard Model, CP violation is directly connected to the quark mass terms and, for three generations of quarks, is described by a single phase of the quark mixing matrix. A complete study of CP violation in the quark sector will certainly help to better understand this phenomenon.

Moreover, observations of the Universe show that there is practically no anti-matter left, while we believe that the Universe has been created in a symmetric way from pure energy, i.e. with the same amount of matter and anti-matter. CP violation in the first moments of our Universe seems necessary to explain the deficit of anti-matter which is generally stated as the present ratio between the number of baryons and the number of photons $\eta = n_B/n_\gamma = (4 \pm 1) \cdot 10^{-10}$ [1]. Primordial Baryo- and Lepto- genesis based on the Standard Model cannot however predict this ratio [2]. One has to invoke the Grand Unified Theories (GUT) to reproduce the η ratio.

Experimentally, the CP-violation in the quark sector consists in the study of asymmetries in meson decays. It has been observed for the first time in the neutral kaon system [3] more than thirty years ago. In the B-meson system, it has been brought to light by the BABAR and Belle experiments [4, 5] with $B_d^0 \rightarrow J/\psi\ K_S^0$ decays. These experiments are still taking data and will certainly run until the first years of LHCb data taking.

These B-factories operate at the $\Upsilon(4S)$ resonance and do not have access to the B_s^0 nor to the B_c^0 particles which have higher masses than the B_d^0 and $B^\pm$ mesons and which can be produced in hadron machines. The LHCb experiment will use the p − p collisions in which all the B-spectrum can be produced. The experiment is due to start in 2007.

We will present in Chapter (1) of this dissertation the theoretical aspects of the CP violation, focusing on the B_s^0-meson sector.

The LHCb experiment is a single arm spectrometer. This geometry has been chosen to take advantages of the angular distribution of the B-mesons. The detector and its

components will be developed in Chapter (2). The trigger system, one of the biggest challenge of this experiment, will also be described there.

The simulation of the detector is of major importance both for the studies during the construction phase as well as during the running of the detector. The different tools used for the present analysis will be briefly described in Chapter (3). The performances of the LHCb experiment will also be detailed.

The present work will focus especially on the study of the $\bar{b} \to \bar{c}c\bar{s}$ quark transition into pure CP eigenstates. These decays are interesting as they are free of any polluting contributions and give a direct access to the weak mixing phase ϕ_s measuring the CP violation in the B_s^0 sector.

Chapter (4) will detail the reconstruction and performances of the $B_s^0 \to J/\psi\,\eta$ selection at LHCb as well as its background rejection for the two decay channels: $B_s^0 \to J/\psi(\mu^+\,\mu^-)\,\eta(\gamma\,\gamma)$ and $B_s^0 \to J/\psi(\mu^+\,\mu^-)\,\eta(\pi^+\,\pi^-\,\pi^0)$.

Chapter (5) will give the estimations of the LHCb experiment sensitivity to the B_s^0 weak mixing phase ϕ_s for the $\bar{b} \to \bar{c}c\bar{s}$ decays to pure CP-eigenstates. They will then be compared to the golden decay mode $B_s^0 \to J/\psi\,\phi$ which is an admixture of CP eigenstates.

Chapter 1

Theoretical Overview
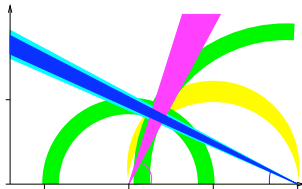
This chapter gives a brief review of the Standard Model of particle physics and with a special emphasis on the electro-weak interaction. The flavor mixing and the CP violating asymmetry in the Standard Model particularly in the B-physics field are introduced. The $B_s^0 \to J/\psi\ \eta$ decay is presented as a possible probe of New Physics provided a large sample of these decays can be reconstructed[1].

ORE than 20 years ago, S. Glashow, A. Salam and S. Weinberg elaborated the *Standard Model of electro-weak interactions* [11, 12, 13] which earned them the Nobel Prize. This theory combined with *Quantum Chromodynamics* (QCD) is part of the more general *Standard Model*[2] (SM) which is the most successful theory of elementary particles at the present time as all its predictions are consistent with experiments.

Physicists believe that the SM is an effective low-energy model of a more fundamental theory, the *Grand Unified Theory* (GUT). However no experimental evidences but hints for physics beyond the SM have been observed yet.

Although the Standard Model is able to describe a huge amount of experimental data[3] open questions still exist, in particular the origin of the fermion masses, the mixing and the electro-weak symmetry breaking. The fact that C, P, CP and T symmetries are observed in strong and electromagnetic interactions, but not in weak interactions is also puzzling.

For the first time CP violation in B-meson decays has been recently observed at B-factories [4, 5, 15] and other exciting results are expected in the next years. However, precise measurements with high statistics are required to constrain the theoretical models and to lead to the discovery of phenomena beyond the Standard Model. Such high statistics will be provided by the LHC.

---

[1]This chapter is inspired by [6, 7, 8, 9, 10].

[2]A distinction between the whole SM and its electro-weak sector will not be needed in this work as most of its topics are governed by electro-weak interactions.

[3]See for instance the impressive review of the electro-weak model from the Particle Data Group [14].

1.1   Discrete symmetries

The intimate connection between symmetries and conservation laws [4] is perhaps nowhere as evident as in elementary particle physics. In quantum mechanics, considerations based on symmetry of the interactions determine the structure of the Hamiltonian. In this context, a few discrete transformations are particularly relevant. They are briefly described below with their effect on the quantum state $|f(\vec{p}, h)\rangle$ of a particle of momentum $\vec{p}$ and helicity $h = \vec{s} \cdot \vec{p}/|\vec{p}|$, $\vec{s}$ being the particle intrinsic spin.

- **Particle−anti-particle exchange**, described by the charge conjugation operator C:

$$\mathrm{C}|f(\vec{p}, h)\rangle = \eta_\mathrm{C}|\overline{f}(\vec{p}, h)\rangle,$$

- **Spatial inversion**, described by the parity operator P:

$$\mathrm{P}|f(\vec{p}, h)\rangle = \eta_\mathrm{P}|f(-\vec{p}, -h)\rangle,$$

- **Time reversal**, described by the operator T:

$$\mathrm{T}|f(\vec{p}, h)\rangle = \eta_\mathrm{T}^s|f(-\vec{p}, h)\rangle^*,$$

where η_C is a phase factor, η_P is the intrinsic parity of the particle and η_T^s is another phase factor depending on the spin.

The three discrete symmetries C, P and T are exact for strong and electromagnetic interactions, while in weak interactions experimental observations show an obvious violation of the parity and charge conjugation. For the combined CP a slight violation has been observed. In particular this aspect has been pointed out in specific systems in sub-nuclear physics, as neutral K-mesons, for which the first observations date back to 1964 [3] and more recently, neutral B-mesons [4, 5, 15].

Together, the combined operation of time reversal, space inversion and charge conjugation, CPT, appears to be a conserved fundamental symmetry: this has important and very general consequences [17]. An immediate consequence is that the mass and the lifetime of an elementary particle and its anti-particle must be equal. Up to now all the experimental observations obtained are consistent with this rule.

We present in this dissertation the prospective studies made for the $\mathrm{B}_\mathrm{s}^0 \rightarrow \mathrm{J}/\psi\,\eta$ channel. This work can be considered as a first step in the direction of future analyzes that will concern CP violation in the B_s^0 sector. In the following sections, a survey on the phenomenology will be presented.

1.2   Standard Model

The Standard Model is a gauge theory based on the $\mathrm{SU(3)_C} \otimes \mathrm{SU(2)_L} \otimes \mathrm{U(1)_Y}$ groups, which describes the strong, weak and electromagnetic interactions via gauge boson exchange: 8 gluons and 1 photon, all massless, for the strong and electromagnetic forces respectively, and 3 massive bosons, $\mathrm{W}^\pm$ and Z^0, for the weak force. Strong interactions are governed

---

[4]The close connection between the standard conservation laws and the symmetries of space and time appears to have originated in 1918 with Noether's famous paper [16]. Indeed this principle is sometimes referred to as "Noether's theorem" although Noether's theorem itself contains only a very partial statement of it.

by the $SU(3)_C$ group while the $SU(2)_L \otimes U(1)_Y$ groups present a unified description of the electro-weak interactions.

Among the fermions, the fundamental constituents of the matter, we distinguish the leptons and the quarks. They present a definite structure and are classified in three families:

$$\begin{bmatrix} \nu_e \\ e^- \end{bmatrix} \begin{bmatrix} u \\ d \end{bmatrix} \qquad \begin{bmatrix} \nu_\mu \\ \mu^- \end{bmatrix} \begin{bmatrix} c \\ s \end{bmatrix} \qquad \begin{bmatrix} \nu_\tau \\ \tau^- \end{bmatrix} \begin{bmatrix} t \\ b \end{bmatrix},$$

where the leptons are defined by:

$$\begin{bmatrix} \nu_\ell \\ \ell^- \end{bmatrix} \equiv \begin{pmatrix} \nu_\ell \\ \ell^- \end{pmatrix}_L, \quad (\ell^-)_R,$$

and each quark appears with three different colors:

$$\begin{bmatrix} q_{up} \\ q_{down} \end{bmatrix} \equiv \begin{pmatrix} q_{up} \\ q_{down} \end{pmatrix}_L, \quad (q_{up})_R, \quad (q_{down})_R.$$

The subscripts L and R refer to the particle helicity. The left (right) helicity field are doublets (singlets) of $SU(2)_L$. Moreover each particle is assigned an anti-particle of the same mass, but opposite charge. The three families differ only through their masses and quantum numbers.

It is the merit of Glashow, Weinberg and Salam to have developed an extremely clever model for the "electroweak interactions" in which they incorporate the successful theory of Quantum Electrodynamics (QED) and provide a description of the weak forces in terms of an exchange of massive vector bosons. The model is clever in the sense that it preserves the masslessness of the photon while giving mass to the weak interaction gauge bosons $W^\pm$ and Z^0. This is achieved by the use of the Higgs mechanism and a suitable choice of the Higgs fields. The gauge boson masses depend on the weak angle θ_W, a parameter which must be determined from the experiments. The spinless Higgs particle is yet to be discovered.

We briefly outline hereafter the main points of this model.

1.2.1 The weak interaction Lagrangian

One gets the following Lagrangian density for the electro-weak interactions:

$$\mathcal{L}_{EW} = \mathcal{L}_{bosons} + \mathcal{L}_{fermions} + \mathcal{L}_{Higgs} + \mathcal{L}_{Yukawa},$$

where the kinetic term for the free massless gauge bosons is $\mathcal{L}_{bosons} = -\frac{1}{4}G^a_{\mu\nu}G^{a\,\mu\nu} - \frac{1}{4}B_{\mu\nu}B^{\mu\nu}$. In this expression:

$$B_{\mu\nu} = \partial_\mu B_\nu - \partial_\nu B_\mu$$

and

$$G^a_{\mu\nu} = \partial_\mu W^a_\nu - \partial_\nu W^a_\mu + g\,\epsilon^{abc}W^b_\mu W^c_\nu \qquad a,\,b,\,c = 1,\,2,\,3,$$

with $\overrightarrow{W}$ and B gauge bosons.

The second term of the electroweak Lagrangian is:

$$\mathcal{L}_{fermions} = \overline{\Psi}_L \gamma_\mu \left(\partial_\mu - ig\frac{\vec{\sigma}}{2}\overrightarrow{W}_\mu - ig'\frac{Y}{2}B_\mu \right) \Psi_L + \overline{\Psi}_R \gamma_\mu \left(\partial_\mu - ig'\frac{Y}{2}B_\mu \right) \Psi_R,$$

describing the free fermion propagation as well as their coupling to the $\vec{W}$ and B gauge fields. In $\mathcal{L}_{fermions}$, the Ψ are the spinor fields of the fermions, g and g' are the coupling constant to the U(1)$_\text{Y}$ and SU(2)$_\text{L}$ gauge groups, Y is the hypercharge defined by Y = $2(\text{I}_3 + \text{Q})$ where I$_3$ is the third component of the weak isospin and Q the electric charge.

In the Standard Model, the coupling of the Higgs boson to the massless bosons $\vec{W}$ and B will give mass to the W gauge bosons. The Higgs mechanism [18] gets rid of this lack introducing a $\mathcal{L}_{Higgs}$ gauge invariant term, which can give a mass to the particles through a symmetry breaking:

$$\mathcal{L}_{Higgs} = \left(\left(\partial_\mu - ig\frac{\vec{\sigma}}{2}\overrightarrow{W}_\mu - ig'\frac{\text{Y}}{2}B_\mu \right) \Phi \right)^\dagger \left(\partial_\mu - ig\frac{\vec{\sigma}}{2}\overrightarrow{W}_\mu - ig'\frac{\text{Y}}{2}B_\mu \right) \Phi - V(\Phi),$$

where $\Phi(x) = \begin{pmatrix} \Phi^+ \\ \Phi^0 \end{pmatrix}$ is a doublet of scalar fields in the minimal SM and $V(\Phi)$ is generally chosen to be $\mu^2\Phi^\dagger\Phi + \frac{\lambda}{4}(\Phi^\dagger\Phi)^2$. We choose Φ^0 to have the non zero value $\frac{v}{\sqrt{2}}$ in vacuum. The scalar field in the vacuum state then is written:

$$\Phi = \Phi_{vac} = \frac{1}{\sqrt{2}} \begin{pmatrix} 0 \\ v \end{pmatrix}.$$

This is the so-called "spontaneous symmetry breaking".

Inserting this scalar field in $\mathcal{L}_{Higgs}$ and identifying the field which multiplies the combination $\frac{1}{2}(1 + \sigma_3) = \begin{pmatrix} 1 & 0 \\ 0 & 0 \end{pmatrix}$ to the photon, one arrives at $\begin{pmatrix} A_\mu \\ Z^0_\mu \end{pmatrix} = \mathcal{R}(\theta_W) \begin{pmatrix} B_\mu \\ W^3_\mu \end{pmatrix}$, $\mathcal{R}(\theta_W)$ being the rotation matrix of angle θ_W, the Weinberg angle.

The fields of the charged vector bosons can then be found: $W^\pm_\mu = \frac{W^1_\mu \pm W^2_\mu}{\sqrt{2}}$. Their masses are $M_W = \frac{g\,v}{2}$ and $M_Z = \frac{g\,v}{2\cos\theta_W}$.

The fermion masses

The Higgs doublet is then used to give mass to the fermions via a Yukawa type coupling. For the leptons, one has:

$$\mathcal{L}_{Yukawa-lepton} = -G_\ell \left[(\overline{L}\Phi)R + \overline{R}(\Phi^\dagger L) \right],$$

where G_ℓ is the Yukawa coupling constant, $L = \begin{pmatrix} \nu_\ell \\ \ell \end{pmatrix}$ is the left-handed doublet and R the right handed singlet. The non-zero vacuum of Φ which breaks the gauge symmetry gives:

$$\begin{aligned} \mathcal{L}_{Yukawa-lepton} &= -G_\ell \left[\overline{L} \begin{pmatrix} 0 \\ v/\sqrt{2} \end{pmatrix} R + \overline{R}\,(0, v/\sqrt{2})\,L \right] \\ &= -\frac{G_\ell\, v}{\sqrt{2}} \left(\overline{\ell}_L\ell_R + \overline{\ell}_R\ell_L \right) = -\frac{G_\ell\, v}{\sqrt{2}}\,\overline{\ell}\ell. \end{aligned}$$

This gives a mass to the charged leptons. In SM, the neutrinos only exist as a left-handed particles and, therefore, do not have mass.

The treatment for the quarks is quite similar. However, the Lagrangian has to allow charged current transformations from a quark of flavor i to another one of flavor j: these coupling are characterized by the Cabibbo-Kobayashi-Maskawa unitary matrix V_{CKM} which gives the quark mass eigenstates in terms of interaction eigenstates (see (1.3)). This kind of mixing does not appear in the lepton sector as the neutrinos do not have mass.

1.2.2 The limitations of the Standard Model

The SM is very powerful in predicting physics phenomena, however some weaknesses are present. The number of parameters (19) is high, gravitation is not included and the model does not explain the mass hierarchy. Moreover, the coupling constants associated to the three gauge groups evolve with energy, in compliance with the renormalization group equations and converge approximatively to an energy of $\sim 10^{16}$ GeV suggesting a unification of the strong and the electro-weak interactions there. At these energies, the Higgs boson mass suffers from radiative corrections which are quadratically divergent with respect to their energies and which can be stabilized only with fine adjustments (gauge hierarchy problem). The Supersymmetry models can bring a solution to this problem, but they have not been experimentally proved yet.

Recent experiments measuring the atmospheric neutrino fluxes and solar neutrino fluxes have observed that:

- The atmospheric muon neutrinos flux depends upon the particles' zenith angle, i.e. upon the distance they travel from their origin to the detector the SuperKamiokande experiment;

- The solar neutrino experiment at the Sudbury Neutrino Observatory (SNO) has determined that the ν_e flux that was originally produced in the Sun becomes a flux of ν_e, ν_μ and ν_τ at earth level. This result has been confirmed by the KamLAND experiment which uses anti-neutrinos from reactors located at about 100 km of their site.

These results show that neutrinos do change flavor in their propagation and that they have different masses; we know at the time being two of the mass differences but we do not know the absolute scale. Neutrinos having mass are certainly beyond the Standard Model.

1.3 Quark mixing

Although the origin of CP violation is a mystery of Particle Physics, one can phenomenologically accommodate it within the Standard Model. The charged current Lagrangian $\mathcal{L}_q^{cc}$ describing the interaction between quarks and W bosons can be written as:

$$\mathcal{L}_q^{cc} = -\frac{g}{\sqrt{2}} \left(J_\mu^{cc\dagger} W^\mu + J_\mu^{cc} W^{\mu\dagger} \right)$$

where g is the weak coupling constant, J_μ^{cc} the charge current and W^μ the W-field. The charge current which couples to the $W^\pm$ can be expanded as [19]:

$$J_\mu^{cc} = (\overline{\text{u}}, \overline{\text{c}}, \overline{\text{t}})_L \, \gamma_\mu V_{\text{CKM}} \begin{pmatrix} \text{d} \\ \text{s} \\ \text{b} \end{pmatrix}_L$$

where V_{CKM} is a 3×3 unitary matrix in flavor space. This unitary matrix connects the electro-weak states $(\text{d}', \text{s}', \text{b}')$ of the down, strange and bottom quarks with their mass eigenstates $(\text{d}, \text{s}, \text{b})$ through [7]:

$$
\begin{pmatrix} \text{d'} \\ \text{s'} \\ \text{b'} \end{pmatrix} = V_{\text{CKM}} \cdot \begin{pmatrix} \text{d} \\ \text{s} \\ \text{b} \end{pmatrix} = \begin{pmatrix} V_{\text{ud}} & V_{\text{us}} & V_{\text{ub}} \\ V_{\text{cd}} & V_{\text{cs}} & V_{\text{cb}} \\ V_{\text{td}} & V_{\text{ts}} & V_{\text{tb}} \end{pmatrix} \cdot \begin{pmatrix} \text{d} \\ \text{s} \\ \text{b} \end{pmatrix} .
$$

It has been introduced in 1973 by Kobayashi and Maskawa [19] who extended the Cabibbo $-$ Glashow $-$ Iliopoulos $-$ Maiani [20, 21] scheme to include a third generation of quark, even before the discovery of the charm quark !

1.3.1   Number of independent parameters

A general $(n \times n)$ complex matrix possesses *a priori* $2n^2$ real parameters. However V_{CKM} being unitary, the number of independent parameters can be reduced to n^2. As one deals with $2n$ quark fields, one has the liberty to choosing $2n-1$ relative phases and thus further reduce the number of parameters by $2n - 1$. The matrix V_{CKM} therefore has

$$
n^2 - (2n - 1) = (n - 1)^2
$$

physically independent parameters.

For $n = 2$, the Cabibbo 2×2 matrix has only one real parameter which has been chosen to be the Cabibbo angle. CP violation cannot be accommodated in the SM as the matrix is real.

For $n = 3$, the Kobayashi $-$ Maskawa 3×3 matrix has four independent parameters of which three can be taken as the mixing angles between generations and one is a complex phase. It is this phase which describes CP violation. It should be emphasized that these four parameters are fundamental constants and need to be experimentally determined.

1.3.2   The V_{CKM} matrix

V_{CKM} may be parameterized on a variety of ways. The Particle Data Group [14] uses the Chau-Keung parameterization [22]:

$$
V_{\text{CKM}} = \begin{pmatrix} c_{12}c_{13} & s_{12}c_{13} & s_{13}e^{i\delta_{13}} \\ -s_{12}c_{23} - c_{12}s_{23}s_{13}e^{i\delta_{13}} & c_{12}c_{23} - s_{12}s_{23}s_{13}e^{i\delta_{13}} & s_{23}c_{13} \\ s_{12}s_{23} - c_{12}c_{23}s_{13}e^{i\delta_{13}} & -c_{12}s_{23} - s_{12}c_{23}s_{13}e^{i\delta_{13}} & c_{23}c_{13} \end{pmatrix} ,
$$

where $c_{ij} = \cos\theta_{ij}$ and $s_{ij} = \sin\theta_{ij}$ control the mixing between the three i, j families while δ_{13} is the CP violation phase. This parameterization presents some interesting characteristics:

- s_{13} corresponds to $|V_{\text{ub}}| \sim \mathcal{O}(10^{-3})$. This implies that $c_{13} \sim 1$ and that the terms V_{ud}, V_{us}, V_{cb} and V_{tb} can be determined by one parameter up to the order $\mathcal{O}(10^{-4})$. This behavior greatly simplifies the parameter values extraction from the experimental data and the comparison with the expectations.

- s_{23} is directly connected to the transition $\text{b} \rightarrow \text{c}$.

- CP violation is suppressed by a factor s_{13}.

In order to describe the characteristics of the V_{CKM} matrix in a more quantitative manner, Wolfenstein [23] proposed a parameterization based on experimental results

$$|V_{\text{us}}|^3 \approx |V_{\text{cb}}|^{3/2} \approx |V_{\text{ub}}|,$$

and on unitarity, to obtain the matrix elements as a series expansions in $\lambda \equiv \sin\theta_{\text{C}} \equiv |V_{\text{us}}| \approx 0.22$. Choosing a phase convention in which V_{ud}, V_{us}, V_{cd}, V_{ts} and V_{tb} are real, Wolfenstein proposed:

$$V_{\text{CKM}} = \begin{pmatrix} 1 - \frac{1}{2}\lambda^2 & \lambda & A\lambda^3(\rho - i\eta) \\ -\lambda & 1 - \frac{1}{2}\lambda^2 & A\lambda^2 \\ A\lambda^3(1 - \rho - i\eta) & -A\lambda^2 & 1 \end{pmatrix} + \delta V_{\text{CKM}},$$

here the series expansion is truncated at order $\mathcal{O}(\delta V_{\text{CKM}}) = \mathcal{O}(\lambda^4)$. The B-meson system, especially for the B_s^0, requires a more accurate determination of the V_{CKM} matrix elements, including $\mathcal{O}(\lambda^5)$ corrections, which are given by [7, 8]:

$$\delta V_{\text{CKM}} = \begin{pmatrix} -\frac{1}{8}\lambda^4 & 0 & 0 \\ \frac{1}{2}A^2\lambda^5\left(1 - 2(\rho + i\eta)\right) & -\frac{1}{8}\lambda^4(1 + 4A^2) & 0 \\ \frac{1}{2}A\lambda^5(\rho + i\eta) & \frac{1}{2}A\lambda^4\left(1 - 2(\rho + i\eta)\right) & -\frac{1}{2}A^2\lambda^4 \end{pmatrix} + \mathcal{O}(\lambda^6).$$

It is also possible to introduce the generalized Wolfenstein parameters:

$$\overline{\rho} = \rho(1 - \frac{\lambda^2}{2}) \quad \text{and} \quad \overline{\eta} = \eta(1 - \frac{\lambda^2}{2}),$$

and then the V_{td} component of the CKM matrix can simply be written, up to corrections of $\mathcal{O}(\lambda^5)$:

$$V_{\text{td}} = A\lambda^3(1 - \overline{\rho} - i\overline{\eta}).$$

In this notation, $\overline{\rho} + i\overline{\eta} = -\dfrac{V_{\text{ud}}V_{\text{ub}}^*}{V_{\text{cd}}V_{\text{cb}}^*}.$

1.3.3 The unitarity triangles (UT)

The unitarity of the CKM matrix, $V_{\text{CKM}}^\dagger V_{\text{CKM}} = 1 = V_{\text{CKM}} V_{\text{CKM}}^\dagger$, leads to the following set of equations:

$$\sum_k V_{ki}V_{kj}^* = \delta_{ij}$$

where k indexes all the quarks. The orthogonality relations are of particular interest since they can be represented as six "unitarity triangles" in the complex plane with rather different shapes [24, 25, 26]:

$$\textbf{(sd)} \quad V_{\text{us}}V_{\text{ud}}^* + V_{\text{cs}}V_{\text{cd}}^* + V_{\text{ts}}V_{\text{td}}^* = 0, \tag{1.1}$$

$$\textbf{(sb)} \quad V_{\text{us}}V_{\text{ub}}^* + V_{\text{cs}}V_{\text{cb}}^* + V_{\text{ts}}V_{\text{tb}}^* = 0, \tag{1.2}$$

$$\textbf{(db)} \quad V_{\text{ud}}V_{\text{ub}}^* + V_{\text{cd}}V_{\text{cb}}^* + V_{\text{td}}V_{\text{tb}}^* = 0, \tag{1.3}$$

$$\textbf{(uc)} \quad V_{\text{ud}}V_{\text{cd}}^* + V_{\text{us}}V_{\text{cs}}^* + V_{\text{ub}}V_{\text{cb}}^* = 0, \tag{1.4}$$

$$\textbf{(ct)} \quad V_{\text{cd}}V_{\text{td}}^* + V_{\text{cs}}V_{\text{ts}}^* + V_{\text{cb}}V_{\text{tb}}^* = 0, \tag{1.5}$$

$$\textbf{(tu)} \quad V_{\text{td}}V_{\text{ud}}^* + V_{\text{ts}}V_{\text{us}}^* + V_{\text{tb}}V_{\text{ub}}^* = 0, \tag{1.6}$$

where the first three relations express the orthogonality of two different columns, and the last three two different rows. Using the Wolfenstein expansion, we see that the sides of the triangles in Eq. (1.3) and (1.6) are all of order λ^3. The triangles in Eq. (1.2) and (1.5) have two sides of order λ^2 and one side of order λ^4 while those in Eq. (1.1) and (1.4) have two sides of order λ and one side of order λ^5. All six triangles have the same area $A_\Delta = |J_{CP}|/2 = A^2\lambda^6|\eta|$ where J_{CP} is the "Jarlskog parameter"[5] and are represented on Fig. (1.1).
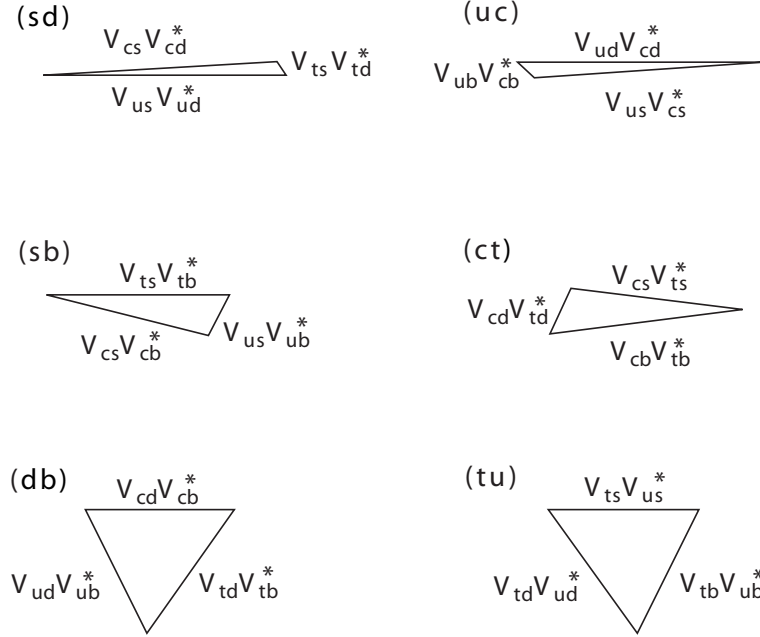
Figure 1.1: *The six unitarity triangles.*

From (1.3) we can define the three angles of the (**db**) triangle:

$$\alpha \equiv \phi_2 \equiv \arg\left[-\frac{V_{td}V_{tb}^*}{V_{ud}V_{ub}^*}\right], \quad \beta \equiv \phi_1 \equiv \arg\left[-\frac{V_{cd}V_{cb}^*}{V_{td}V_{tb}^*}\right], \quad \gamma \equiv \phi_3 \equiv \arg\left[-\frac{V_{ud}V_{ub}^*}{V_{cd}V_{cb}^*}\right].$$

Another characteristic angle, χ, of unitarity triangles of order $\mathcal{O}(\lambda^2)$, essential for the B_s^0 system, can be defined from the Eq. (1.2) and triangle (**sb**), as well as its equivalent for the K-system, χ' (Eq. (1.1)) and triangle (**sd**):

$$\chi \equiv \beta_s \equiv \arg\left[-\frac{V_{cb}V_{cs}^*}{V_{tb}V_{ts}^*}\right] \simeq \lambda^2\eta \simeq \arg(V_{ts}) - \pi, \quad \chi' \equiv \beta_K \equiv \arg\left[-\frac{V_{us}V_{ud}^*}{V_{cs}V_{cd}^*}\right] \simeq A^2\lambda^4\eta. \tag{1.7}$$

Several models going beyond the SM predict an additional contribution to V_{CKM} due to New Physics in such a way that $\beta^{\text{measured}} \rightarrow \beta - \beta^{\text{new physics}}$ and $\alpha^{\text{measured}} \rightarrow \alpha - \alpha^{\text{new physics}}$. Thus the requirement that the sum of the three angles add up to π will not be fulfilled if New Physics were present.

---

[5]The "Jarlskog parameter" J_{CP} represents a measure of the "strength" of the CP violation within the Standard Model [27].

1.3.4 Measurements of the unitarity triangles parameters

A very systematic way to search for New Physics consists in measuring both the three angles and the sides of the triangles in order to over-constrain the measurements and to look for inconsistencies. While β angle can be precisely studied at the present B-factories, the other angles will be known with reduced accuracy. This is the reason why LHCb experiment, as well as "Super B-factories"[6], has been proposed. The different characteristics of the unitarity triangles can be measured through specific decays:
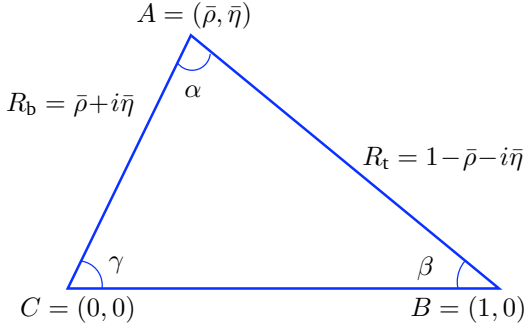
Figure 1.2: *The main unitary triangle (db), corresponding to relation (1.3).*
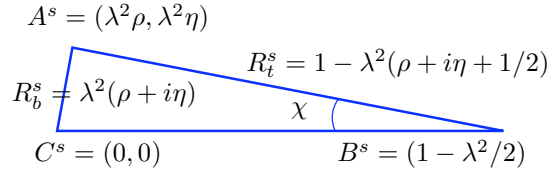
Figure 1.3: *The unitary triangle corresponding to relation (1.2). This triangle (sb) is squashed due to one side (A^sC^s) being $\mathcal{O}(\lambda^2)$ and the two others $\mathcal{O}(1)$.*

α $B_d^0 \to \rho\,\pi$, as well as $B_d^0 \to \pi^+\,\pi^-$, gives access to $\sin(2\alpha)$ but the second decay requires the knowledge of the "penguin pollution", which can be extracted from $B_d^0 \to K^\pm\,\pi^\mp$.

β The $B_d^0 - \overline{B}_d^0$ mixing phase ϕ_d turns out to be equal to 2β and can be extracted from $B_d^0 \to J/\psi\,K_S^0$ and similar channels. $B_d^0 \to \phi\,K_S^0$ also allows the measurement of 2β but is dominated by penguin loops. Both measurements giving different results could show signs of New Physics.

γ This angle can be accessed by the $B_d^0 \to D^{(*)}\,\pi$ channels, which give $\gamma + \phi_d$, with ϕ_d obtained from the measurement described above. There is also the $B_s^0 \to D_s\,K$ channel, which is sensitive to $\gamma + \phi_s$.

χ This angle can be estimated with the B_s^0 mixing phase, ϕ_s, which is equal to -2χ in the SM and can be extracted from asymmetries in $B_s^0 \to J/\psi\,\phi$, $B_s^0 \to J/\psi\,\eta$, $B_s^0 \to \eta_c\,\phi$ or $B_s^0 \to J/\psi\,\eta'$.

$|\mathbf{R_b}|$ This is the length of the CA side of the unitarity triangle (**db**) which involves the ratio $|V_{ub}|/|V_{cb}|$. Both the numerator and the denominator can be obtained via semi-leptonic decays of B-mesons, e.g. $b \to u\ell\overline{\nu}$ or $b \to c\ell\overline{\nu}$ decay processes.

---

[6]"Super B-Factories" [28] are colliders working at much higher particle intensities than the present ones. They would expand the existing programs at SLAC and KEK, and complement the LHCb physics program. Luminosity 40 times higher than that in current B-factories, producing 10 billion B-meson pairs per year, will allow studies of rare B-decays, enlightening the asymmetries to a high degree of accuracy. Like BABAR and Belle, the Super B-Factories would detect B-meson decays produced in e^+-e^- collisions, and will allow access to rare decays involving neutrinos or multiple photons which are difficult or impossible to study at a proton collider like the LHC.

$|\mathbf{R_t}|$ This is the length of the AB side of the unitarity triangle (**db**), $|R_t| = \frac{1}{\lambda}\left|\frac{V_{td}}{V_{cd}}\right|$, where
the problematic term is V_{td}. However it can be determined with the help of the mass
difference $\Delta m_{d,s}$ of the mass eigenstates of the neutral B_d^0 and B_s^0 meson systems
with $\frac{\Delta m_s}{\Delta m_d} = \frac{m_{B_s^0}}{m_{B_d^0}}\xi^2\frac{|V_{ts}|^2}{|V_{td}|^2}$ where ξ (of order unity) expresses hadronic structure
functions. More specifically the ratio $\Delta m_d/\Delta m_s$ is independent of m_t and short dis-
tance QCD corrections. In principle, this ratio is affected by much smaller theoretical
uncertainties than the hadronic matrix elements appearing in Δm_d and Δm_s sepa-
rately. The determination of $|V_{td}|/|V_{ts}|$ can also be done with rare decays through
$b \to \ell\ell$d,s transitions.

1.4 Neutral B-meson system

The B-mesons are quark−anti-quark bound states of well-defined flavor, known as flavor
eigenstates, and contain one b-quark. They have been discovered by the CUSB and CLEO
experiments in 1981 [29, 30, 31]. Tab. (1.1) gives the masses and lifetimes of the different
B-mesons as well as the Λ_b^0 baryon.

b-particles		Mass [MeV/c^2]		Lifetime [ps]
B_u^+	(**u$\overline{\text{b}}$**)	5279.0 $\pm$	0.5	1.643 $\pm$ 0.010
B_d^0	(**d$\overline{\text{b}}$**)	5279.4 $\pm$	0.5	1.528 $\pm$ 0.009
B_s^0	(**s$\overline{\text{b}}$**)	5369.6 $\pm$	2.4	1.472 $\pm$ 0.045
B_c^+	(**c$\overline{\text{b}}$**)	6400 $\pm$ 400		0.45 $\pm$ 0.12
Λ_b^0	(**udb**)	5624 $\pm$ 9		1.232 $\pm$ 0.072

Table 1.1: *Mass and lifetime of different b-particles [14, 32].*

If only the strong and the electromagnetic interactions were present, then the B_q^0 and
the $\overline{B}_q^0$ would be stable and form a particle−anti-particle pair with the same mass. How-
ever, due to the presence of weak interactions, these mesons decay. Since there is not
any conservation law which prevents the B_q^0 and the $\overline{B}_q^0$ from having both real and virtual
transitions to a common state, they can oscillate among themselves before decaying. This
phenomenon is known as mixing.

1.4.1 B-meson decays

The weak decays of the B-mesons can be
divided into leptonic, semi-leptonic and
non-leptonic transitions. The leptonic
modes $B^- \to \ell^- \overline{\nu}_\ell$, where ℓ stands for e
and μ, have branching ratios at the 10^{-5}
and 10^{-4} level, and are very hard to mea-
sure. The semi-leptonic decays are caused
by $b \to u\ell\overline{\nu}$ and $b \to c\ell\overline{\nu}$ transitions.
They are used to measure $|R_b|$ (see Section
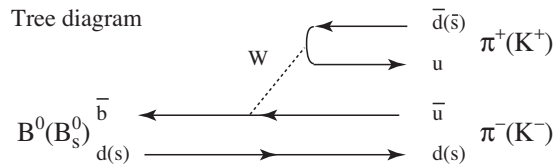
Figure 1.4: *The tree diagram which generates* $B_d^0 \to \pi^+ \pi^-$ *and* $B_s^0 \to K^+ K^-$ *decays. This figure comes from [33].*

(1.3.4)) and the indirect CP violation (see Section (1.5.2)).

For the SM description of CP violation, the major role is played by the non-leptonic B-decays. At the quark level, these decays involved the transitions $b \rightarrow q\bar{q}d(s)$ transitions where q ϵ {u, d, c, s}.

The two kind of diagrams which contribute to the non-leptonic B-meson decays are the "tree" (current−current) and "penguin" (loop) diagrams. They are illustrated on Fig. (1.4 and 1.5).

Example of penguin diagrams
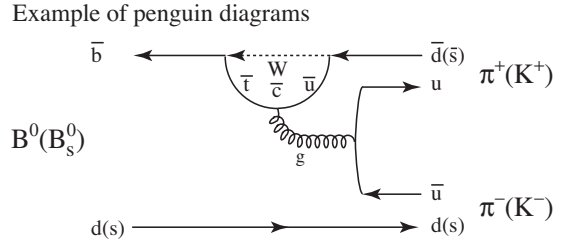
Figure 1.5: *Example of a penguin diagram which generates $B_d^0 \rightarrow \pi^+ \pi^-$ and $B_s^0 \rightarrow K^+ K^-$ decays. This figure comes from [33].*

1.4.2 $B_q^0 - \overline{B}_q^0$ mixing

Mixing is the process in which a neutral meson such as K^0, B_d^0 or B_s^0 oscillates from its particle state to its anti-particle state and vice versa. This is a second-order weak interaction illustrated in Fig. (1.6) for the B-mesons. Due to the particular hierarchy of the CKM matrix elements and to its mass only the top quark contributes significantly to the $B_q^0 - \overline{B}_q^0$ mixing. Unlike the Kaon case, the charm and the mixed top-charm contributions are negligible here, which considerably simplifies the analysis [8].
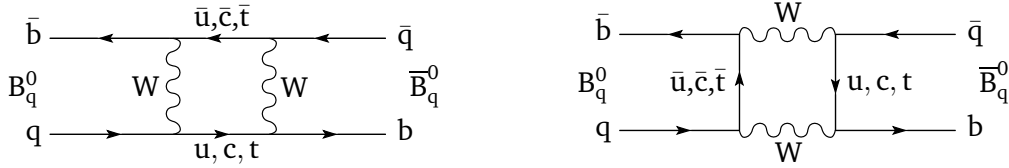
Figure 1.6: *Box diagrams illustrating the $B_q^0 - \overline{B}_q^0$ mixing, q stands for d or s.*

The $|B_q^0\rangle$ and $|\overline{B}_q^0\rangle$ states of neutral B-mesons are eigenstates of the strong and electromagnetic forces, with definite flavor content. Oscillations from one state to another can only occur through weak interactions which are also responsible for the decay of the B_q^0 and $\overline{B}_q^0$.

After the creation of a B_q^0 at time $t = 0$, the meson state observed at time t can be described by a superposition of the two flavor states:

$$|\psi\rangle = a(t)|B_q^0\rangle + b(t)|\overline{B}_q^0\rangle.$$

Applying a matrix notation, the Wigner-Weisskopf formalism [34, 35] yields an effective time dependent Schrödinger equation of the form:

$$i\frac{d}{dt}\begin{pmatrix} a(t) \\ b(t) \end{pmatrix} = \mathcal{H}_{\text{eff}}\begin{pmatrix} a(t) \\ b(t) \end{pmatrix} = (\mathbf{M} - \frac{i}{2}\mathbf{\Gamma})\begin{pmatrix} a(t) \\ b(t) \end{pmatrix}$$

where $\mathbf{M}$, the mass matrix, and $\mathbf{\Gamma}$, the decay matrix, are both 2×2 Hermitian matrices, while the effective Hamiltonian $\mathcal{H}_{\text{eff}}$ is not Hermitian. Virtual intermediate states contributes to $\mathbf{M}$ while physical decay channels common to B_q^0 and $\overline{B}_q^0$ contribute to $\mathbf{\Gamma}$. As CPT

invariance guarantees that the diagonal element of the two matrices are equal[7], $\mathbf{M}$ and $\mathbf{\Gamma}$ can be detailed as:

$$\mathbf{M} = \begin{pmatrix} M_0^q & M_{12}^q \\ M_{12}^{q*} & M_0^q \end{pmatrix}, \qquad \mathbf{\Gamma} = \begin{pmatrix} \Gamma_0^q & \Gamma_{12}^q \\ \Gamma_{12}^{q*} & \Gamma_0^q \end{pmatrix}.$$

The off-diagonal terms in these matrices, M_{12}^q and Γ_{12}^q are particularly important in the discussion of CP violation. They are the dispersive and absorptive parts of the transition amplitudes from B_q^0 to $\overline{B}_q^0$. In the Standard Model these contribution arise from the box diagram with two W exchanges visible on Fig. (1.6). The large mass of the B-mesons makes the QCD calculation of these quantities much more reliable than the corresponding calculation for the Kaon mixing.

The eigenvalues of the effective Hamiltonian $\mathcal{H}_{\text{eff}}$ are then given by:

$$\lambda_{\pm} = \left(M_0^q - \frac{i}{2}\Gamma_0^q \right) \pm \frac{q}{p} \left(M_{12}^q - \frac{i}{2}\Gamma_{12}^q \right),$$

with the corresponding physical eigenstates:

$$|B_{\pm}^q\rangle = p|B_q^0\rangle \pm q|\overline{B}_q^0\rangle \tag{1.8}$$

where the coefficients obey the normalization $|p^2| + |q^2| = 1$. Since the $|B_{\pm}^q\rangle$ have definite mass, they can be labeled $|B_H^q\rangle$ for the heavier state (originally $|B_-^q\rangle$) and $|B_L^q\rangle$ for the lighter one (originally $|B_+^q\rangle$). The mass difference Δm_q and the width difference $\Delta\Gamma_q$ between the neutral B-mesons are defined as follows:

$$\Delta m_q \equiv m_H - m_L > 0, \qquad m = \frac{m_H + m_L}{2},$$

$$\Delta\Gamma_q \equiv \Gamma_L - \Gamma_H, \qquad \Gamma = \frac{\Gamma_H + \Gamma_L}{2}.$$

The mass difference Δm_q is positive by definition. As Γ_L is the longer-lived B-meson and Γ_H the shorter-lived B-meson, hence $\Delta\Gamma_q$ is expected to be positive in the Standard Model [36]. The magnitude of the oscillation (mixing) between B_q^0 and $\overline{B}_q^0$ is given by the size of the oscillation parameter x_q, defined as:

$$x_q \equiv \frac{\Delta m_q}{\Gamma_q}, \tag{1.9}$$

where Γ_q is the proper time of the B_q^0 meson. With these conventions, the ratio q/p is related to the off-diagonal mass and decay matrix elements and given by:

$$\frac{q}{p} = -\sqrt{\frac{M_{12}^{q*} - \frac{i}{2}\Gamma_{12}^{q*}}{M_{12}^q - \frac{i}{2}\Gamma_{12}^q}}, \tag{1.10}$$

as well as Δm_q and $\Delta\Gamma_q$:

$$
\begin{aligned}
(\Delta m_q)^2 - \frac{1}{4}(\Delta\Gamma_q)^2 &= 4\,|M_{12}^q|^2 - |\Gamma_{12}^q|^2, \\
\Delta m_q \Delta\Gamma_q &= -4\,\Re\mathrm{e}\left(M_{12}^{q*}\Gamma_{12}^q\right).
\end{aligned}
\tag{1.11}
$$

---

[7]CPT is a good symmetry of nature which requires that particle and anti-particle masses and lifetimes are identical.

The minus sign in Eq. (1.10, 1.11) arises from our convention of $\Delta\Gamma_q$. The same convention for Δm_q and $\Delta\Gamma_q$ can be found in [9]. The time evolution of the mass eigenstates is given by:

$$|B_j(t)\rangle = e^{-im_j t} e^{-\Gamma_j t/2} |B_j\rangle, \quad j = H, L.$$

From this equation and Eq. (1.8) we get the time evolution of the initially pure $|B_q^0\rangle$ and $|\overline{B}_q^0\rangle$ states:

$$|B_q^0(t)\rangle = g_+(t)|B_q^0\rangle + \frac{q}{p}g_-(t)|\overline{B}_q^0\rangle, \tag{1.12}$$

$$|\overline{B}_q^0(t)\rangle = g_+(t)|\overline{B}_q^0\rangle + \frac{p}{q}g_-(t)|B_q^0\rangle, \tag{1.13}$$

where:

$$g_\pm(t) \equiv \frac{1}{2}\left(e^{-i\lambda_+ t} \pm e^{-i\lambda_- t}\right). \tag{1.14}$$

1.4.3 Standard Model predictions

The SM predicts that the ratio $\Delta\Gamma_q/\Gamma_q$ is small for the $B_d^0 - \overline{B}_d^0$ system (less than 1%) but larger for the $B_s^0 - \overline{B}_s^0$ system to $\sim 10\%$ [14]. This width difference is caused by the presence of final states that can be reached by both the B_q^0 and the $\overline{B}_q^0$ mesons. Such decays involve $b \to c\bar{c}q$ transitions which are Cabbibo-suppressed if $q = d$ and Cabbibo-allowed if $q = s$.

The neutral Kaon sector has to deal with a large difference in the lifetime of the K_S^0 and K_L^0 with two close masses. This is the opposite in the B-meson sector where it is the mass difference which is non negligible [14]:

$$\Delta m_d = m_{B_d^0 H} - m_{B_d^0 L} = (0.502 \pm 0.007) \text{ ps}^{-1},$$
$$x_d = 0.771 \pm 0.012,$$

and:

$$\Delta m_s = m_{B_s^0 H} - m_{B_s^0 L} > 14.4 \text{ ps}^{-1}, \quad \text{CL. 95\%},$$
$$x_s > 20.6, \quad \text{CL. 95\%}.$$

1.4.4 Time dependent decay rates

The time dependent decay rates from a neutral meson system B_q^0 or $\overline{B}_q^0$ into a final state f through the transition matrix T depends on the two decay amplitudes[8]:

$$A_f \equiv \langle f|T|B_q^0\rangle,$$
$$\overline{A}_f \equiv \langle f|T|\overline{B}_q^0\rangle.$$

$|B_q^0\rangle$ born at time $t = 0$ as B_q^0, i.e. eigenvector of the strong interaction (flavor eigenstate), will evolve in time according to Eq. (1.12) and decay into the final state f with the amplitude:

$$A\left[B_q^0(t) \to f\right] = \langle f|T|B_q^0(t)\rangle = g_+(t)\,A_f + \frac{q}{p}g_-(t)\,\overline{A}_f.$$

---

[8]Henceforth we will ignore the production mechanism and concentrate on the decay rates.

Similarly, the decay amplitude for a state born as $\overline{\mathrm{B}}_{\mathrm{q}}^{0}$ at time $t = 0$ is given by:

$$A\left[\overline{\mathrm{B}}_{\mathrm{q}}^{0}(t) \to f\right] = \langle f|T|\overline{\mathrm{B}}_{\mathrm{q}}^{0}(t)\rangle = g_{+}(t)\,\overline{A}_{f} + \frac{p}{q}g_{-}(t)\,A_{f}.$$

The corresponding decay rates to CP conjugated states f and $\overline{f}$ can be written:

$$
\begin{aligned}
\Gamma\left(\mathrm{B}_{\mathrm{q}}^{0}(t) \to f\right) &= |A_{f}|^{2}\left\{|g_{+}(t)|^{2} + |\lambda_{f}|^{2}\,|g_{-}(t)|^{2} + 2\,\Re\mathrm{e}\left[\lambda_{f}g_{+}^{*}(t)g_{-}(t)\right]\right\}, \\
\Gamma\left(\mathrm{B}_{\mathrm{q}}^{0}(t) \to \overline{f}\right) &= \left|\overline{A}_{\overline{f}}\right|^{2}\left|\frac{q}{p}\right|^{2}\left\{|g_{-}(t)|^{2} + \left|\overline{\lambda}_{\overline{f}}\right|^{2}\,|g_{+}(t)|^{2} + 2\,\Re\mathrm{e}\left[\overline{\lambda}_{\overline{f}}g_{+}(t)g_{-}^{*}(t)\right]\right\}, \\
\Gamma\left(\overline{\mathrm{B}}_{\mathrm{q}}^{0}(t) \to f\right) &= |A_{f}|^{2}\left|\frac{p}{q}\right|^{2}\left\{|g_{-}(t)|^{2} + |\lambda_{f}|^{2}\,|g_{+}(t)|^{2} + 2\,\Re\mathrm{e}\left[\lambda_{f}g_{+}(t)g_{-}^{*}(t)\right]\right\}, \\
\Gamma\left(\overline{\mathrm{B}}_{\mathrm{q}}^{0}(t) \to \overline{f}\right) &= \left|\overline{A}_{\overline{f}}\right|^{2}\left\{|g_{+}(t)|^{2} + \left|\overline{\lambda}_{\overline{f}}\right|^{2}\,|g_{-}(t)|^{2} + 2\,\Re\mathrm{e}\left[\overline{\lambda}_{\overline{f}}g_{+}^{*}(t)g_{-}(t)\right]\right\}, \quad (1.15)
\end{aligned}
$$

where:

$$\lambda_{f} \equiv \frac{q}{p}\frac{\overline{A}_{f}}{A_{f}}, \qquad \lambda_{\overline{f}} \equiv \frac{q}{p}\frac{\overline{A}_{\overline{f}}}{A_{\overline{f}}} \quad \text{and} \quad \overline{\lambda}_{\overline{f}} \equiv \frac{1}{\lambda_{\overline{f}}}, \qquad (1.16)$$

while the functions governing the time evolution, from Eq. (1.14), are given by:

$$
\begin{aligned}
|g_{\pm}(t)|^{2} &= \frac{1}{4}\left[e^{-\Gamma_{H}t} + e^{-\Gamma_{L}t} \pm e^{-\Gamma t}\cos\left(\Delta m_{\mathrm{q}}t\right)\right] \\
&= \frac{e^{-\Gamma t}}{2}\left[\cosh\left(\frac{\Delta\Gamma_{\mathrm{q}}t}{2}\right) \pm \cos\left(\Delta m_{\mathrm{q}}t\right)\right], \\
g_{+}^{*}(t)g_{-}(t) &= \frac{1}{4}\left[-e^{-\Gamma_{H}t} + e^{-\Gamma_{L}t} + 2ie^{-\Gamma t}\sin\left(\Delta m_{\mathrm{q}}t\right)\right] \\
&= \frac{e^{-\Gamma t}}{2}\left[\sinh\left(\frac{\Delta\Gamma_{\mathrm{q}}t}{2}\right) + i\sin\left(\Delta m_{\mathrm{q}}t\right)\right].
\end{aligned}
$$

1.5   CP violation

The possible manifestations of CP symmetry violation can be classified in a model-independent way in three categories:

1. **CP violation in the decay**[9], when the amplitude for the decay and its CP conjugate process have different magnitudes:

$$\left|\frac{\overline{A}_{\overline{f}}}{A_{f}}\right| \neq 1;$$

2. **CP violation in the mixing**:

$$\left|\frac{q}{p}\right| \neq 1;$$

3. **CP violation in the interference between a decay without mixing** ($\mathrm{B}_{\mathrm{q}}^{0} \to \mathrm{f}$) **and a decay with mixing** ($\mathrm{B}_{\mathrm{q}}^{0} \to \overline{\mathrm{B}}_{\mathrm{q}}^{0} \to \mathrm{f}$):

$$|\lambda_{f}| = \left|\frac{q}{p}\frac{\overline{A}_{f}}{A_{f}}\right| = 1, \quad \Im\mathrm{m}\lambda_{f} \neq 0.$$

---

[9]This asymmetry can be present in both charged and neutral decays.

1.5.1 CP violation in decay
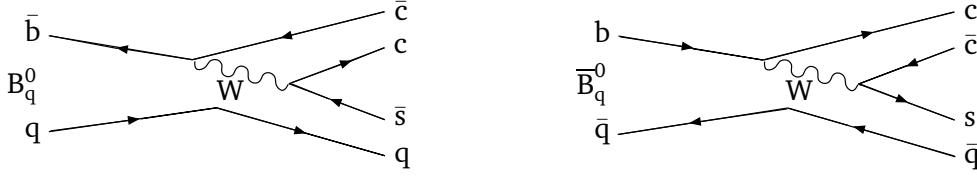
Figure 1.7: *Diagrams illustrating a B_q^0 ($\overline{B}_q^0$ resp.) decaying through a $\bar{b} \to \bar{c}c\bar{s}$ ($b \to c\bar{c}s$ resp.) quark transition.*

For any final state f or $\overline{f}$, illustrated in Fig. (1.7), the quantity $\left| \overline{A}_{\overline{f}}/A_f \right|$ is independent of the phase conventions discussed in Appendix (A). There are two types of phase that may appear in A_f and $\overline{A}_{\overline{f}}$:

1. The **weak phases** coming from the V_{CKM} matrix, that contribute to the two amplitudes with opposite signs;

2. The **strong phases** which contribute to A_f and $\overline{A}_{\overline{f}}$ with terms of the same sign and which are related to final states strong interaction.

It is therefore useful to write each contribution to A in three parts: its magnitude A_i, its weak phase term $e^{i\phi_i}$, and its strong phase term $e^{i\delta_i}$. Then if several amplitudes contribute to $B_q^0 \to f$, the amplitude A_f and the CP conjugate amplitude $\overline{A}_{\overline{f}}$ are given by:

$$A_f = \sum_i A_i e^{i(\delta_i + \phi_i)}, \quad \overline{A}_{\overline{f}} = \sum_i A_i e^{i(\delta_i - \phi_i)},$$

The convention independent quantity is then:

$$\left| \frac{\overline{A}_{\overline{f}}}{A_f} \right| = \left| \frac{\sum_i A_i e^{i(\delta_i - \phi_i)}}{\sum_i A_i e^{i(\delta_i + \phi_i)}} \right|$$

This relation shows that CP violation is due to the presence of weak phases. This type of CP violation, also called **direct CP violation**, will not occur unless if there are at least two amplitudes with different weak phases and different strong phases. Then the condition to have CP violation in the decay is:

$$\left| \frac{\overline{A}_{\overline{f}}}{A_f} \right| \neq 1 \quad \Longrightarrow \quad \text{CP violation.}$$

The CP violation in the decay has been observed by BABAR and Belle in the $B_d^0 \to K^+ \pi^-$ decay in 2004. The average value combining BABAR [37], Belle [38], CDF [39] and CLEO [40] is:

$$
\begin{aligned}
A_{K^-\pi^+} &\equiv \frac{\Gamma(\overline{B}_d^0 \to K^- \pi^+) - \Gamma(B_d^0 \to K^+ \pi^-)}{\Gamma(\overline{B}_d^0 \to K^- \pi^+) + \Gamma(B_d^0 \to K^+ \pi^-)} \\
&= -0.109 \pm 0.019.
\end{aligned}
$$

1.5.2 CP violation in mixing

A second quantity that is independent of phase conventions and physically meaningful is:

$$\left|\frac{q}{p}\right|^2 = \left|\frac{M_{12}^* - \frac{i}{2}\Gamma_{12}^*}{M_{12} - \frac{i}{2}\Gamma_{12}}\right|. \tag{1.17}$$

If CP is conserved, the mass eigenstates must be CP eigenstates. In that case the relative phase between M_{12} and Γ_{12} vanishes and $|q/p|^2 = 1$. Therefore Eq. (1.17) implies:

$$\left|\frac{q}{p}\right| \neq 1 \quad \Longrightarrow \quad \text{CP violation.}$$

This kind of CP violation is called CP violation in the mixing and is often referred to as **indirect CP violation**. It results from the mass eigenstates being different from the CP eigenstates. This implies that the probabilities for an initially pure $|B_q^0\rangle$ eigenstate to decay as $|\overline{B}_q^0\rangle$ or an initially pure $|\overline{B}_q^0\rangle$ eigenstate to decay as $|B_q^0\rangle$ after a time t are not the same.

To measure experimentally this asymmetry one can study the semi-leptonic B-meson decays (where the lepton charge gives the B-flavor). This consists in measuring the semi-leptonic asymmetry:

$$A_{SL} = \frac{\Gamma(B^+ \to \ell^+ \nu_\ell X) - \Gamma(B^- \to \ell^- \overline{\nu}_\ell X)}{\Gamma(B^+ \to \ell^+ \nu_\ell X) + \Gamma(B^- \to \ell^- \overline{\nu}_\ell X)} = \frac{1 - \left|\frac{q}{p}\right|^4}{1 + \left|\frac{q}{p}\right|^4}.$$

CP violation in the mixing has been observed in the semi-leptonic decays $K_L^0 \to \pi^- \ell^+ \nu_\ell$ and $K_L^0 \to \pi^+ \ell^- \overline{\nu}_\ell$ [14]:

$$\delta_K = \frac{\Gamma(K_L^0 \to \pi^- \ell^+ \nu_\ell) - \Gamma(K_L^0 \to \pi^+ \ell^- \overline{\nu}_\ell)}{\Gamma(K_L^0 \to \pi^- \ell^+ \nu_\ell) + \Gamma(K_L^0 \to \pi^+ \ell^- \overline{\nu}_\ell)} = (3.27 \pm 0.12) \cdot 10^{-3}.$$

However, this CP violation has still not be experimentally observed in the B-mesons system and the average result [41] is:

$$A_{SL}^B = (-0.05 \pm 0.71)\%,$$

which is equivalent to:

$$\left|\frac{q}{p}\right| = 1.0003 \pm 0.0035.$$

In the case of hadronic decays, the situation is much more complex. In order to calculate the deviation of $|q/p|$ from 1, $\Im m(\Gamma_{12}/M_{12})$ has to be calculated. This involves large hadronic uncertainties, in particular in the hadronization model for Γ_{12}. Thus even if such asymmetries are observed, it will be difficult to relate their values to the V_{CKM} parameters.

1.5.3 Mixing induced CP violation

Let's consider again neutral B-meson decays into final CP eigenstates, f_{CP}. Such states are accessible in both B_q^0 and $\overline{B}_q^0$ decays as shown on Fig. (1.8). The quantity of interest here which is independent of phase conventions and physically meaningful is λ_f, given in
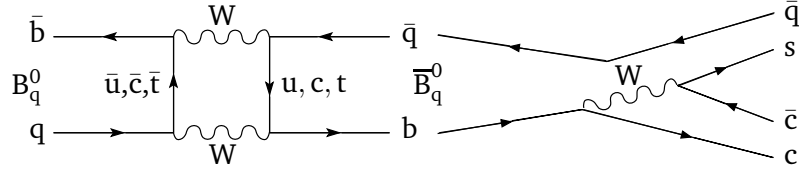
Figure 1.8: *Diagram illustrating a $\overline{B}^0_q$ mixing into a B^0_q and then decaying through a $b \to c\bar{c}s$ quark transition.*

Eq. (1.16). When CP is conserved we know that $|q/p| = 1$, $\left|\overline{A}_{\bar{f}}/A_f\right| = 1$ and furthermore the relative phase between (q/p) and $(\overline{A}_{\bar{f}}/A_f)$ vanishes. One can however still observe CP violation even if $|q/p| = 1$ and $\left|\overline{A}_{\bar{f}}/A_f\right| = 1$, provided that:

$$|\lambda_f| = 1, \quad \Im m\lambda_f \neq 0.$$

This type of CP violation is called CP violation in the interference between a decay with and a decay without mixing. It contains aspects of both direct and indirect CP violation. We now want to point out the importance of this mechanism: the theoretical estimate of direct CP violating quantities is usually plagued by hadronic uncertainties which consist for instance in the difficulty to estimate the strong phases, and hence to extract the weak phases. In this case, instead, for processes dominated by a single amplitude, the strong phase will cancel.

1.5.4 CP violation in neutral B-sector

The neutral B sector has several properties which allow to simplify the CP violation formalism [9]. We can assume that the very small effect of CP violation in the $B^0_q - \overline{B}^0_q$ mixing can be neglected [7, 8]. This leads to the following approximations:

$$\text{Both } B^0_d \text{ and } B^0_s \text{ systems} \implies |\Gamma_{12}| \ll |M_{12}| \implies \Delta m_q = 2\,|M_{12}|,$$

$$\text{and } \left|\frac{q}{p}\right| = 1 \implies |\lambda_f| = \left|\frac{\overline{A}_{\bar{f}}}{A_f}\right|; \tag{1.18}$$

$$\text{Only for } B^0_d \text{ systems} \implies \Delta\Gamma_d = 0. \tag{1.19}$$

For the B^0_q systems, we use the second approximation (Eq. (1.18)) to transform the time-dependent decay probabilities of Eq. (1.15) into (we only write here the two time depen-

dent decay amplitudes $B_q^0(t) \to f$ and $\overline{B}_q^0(t) \to f$):

$$\Gamma[B_q^0(t) \to f] = \frac{|A_f|^2 + |\overline{A}_f|^2}{2} e^{-\Gamma_q t} \left\{ \cosh\left(\frac{\Delta\Gamma_q t}{2}\right) + D_f \sinh\left(\frac{\Delta\Gamma_q t}{2}\right) \right.$$

$$\left. - C_f \cos\left(\Delta m_q t\right) - S_f \sin\left(\Delta m_q t\right) \right\},$$

$$\Gamma[\overline{B}_q^0(t) \to f] = \frac{|A_f|^2 + |\overline{A}_f|^2}{2} e^{-\Gamma_q t} \left\{ \cosh\left(\frac{\Delta\Gamma_q t}{2}\right) + D_f \sinh\left(\frac{\Delta\Gamma_q t}{2}\right) \right.$$

$$\left. + C_f \cos\left(\Delta m_q t\right) + S_f \sin\left(\Delta m_q t\right) \right\}, \quad (1.20)$$

where[10]:

$$D_f \equiv \frac{2\,\Re e(\lambda_f)}{1 + |\lambda_f|^2}, \quad C_f \equiv \frac{|\lambda_f|^2 - 1}{1 + |\lambda_f|^2}, \quad S_f \equiv \frac{2\,\Im m(\lambda_f)}{1 + |\lambda_f|^2}. \quad (1.21)$$

In order to test CP, we must compare $B_q^0(t) \to f$ to $\overline{B}_q^0(t) \to \overline{f}$, or $B_q^0(t) \to \overline{f}$ to $\overline{B}_q^0(t) \to f$. To simplify the discussion we will henceforth concentrate on decays into self-conjugated final states f_{CP} which are CP eigenstates:

$$\mathcal{CP}|f_{CP}\rangle = \eta_{f_{CP}}|f_{CP}\rangle,$$

where $\eta_{f_{CP}} = \pm 1$ is the eigenvalue of the final state.

If we do not consider CP violation in the mixing and that only a single amplitude $A_{f_{CP}} = \overline{A}_{f_{CP}}$ with one weak phase is present in the decay, we obtain (Appendix (A)):

$$|\lambda_{f_{CP}}| = 1, \quad C_{f_{CP}} = 0, \quad S_{f_{CP}} = -\eta_{f_{CP}} \sin(\phi_{CKM}), \quad D_{f_{CP}} = \eta_{f_{CP}} \cos(\phi_{CKM}), \quad (1.22)$$

where the CKM phase is defined as:

$$\phi_{CKM} \equiv \phi_M - 2\phi_D. \quad (1.23)$$

Here $\phi_M \equiv arg[V_{tq}^* V_{tb}]$ is the mixing phase and $\phi_D \equiv arg[V_{cb} V_{cq}^*]$ is the decay phase. This latter can be expressed in terms of angle of the unitarity triangle as follows:

$$\phi_D = \begin{cases} -\gamma & \text{for dominant } \overline{b} \to \overline{u}u\overline{r} \text{ CKM amplitudes,} \\ 0 & \text{for dominant } \overline{b} \to \overline{c}c\overline{r} \text{ CKM amplitudes,} \end{cases} \quad r = d, s.$$

The mixing phase can be related to angles of the unitarity triangle as follow:

$$\phi_M \equiv 2arg[V_{tq}^* V_{tb}] \equiv \begin{cases} \phi_d \simeq 2\beta = \mathcal{O}(0.8)\,\text{rad} & \text{for } q = d, \\ \phi_s \simeq -2\lambda^2\eta \simeq -2\chi = \mathcal{O}(-0.04)\,\text{rad} & \text{for } q = s. \end{cases}$$

Finally we can consider only $\overline{b} \to \overline{c}c\overline{s}$ quark transition decays. This is effectively the channels studied in the present dissertation, i.e. the $B_s^0 \to J/\psi\,\eta$, the $B_s^0 \to \eta_c\,\phi$ and the $B_s^0 \to J/\psi\,\phi$ channels. In this case the decay phase that is the phase of $V_{cb}V_{cq}^*$ vanishes. All these peculiarities render that kind of decay the "promised land" of the CP violation in the B-system.

---

[10]Here is a place where competing definitions abound in the literature. For example, reference [9] uses $a^{dir} = C_f$ and, because of the sign change in the definition of q, $a^{int} = -S_f$.

B_s^0 system With these conventions, the time dependent decay rates (1.20) for $\bar{b} \to \bar{c}c\bar{s}$ decays to CP eigenstates, when this decay is dominated by only one phase, can be written as follows:

$$\Gamma[B_s^0(t) \to f_{\mathrm{CP}}] = |A_{f_{\mathrm{CP}}}|^2\ e^{-\Gamma_{\mathrm{s}} t} \left\{ \cosh\left(\frac{\Delta\Gamma_{\mathrm{s}} t}{2}\right) + \eta_{f_{\mathrm{CP}}} \cos\left(\phi_{\mathrm{s}}\right) \sinh\left(\frac{\Delta\Gamma_{\mathrm{s}} t}{2}\right) \right.$$

$$\left. - \eta_{f_{\mathrm{CP}}} \sin\left(\phi_{\mathrm{s}}\right) \sin\left(\Delta m_{\mathrm{s}}\, t\right) \right\},$$

$$\Gamma[\overline{B}_s^0(t) \to f_{\mathrm{CP}}] = |A_{f_{\mathrm{CP}}}|^2\ e^{-\Gamma_{\mathrm{s}} t} \left\{ \cosh\left(\frac{\Delta\Gamma_{\mathrm{s}} t}{2}\right) + \eta_{f_{\mathrm{CP}}} \cos\left(\phi_{\mathrm{s}}\right) \sinh\left(\frac{\Delta\Gamma_{\mathrm{s}} t}{2}\right) \right.$$

$$\left. + \eta_{f_{\mathrm{CP}}} \sin\left(\phi_{\mathrm{s}}\right) \sin\left(\Delta m_{\mathrm{s}}\, t\right) \right\}. \tag{1.24}$$

We define the CP asymmetry as:

$$A_{\mathrm{CP}}(t) \equiv \frac{\Gamma[\overline{B}_s^0(t) \to f_{\mathrm{CP}}] - \Gamma[B_s^0(t) \to f_{\mathrm{CP}}]}{\Gamma[\overline{B}_s^0(t) \to f_{\mathrm{CP}}] + \Gamma[B_s^0(t) \to f_{\mathrm{CP}}]} \tag{1.25}$$

$$= \frac{-\eta_{f_{\mathrm{CP}}} \sin\left(\phi_{\mathrm{s}}\right) \sin\left(\Delta m_{\mathrm{s}} t\right)}{\cosh\left(\frac{\Delta\Gamma_{\mathrm{s}} t}{2}\right) - \eta_{f_{\mathrm{CP}}} \cos\left(\phi_{\mathrm{s}}\right) \sinh\left(\frac{\Delta\Gamma_{\mathrm{s}} t}{2}\right)}.$$

B_d^0 system Setting $\Delta\Gamma_{\mathrm{d}} = 0$, the time dependent decay rates reduce to:

$$\Gamma[B_d^0(t) \to f_{\mathrm{CP}}] = |A_{f_{\mathrm{CP}}}|^2\ e^{-\Gamma_{\mathrm{d}} t} \left\{ -\eta_{f_{\mathrm{CP}}} \sin\left(\phi_{\mathrm{d}}\right) \sin\left(\Delta m_{\mathrm{d}}\, t\right) \right\},$$

$$\Gamma[\overline{B}_d^0(t) \to f_{\mathrm{CP}}] = |A_{f_{\mathrm{CP}}}|^2\ e^{-\Gamma_{\mathrm{d}} t} \left\{ +\eta_{f_{\mathrm{CP}}} \sin\left(\phi_{\mathrm{d}}\right) \sin\left(\Delta m_{\mathrm{d}}\, t\right) \right\}.$$

The asymmetry (1.25) becomes:

$$A_{\mathrm{CP}}(t) = -\eta_{f_{\mathrm{CP}}} \sin\left(\phi_{\mathrm{d}}\right) \sin\left(\Delta m_{\mathrm{d}} t\right).$$

1.6 The $B_s^0 \to J/\psi\ \eta$ channel at LHCb

The identification of the B_s^0 state is quite recent. The Aleph experiment observed this state and measured its mass for the first time in 1993 [42] the same year as CDF did [43]. LEP experiments have studied this B-state, obtaining in the following years the mean life time of this meson. Nevertheless, the $B_s^0 - \overline{B}_s^0$ mixing, despite the efforts of the experimental teams both at LEP and Tevatron, has not been directly observed; besides, the $\Delta\Gamma_{\mathrm{s}}$ measurement has not been achieved up to now.

The B_s^0 mass and the mean lifetime measurements obtained by the LEP experiments and by CDF were based mostly on the study of semi-leptonic decay channels, in which D_s mesons are produced, and of the rare decay to $J/\psi\ \phi$ where the low branching ratio $\mathcal{BR}(B_s^0 \to J/\psi\ \phi) \simeq 10^{-3}$ is compensated by a clear signature and good signal to noise ratio.

Since it is important to have large data samples available to study B_s^0 decays, these constitute one of the central targets of the LHCb experiment. There are important differences between the B_d^0 and B_s^0 systems:

- Within the Standard Model, a large $B_s^0 - \overline{B}_s^0$ mixing parameter $x_s \equiv \Delta m_s / \Gamma_s = \mathcal{O}(20)$ is expected, whereas the B_s^0 mixing phase $\phi_s \sim \mathcal{O}(-0.04)$ rad is expected to be small.

- There may be a sizable width difference $\Delta\Gamma_s / \Gamma_s = \mathcal{O}(10\%)$, whereas $\Delta\Gamma_d$ is negligible.

1.6.1 $B_s^0 \to J/\psi\ \eta$ CP asymmetry

The decay processes to the $J/\psi\ \eta$ final state are analogous to the $J/\psi\ K_S^0$ decay in the B_d^0 sector[11]. The final state is a pure CP-even eigenstate with eigenvalue $\eta_{J/\psi\ \eta} = +1$, unlike the final states $B_s^0 \to J/\psi\ \phi$ where, due to the presence of the two vector mesons, both CP eigenstates are present. The subprocess at quark level $\bar{b} \to \bar{c}c\bar{s}$ is dominated by the tree diagram. Contributions to more complex diagrams are of order $\mathcal{O}(\lambda^2)$.

The CP asymmetry amplitude in this case is dominated by the interference between decays with and without mixing and is given by:

$$\Im m(\lambda_{B_s^0 \to J/\psi\ \eta}) = -\sin(-2\chi),$$

This angle is expected to be of the order $\mathcal{O}(\lambda^2)$ and is significantly more difficult to measure compared to the β angle of the (**bd**) triangle. However any observation of a sizable asymmetry will imply the existence of New Physics.

1.6.2 $B_s^0 \to J/\psi\ \eta$ branching fraction

The estimation of the branching ratio of this channel is based on the comparison with the channel $B_d^0 \to J/\psi\ K_S^0$. The amplitudes of the two processes indeed differ only by the kinematics and by the non perturbative hadronic contributions, the role of the spectator quark d or s being neglected. They do not depend on the V_{CKM} matrix elements that are the same at the tree level. After these hypotheses, the branching ratio of $B_s^0 \to J/\psi\ \eta$ can be expressed as [44]:

$$\mathcal{BR}(B_s^0 \to J/\psi\ \eta) = \mathcal{BR}(B_d^0 \to J/\psi\ K_S^0)\,|S_\eta|^2 \left(\frac{m_{B_d^0}}{m_{B_s^0}}\right)^3 \left(\frac{\lambda_{B_s^0}}{\lambda_{B_d^0}}\right)^{3/2},$$

where the function λ accounts for the kinematic effects in the decays and where

$$S_\eta = \frac{-\sin(\theta_P)}{\sqrt{3}} - \frac{2\cos(\theta_P)}{\sqrt{6}}$$

is the strange quark contribution to the η particle. θ_P is the mixing angle between the $I = 0$ ground-state of the pseudoscalar octet η_8 with the pseudoscalar singlet η_1:

$$\begin{aligned}
\eta &= \eta_8 \cos\theta_P - \eta_1 \sin\theta_P, \\
\eta' &= \eta_8 \sin\theta_P + \eta_1 \cos\theta_P.
\end{aligned}$$

The mixing angle θ_P is not well determined and varies between $-20°$ and $-10°$ at a confidence level of 90% [14]. Using the branching fraction $(8.5 \pm 0.5)\cdot 10^{-4}$ for the decay of $B_d^0 \to J/\psi\ K_S^0$ we obtain for $B_s^0 \to J/\psi\ \eta$ a result varying between $3.12 \cdot 10^{-4}$ and $4.76 \cdot 10^{-4}$. The behavior of the branching fraction is shown on Fig. (1.9) for angles between -90° to 0°. The uncertainty on these branching ratios is roughly 40%.

---

[11]One of the most prominent B-decay is the $B_d^0 \to J/\psi\ K_S^0$. It originates from $\bar{b} \to \bar{c}c\bar{s}$ quark-level decays. The important feature of this channel is that the penguin contribution can be neglected. This implies no direct CP violation and gives for the mixing induced CP asymmetry: $\Im m(\lambda_{B_d^0 \to J/\psi\ K_S^0}) = \sin(2\beta) + \mathcal{O}(\lambda^3)$.
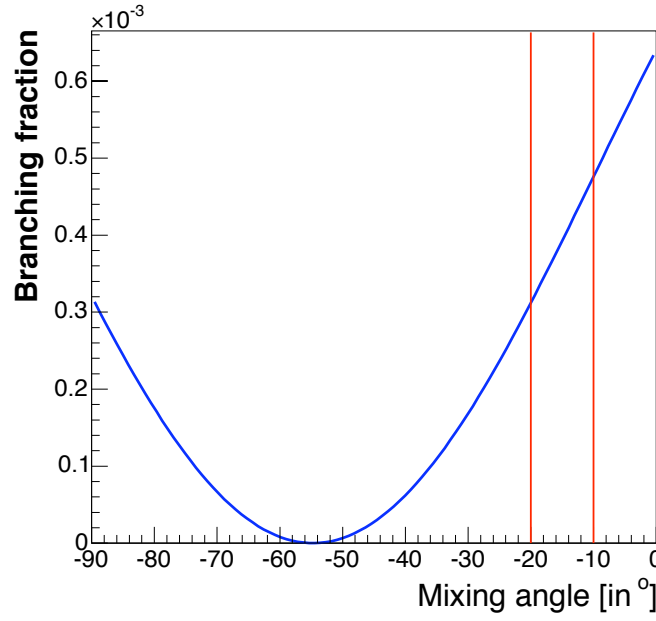
Figure 1.9: *Branching fraction of the $B_s^0 \to J/\psi \, \eta$ decay channel with respect to the η mixing angle. θ_P varies from $-20°$ to $-10°$, 90% CL interval enclosed by the two red lines.*

1.6.3 Experimental aspects of $B_s^0 \to J/\psi \, \eta$

This decay of the B_s^0 has never been observed. Only an upper limit at 90% confidence level has been set $\mathcal{BR}(B_s^0 \to J/\psi \, \eta) < 3.8 \cdot 10^{-3}$, by the L3 experiment at LEP. As will be shown later in this dissertation, the J/ψ is reconstructed in the channel $J/\psi \to \mu^+ \, \mu^-$ with high identification efficiencies and a high trigger efficiency.

From an experimental point of view, the search of the η, decaying in the channel $\eta \to \gamma\gamma$, presents a more difficult challenge especially in the identification of "low" energy photons, down to few GeV/c^2. This work has the aim to start an investigation on the $B_s^0 \to J/\psi(\mu^+ \, \mu^-) \, \eta(\gamma \, \gamma)$ and $B_s^0 \to J/\psi(\mu^+ \, \mu^-) \, \eta(\pi^+ \, \pi^- \, \pi^0 \to (\gamma \, \gamma))$ processes with the simulated data of LHCb.

These two decays are illustrated on Fig. (1.10 and 1.11). The J/ψ and the η particles have a very short lifetime. Therefore their decay vertices and the decay vertex of the B_s^0 should overlap. This is not shown on these drawings for reasons of clarity.
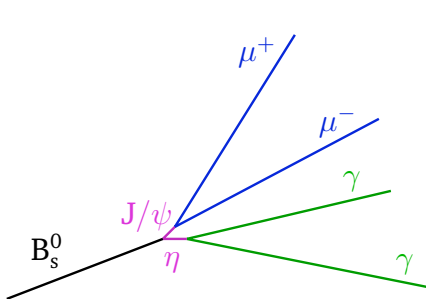
Figure 1.10: *$B_s^0 \to J/\psi(\mu^+ \, \mu^-) \, \eta(\gamma \, \gamma)$ decay mode.*
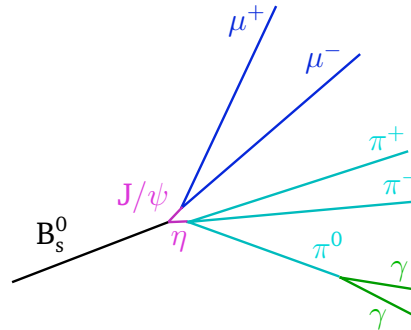
Figure 1.11: *$B_s^0 \to J/\psi(\mu^+ \, \mu^-) \, \eta(\pi^+ \, \pi^- \, \pi^0)$ decay mode.*

Chapter 2

The LHCb Experiment

This chapter describes the Large Hadron Collider beauty (LHCb) detector and its experimental environment. It begins with the description of the Large Hadron Collider (LHC). Then LHCb is introduced with all its sub-detectors. Finally, the triggering system of the experiment is presented.

THE Large Electron Positron collider (LEP) at the European Center for Particle Physics (CERN) has had a superb career in testing the Standard Model. In its first stage, LEP1 recorded out the following achievements at the Z^0 pole:

- The Z^0 mass was measured to 0.03 GeV/c^2.

- The Z^0 lineshapes were measured at the 10^{-3} level, which has allowed the determination of the invisible width and the conclusion to be drawn that there are only three light neutrinos and essentially no width for other unseen processes.

- The effective weak mixing angle was also measured precisely: $\sin^2\theta_W^{eff} = 0.23184 \pm 0.00023$ (LEP1 only).

From 1996, the machine was upgraded to continuously ramp the energy from $\sqrt{s} = 161$ GeV to $\sqrt{s} = 208$ GeV, thus allowing:

- The determination of the W$^\pm$ mass: $M_{W^\pm} = (80.457 \pm 0.046)$ GeV/c^2 (LEP2 only);

- The study of the gauge boson self-interaction;

- The global fits to electroweak data: the fit using only LEP data yields a top quark mass of $m_t = 179^{+13}_{-10}$ GeV/c^2 in agreement with the direct observations of top events, and a lower limit to the Higgs mass $m_{H^0} > 135^{+263}_{-83}$ GeV/c^2.

In the last operational year of LEP, the four experiments were able to set a lower limit to the Higgs mass at $m_{H^0} > 114.4$ GeV/c^2 at 95% C.L.

Other models beyond the Standard Model, such as supersymmetric models, have also predicted the existence of a series of Higgs bosons; they also predict new phenomena which are not allowed in the Standard Model, like the boson↔fermion decay or the possibility of extra dimensions. The ones belonging to the supersymmetry group are very

promising, especially the most "standard" of these models which is called the Minimal SuperSymmetrical Model (MSSM).

These considerations led the particle physics community to propose a new collider, which has much higher energies than the LEP in order to explore unknown energy scales, where effects of New Physics are expected to be important. A hadron circular accelerator has been chosen. This change of technology from LEP to LHC is necessary as the TeV scale cannot be reached by circular $e^+ - e^-$ colliders due to the high energy loss via synchrotron radiation. The 27 km ring of the LEP accelerator will be reused and its injection scheme upgraded with only minor civil engineering modifications: this allows CERN to concentrate its efforts on the instrumentation and experiments.

2.1 The LHC accelerator

The LHC accelerator, illustrated on Fig (2.1), is a collider with two proton beams running in opposite directions and colliding with a center of mass energy of $\sqrt{s} = 14$ TeV. The main experimental topics of this machine are the search for Higgs and SUSY particles (ATLAS and CMS), the quark-gluon plasma (ALICE), the study of CP violation effects and B-physics (mainly by LHCb, but also to a lower extend by ATLAS and CMS) and possible effects of physics beyond the Standard Model as well as the measurements of total cross section, elastic scattering and diffractive processes at LHC energies (TOTEM).

The colliding protons are first accelerated through a linear accelerator (the LINAC) up to 50 MeV and injected into the two Proton Synchrotron Booster (PBS) rings. The Proton Synchrotron (PS) is then fed with 1 GeV particles which will accelerate them up to 26 GeV before their injection in the Super Proton Synchrotron (SPS) where they will reach an energy of 450 GeV. They finally enter the LHC via the two new tunnels TI 2 and TI 8 (see Fig (2.1)). The final energy of 7 TeV is limited by the magnetic field of 8.34 T in the super-conducting magnets even though a field of 9 Tesla would technically be feasible.

2.1.1 The luminosity

The production cross section for a Higgs with a mass between 114 and 219 GeV (these are the present 95% CL limits combining direct and indirect searches [46]) increases rapidly with $\sqrt{s}$ but is still of a few tens of femtobarns at the LHC energy. This is why a very high luminosity is needed. This necessity is also required for New Physics phenomena which are characterized by very small signal to background ratios. Therefore the LHC design luminosity has been fixed to $\mathcal{L} = 10^{34}$ cm^{-2}s^{-1}. This highest luminosity will only be reached after 1 to 4 years of operation and improvements.

The luminosity at a given interaction point is given by:

$$\mathcal{L} = \frac{N_1 N_2 k_b f \gamma F}{4\pi \beta^* \epsilon}$$

where $N_{1,2}$ are the number of protons per bunch, k_b the number of bunch crossings at the considered interaction point, f the revolution frequency and $\gamma = E_p/m_p$ the relativistic factor. The normalized transverse emittance ϵ characterizes the compactness and divergence of the bunches and depends on beam-beam effects. The amplitude function β^* measures the ability of the magnets to focus the beam at the interaction point (IP) and finally $F \approx 0.9$ is a factor taking into account the crossing angle of the two beams [47]. The nominal value of these parameters are presented in Tab. (2.1). An important
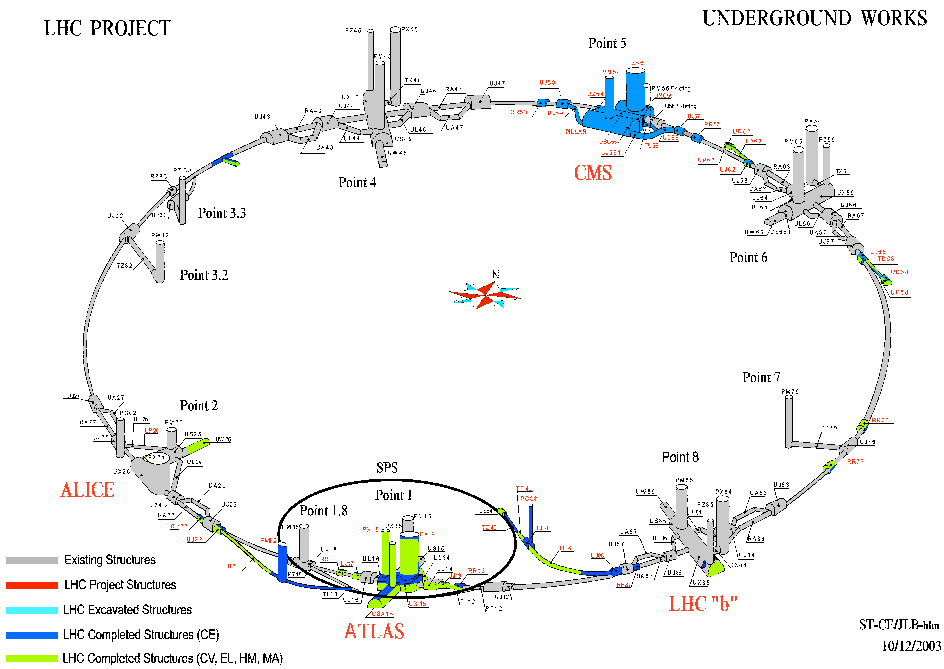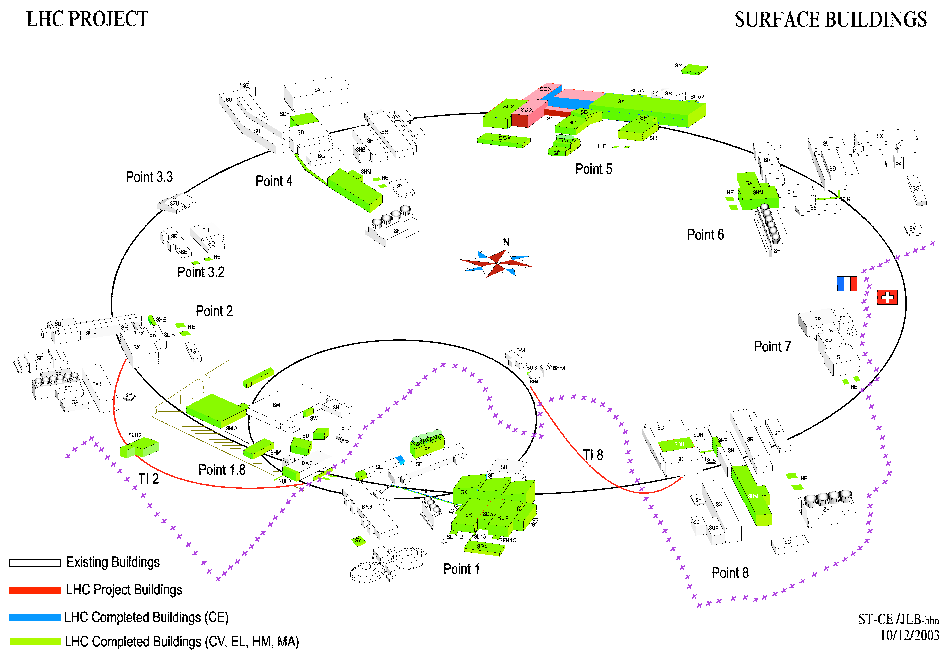
Figure 2.1: *Schematic diagram of the LHC accelerator ring at the surface and underground. The general purpose experiments ATLAS and CMS are located at points 1 and 5, the heavy ion experiment ALICE is situated at interaction point 2 and the LHCb experiment is located at interaction point 8. TOTEM is also situated at point 5. These figures are taken from [45].*

issue for the electronic design of the LHC experiments is the bunch crossing frequency $k_b^{max} f \approx 40$ MHz. This defines the basic clock cycle of the front-end electronics.

The luminosity at LHCb will be locally controlled by defocusing the beams at the IP 8 to yield a mean value of $\mathcal{L}_{\mathrm{LHCb}}^{av} = 2 \cdot 10^{32}$ cm^{-2}s^{-1}. This choice is motivated by the requirement of having mostly one inelastic collision per bunch crossing. The number of p$-$p interactions occurring in a given bunch crossing n, follows the Poisson distribution:

$$P(\mu, n) = \frac{\mu^n}{n} e^{-\mu},$$

Parameters		Values
N_1, N_2		$1.05 \cdot 10^{11}$
k_b		2835
f	[Hz]	11245.5
γ		7460.6
ϵ	[μm$\times$rad]	3.75
β	[m]	0.5

Table 2.1: *The design luminosity of $\mathcal{L} = 10^{34}$ cm^{-2}s^{-1} is calculated with those LHC performance parameters.*

where μ denotes the average number of p $-$ p collisions per bunch crossing. Figure (2.2) shows the probability of the proportion of events with $n = 0$, 1, 2, 3 or 4 p $-$ p interactions per bunch crossing as a function of the LHC luminosity.

To accurately measure the lifetime of the B-mesons, the primary vertex coordinates have to be determined with the best possible precision. This can be achieved in events with a single interaction ($n = 1$). From the figure (2.2), assuming an inelastic cross section of $\sigma_{inelastic} = 80$ mb, the probability is the greatest when the LHCb luminosity is $\mathcal{L} = 4 \cdot 10^{32}$ cm^{-2}s^{-1} (dotted line on the Figure). However, running at this luminosity coincides with increasing the number of multiple interactions ($n > 1$). The compromise solution is to run at $\mathcal{L}_{\mathrm{LHCb}}^{av} = 2 \cdot 10^{32}$ cm^{-2}s^{-1} (dashed-dotted line of the Figure) for which the detector occupancies in the tracking detectors will be lower and radiation damage will be reduced. Nevertheless studies are performed to evaluate the possibility of LHCb to run at higher luminosity.

Figure 2.2: *Probability distribution for the number of events with 0, 1, 2, 3 and 4 interactions per bunch crossing w.r.t. the LHC luminosity (the dash-dotted line is $\mathcal{L}_{LHCb}^{av} = 2 \cdot 10^{32}$ cm^{-2}s^{-1}).*

2.1.2   Proton beams and bunch structure

Unlike the LEP beams where electrons and positrons were accelerated by the same Radio Frequency (RF) system and travelled in the same beam pipe, the two protons beams of the LHC require two separated acceleration beam pipes which join together at eight interaction points. A p $-$ $\overline{\mathrm{p}}$ collider would have needed a "simpler" acceleration scheme, but at energies of $\sqrt{s} = 14$ TeV, the hadron-hadron cross section is largely dominated by

gluon fusion: the construction of a $p - \overline{p}$ collider would therefore not be worth the cost of building a $\overline{p}$ complex, the intensity of which is in any case limited.

This high luminosity can be achieved by filling the ring with a large number of very dense bunches. The density foreseen is 10^{11} protons per bunch. At such densities one has to cope with disturbances due to the bunch crossing and cannot increase the bunch density beyond a certain $beam - beam$ limit in order to preserve a sufficiently long beam lifetime[1].

The Radio Frequency of the LHC operates at 400 MHz. However, only every tenth RF bucket can be filled; this corresponds to a minimum bunch distance of 7 m (or 25 ns) and a total number of 3564 bunches along the circumference of the ring. The bunch crossing structure is given by [48]:

$$3564 \ = \ ([[(72b+8e)3+30]2+[(72b+8e)4+31e])3+([[(72b+8e)3+30e]3+81e),$$

where b stands for bunch and e for empty. This is due to the filling scheme of the injector: the PS has 81 bunches with 25 ns space, called PS-train, and the SPS has 3 PS-trains. Empty bunches arise due to a non-integer ratio of the PS, SPS and LHC revolution frequencies. This results in actually 2835 filled bunches. This bunch structure has no simple symmetry pattern, all the filled bunches only meet when the two trains collide head-on and there are effectively $k_b^{eff} = 2835$ bunch crossings. This happens only at two points: IP 1 (ATLAS) and IP 5 (CMS). At any other interaction point some filled bunches b meet empty bunches e and some luminosity is lost.

The LHCb experiment is located at IP 8 and therefore shifted with respect to IP 1 by $1/4$ cycle ($1/8$ for each beam). Additionally the LHCb interaction point is shifted by 11.2 meters (3 half bunch spacing) for geometrical reasons. The structure, there, is [48]:

$$
\begin{aligned}
3564 \ = \ & [(3a+69ab+3b+5e) \times 3 + 30e] \times 2 + (3a+69ab+3b+5e) \times 3 + 72a + 39e + \\
& [(3a+69ab+3b+5e) \times 3 + 30e] \times 2 + (3a+69ab+3b+5e) \times 4 + 31e + \\
& [(3a+69ab+3b+5e) \times 3 + 30e] \times 2 + (3a+69ab+3b+5e) \times 4 + 31e + \\
& [(3a+69ab+3b+5e) \times 3 + 30e] \times 2 + (3a+69ab+3b+5e) \times 3 + 3e + 72b + 36e,
\end{aligned}
$$

where ab stands for real collision between the two beams, a are bunches from beam a only, b are bunches from beam b only, and e represents no bunches from either beam a or b. This fact gives $k_b^{LHCb} = 2622$ bunch crossings, i.e. only 73,6% of all bunch crossings are expected to give an interaction. This and the modification of the LHC optics at the IP 8 decrease the luminosity down to $\mathcal{L}_{\text{LHCb}}^{av} = 2 \cdot 10^{32}$ cm^{-2}s^{-1}, as required by the LHCb experiment.

The bunch size at the interaction point is expected to have a Gaussian shape. The longitudinal and transverse dimensions are given by $\sigma_\parallel = 7.5$ cm and $\sigma_\perp = 75$ μm respectively. The interaction volume, due to the crossing of two bunches, is also a Gaussian and has $\sigma_\parallel = 5.3$ cm longitudinally and $\sigma_\perp = 53$ μm transversally.

---

[1]While only a tiny fraction of the particles interacts, all the others are deflected by the strong electromagnetic field of the opposite bunch. These deflections, which are stronger for denser bunches, accumulate turn after turn and may eventually lead to particle loss.

2.1.3   Bottom quark production at LHC

As the proton is not an elementary particle, the observed and studied collisions are essentially gluon↔gluon fusion (which is more probable than gluon↔quark or quark↔quark) [50]. At LHC energies, the heavy quarks are mainly produced by gluon fusion. The resulting B-hadrons are in a fairly flat rapidity distribution. Because of the large rapidity interval of the LHC, the B-hadrons from both b and $\bar{b}$ will end in the same forward (or the same backward) cone as illustrated in Fig. (2.3). The "forward/backward doublecone" polar angle distribution motivates the design of the LHCb detector, which is described in Section (2.2).
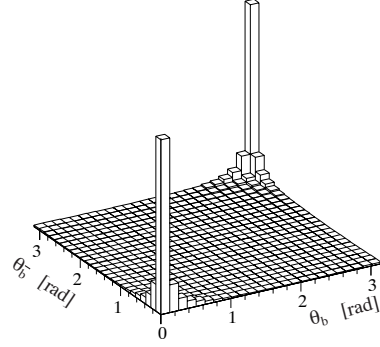
Figure 2.3: *Polar angle θ of b- and $\bar{b}$-hadrons directions at LHC. This figure is taken from [49].*

The hadronic b quark production parameters at $\sqrt{s} = 14$ TeV are obtained by extrapolation from SPS (UA1) and Tevatron (CDF and DØ) data. The relevant cross sections at LHC are given in Tab. (2.2). The cross section $\sigma_{b\bar{b}}$ ranges from 175 to 950 μb, depending on the extrapolation [50]. The value of 500 mb is a mean value of the b$\bar{b}$ production cross section and is assumed to be the central one by all the LHC experiments.

Cross sections				
Total	σ_{tot}	=	100	mb
Inelastic	σ_{inel}	=	80	mb
c$\bar{c}$	$\sigma_{c\bar{c}}$	=	3.5	mb
b$\bar{b}$	$\sigma_{b\bar{b}}$	=	500	μb

Table 2.2: *Cross sections assumed for the LHC experiments.*

2.1.4   Forward geometry detectors

During the first three years of the LHC, the relatively low luminosity, $\mathcal{L} = 10^{33}$ cm^{-2}s^{-1}, will allow the ATLAS and CMS experiment to carry out most of their B-physics program with a better precision than the e$^+$e$^-$ B-factories. They will collect $\sim 2.6 \cdot 10^6$ reconstructed "physics" events per year, dominated by b $\rightarrow$ J/ψ decays. This result is however strongly dependent on the success of the trigger strategies adopted by these two experiments. For us, the physics potential of LHCb can be fully exploited right at the start with the LHC initial expected luminosity and we will be able to collect $\sim 3.4 \cdot 10^6$ reconstructed events per year.

The most obvious difference between the three detectors is that LHCb is a forward spectrometer while ATLAS and CMS are central detectors. Although LHCb is the only LHC detector which has been specifically optimized for B-physics, there are several issues for which the forward geometry presents obvious advantages.

- **The forward geometry** enables us to detect the correlated b$\bar{b}$ production which peaks in the forward and backward cone;

- **The forward geometry** is much more open, simplifying the mechanical design and maintenance requirements;

- **LHCb** is able to obtain a much better vertex resolution than the central detectors, since the forward geometry allows the vertex detector to be situated much closer to the interaction point.

On the other hand a few disadvantages arise from this geometry:

- **In LHCb** the minimum-bias events[2] also peaks in the same forward and backward regions as the signal $b\bar{b}$, but will be reduced by dedicated high P_T triggers;

- **The forward geometry** has to cope with much higher particle density in the region close to the interaction point than for the central detector. This constrains the technology there to be radiation hard.

2.2 The LHCb experiment
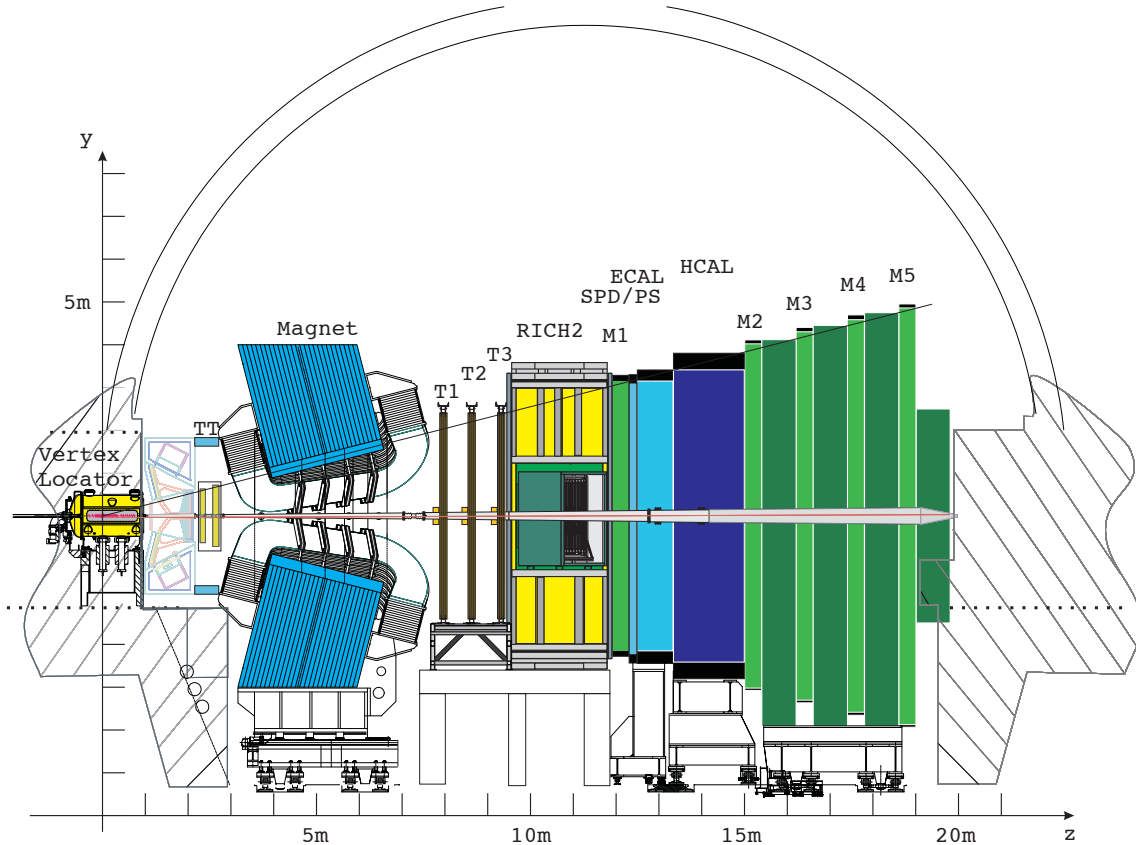
Figure 2.4: *Side view of the LHCb detector (non-bending plane, y–z). This figure is taken from [33].*

LHCb is an experiment dedicated to CP violation study in the B-mesons system, from which several discoveries are expected. The "Technical Proposal" [49], i.e. the feasibility study for the experiment, has been approved in 1998, even though the development and design of the detector is still on-going. This detector is being assembled at the interaction point 8 which was the Delphi pit during the LEP time. The cave has a useful length of about 20 meters along the beam. Being a single arm spectrometer, LHCb can use the whole experimental area and double the measurable trajectory of the particles compared to a central detector. With a forward spectrometer, the experimental polar angle coverage

---

[2]The vast majority of interactions, called minimum-bias events, are fusion processes of gluons or quarks with a small energy transfer resulting in events with a large number of hadrons of low momentum. Identifying the interesting events from the background requires some clear signatures, e.g. high transverse momentum.

around the direction of one of the proton beams ranges from 10 to 300 mrad in the $x - z$ plane and from 10 up to 250 mrad in the $y - z$ plane, see Fig. (2.4); LHCb therefore loses only:

- Half of the B-mesons produced on the other side, in the "missing arm";

- B-mesons produced with an angle less than 10 mrad which stay in the beam pipe.

Thus, there remains about 35%[3] of B's which can be studied, i.e. which can be tagged and have their daughter particles inside the acceptance.

The strong points of the LHCb detector are:

- **Vertexing and decay time resolution:** An excellent time resolution is required to study the fast B_s^0 oscillation and its CP asymmetry. It is therefore mandatory to reconstruct very precisely the vertices, especialy the displaced secondary vertex which is a distinctive characteristic of b-hadron decays.

- **Particle identification:** There are two essential points in particle ID at LHCb, the hadron (π/K) identification and the lepton (e/μ) ID.

   – Hadron identification is used in the kaon tagging and in the reconstruction of selected decay channels; for instance:

      * $B_d^0 \to \pi^+ \pi^-$ $\left(\mathcal{BR} = (4.8 \pm 0.5) \cdot 10^{-6} \right)$ is heavily contaminated by $B_d^0 \to K^\pm \pi^\mp$ $\left(\mathcal{BR} = (1.85 \pm 0.11) \cdot 10^{-5} \right)$, $B_s^0 \to K^\mp \pi^\pm$ $\left(\mathcal{BR} < 2.1 \cdot 10^{-4} \right)$ and $B_s^0 \to K^+ K^-$ $\left(\mathcal{BR} = 5.9 \cdot 10^{-5} \right)$ decays. The asymmetry in $B_d^0 \to \pi^+ \pi^-$ is used for the determination of α;

      * $B_s^0 \to D_s^\mp K^\pm$ must be distinguished from $B_s^0 \to D_s^\mp \pi^\pm$ which is ten times more numerous. The asymmetry in $B_s^0 \to D_s^\mp K^\pm$ is used for the determination of $(\gamma + \phi_s)$.

   – Lepton ID is used in the different triggers and in the lepton tagging.

- **Precise mass reconstruction:** To reject the combinatorial background due to random combinations of tracks, the mass determination requires an excellent momentum measurement for the detected particles.

- **Triggering:** A high performance trigger is needed to distinguish minimum-bias events from events with B-mesons. This can be achieved by triggering on particles with large transverse momentum and displaced decay vertices.

2.2.1   Detector reoptimization

In 2001-2003, the LHCb detector underwent an extensive reoptimization phase from which significant changes ensued. They are described in the "Reoptimized LHCb Detector, Design and Performances" Technical Design Report [33] which was completed in September 2003. The two main objectives of this modification were:

1. **Reduction of the material budget:** In 2001, we realised that the material budget of the experiment had increased dangerously and might deteriorate the tracking

---

[3]The value depends on the B-meson flavor - essentially B_d^0 or B_s^0- and on the considered decay channel [51].

abilities of the detector: secondary particles might increase the occupancy of the detectors to an unbearable level and the thickness of the detectors might prevent the observation of electromagnetic particles and degrade the resolution of the momentum measurement.

2. **Improvement of the trigger:** We will use the fringe field of the dipole magnet in the upstream region to get a rough estimate of the P_T of the particles from the tracking itself: large impact parameter tracks found in the VELO will be extrapolated to the "Trigger Tracker" (TT) and their momentum measured. The informations from the VELO as well as from the TT will be used in the Level-1 trigger. Details on the triggering scheme of LHCb will be presented in Section (2.5).

This reoptimization led to many changes in the design of the detector:

- **Reduction of the amount of material:** Lighter materials have been used in the VELO, beam pipe and RICH1.

- **Removal of the magnetic shield:** The shielding plate designed to protect the VELO and RICH1 from the magnetic field has been removed, allowing the B-field to extend and the P_T information to be measured for the trigger.

- **Reorganized tracking strategy:** From the eleven tracking stations designed in the Technical Proposal [49] only four remain.

2.2.2 The subdetectors

LHCb can be divided in five main subdetector systems (see Fig. (2.4)):

- **The vertex detector system (VELO):** It contains a silicon vertex detector and a pile-up veto counter. These are used in the event trigger and for the reconstruction of vertices. The vertex detector itself is enclosed by a vacuum tank and the beam pipe.

- **Aerogel and gas RICH counters (RICH):** They are used for particle identification.

- **A spectrometer consisting of a tracking system and a dipole magnet:** It measures the track momenta and provides information on the trajectories of charged particles.

- **Electromagnetic and hadronic calorimeters (ECAL and HCAL):** They are used to trigger on b$\bar{\text{b}}$-events and to identify electrons, photons and hadrons. The electromagnetic calorimeter is optimized for efficient π^0 reconstruction.

- **A muon detector composed of iron filters, interleaved with tracking chambers:** It serves to identify the muons for the trigger and, in the offline analysis, to tag the b-flavor.

A right-handed coordinate system is used with its origin at the center of the interaction volume, with the $z-$axis along the beam direction and the $y-$axis pointing upwards. Charged particles are bent in the horizontal $x - z$ plane.

The remainder of this chapter describes the reoptimized LHCb subdetectors. The components of the detector are divided into three categories: the tracking system (Section 3.2), the particle identification (Section 2.4) and the trigger (Section 2.5).

2.3 The tracking system

In the original design of the LHCb experiment as presented in the Technical Proposal [49] the main tracking system consisted of eleven stations. In the revised detector layout, as shown on Fig. (2.4), only four stations remain: one in between RICH1 and the magnet (the Trigger Tracker) and the three others between the magnet and RICH2 (T1−T3).

The main goal of the tracking system is to obtain a relative particle momentum resolution of $\delta P/P \sim 0.4\%$ for every charged particle issued from a B-decay, which gives a invariant B-mass resolution of ~ 15 MeV/c^2.

The detection of the charged particles and their momentum measurement depend on:

- **The warm Magnet**;

- **The Vertex Locator** (VELO), around the interaction point;

- **The Trigger Tracker** (TT) located after the RICH1;

- **Three Tracking Stations (T1 to T3)** located between the magnet exit and the RICH2;

- **The Beam Pipe**.

The VELO and TT station are microstrips silicon detectors, T1, T2 and T3 are composed of two different detectors:

- In the central part around the beam pipe which represents only 2% of the total area of the stations but receives about 20% of the tracks, microstrip Si detectors are used. They will have to sustain charged particle fluxes up to $5 \cdot 10^5$ cm^{-2}s^{-1}. These subdetectors are named **Inner Tracker** which composed the **Silicon Tracker** with the Trigger tracker.

- In the external area, we use drift straw tubes: they form the **Outer Tracker**.

2.3.1 The magnet

The magnet geometry [52] is completely determined by the LHCb acceptance which requires a dipole field with a bending power of $\int B dl = 4$ Tm and an aperture of ± 300 mrad horizontally and ± 250 mrad vertically. The accuracy of the track momentum measurements depends on the value of the magnetic field seen by the particles along their trajectory. The design precision of 0.4% for momenta up to 200 GeV/c has resulted in a bending power of 4 Tm for tracks originating near the interaction point. Moreover a uniform field is essential to increase the reliability of the track reconstruction. The non-uniformity of the bending power is expected to be less
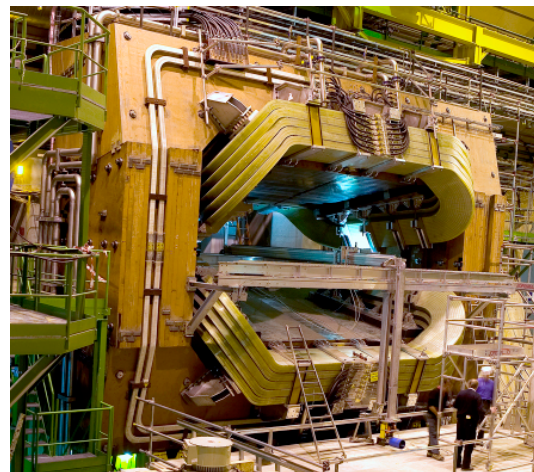
Figure 2.5: *The LHCb magnet and surrounding iron yoke. The field mapping machine is mounted inside. This picture is taken form the "Press Office Photo Selection" of the CERN.*

than $\pm 5\%$ in the acceptance. The collaboration adopted the choice of a warm dipole magnet, i.e. without superconducting coils, shown on Fig. (2.5). A cold magnet was assumed in the Technical Proposal, but finally its reduced electrical power requirements were seen not to be worth the high cost, mechanical risks and construction time. The magnet consists of 9 km of aluminum conducting wires inside a 120 kilotons steel plate yoke.

2.3.2 The silicon vertex detector

Vertex reconstruction is a fundamental issue for LHCb. The B-meson lifetime is long enough to be measured, but requires a very good precision to allow the separation of the secondary vertex, i.e. the B-decay, from the primary vertex which is the proton−proton collision. The Vertex Locator [53, 33] has to provide a B-meson proper time resolution of the order or better than 50 fs.
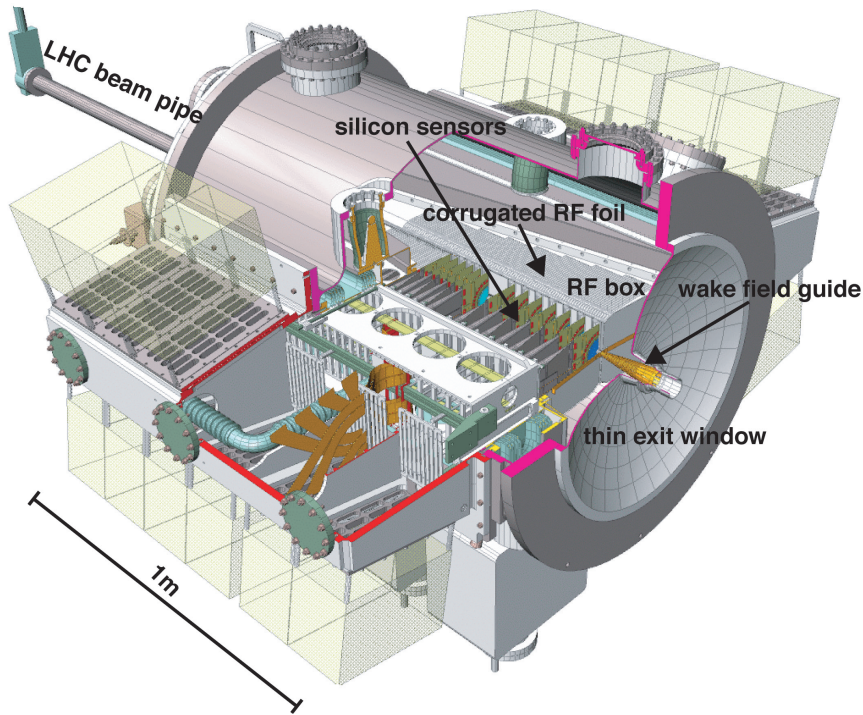
Figure 2.6: *3D view of the vacuum vessel with the silicon sensors (TDR layout with 25 stations) and the corrugated RF-foils. This figure is taken from [33].*

The VELO has also to provide accurate measurements of track coordinates close to the interaction point and associate them to their vertex. It finally plays an important role in the High Level Trigger, telling the acquisition system about possible displaced vertices which are signatures of B-mesons in the event. Moreover, it has to detect all the tracks within the LHCb acceptance ($1.6 < \eta < 4.9$ where η is the pseudo-rapidity[4]).

The forward detector geometry allows to achieve these objectives by placing the sensors as close to the beam as possible. For this reason, all the detector and the readout

---

[4]The pseudo-rapidity is a handy variable to approximate the rapidity when the mass and the momentum of a particle are not known. It is defined via the angle θ, angle between the particle momentum and the beam axis, as $\eta = -\ln(\tan(\theta/2))$. $\eta = 1.6$ corresponds to an angle of 400 mrad and $\eta = 4.9$ to an angle of 15 mrad.

electronics are located inside a special vacuum vessel which includes a Roman pot system to move the detector away from the beam during the filling of the collider, Fig. (2.6). The operation of a similar device has been successfully tested in 1990 at the SppS collider by the P238 collaboration [54].

Due to the movements of the detector before and after the injection phase misalignments of the stations are possible and corrected by a software table updated at the beginning of each run. Other external constraints have to be taken into account:

- Beam bunches generate wake fields[5] which can affect the VELO (RF pick-up, losses) and the LHC beams (instabilities). A RF-foil has to be interleaved between the sensors along the beam to get rid of these electromagnetic effects.

- Because the VELO has to be integrated into the LHC machine vacuum, particular attention was paid to the mechanical constraints on the detector and to the minimization of risks for the LHC.

- Close to the interaction point, the VELO suffers from a very hard radiation environment. Therefore the acquisition electronics has to be placed as far from the beam as possible, that is around the disks, and be radiation hard.
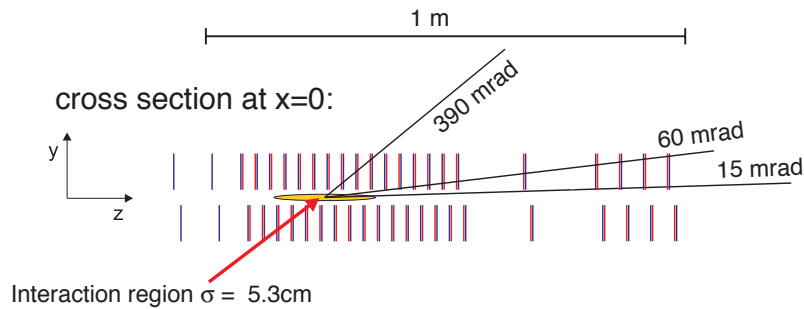
Figure 2.7: *Pile-up veto counter and* VELO *station setup shown in the* $y - z$ *plane. The pile-up veto consists of the two single plane of silicon stations situated at the lowest* z *positions. The* VELO *is made of 21 stations, each consisting of two silicon planes. This figure is taken from [33].*

Fig. (2.7) represents the layout of the VELO and the pile-up veto stations. The VELO consists of 21 silicon disk-shaped stations placed along the beam direction. Each station is made of two planes of sensors, measuring the radial and the angular components of all tracks. In these planes, two hemispherical silicon strip detectors are placed on each side of the beam. The previous design used four more stations. They have been removed to reduce the amount of material.

---

[5]Wake fields, generated by a moving particle in the accelerator pipe and objects such as RF cavities, bellows, stripline monitors etc., affect the motion of particles in the tail part of the beam causing the parasitic loss, beam energy spread, and instabilities.
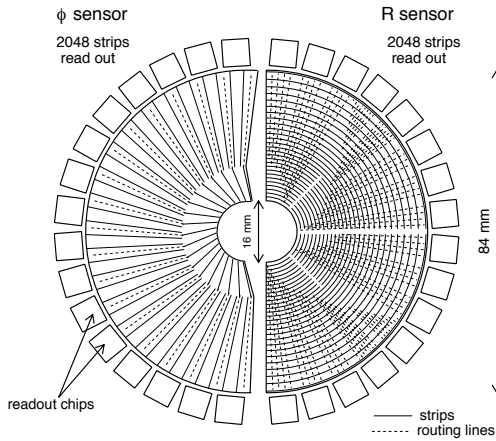
Figure 2.8: *Schematic view of the r and φ silicon sensors. The φ sensor strips have a stereo angle to resolve ambiguities. Figure taken from [53].*

Fig. (2.8) shows the two different sensors found in a station. The sensors are placed in a primary vacuum of $\lesssim 10^{-4}$ mbar. The inner active radius is limited to 8 mm due to the LHC machine constraints and the outer radius of 42 mm is imposed by the magnet acceptance. Both are made from 220 μm thick n-on-n single sided silicon wafers. The r sensor strip pitch increases with the radius from 40 to 92 μm and the one of the φ sensor goes from 37 to 98 μm with a 10° to 20° stereo angle. They both cover 182°. The overlap allows to cover completely the acceptance.

The resolution on the primary vertex position is ∼40 μm in z and ∼10 μm in x and y. For secondary vertices the spatial resolution depends on the number of tracks but on average it varies from 150 to 300 μm in z. This roughly corresponds to a resolution of 50 fs for the B-lifetime.

Any charged particle crossing a sensor ionizes the conducting strips (generally one or two, depending on the crossing angle and the position of the strips with respect to the particle trajectory) which generates an electric pulse collected by the electronic readout. This latter consists of 16 chips per sensor, which accept input data at 40 MHz kept in an analog pipeline for up to 4 μs until the Level-0 trigger decision is received. Then 32 readout lines are serialized through an analog link of 60 meters up to a radiation free environment where the off-detector Level-1 electronics checks the data integrity, digitizes the signals, performs a zero-suppression and finds the clusters before sending the results to the Level-1 trigger. Events accepted are processed and transfer to the High Level Trigger and subsequently to storage.

2.3.3 The Trigger Tracker

The TT station [55, 33] fulfills a two-fold purpose. First, it is used in the Level-1 trigger to assign the transverse momentum information to the tracks. Second, it is used in the offline analysis to reconstruct the trajectory of low-momentum particles that are bent out of the detector acceptance in the field of the magnet and thus never reach T1-T3 stations as well as long lived neutral particles, decaying outside of the VELO.

The Trigger Tracker covers a rectangular area of approximately 130 cm in height and 160 cm in width. It is composed of four planes of silicon strip detectors with a strip pitch of 183 μm. They are split into two pairs separated by 27 cm: TTa centered at $z = 235$ cm and TTb at $z = 262$ cm. As for the Inner Tracker and the Outer Tracker, the first and fourth plane have a vertical readout strip ($x-$layout) and the second and third are stereo layers with an angle of $+5°$ ($u-$layer) and $-5°$ respectively ($v-$layer). These are illustrated on Fig. (2.9 and 2.10). The detector operates at about 5°C to reduce the leakage current[6].

---

[6]The leakage current is the unwanted current leaking between two electrodes under voltage. In detectors, it can be observed in wire or semiconductor detectors, without ionization due to charged particle interactions. Radiation damage can increase the leakage current, which translates into a decrease of the signal-over-noise ratio.

Figure 2.9: *Front view of a $x-$layer in TTa.*
Dimensions are in cm. Figure issued from
[33].

Figure 2.10: *Layout of the $u-$layer in TTa. Di-*
mensions are in cm. Figure issued from [33].

2.3.4 The Outer Tracker

The Outer Tracker (OT) [56], situated around T1, T2 and T3, detects the track positions in
the acceptance of LHCb which have a radial angle larger than about 15 mrad. Thanks to a
moderate particle density, the foreseen technology is gas drift chambers. Its advantage is
a rather low cost for a good spatial resolution. The selected gas is the mixture $Ar(75\%) -$
$CF_4(15\%) - CO_2(10\%)$, which was chosen to optimize the drift speed.
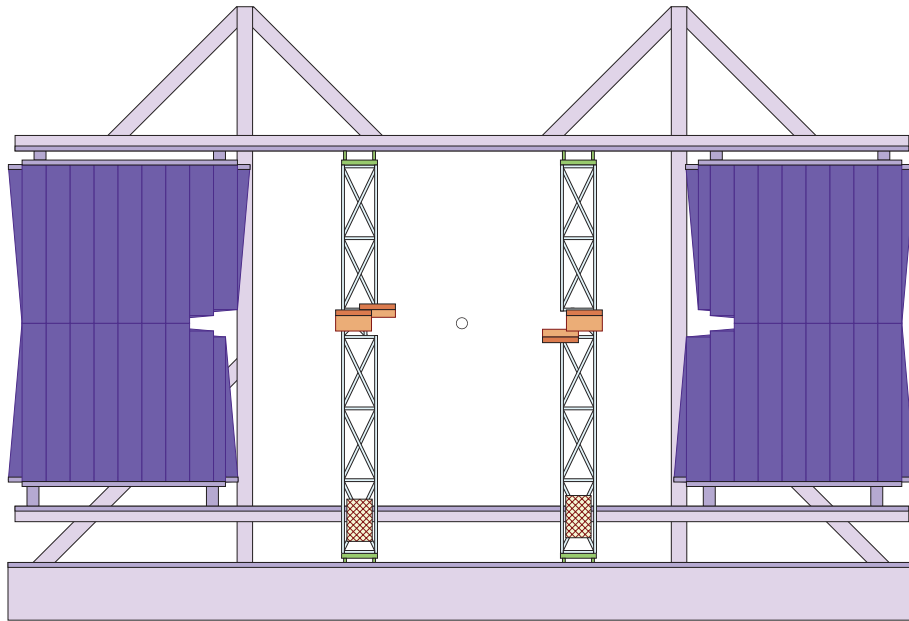
Figure 2.11: *Front view of an opened tracking station showing the beam pipe in the middle,*
the Inner Tracker boxes and then the Outer Tracker straw tubes on the outside. This figure is
taken from [55].

The Outer Tracker is made of drift cells, called straw tubes, with the anode collecting

the signal in the middle. They are gathered in modules of 34 cm wide. A station is made of 4 layers of modules. The first and fourth have a vertical alignment (x−layer) , while the second and third have a stereo angle of $+5°$ and $−5°$(u−layer and v−layer). The readout electronic is placed at the tubes ends, outside the acceptance.

The radius of these tubes is limited to 5 mm by the total drift time for a correct assignment of the signal to the corresponding event. A maximum drift time of 50 ns (two bunch crossings) is imposed to facilitate the pattern recognition of tracks. It can happen then that two events are piled-up in the OT.

Fig. (2.11) shows the left and right, individually removable, half side of the Outer Tracker mounted on rails.

2.3.5 The Inner Tracker

The high track density at small polar angles does not permit the use of drift chambers technology. A specific detector has thus been developed, based on silicon microstrip sensors [55]. It covers a cross-shaped area around the beam pipe, approximately 120 cm wide and 40 cm high. Each station consists of four detection layers, as for TT and the OT, with a u and a v stereo layer sandwiched in between two x−planes Fig. (2.12 and 2.13). The detector is divided in four parts of detection: left, right, top and bottom. The overall sensitive surface of the three stations amounts to $\sim$ 4.2 m^2. Large strip pitches ($\sim$198 μm) and long read-out strips (up to 22 cm length) are employed in order to minimize the number of read-out channels.
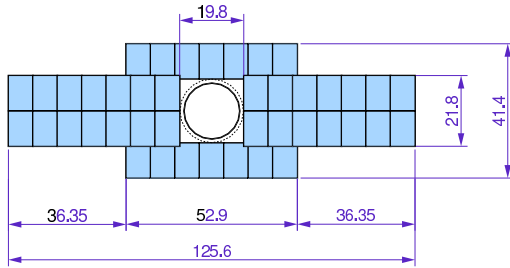
Figure 2.12: *Layout of x−layer in T2. Dimensions are given in cm. This figure is taken from [55].*
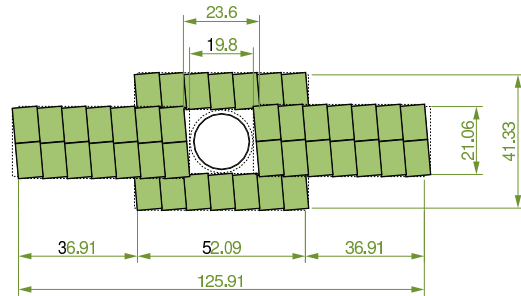
Figure 2.13: *Layout of u−layer in T2. Dimensions are given in cm. This figure is taken from [55].*

The innermost region of the Inner Tracker expects charged particle fluxes up to $5 \cdot 10^5$ cm^{-2}s^{-1}, which decreases rapidly with increasing distances from the beam axis. The readout granularity of the detector has to match the expected particle fluxes in order to ensure low occupancies which are essential to obtain high reconstruction efficiency. The z−coordinates of the three stations are $z = 770$ cm (T1), 840 cm (T2) and 910 cm (T3). They are located just in front of the Outer Tracker stations, allowing an overlap of 1 cm.

Part of the front-end electronics is situated inside the acceptance of the experiment. As the momentum resolution is dominated by multiple scattering, minimization of material budget is an important criterion for the design of this detector as is the choice of its radiation hardness. The front-end electronics has a fast shaping time ($\sim$ 35 ns) in order to avoid the reconstruction of overlapping events from consecutive bunch crossings.

2.3.6 The beam pipe

The beam pipe looks like a conical tube passing through the center of the sub-detectors as shown on Fig. (2.14) [33].
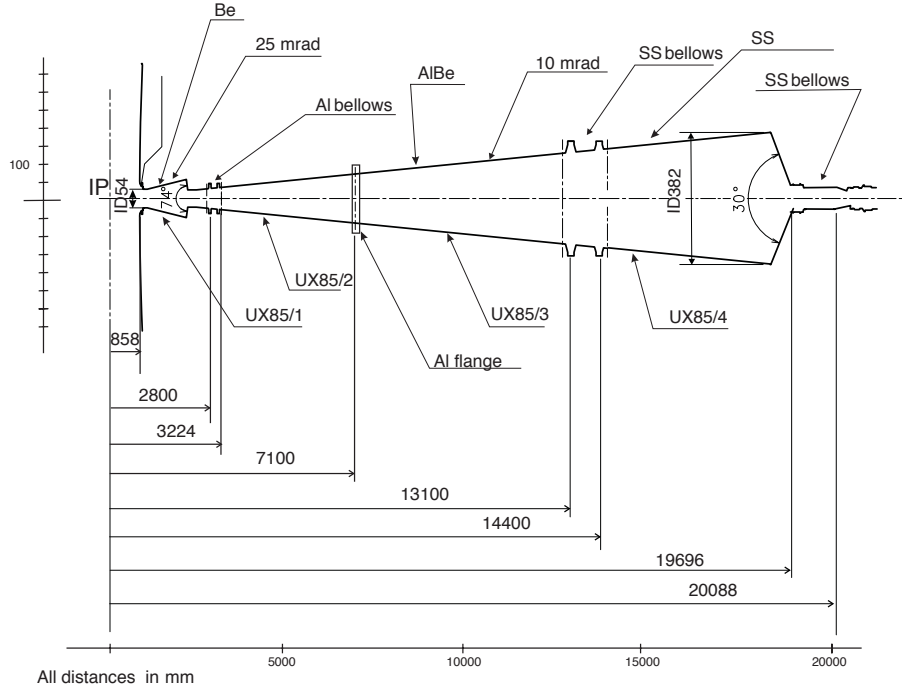
Figure 2.14: *Layout of the beam pipe. The second section is now completely made of Beryllium. The scale in the vertical axis has been enlarged with respect to Fig. (2.4). This figure is taken from [33].*

Many particles are produced at small polar angle in a p − p collision. They can interact with the material of the pipe and produce secondary particles which can overwhelm the sub-detectors. The consequences would then be:

- Detection of a large number of particles with "abnormal" trajectories, i.e. not pointing to the interaction region;

- Creation of high fluence of particles in places around the beam pipe, which can be harmful to the front-end electronics located on the detectors near the beam.

In order to minimize these unwanted interactions the beam pipe is designed as a cone centered on the interaction point. Thus the emitted particles with a polar angle smaller than the cone aperture never interact with LHCb detector matter. After the vertex detector, the beam pipe is composed of:

- A beryllium conic section of 1.5 m long, with an aperture of 25 mrad and a thickness of 1 mm;

- A second beryllium conic section of 16 m long and 15 mrad of angular aperture with an increasing thickness of 1.0 to 2.4 mm.

2.4 The particle identification

As already discussed, particle identification is a fundamental requirement for the LHCb experiment. The measurement of CP violation parameters is feasible only if leptons and hadrons are well identified over a wide momentum range. This is provided by the Ring-Imaging-Cherenkov (RICH) for π/K separation, the electronic calorimeter (ECAL) for electrons, photons and π^0's, the hadronic calorimeter (HCAL) for hadrons, and the Muon System.

2.4.1 The RICH's

Ring Imaging Cherenkov (RICH) detectors allow the identification and the separation of pions and kaons. This is a crucial information to increase the signal to background ratio for B-decays and to provide a kaon tag for CP asymmetry measurements. There are two RICH detectors in LHCb referred to as RICH1 and RICH2 [33, 57]. They allow a good separation of pions and kaons in the momentum range from 1 to 150 GeV/c, which represents more than 90% of the π and K from the B-decay channels. These particles also serve to tag the B-flavor, especially the high P_T kaons.

Cherenkov radiation is an effect discovered by P.A. Cherenkov in 1934 while studying the effects of gamma rays on liquids [58]. When a particle of charge Z passes through an optical medium of refractive index $n > 1$ at a velocity $\beta = \dfrac{v}{c} > \dfrac{1}{n}$, an electromagnetic wave is emitted. Its propagation direction forms an angle θ_C with respect to the trajectory of the particle in such a way that $\cos(\theta_C) = 1/\beta n$.

In the classical approximation, the number of emitted photons depends on the length L of the radiator. It is given by $N = 2\pi Z^2 \alpha L \sin\theta_c^2 (1/\lambda_1 - 1/\lambda_2)$, where λ_1 and λ_2 define the wave length range of the detected photons and α is the fine-structure constant. The energy loss of the incident particle is negligible in LHCb ($\mathcal{O}(\text{keV})$). A one meter thick radiator produces $\sim$120 photons in the range $400 < \lambda < 700$ nm. Assuming that the photodetectors have a quantum efficiency of $\sim$0.3, one can get 40 photo-electrons.

The RICH counter detects ring images formed by the Cherenkov photons emitted along the track of a charged particle traversing the detector. Given the momentum of the particle, the measurement of the radius of the produced ring allows the separation of particles of different masses, in particular pions and kaons. The momentum and entry point of the particle is given by the tracking system. Focusing mirrors direct the ring onto a compact array of photodetectors, the Hybrid Photon Detectors (HPDs). These mirrors send the image in a region outside the acceptance of LHCb where the photo-detectors can be placed without being harmed by the magnetic field and where the radiation is low enough to allow the use of non radiation hard electronics.

The only possibility to cover the required momentum scale (1 GeV/c$< p <$150 GeV/c) is the use of two RICH detectors with different refractive index ranges. As the polar angle of the particles is strongly correlated to their momentum, the most energetic particles will have low polar angle (20 mrad $< \theta_C <$ 50 mrad). Therefore three radiators are used:

- A silica aerogel, with $n = 1.03$, for low momentum particles;

- C_4F_{10}, with $n = 1.0015$, for intermediate momentum particles;

- CF_4, with $n = 1.00046$, adapted to high momentum particles.
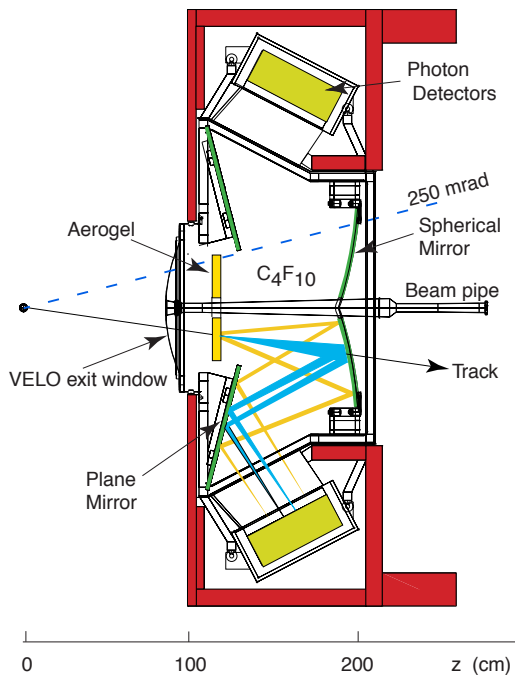
Figure 2.15: *Layout of the vertical RICH1 detector. This figure is taken from [33].*
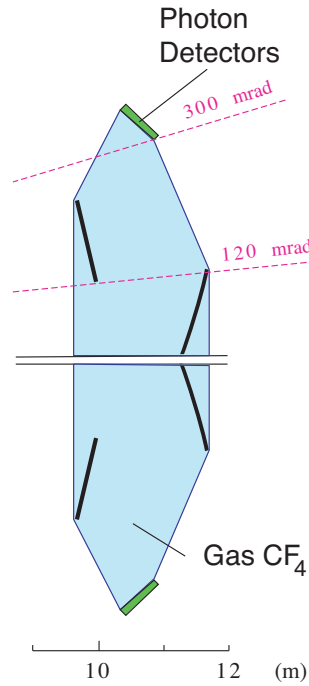
Figure 2.16: *Layout of the vertical RICH2 detector. This figure is taken from [59].*

At LHCb, the two RICH detectors have to identify charged particles over a large momentum range and within an acceptance of 10-330 mrad. A 3σ separation versus the momentum of pions and kaons is achieved over the momentum range 1-150 GeV/c.

RICH1, the upstream detector: Shown on Fig. (2.15), RICH1 is designed to identify low-to-intermediate momentum tracks (1-40 GeV/c). Its angular acceptance runs from 25 to 330 mrad in both $x-$ and $y-$planes. It is placed upstream of the magnet between the VELO and TT and occupies about 1 m along the beam axis. RICH1 contains both a 5 cm-thick aerogel and a gaseous $\sim$95 cm long C_4F_{10}.

RICH2, the downstream detector: RICH2 (Fig. (2.16)) has an acceptance aperture of 10-120 mrad in x and 10-100 mrad in y. Positioned between T3 and the first muon chamber, it provides a momentum coverage from 5 to 150 GeV/c. It is filled with CF_4 and is length is 170 cm along the beam axis.

2.4.2   The calorimeters

The purpose of the calorimeter system is to detect and measure the total energy of high P_T hadrons, electrons and photons for physics analyzes and for Level-0 trigger, identify the electrons to tag the B-meson flavor and to reconstruct π^0 and γ, especially those coming from a B-decay.

The LHCb calorimeter system consists of a Scintillator Pad Detector (SPD), a PreShower (PS), an Electronic Calorimeter (ECAL) and a Hadron Calorimeter (HCAL), each of which is divided into regions with different cell sizes [60]. The three first detectors have their cells gathered in three areas - "*inner*", "*middle*" and "*outer*" - as shown on Fig. (2.17), whereas the HCAL is divided in two parts as shown on Fig. (2.18). The chosen segmentation is a compromise between a small number of readout channels and a low occupancy

with reasonable position and momentum resolution.
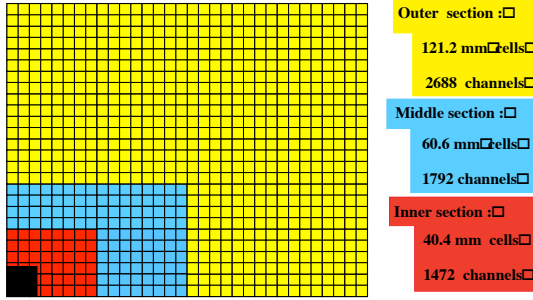
Figure 2.17: *Transverse segmentation of the SPD, PS and ECAL cells. A square represents a "module". One quarter of the detector front face is shown. Figure from [60].*
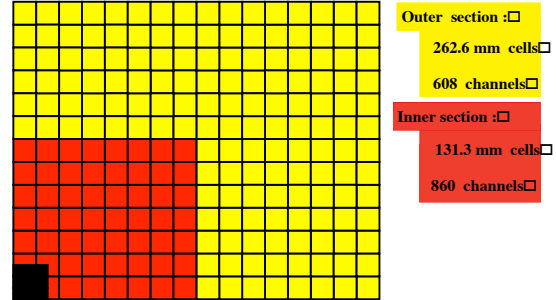
Figure 2.18: *Transverse segmentation of the HCAL cells. A square represents a "module". One quarter of the detector front face is shown. Figure from [60].*

- **The SPD and PS:** These sub-detectors are located in front and after the 12 mm (2 radiation lengths[7]) lead converter. They both consist of scintillator tiles of the same transverse size as the ECAL modules and have a thickness of 15 mm. The scintillation light is first shifted in wave length using wave length shifter fibers "immersed" in grooves machined in the scintillator tiles, before being sent via clear fibers to multianode (8×8) photo-multipliers located above and under the detector.

  Minimum ionizing particles produce an average of 25 photoelectrons in these scintillators. The purpose of the SPD and the PS is two-fold:

  – The SPD allows to distinguish between charged and neutral particles.
  – The PS allows to have a fast pion versus electron rejection which can be used in the trigger: for an electron efficiency of 95%, a pion rejection of 92% can be achieved. Pion rejection can further be increased in off-line analyzes combining the ECAL and the spectrometer data.

- **The ECAL:** The LHCb electromagnetic calorimeter (ECAL) uses the "Shashlik"[8] technology. It is build from individual modules that are made from 66 lead absorber plates (2 mm) inter-spaced with scintillator tiles (4 mm thick) as active material. Its total thickness corresponds to 25 radiation lengths and 1.1 interaction lengths[9]. Wavelength-shifting fibers penetrate the lead/scintillator stack through holes and are readout at the back of the sampling structure by photomultipliers. The ECAL structure is segmented into three sections with one type of module per section, which can be seen on Fig. (2.17). All three types of module have an identical square size of 121.2 mm, but differ by the number of readout cells. The ECAL section closest to the beam pipe consists of 167 modules containing 9 readout cells each, the middle section has 448 modules containing 4 cells each, and the 2688 outer-section modules are made from a single cell.

[7]The radiation length of a material is defined as the distance over which the electron energy is reduced by a factor $1/e$ due to radiation loss only.
[8]So named because the scintillator tiles are pierced by the wavelength-shifting fibers as on a skewer.
[9]The interaction length of a material is defined as the distance before which a particle undergo an interaction that is neither elastic nor quasi-elastic.

The design resolution is $\sigma(E)/E = 10\%/\sqrt{E} \oplus 1.5\%$ where the first term is the stochastic component and represents the statistics related fluctuations, such as the intrinsic shower fluctuation, the photoelectrons statistics, etc. The second term is due to the detector non-uniformity and calibration uncertainty; $\oplus$ means that the two terms have to be added in quadrature; E is expressed in GeV.

- **The HCAL:** The LHCb Hadron Calorimeter (HCAL) is a sampling device made out of steel and scintillating tiles, as absorber and active material respectively. The sampling structure, shown on Fig. (2.18), is on average 4 mm of scintillator for 16 mm of iron. The special feature of this sampling structure is the orientation of the scintillating tiles that runs parallel to the beam axis. Wavelength shifting fibers runs along the edges of the scintillator tiles that are staggered in depth and bring the scintillating light to photomultiplier tubes that are fixed at the end of the sampling structure. With an overall material thickness of 1.2 meters, 5.6 interaction lengths, the energy resolution obtained is $\sigma(E)/E = 80\%/\sqrt{E} \oplus 10\%$.

2.4.3 Muon detector

Muons are present in several final states of B-decays sensitive to CP violation as in the two "golden channels": $B_d^0 \to J/\psi(\mu^+ \, \mu^-) \, K_S^0$ and $B_s^0 \to J/\psi(\mu^+ \, \mu^-) \, \phi$. Moreover, muons will provide a clean identification of the B-flavor through its semi-leptonic decay and thus are essential to the tagging. In addition, the study of rare B-decays such as the flavor changing neutral current decay $B_s^0 \to \mu^+ \, \mu^-$ may reveal New Physics beyond the Standard Model.

The Muon System is made of five stations (M1 to M5) covering an acceptance of ± 300 mrad horizontally and ± 200 mrad vertically. M1 is placed in front of the SPD/PS. M2-M5 follow the Hadron Calorimeter and are separated by 800 mm thick iron filters. The stations cover an area of 435 m^2. The total absorber (including the calorimeters) is approximately 20 interaction lengths. The acceptance of the Muon System is about 46% for the muons from inclusive b-decays. Each station is divided into four regions, R1 to R4 (Fig. (2.19)), with increasing distance from the beam axis. The granularity of the readout is finer in the horizontal plane, in order to give an accurate measurement of the track momentum. The information must be gathered within 20 ns, the detectors are therefore optimized for this purpose. The choice went to Multi Wire Proportional Chambers (MWPC) with 2 mm wire spacing and a small gas gap (5 mm). Triple-GEM[10] detectors are used in the innermost region (R1) of station M1 which has to sustain a rate of ~ 460 kHz/cm^2. There are 1380 chambers in the Muon System, of 20 different sizes.

2.5 Event trigger

Given the luminosity at LHCb and the inelastic p $-$ p cross section, storage devices will not be able to record all the events produced and even not all potentially reconstructible B-meson events. This requires that the fraction of interesting events must be enhanced with respect to the rest of the events and that the total number of events which we want to record be reduced to an acceptable level.

---

[10]The triple-GEM is a multi-step gas avalanche detector that exhibits a high rate capability with a time resolution below 10 ns
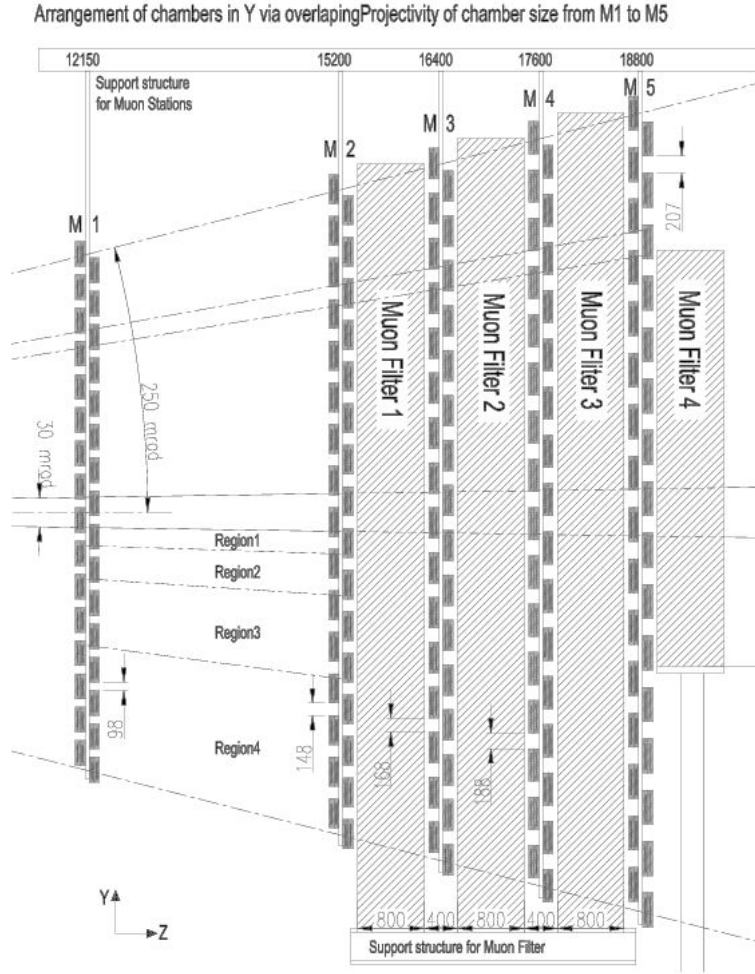
Figure 2.19: *Sideview of the Muon System in the $(y - z)$ plane. This figure is taken from [61].*

2.5.1 Trigger

Due to the large mass difference between the b-hadrons and their products, the formers tend to decay into large E_T leptons, hadrons or photons. Moreover, as those b-hadrons have a relatively long lifetime, their decay vertex is a few millimeters away from the collision point which means that the impact parameters of the decay products, with respect to the primary vertex, has to be large. These two characteristics which are typical to B-decays, allow a good rejection of minimum-bias events and combinatorial background. This rejection can be further improved with cuts on the so-called "global event variables", such as charged track multiplicity and number of interactions per event.

Due to the small cross-section of $b\bar{b}$ pair production compared to the inelastic scattering of protons (see (2.1.3)) a small fraction of bunch crossings give birth to interesting events in LHCb. The data reduction level depends on the capacity of the off-line storage devices and the data flow obtained from the entire detector. LHCb has about one million

readout channels, which at a bunch crossing of 40 MHz corresponds to a data flow of 40 TB/s whereas only 20 MB/s can be stored on tapes. Therefore the data reduction must be at least a factor 200k. This can only be done with a multi-level trigger scheme with simple and fast selection at the beginning of the chain to create more comfortable conditions for the operations of more sophisticated and slow algorithms at the end. Temporary data storage in pipeline buffers reduces the dead time effect due to the limited latency of each trigger (~ 750 ns and ~ 1050 ns respectively).

LHCb has a 3-level trigger system [62]. Logically they can be split into two groups. The first group of triggers, Level-0 (L0) and Level-1 (L1), uses local informations from individual detectors. At Level-0 only raw data are considered. The Level-1 requires data after zero level subtraction and clustering of hits. The High Level Trigger (HLT) employs more complex algorithms which gather data from several detectors and is essentially a software triggering level working on the whole event. This scheme is shown on Fig. (2.20).

2.5.2 Level-0 trigger

The Level-0 trigger exploits the relatively high transverse momentum of the B-decay products compared to that of minimum-bias events. Four "high P_T triggers" run in parallel for electrons, photons, hadrons and muons. The first three share a common algorithm with different selection cuts and uses raw calorimeter informations, while the last one depends on muon detectors. The *Pile-Up Veto* is also used at this level to identify the vetoed events with multiple interactions. The L0 reduces the event rate to ~ 1 MHz. The decision is then taken by the L0 Decision Unit (L0DU). The maximal time to establish the L0 checks of an event is fixed at 4.2 μs. This presumes a 168 events long buffer (168×25 ns) in which the data are waiting for a decision in a pipeline queue.

- **The electron trigger** combines data of M1, the SPD, the preshower and the ECAL to search for high E_T electrons. The event is accepted if $E_T > 2.8$ GeV. This cut is tuned to achieve a suppression of $\sim$100 against inelastic p $-$ p interactions.

- **The photon trigger** is like the electron trigger but with M1 used as a veto. The E_T must be greater than 2.6 GeV which leads to a rejection factor of about 150 of minimum-bias events.

- **The hadron trigger** uses the HCAL, the PS and M1, and accepts an event with a hadron of $E_T > 3.6$ GeV. The minimum-bias reduction factor is here 17.

- **The muon trigger** first reconstructs the tracks with all the five muon chambers M1-M5, then it checks for a compatibility with the hypothesis of a high P_T muon coming from the vertex region. If $E_T > 1.1$ GeV for a single muon or $E_T > 1.3$ GeV for more muons, the event is accepted.

- **The Pile-Up Veto** detects primary vertices. As a large fraction ($\sim 40\%$) of the bunch crossings contains more than one p $-$ p interaction and as these events are preferably accepted by high P_T triggers, they reduce the L0-bandwidth and therefore have to be removed. The rejection is done using two r sensors placed upstream of the VELO. The event is rejected when two or more "primary vertices" are found with these sensors.

- **The L0DU** combines all the informations from the Level-0 subtriggers into one decision per event. It accepts events when at least one of the largest E_T of the e$^\pm$, γ,
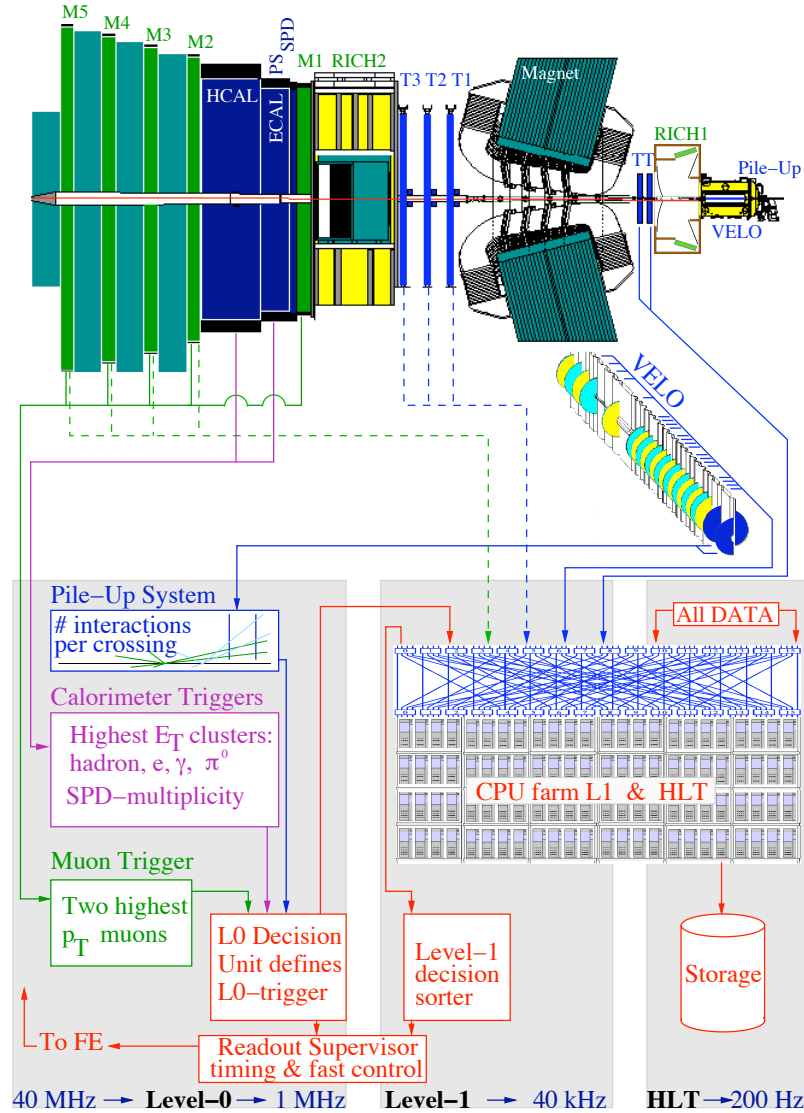
Figure 2.20: *Overview of the three trigger levels. Muon stations are used to reconstruct two muons per quadrant. The SPD, PS, ECAL and HCAL are used to reconstruct the hadron, $e^{\pm}$, γ and π^0 with the largest transverse energy, the charged particle multiplicity and the total energy. The Pile-Up detector has to recognize multiple interactions in a bunch crossing. Level-1, uses the informations of VELO, TT and Level-0 and reduces the rate to 40 kHz. T1-T3 and M2-M5 can also be included in Level-1. The HLT uses all data in the event apart from the RICH to reduce the rate down to 200 Hz. Level-0 is made using full custom electronics while Level-1 and HLT are software triggers which share a farm of 1800 CPU's. This figure is taken from* [62].

π^0, hadron or muon is above the threshold provided that the *Pile-Up Veto* detects less than three tracks coming from another primary vertex. If the sum of the E_T of the two largest E_T muons are above a threshold. The L0DU also sends out a positive signal irrespective of the *Pile-Up Veto* result.

2.5.3 Level-1 trigger

The second trigger level, Level-1, reduces the event rate from 1 MHz to an output rate of 40 kHz, using the information of the VELO, TT and the summary information from L0. The L1 algorithm reconstructs tracks in the VELO, matches them to the L0 muon and calorimeter candidates and measures their momenta with the help of the fringe field of the magnet between the VELO and the TT station. High impact parameters, as well as the high P_T of the tracks, are used to select good events from minimum-bias. Both Level-1 trigger and HLT are executed on a 1800 node CPU farm, where L1 has priority over HLT due to its smaller latency ($\sim$ 50 ms compared to $\sim$ 200 ms).

Events are selected according to six parallel trigger lines:

- **Generic (P_T):** The logarithmic sum of the transverse momenta must be
  $\ln\left(P_T^1/\mathrm{MeV}\right) + \ln\left(P_T^2/\mathrm{MeV}\right) > 13.915$ for tracks with an impact parameter $0.15 < IP < 3$ mm and a pile-up veto up to 2 primary vertices.

- **Single-muon:** One reconstructed μ is required to have his impact parameter larger than 0.15 mm and his $P_T > 2.3$ GeV/c. The pile-up veto is increased to 3 primary vertices.

- **Dimuon general:** The invariant mass of the two muon candidates must exceed 500 MeV and $IP_{\mu\mu} > 0.05$ mm[11].

- **Dimuon J/ψ:** This trigger aims to select unbiased J/ψ or higher mass particles decaying leptonically, with only mass cuts:
  $\left|\mathrm{m}_{\mu\mu} - \mathrm{m}_{\mathrm{J}/\psi}\right| < 500$ MeV or $\mathrm{m}_{\mu\mu} > \mathrm{m}_\mathrm{B} - 500$ MeV.

- **Electron:** The maximal $E_T(\mathrm{e})$ has to be greater than 3.42 GeV and $\ln\left(P_T^1/\mathrm{MeV}\right) + \ln\left(P_T^2/\mathrm{MeV}\right) > 13.0$.

- **Photon:** The maximal $E_T(\gamma)$ has to be greater than 3.1 GeV and $\ln\left(P_T^1/\mathrm{MeV}\right) + \ln\left(P_T^2/\mathrm{MeV}\right) > 13.0$.

2.5.4 High Level Trigger

The purpose of this trigger is to keep events with specific decay b-hadron modes, events with a D* or events with muons using all the detector information available (except the RICHs). Its first step is to reconstruct the VELO tracks and the primary vertex rather than using the information from L1. A fast pattern recognition algorithm then links the VELO tracks to TT and then to the tracking stations T1-T3; in its second step a set of selection cuts dedicated to specific final states is applied.

The High Level Trigger has a latency of about 200 ms and a minimum-bias suppression factor of 20, which reduces the L1 output rate from 40 kHz to 2 kHz. At this frequency the remaining events are fully reconstructed and particle identification applied before being written onto a storage device.

The event rates at HLT-level aim to maximize the physics output, given the available and expected computing resources, divided in four streams, summarized in Tab. (2.3):

- **Exclusive B-candidates at $\sim$200 Hz:** This is the core physics stream with exclusively reconstructed decays, including sidebands and control channels.

---

[11]$IP_{\mu\mu}$ is the smallest positive IP to any primary vertex, fixed to zero if there is no positive IP

- **D* candidates at ~300 Hz:** These events allow to measure the particle identification (PID) efficiency and the miss-identification rate. They can also be used for CP-measurements in D-decays. The selection is made through a blind PID on the D*, with $D^0 \rightarrow hh$, and no D^0 mass cut.

- **Dimuon candidates at ~600 Hz:** These events are used to study the uncertainty on the lifetime measurements using prompt J/ψ through selecting lifetime unbiased dimuon pairs with a mass above 2.5 GeV/c^2.

- **Inclusive b-candidates at ~900 Hz:** This sample includes events with high P_T and high-IP muon especially used for systematic studies of the trigger efficiency and for data mining.

Event type	HLT rates	Events/(2fb^{-1})	Physics program
Exclusive B-candidates	200 Hz	$2 \cdot 10^9$	Core B-program
D* candidates	300 Hz	$3 \cdot 10^9$	Charm (mixing & CPV)
High mass dimuon candidates	600 Hz	$6 \cdot 10^9$	Unbiased b $\rightarrow$ J/ψ X
Inclusive B-candidates (b $\rightarrow \mu$)	900 Hz	$9 \cdot 10^9$	B (data mining)

Table 2.3: *HLT-output rates*

The data flow of the HLT, for exclusive B-candidates, is sketched in Fig. (2.21). First the HLT-Generic decision is made by re-doing the L1-Generic line with an improved precision (so-called L1-confirmation), in particular with better momentum determination. The particles are then reconstructed as pion and kaon candidates to which the photons and electrons are added. Afterwards, the kaons and pions are combined to make composite particles like D^0, ϕ, K*, ... Additionally, the generic HLT selects all dimuon candidates before any mass cut. Finally the shared particles are combined to create B-candidates for all the core physics channels.

2.5.5 Data Acquisition

The philosophy of the Online System (Data Acquisition and Experimental Control) [64] system is rather standard. It is implemented as a multi-level system. The data are stored in pipeline buffers while waiting for a positive decision from the corresponding trigger level. The buffer length depends on the complexity of the algorithm and the available computing power. The pipeline lengths at Level-0 and Level-1 are proportional to the latency of these triggers.

Following the Level-1 trigger, Front-End multiplexers (FEM) combine the zero-suppressed data from many detector channels onto the Front-End links (FEL). The Readout Unit (RU) receives the informations from several FELs and assemble them into larger sub-events. Then each sub-event is transferred via the readout network to the Sub-Farm Controller (SFC) which then combines all of them into complete events. They are then processed by the High Level Trigger and, finally, the SFC dispatches the accepted events via the readout network to the storage sub-system.

The DAQ also includes the Experiment Control System (ECS) which will monitor and control the operational state of the LHCb detector and the associated experimental equipment such as the gas systems, high voltages and readout electronics. The ECS is designed
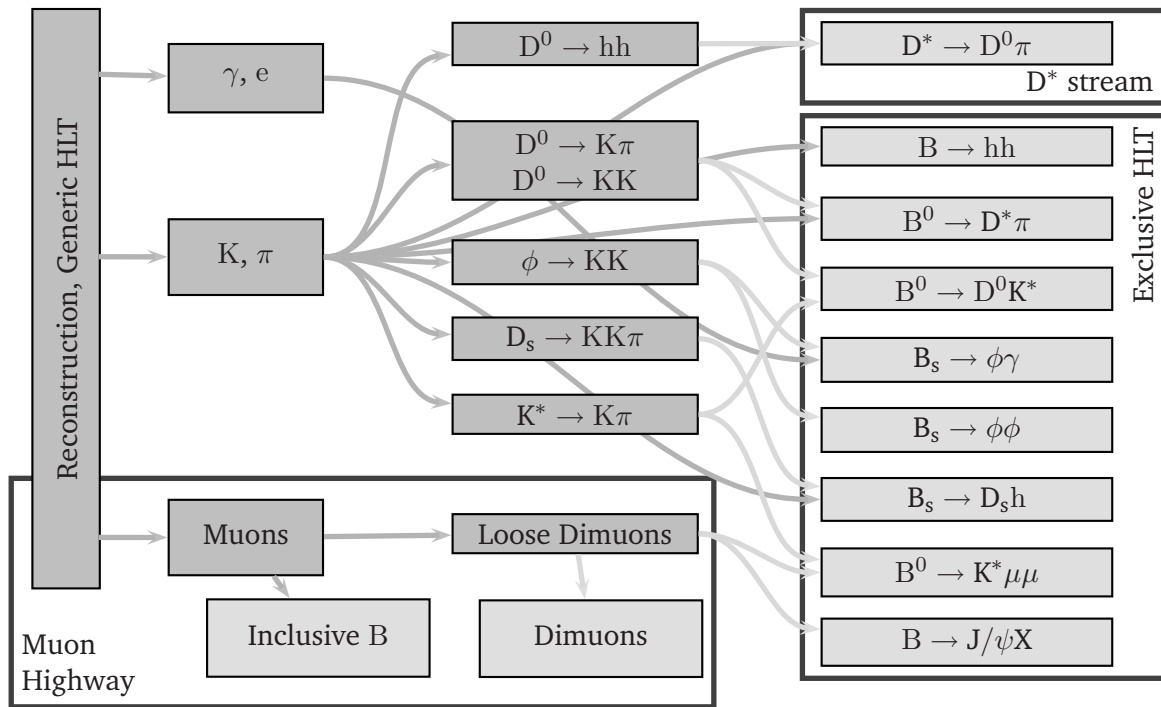
Figure 2.21: *Simplified data flow in the HLT. Each gray box is an algorithm (or a set of algorithms). This figure is taken from [63].*

to operate the experiment from the control room during data taking. Nevertheless it also allows the operation of the different sub-systems in stand-alone mode, when necessary. The ECS also stores data from the detector such as temperatures and positions, allowing them to be accessible by both the reconstruction and physics analysis programs.

Chapter 3

Simulation and physics performances at LHCb
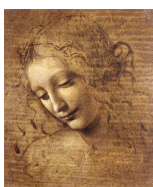
In this chapter, the full simulation of the detector is presented. The software structure is described first. Then the tracking and tagging of events in the simulation are presented. The main physics performances regarding the CKM parameters are then discussed. Finally the $B_s^0 \rightarrow J/\psi\ \eta$ decays in the LHCb environment are described.

$\mathcal{I}$N modern particle physics the complexity of the experiments and the large amount of data require a large computing facilities and an enormous effort on high performances software. In LHCb as well as in any other high energy physics experiments, a computing group is responsible for preparing the tools needed both in the design phase of the detector and in the final physics studies. The different parts of these developments as well as the physics performances of the LHCb detector are explained in this section.

3.1   Simulating LHCb

All of the physics results presented in this dissertation were obtained with a full simulation of the LHCb detector. Until 2001, all studies were carried out using a fortran based program, which performed the tasks of event generation, detector simulation, reconstruction and analysis. Presently, the LHCb software has migrated to an object oriented (OO) C++ framework named GAUDI [65, 66]. All tasks are now almost fully implemented within this framework.

Fig. (3.1) shows the structure of the software used and the data flow between the logical blocks. First the **generator** simulates the collisions of two protons and thus generates
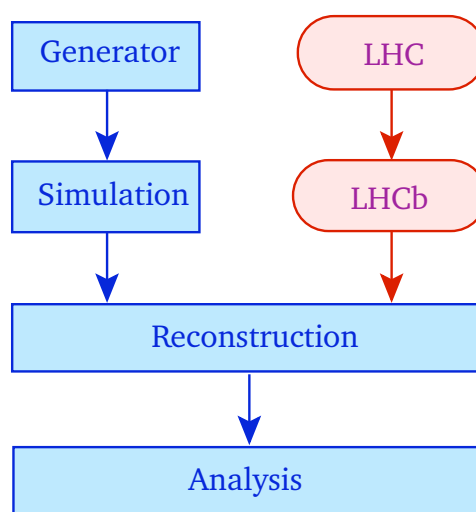
Figure 3.1: *Block diagram of the structure of LHCb software.*

the particles to be propagated through the detector. The **simulation** then emulates as far as possible the response of the real detector. On the other branch of Fig. (3.1), the information is produced by the real apparatus, the **LHC** then **LHCb**. The digitized data coming out of either the simulated or the real detector feeds the **reconstructions** stage, thus building up a synthetic view of the event. Physics parameters are finally extracted from the **analysis**.

During the development period, LHC and LHCb (the two rounded boxes of Fig (3.1)) do not exist and the other boxes are in constant evolution. The rounded boxes of the figure will only be connected to the rest of the diagram once the real detector will be operational. Therefore, as of September 2005, the full detector exists only in a simulation which uses Monte Carlo (MC) techniques. At this point, the simulation produces reference distributions which will be compared to the ones obtained from the real data. On the other hand, the reconstruction software which is presently written must be re-usable as it is with the real data.

The generation and simulation has been split into four different stand-alone programs:

- GAUSS [67] simulates the behavior of the LHCb detector to allow understanding of the experimental conditions and performance. It manages the $p - p$ interactions via PYTHIA 6.2 [68], the B-meson decays via EVTGEN [69] and the interaction of these particles with the detector via GEANT 4 [70]. These three steps are detailed here after. Gauss also handles the simulation of the running conditions, the smearing of the interaction region due to the size of the proton bunches and the variation of luminosity during the fill due to the finite lifetime of the beam.

  - PYTHIA generates the $p - p$ minimum-bias interaction with a center of mass energy of $\sqrt{s} = 14$ TeV. The program is based on the combination of analytical results and various QCD-based models. PYTHIA can be parameterized to reproduce accurately the experiment conditions, especially dealing with the multiplicity of tracks. The oscillation parameters for the B^0_d and B^0_s are fixed to $x_d = 0.739$ and $x_s = 29.4$ respectively (this corresponds to $\Delta m_d = 0.502$ ps^{-1} and $\Delta m_s = 20$ ps^{-1}).
  - EVTGEN was originally developed for the BABAR collaboration and is designed to simulate the B-decay physics. It provides a framework to handle complex sequential and CP violating decays.
  - GEANT4 simulates all the interactions of the particles with the detector. Therefore, the geometry and materials must be described in details − including passive materials as the beam pipe, the structures and the supports. Particles of low momentum, principally due to secondary interactions, are taken into account down to 10 MeV for hadrons and 1 MeV for electrons and photons. The development parameters for electromagnetic and hadronic showers are chosen to reproduce the test beam data.

- BOOLE [71] digitization program is the final stage of the LHCb simulation. The digitization step includes the simulation of the detector response and of the read-out electronics as well as of the L0-trigger hardware. The output has the same format as the real data coming from the detector.

  The detection efficiencies and resolutions of the different parts of the detector are adjusted to the test beam results. The electronic noise and "cross-talk[1]" effects are

---

[1]The cross-talk is the interference noise caused by an adjacent channel.

also included into the simulation. The spillover effect, due to longer than 25 ns detector responses, are also taken into account by BOOLE.

- **BRUNEL** [72] is the LHCb reconstruction program. It associates hits from the different sub-detectors to form tracks and identifies the particles with the help of the RICH, ECAL and HCAL. More details on the reconstruction are presented in Section (3.2).

- **DAVINCI** [73] allows the off-line selection of specific b-hadron final states. The procedure consists in finding and identifying the correct particles of the observed b-decays. Selection criteria are therefore applied to each particle, for example on the transverse momentum P_T, the impact parameter IP, the particle identification PID. It is easy to combine these particles to form vertices and intermediate resonances. Other criteria such as the vertex quality (χ^2 deducted from the different momentum and position errors), the mass of the reconstructed particles, the flight distance of long lived candidates, are used to select the good candidates. The initial b-mesons can then be reconstructed as well as its entire decay chain. The present $B_s^0 \rightarrow J/\psi\, \eta$ selections have been performed with this software, DAVINCI v12r12, and with the specific Bs2JpsiEta v4r2 package which uses the algorithms developed for the HLT.

3.2 LHCb track reconstruction

The track reconstruction, described in details in [33], is one of the most challenging part of the LHCb experiment. The hadronic machine environment renders this task very complex. The reconstruction goal is to combine the measured hits in the tracking system to form the particle trajectories. This aims to measure the momentum of these particles using the trajectory deflection due to the magnetic field and help in their identification.

3.2.1 Different types of tracks
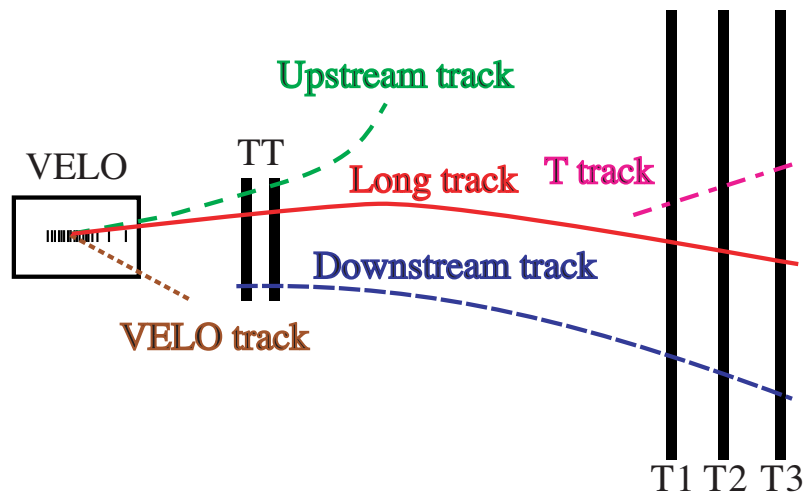
Figure 3.2: *Schematic illustration of the various track types: long, upstream, downstream, VELO and T tracks. The magnet is situated between TT and T1. This figure is taken from Ref. [33].*

Fig. (3.2) represents a schematic view of the main tracking system and the various type of tracks as defined in LHCb. As described in Section (3.2), the tracking system consists of the Vertex Detector, the Trigger Tracker stations, the magnet and the three Tracking Stations. Five different categories of tracks can be defined: long, upstream, downstream, VELO and T tracks.

Long tracks are those which generate hits in all parts of the tracking system. With the exception of K_S^0, Λ and soft pions studies, this is the only track type used in the current physics studies of LHCb.

The upstream tracks (also known as V $\rightarrow$ TT tracks) are in general low momentum ones which do not traverse the magnet and therefore leave hits only in the VELO and TT stations. They are used to understand the photon background in RICH1 as they may generate Cherenkov radiation when passing through this detector and to look for slow pions (coming from a D* for instance).

The other track types shown in Fig. (3.2) are the VELO, TT $\rightarrow$ T (downstream) and T tracks. The first category is typically composed of large angle or backward tracks, which leave hits only in the VELO, and is used in the primary vertex reconstruction. The TT $\rightarrow$ T tracks leave hits in the TT and T1$-$T3 stations only. These are mainly the decay products of the K_S^0 and Λ particles that have decayed outside the VELO. Finally T tracks are those which leave hits only in the T1$-$T3 stations and are typically produced in secondary interactions.

Figure 3.3: *Momentum resolution of a long track from* B-*decay (Gaussian fit). This figure is taken from Ref. [33].*

In the $B_s^0 \rightarrow J/\psi\ \eta$ reconstruction, only long tracks and photons are needed. The momentum resolution for those tracks is shown on Fig. (3.3), where the reconstructed momentum is compared to the true particle momentum. The average momentum resolution is $\delta P/P = 0.37\%$. More details on the performance of long tracks are presented in Section (3.2.3).

3.2.2　Reconstruction strategy

The reconstruction is based on the use of the detector signals of the VELO, TT and T1 to T3 stations. The track reconstruction starts with a search for track "seeds", the initial track candidates, in the VELO and T stations. In the VELO, where the magnetic field can be neglected, the seeds are reconstructed as straight segments. In the tracking stations the seed is parameterized as a parabola, due to a weak but not negligible bending field (see Fig. (3.2 or 3.4)).

The reconstruction is divided in several steps corresponding to the different types of tracks:

1. **The long track** search starts with VELO seeds, in an attempt to form a track with each hit of the T stations successively. Once a combination has been found, the momentum and the trajectory of the particle in the detector is determined. Around this trajectory, hits of the same track from other detectors, including TT, are looked at.

When a sufficient number of hits along a trajectory are collected, the track is reconstructed. This method is referred to as the **forward tracking** algorithm [74]. About 90% of the long tracks are reconstructed with this algorithm. After this method has been applied to all the seeds of the VELO, the used hits of the T stations are discarded and the search for T seeds begins. They are extrapolated to the VELO and combined with corresponding VELO-seeds. This method reconstructs about 5% more long tracks. All the seeds used by these methods are removed before searching for other track types.

2. Two separate methods assume **upstream** and **downstream** track searches. These algorithms are described in Ref. [75, 76] and reconstruct tracks which associate the remaining seeds of the VELO and T stations to TT hits. To reduce the number of ghost tracks[2] in the upstream search, hits both in TTa and TTb stations are required. Moreover, the hits in TTa define the momentum of the track candidate while the hits in TTb confirm the presence of the track.

3. The remaining seeds are stored as tracks, either with no (**VELO tracks**) or poor (**T tracks**) momentum estimate.
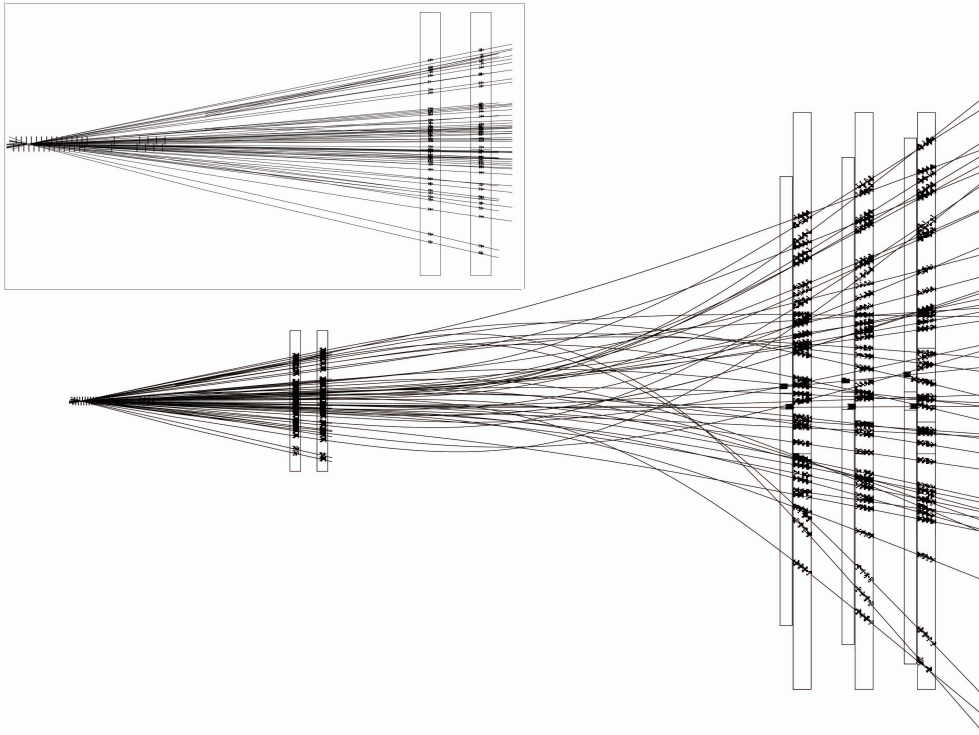
Figure 3.4: *Display of the reconstructed tracks and assigned hits in a $B_d^0 \to J/\psi\,K_S^0$. The insert shows a zoom of the VELO and TT region. This particular event contains 50% more hits than the average. This figure is taken from Ref. [33].*

Once the track search have been performed, the trajectories are refitted using a Kalman Filter fit [77]. The average number of reconstructed tracks, for $b\bar{b}$ events, is 72 where 26

---

[2]A ghost track is a track which have been reconstructed from a collections of hits that have less than 70% hits coming from any real MC particle.

are long, 11 upstream, 4 downstream, 26 VELO and 5 T. These numbers correspond to the tracks of the B-decay products plus the entire underlying event. Fig. (3.4) shows the reconstructed tracks and their hits for a $B_d^0 \to J/\psi \, K_S^0$ event.

3.2.3   Reconstruction performances

The performances described in this section are extracted from Ref. [33]. Only the long tracks performances are treated, as they are the only tracks used for this study. Fig. (3.5)
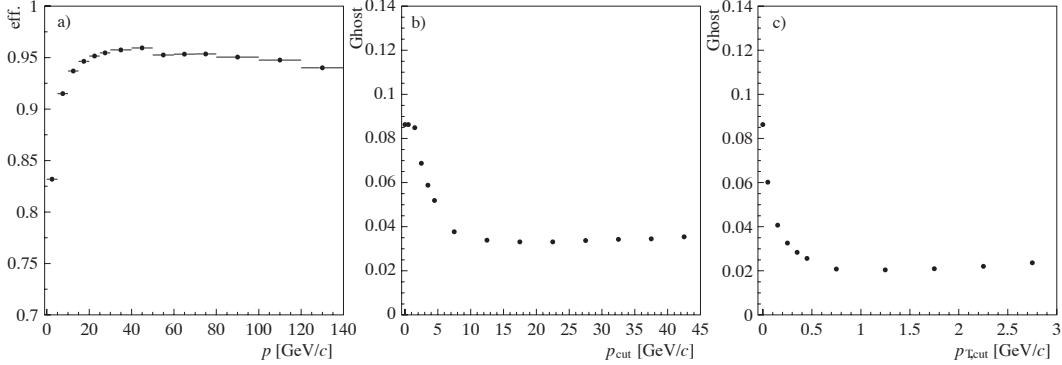
Figure 3.5: *Long track reconstruction performances: a) efficiency as a function of the momentum of the generated track; b) ghost rate for tracks with a reconstructed momentum greater than p_{cut}; c) ghost rate for tracks with a reconstructed transverse momentum greater than $p_{T,cut}$. This figure is taken from Ref. [33].*

shows the reconstruction efficiency for long tracks as a function of the momentum as well as the ghost rate as function of cuts on the momentum and the P_T applied to these tracks. For long tracks with a momentum larger than 10 GeV/c, the average efficiency of reconstruction is 94% (for particles from B-decays, this percentage reaches 95 to 96%). The average ghost rate is 9%, however most of these tracks have a low P_T and can easily be removed in the physics analysis selection. For instance the P_T of each hadron must be larger than 1.2 GeV/c for the $B_d^0 \to hh$ channels and the two products of the $B_s^0 \to J/\psi \, \phi$ must have their $P_T > 0.5$ GeV/c. Fig. (3.6) shows the resolution obtained on the momentum and the impact parameter (IP) as a function of the momentum and the inverse P_T respectively. The resolution on the IP varies linearly with $1/P_T$ and can be parameterized as $\sigma_{IP} = 14 \; \mu\mathrm{m} + 35 \; \mu\mathrm{m}/P_T$ where P_T is expressed in GeV/c.

3.2.4   Definition of reconstructible and reconstructed

We introduce here two definitions which will be used in Chapter (4) for the determination of the reconstruction and selection efficiencies. *Reconstructible events* are those generated signal events which have the potential to be reconstructed. An event is reconstructible if all the final tracks are reconstructible. Of these events, the adjective *reconstructed* is applied to those events which have been successfully reconstructed. More specifically these two terms can be defined in terms of the track types illustrated in Fig. (3.2).

   Reconstructible: A long track is considered as *reconstructible* if it is reconstructible as both a VELO and a T track. This means that the particle has left at least 3 "r" and 3 "ϕ" hits in the VELO stations and 1 "x" and 1 "u,v" hit in each of the three tracking stations.
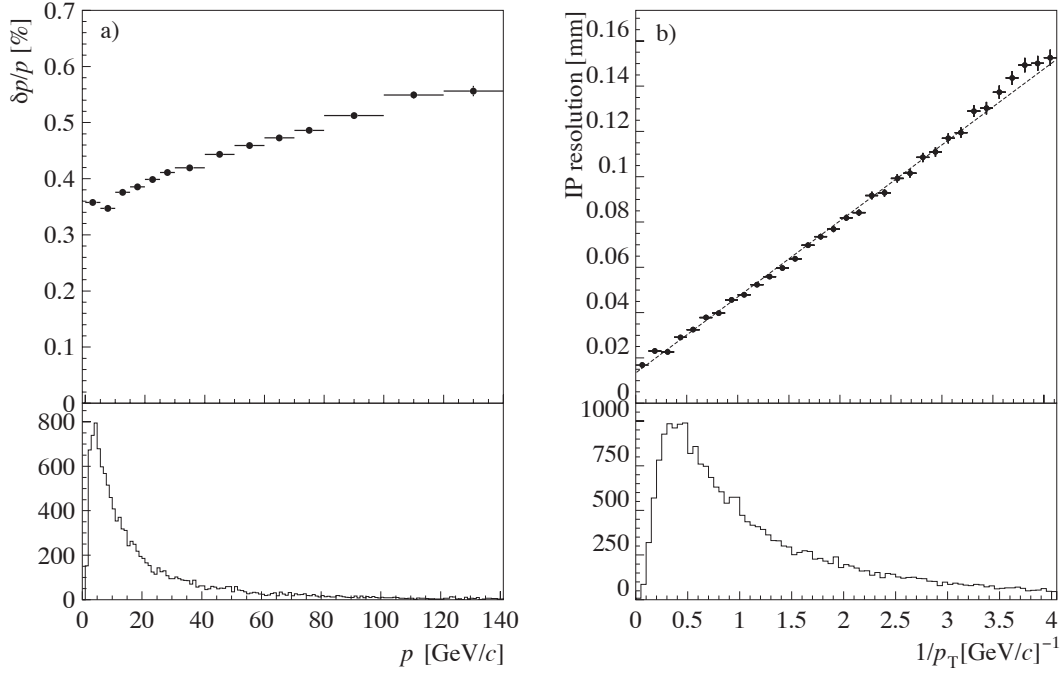
Figure 3.6: *Resolution of the parameters of the reconstructed tracks at the production vertex: a) momentum resolution as a function of the momentum, b) impact parameter resolution as a function of $1/P_T$. B-decay particle spectra (p and P_T) are shown in the lower part of the plot. This figure is taken from Ref. [33].*

Reconstructed: A long track is considered *reconstructed* if it has been reconstructed by the VELO, TT and T1−T3 stations separately.

3.3 Flavor tagging

CP violation studies in neutral B-meson decays require the knowledge of the flavor state at production of the reconstructed B. This is achieved by determining the flavor of the other b quark in the event and is called **opposite side tagging**. This can be done detecting the charge of the lepton from semi-leptonic b-decays, the charge of the kaon from the b → c → s decay chain or the charge of the inclusive secondary vertex from the "opposite side" b-decay. The tagging particle selection is performed by looking at kaons and leptons with high P_T and large impact parameter. The highest P_T lepton or the highest P_T kaon is chosen in the case of multiple candidates.

The **same side tagging** algorithms determine directly the flavor of the B-signal meson by exploiting the correlation in the fragmentation decay chain, looking at a charged kaon from the s̄/s extra quark produced with a B_s^0 ($\bar{b}$ s)/$\overline{B}_s^0$ (b s̄).

The results for the tagging efficiencies ε_{tag}, the wrong tag probability ω_{tag} and the effective tagging efficiency for a few benchmark channels are summarized in Tab. (3.1). These results have been obtained with the version v5r5 of the Flavor Tagging algorithm with "cheated" selection[3]. The results are similar to the one obtained with the version

---

[3]By "cheated" selection one means that no cuts are applied on the signal events and that only the reconstructed events which can be linked to the MC truth are selected.

v6r2 used for the present analysis. The effective efficiencies ε_{tag}^{eff} is defined as:

$$\varepsilon_{tag}^{eff} = \varepsilon_{tag} \cdot D^2 = \varepsilon_{tag} \cdot (1 - 2 \cdot \omega_{tag})^2,$$

where D is the dilution factor. The statistical error on an observed CP-asymmetry A_{obs} and coming from the tagging is inversely proportional to $\sqrt{\varepsilon_{tag}^{eff}}$:

$$\sigma_{A_{\mathrm{CP}}}^2 = \frac{1 - A_{\mathrm{obs}}^2}{N_{phys} \cdot \varepsilon_{tag} \cdot (1 - 2 \cdot \omega_{tag})^2} = \frac{1 - A_{\mathrm{obs}}^2}{N_{phys} \cdot \varepsilon_{tag}^{eff}},$$

N_{phys} being the number of selected and triggered events.

Decay	ε_{tag} [%]	ω_{tag} [%]	ε_{tag}^{eff} [%]
$B_d^0 \to \pi^+ \pi^-$	64.2	35.7	5.2
$B_d^0 \to J/\psi\ K^*$	58.1	36.7	4.0
$B_s^0 \to D_s\ K$	64.7	30.8	9.5
$B_s^0 \to D_s\ \pi$	64.6	30.9	9.4
$B_s^0 \to J/\psi\ \phi$	59.8	33.0	6.9
$B_s^0 \to K^+\ K^-$	61.8	29.4	10.5

Table 3.1: *Performance of the tagging evaluated for several different* B-*decays after L1&L0 triggers and after the "cheated" selection. These values are taken from Ref. [78].*

3.4 Systematic errors

In a precision experiment like LHCb and in order to exploit the large statistical samples which are expected, systematic errors must be well mastered. A particular attention is devoted to errors which can bias the CP-violation measurements like charge-dependent detection efficiency as difference in the detection efficiency between positively and negatively charged particles can introduce a fake CP asymmetry. This is particularly important for CP violation measurements in which the final state is not a CP-eigenstate and for the flavor tagging.

This effect will be corrected by reversing regularly the polarity of the magnetic field. This can be frequently done as LHCb has chosen to use a warm magnet. Large control samples without CP asymmetry will also be used to better understand the tagging performances. Flavor specific decays such as $B_d^0 \to J/\psi\ K^*$ and $B_s^0 \to D_s^-\ \pi^+$ allow to extract the wrong tag fraction. The CP asymmetry of the background can be studied using the B-mass sidebands while the asymmetries of $b\bar{b}$ production are tested using the large control samples or fitted from the signal samples.

3.5 CP reaches in benchmark channels

The different ways to extract the CKM phases are explained in Section (1.3.4). In Tab. (3.2) one can find the performance of the LHCb experiment for some promising decay channels [33]. All the numbers are given for one year of data taking (10^7 seconds), at a luminosity of $\mathcal{L}_{\mathrm{LHCb}}^{av} = 2 \cdot 10^{32}$ cm^{-2}s^{-1} (i.e. an integrated luminosity of 2 fb^{-1}). For the determination of α, more theoretical input will be needed, as the penguin contribution

cannot be neglected. The decay $B_d^0 \rightarrow \phi\, K_S^0$ is entirely governed by penguin diagram, but its asymmetry is expected to be the same as the one of $B_d^0 \rightarrow J/\psi\, K_S^0$. Should this not be the case, this will be the manifestation of New Physics. After one year of LHCb data taking,

CKM Parameter	Channel	Vis. BR ($\times 10^6$)	$2\mathrm{fb}^{-1}$ Yield	B/S	Physics Performance	Refs.
β	$B_d^0 \rightarrow J/\psi K_S^0$	19.8	241 k	0.82	$\sigma(\sin 2\beta) = 0.02$	[33, 79, 80]
	$B_d^0 \rightarrow \phi\, K_S^0$				To be studied	
γ	$B_d^0 \rightarrow D^* \pi$	71	206 k	< 0.3	$\sigma(\gamma) = \mathcal{O}(10°)$	[10, 81]
	$B_s^0 \rightarrow D_s K$	10	5.4 k	< 1.0	$\sigma(\gamma) \approx 15°$	[33, 82]
α	$B_d^0 \rightarrow \pi\, \pi$	4.8	26 k	< 0.7	theory dependent	[10, 83]
	$B_d^0 \rightarrow \rho\, \pi$	20	4.4 k	< 7.1	$2.5° < \sigma(\alpha) < 5.0°$	[10]
χ	$B_s^0 \rightarrow J/\psi\, \phi$	31	125 k^i	< 0.3	$\sigma(-2\chi) \approx 0.03^i$ rad	[84], ibid.
	$B_s^0 \rightarrow J/\psi\, \eta(\gamma\gamma)^{ii}$	10.6	8.9 k	2.2	$\sigma(-2\chi) \approx 0.11$ rad	ibid.
$|V_{td}|/|V_{ts}|$	$B_s^0 \rightarrow D_s\, \pi$	120	80 k	0.32	$\sigma(\Delta m_s) \approx 0.01 \; \mathrm{ps}^{-1}$	[33, 85]
	$B_{s,d}^0 \rightarrow \mu\mu\, X_{s,d}$	5.7	25 k	0.12	$\sigma(|V_{td}|/|V_{ts}|) \approx 11\%$	[86]

Table 3.2: *Performances of the LHCb experiment after one year of data taking for selected benchmark channels. ^{i} These values have been updated in the present work to take into account the new triggers and analysis software. ^{ii} The results for this channel are obtained using the average between the interval bounds for the η mixing angles (see Sec. (1.6.2)).*

the situation could be the one shown on Fig. (3.7) if the Standard Model is correct and complete. The measurement of γ may be incompatible with the intersection of $|V_{td}|/|V_{ts}|$ circle and β. This will open a highway to the discovery and hopefully the understanding of physics beyond the Standard Model.
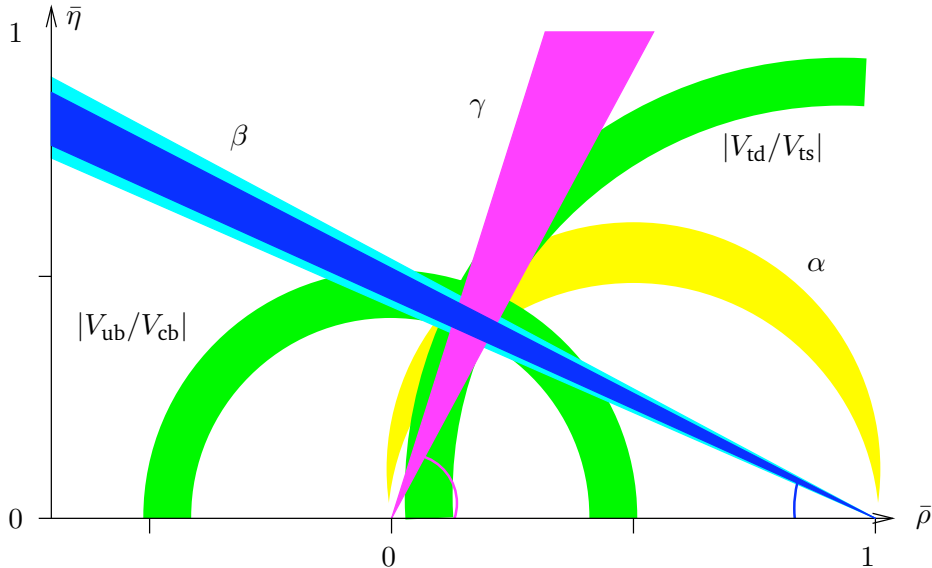
Figure 3.7: *After one year of running at LHCb, the constrains on the unitarity triangle (db) could be as shown on this figure, taken from Ref. [33].*

The current fit results on the CKM angles of the unitarity triangles at 90% confidence level are, (as of August 1st 2005) [87]:

- $\beta = \left(23.22^{+1.70}_{-2.12}\right)^\circ, \quad \gamma = \left(58.6^{+15.7}_{-15.1}\right)^\circ, \quad \alpha = \left(98.1^{+16.8}_{-15.7}\right)^\circ,$

- $\chi = \left(1.039^{+0.155}_{-0.194}\right)^\circ, \quad |V_{td}|/|V_{ts}| = 0.1982^{+0.0261}_{-0.0256}.$

3.6 $B_s^0 \to J/\psi\ \eta$ at LHCb

3.6.1 Visible branching ratios

The different branching ratios involved in this analysis are summarized in Tab. (3.4). They are used to estimate the annual production yield at $2\ \text{fb}^{-1}$ of each decay[4]. The $B_s^0 \to J/\psi\ \eta$ fraction is estimated from the $B_d^0 \to J/\psi\ K_S^0$ (see Section (1.6.2)).

In addition to the $b\bar{b}$ cross section and the luminosity of LHCb (see Section (2.1.1)) and the visible branching fraction of the decays, one also needs the b-quark hadronization fraction to predict the different yields. The hadronization fractions, i.e. the probabilities that a b-quark hadronizes into the given b-hadrons of interest, are given in Tab. (3.3). As we can observe, only 10% of the b-quarks produce a B_s^0.

b-hadron	Production fraction
$B_u^\pm$	0.397 ± 0.010
B_d^0	0.397 ± 0.010
B_s^0	0.107 ± 0.011
Λ_b^0	0.099 ± 0.017
$B_c^\pm$	$-$

Table 3.3: *Hadronization probabilities for b-quark to form b-hadron [14].*

Decay	Visible branching fractions	
	$\theta_p = -20^\circ$	$\theta_p = -10^\circ$
$J/\psi \to \mu^+\ \mu^-$	$(5.88 \pm 0.10) \cdot 10^{-2}$
$J/\psi \to \mu^+\ \mu^-\ \gamma$	$(8.8\ \pm 1.4) \cdot 10^{-3}$
$J/\psi \to \mu^+\ \mu^-\ \{\gamma\}$	$(6.76 \pm 0.14) \cdot 10^{-2}$
$\eta \to \gamma\gamma$	$(39.43 \pm 0.26) \cdot 10^{-2}$
$\eta \to \pi^+\pi^-\pi^0$	$(22.6\ \pm 0.4) \cdot 10^{-2}$
$B_s^0 \to J/\psi\ \eta$	$(3.1 \pm 1.2) \cdot 10^{-4}$	$(4.8 \pm 1.9) \cdot 10^{-4}$
$B_s^0 \to J/\psi(\mu^+\ \mu^-)\ \eta(\gamma\ \gamma)$	$(8.3 \pm 3.5) \cdot 10^{-6}$	$(12.8 \pm 5.3) \cdot 10^{-6}$
$B_s^0 \to J/\psi(\mu^+\ \mu^-)\ \eta(\pi^+\ \pi^-\ \pi^0)$	$(4.7 \pm 2.0) \cdot 10^{-6}$	$(7.3 \pm 3.1) \cdot 10^{-6}$

Table 3.4: *Visible branching fractions for the relevant decay channels. θ_p is the η mixing angle defined in (1.6.2) and belongs to $\theta_p \in [-20^\circ, -10^\circ]$.*

3.6.2 Annual production yield of $B_s^0 \to J/\psi\ \eta$

The foreseen average luminosity at the LHCb interaction point is $\mathcal{L}_{\text{LHCb}}^{av} = 2 \cdot 10^{32}\ \text{cm}^{-2}\text{s}^{-1}$ (see Section (2.1.1)). Knowing that one year of data taking corresponds to about $t_{year} = 10^7$ seconds, we obtain the yearly integrated luminosity of $2\ \text{fb}^{-1}$. For a production cross

---

[4]Actually no measurements have been done for the $J/\psi \to \mu^+\ \mu^-\ \gamma$ channel. However its branching fraction should be the same than for the $J/\psi \to e^+\ e^-\ \gamma$ decay: $\mathcal{BR}(J/\psi \to e^+\ e^-\ \gamma) = (8.8 \pm 1.4) \cdot 10^{-3}$.

section of b$\overline{\text{b}}$ pairs of $\sigma_{\text{LHCb}}^{\text{b}\overline{\text{b}}} = 500\ \mu$b (see Section (2.1.1)), the number of b$\overline{\text{b}}$ pairs produced during one year is:

$$N_{\text{b}\overline{\text{b}}}^{\text{2fb}^{-1}} = \mathcal{L}_{\text{LHCb}}^{av} \cdot t_{year} \cdot \sigma_{\text{LHCb}}^{\text{b}\overline{\text{b}}} = 1 \cdot 10^{12}.$$

The number of $B_s^0 \to J/\psi\ \eta$ events produced during one year can be estimated multiplying $N_{\text{b}\overline{\text{b}}}^{\text{2fb}^{-1}}$ by the hadronization factor for a b-quark to produce a B_s^0 (see Section (3.7)) and then by the visible branching ratio of the decay of interest, taking into account all the subdecays (see Section (3.7)). Then we can calculate the different 2 fb^{-1} yields with the equation:

$$N_{B_s^0 \to J/\psi\ \eta}^{\text{2fb}^{-1}} = N_{\text{b}\overline{\text{b}}}^{\text{2fb}^{-1}} \times 2 \times \text{BR}(\text{b} \to B_s^0) \times \text{BR}(B_s^0 \to J/\psi\ \eta).$$

The results, which depend on the mixing angle θ_P of the η (see (1.6.2)), are presented in Tab. (3.5).

Decay	2 fb^{-1} yield	
	$\theta_p = -20°$	$\theta_p = -10°$
$(\text{p} - \text{p}) \to \text{b}\overline{\text{b}}$	$1 \cdot 10^{12}$	
$\text{b}\overline{\text{b}} \to B_s^0$	$(2.14 \pm 0.22) \cdot 10^{11}$	
$B_s^0 \to J/\psi\ \eta$	$(6.6\ \pm 2.6)\ \cdot 10^7$	$(10.3 \pm 4.1) \cdot 10^7$
$B_s^0 \to J/\psi(\mu^+\ \mu^-)\ \eta(\gamma\ \gamma)$	$(1.8\ \pm 0.8)\ \cdot 10^6$	$(2.7 \pm 1.2) \cdot 10^6$
$B_s^0 \to J/\psi(\mu^+\ \mu^-)\ \eta(\pi^+\ \pi^-\ \pi^0)$	$(1.0 \pm 0.45) \cdot 10^6$	$(1.6 \pm 0.7) \cdot 10^6$

Table 3.5: *Production yield at 2 fb^{-1} for the relevant decay channels with respect to the η mixing angle θ_P*

One can conclude that for proton$-$proton collisions at $\sqrt{s} = 14$ TeV, the production cross section for b$\overline{\text{b}}$ pairs allows to produce a large number of $B_s^0 \to J/\psi\ \eta$ decays.

3.6.3 Possible background contributions

The various background contributions which can perturb the reconstruction of the $B_s^0 \to J/\psi\ \eta$ decays are the following:

- **The b$\overline{\text{b}}$ inclusive events.** These events represents the main source of our background because of their statistics (10^{12} events with a b$\overline{\text{b}}$ pair per year, to be compared to a few millions of signal events) and of their multiplicity which may result in combinatorial background. Moreover, the tracks from b-hadrons form a vertex which is displaced with respect to the primary vertex, which is the main selection criterion to reject background events.

- **The $H_b \to J/\psi$ X events.** H_b stands for a b-hadron and X for any possible hadron of group of hadrons. This subgroup of the above b$\overline{\text{b}}$ inclusive events can be an important background contribution, due to the presence of a B or a Λ_b^0 and of the J/ψ. The large number of photons in the final state can mimic the presence of an η or a π^0.

- **The prompt J/ψ events.** Although the prompt J/ψ does not present a displaced vertex with respect to the primary one (PV) they can be a problem due to their large production yields.

In Tab. (3.6) are presented the branching ratio and the 2 fb^{-1} production yields for particular channels of the $H_b \to J/\psi$ X background. All these channels have a much larger production yield than the two decays of interest (to be compared with Tab. (3.5)) and may contribute dangerously to the signal contamination.

Decay	BR$^{\text{vis}}$ (10^{-6})	$N^{2\text{fb}^{-1}}$ (10^3)
$B_d^0 \to J/\psi(\mu^+ \ \mu^-) \ K^*(K^+ \ \pi^-)$	59 ± 3	670
$B_d^0 \to J/\psi(\mu^+ \ \mu^-) \ K_S^0(\pi^+ \ \pi^-)$	19.8 ± 1.3	216
$B^+ \to J/\psi(\mu^+ \ \mu^-) \ K^+$	68 ± 3	1740
$B_s^0 \to J/\psi(\mu^+ \ \mu^-) \ \phi(K^+ \ K^-)$	31 ± 11	100
$B_s^0 \to J/\psi(\mu^+ \ \mu^-) \ \eta'(\pi^+ \ \pi^- \ \eta)$	5.9 ± 2.4	2.
$\Lambda_b^0 \to J/\psi \ \Lambda$	20.3 ± 12.1	18.5

Table 3.6: *Branching ratios and annual signal yield at 2 fb^{-1} for $H_b \to J/\psi$ X background channels. The yields of the first four channels are taken from the TDR [33], without HLT. The two last are taken from [88] and [89] respectively.*

More generally inclusive J/ψ events, where both prompt J/ψ and J/ψ coming from a b-hadron are present, are used to estimate the background-to-signal ratio of the $H_b \to J/\psi$ X contribution. The branching ratio of the decays $H_b \to J/\psi$ X is $(1.16 \pm 0.10)\%$ [14].

For the third type of background contribution, the prompt J/ψ, PYTHIA generates the J/ψ production via the gluon fusion:

$$gg \to J/\psi + g, \quad gg \to \chi_{0c} + g, \quad gg \to \chi_{1c} + g, \quad gg \to \chi_{2c} + g \quad \text{and} \quad gg \to J/\psi + \gamma.$$

To obtain the prompt J/ψ production cross section we need to take into account the branching fraction of $\chi_{0c} \to J/\psi\gamma$, $\chi_{1c} \to J/\psi\gamma$ and $\chi_{2c} \to J/\psi\gamma$ $\big((1.18 \pm 0.14)\%,$ $(31.6 \pm 3.3)\%$ and $(20.2 \pm 1.7)\%$ respectively [14]$\big)$. Finally we are able to estimate the production cross section for the prompt J/ψ to 0.185 mb which gives $0.37 \cdot 10^{12}$ prompt J/ψ per year at the actual luminosity [90].

3.7 Data samples

3.7.1 Data samples

The analysis presented in next chapter was carried out with Monte Carlo samples of different sizes. The two studied decay modes are $B_s^0 \to J/\psi(\mu^+ \ \mu^-) \ \eta(\gamma \ \gamma)$ and $B_s^0 \to J/\psi(\mu^+ \ \mu^-) \ \eta(\pi^+ \ \pi^- \ \pi^0)$. For the first channel, 280 tapes of 500 events were generated but one was corrupted. This leaves 139'500 events for the analysis or more exactly $138'922 \pm 370$ independent events. This lower value is due to an error in the random seed generation. We will return to this point in the next section. For the $B_s^0 \to J/\psi \ \eta(\gamma \ \gamma)$ channel, the fraction $f_{indep}^{\gamma\gamma}$ of independent events is then $f_{indep}^{\gamma\gamma} = 0.9959 \pm 0.0002$. For the second decay, 343 tapes of 500 events were created, which gives 171'500 events. This corresponds to $170'626 \pm 409$ independent events and a fraction $f_{indep}^{\pi^+\pi^-\pi^0} = 0.9949 \pm 0.0002$.

The background rejection calculations and the estimates of the background to signal (B/S) ratios for these channels were performed with approximately 18M inclusive $b\bar{b}$ (we will call this sample "v1"). This corresponds to ~ 10.5M independent events and a fraction $f_{indep}^{b\bar{b}} = 0.5833 \pm 0.0001$. Another 20M independent events, without any generation bug

(this will be the "v2" data sample), have been used to check the background rejection on $b\bar{b}$ unbiased events by tuning the selection cuts.

The estimation of the B/S have been also checked with 1.7M inclusive J/ψ events. This corresponds to $1'617'000 \pm 1'200$ independent events leading to a fraction of $f_{indep}^{\text{incl } J/\psi} = 0.951 \pm 0.001$.

More details concerning the data samples as well as the different technicalities of the specific decay channels for the J/ψ background studies can be found in [91]. They all suffers from the generation bug and need the same treatment as the other samples to determine the fraction of independent events.

In each of the signal and inclusive $b\bar{b}$ samples, a cut is imposed a the generator level in such a way that the particles have a true polar angle of less than 400 mrad. This is to avoid the tracking and reconstruction of events for which the decay products are in any case not in the acceptance. For the signal samples, the cut is applied on the decaying B-meson and has an efficiency of $\varepsilon_{gen}^{signal} = (34.8 \pm 0.3)\%$. For the inclusive $b\bar{b}$ sample, the cut is imposed to one of the b-hadrons and has an efficiency of $\varepsilon_{gen}^{b\bar{b}} = (43.4 \pm 0.3)\%$. The inclusive J/ψ cut efficiency is $(\varepsilon_{gen}^{incl. \ J/\psi} = (38.9 \pm 0.4)\%$. The so-called "MC sample" are those remaining after this cut.

3.7.2 MC random number generation

The production of a MC event at LHCb uses a random number (seed) which is generated as a 32 bit number. Unfortunately one of the algorithms of the generation chain was actually limited to the use of the 24 least significant bits. Therefore instead of the previously thought $2^{32} = 4'294'967'296$ different events, only $2^{24} = 16'777'216$ seeds were randomly chosen. The consequence is that for a 18M event sample (used as $b\bar{b}$ events to fine tune the selection criteria), only $\sim$10.5M events are actually independent (in the best situation, i.e. when all the seeds are used at least once).

This bug is present in all the data samples produced during the Data Challenge 2004 (DC04). Only the $b\bar{b}$ "v2" sample does not suffer from this problem as it has been produced later. A correction factor must then be applied to any registered event numbers, to avoid over-estimations of selected data or background rejection. The number of independent events N_{indep} and its error $\sigma_{N_{indep}}$ become [92]:

$$
\begin{aligned}
N_{indep} &= M - M \cdot (1 - \frac{1}{M})^N \approx M \cdot (1 - e^{-\frac{N}{M}}), \\
\sigma_{N_{indep}}^2 &= M \cdot (M-1) \cdot (1 - \frac{2}{M})^N + M \cdot (1 - \frac{1}{M})^N - M^2 \cdot (1 - \frac{1}{M})^{2N} \\
&\approx N_{indep} \cdot e^{-\frac{N}{M}},
\end{aligned}
$$

where $M = 2^{24}$ and N is the number of events in the original sample. We can then calculate the fraction of independent events in a sample $f_{indep} = N_{indep}/N$. This fraction is assumed to be the same in all subsets of an initial sample. Therefore the event selection efficiencies remain the same whereas the binomial errors on these efficiencies do not.

Chapter 4

$B_s^0 \to J/\psi\,\eta$ event selection

μ⁺
μ⁻
J/ψ
γ
B_s^0
η
γ
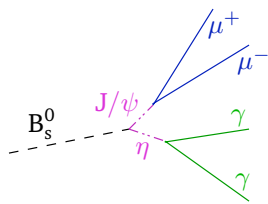
This chapter presents the analysis of the B_s^0 decay in the CP eigen-state $J/\psi\,\eta$ using the full LHCb simulation. We first describe the pre-selection, then the different $B_s^0 \to J/\psi\,\eta$ decay modes and selection strategies are presented. Finally we discuss the resolutions (mass, proper time, etc.), efficiencies (trigger, tagging, selection, etc.) and background contributions.

§ROM the huge amount of p−p events that LHCb will collect ($\sim 20 \cdot 10^9$ per year), very few do have a $B_s^0 \to J/\psi\,\eta$ decay ($\sim 10 \cdot 10^3$ per year). Therefore a very tight selection is required to eliminate the unwanted contribution to the signal sample.

We will use the Monte Carlo simulations for the $B_s^0 \to J/\psi\,\eta$ events and for the background to search for the adequate selection cuts to be applied in order to extract the signal. This study will enable us to determine:

1. The signal yield;

2. The acceptance of our apparatus to these events;

3. The resolution of the apparatus, particularly the resolution in terms of the B_s^0 proper time;

4. The background-over-signal ratio.

These studies will allow us to determine the sensitivity of the LHCb experiment in the determination of the weak phase ϕ_s with $J/\psi\,\eta$.

For the present analysis, the selection has been done in two stages. The aim of the initial step was to reduce the number of signal and background data sets, rendering them more manageable. This requires a preliminary series of cuts which are refined in the second stage. Its main purpose is to maintain a high efficiency for the signal while providing a very large rejection of the combinatorial background.

4.1 Particle identification

At the beginning of the selection the reconstructed tracks of each event are assigned a particle identification (PID) based upon the different sub-detector available information. The PID is provided by the RICH counters (π, K, p), the ECAL and HCAL (e, γ, hadrons) and the muon system (μ). The PID is not unique and several PID can be assigned to a single track.

The PID information is used in the offline selection through the likelihood hypothesis combining the information of all detectors. For example:

$$
\begin{aligned}
\mathcal{L}(\mathrm{e}) &= \mathcal{L}^{RICH}(\mathrm{e})\mathcal{L}^{\mathrm{CALO}}(\mathrm{e})\mathcal{L}^{\mathrm{MUON}}(\mathrm{non}\ \mu), \\
\mathcal{L}(\mu) &= \mathcal{L}^{RICH}(\mu)\mathcal{L}^{\mathrm{CALO}}(\mathrm{non}\ \mathrm{e})\mathcal{L}^{\mathrm{MUON}}(\mu), \\
\mathcal{L}(h) &= \mathcal{L}^{RICH}(h)\mathcal{L}^{\mathrm{CALO}}(\mathrm{non}\ \mathrm{e})\mathcal{L}^{\mathrm{MUON}}(\mathrm{non}\ \mu),
\end{aligned}
$$

where h represents a hadron, e stands for an electron and μ for a muon. Each of these functions computes the probability of being of the given type of particle. If there are more than one estimator from a given detector, they can be simply combined by taking the product of their individual likelihoods.

A delta log likelihood (DLL) function compares two different hypothesis and allows to discriminate the correct from the wrong PID assignments. It is defined as:

$$
\Delta \ln \mathcal{L}_{AB} = \ln \mathcal{L}(A) - \ln \mathcal{L}(B) = \ln \left[\frac{\mathcal{L}(A)}{\mathcal{L}(B)} \right], \tag{4.1}
$$

where A, B stand for the hypothesis to have a particle A, B. The function 4.1 tends to be positive for correctly A-type identification and negative for correctly B-type identification.

However this method can only be applied to charged tracks, γ and π^0 need another treatment. Photons are reconstructed and identified with the ECAL as neutral clusters as explained in Section (2.4.2). The identification of photons converted in the passive material behind the magnet is based on whether there is a hit in the SPD cell in front of the central cell of the ECAL cluster. Electrons which radiate before the magnet have a characteristic signature with a row of ECAL clusters ending at the impact of the electron.

The neutral pions are reconstructed from two photons. At low momentum (less than 3 GeV/c) they are mostly reconstructed as a "resolved" pair of well separated photons, while for higher P_T a large fraction of the pairs cannot be resolved by the ECAL granularity (they are usually called "merged" π^0).

As neutral particles do not leave hits in the tracking system, it is impossible to reconstruct their direction. As a result each photon is assigned an origin pointing to the origin of the detector, in the middle of the VELO. It is then possible in a specific analysis to move this origin to any vertex and correct the four momentum and covariance matrix accordingly.

4.2 Pre-selection studies

The aim of the "pre-selection" stage is to reduce the huge amount of possible combinations to form a B_s^0 decay, especially due to the high photons and pion multiplicity. A set of cuts is applied to the different particles and on their reconstruction parameters. The pre-selection only considers signal decays constructed from long tracks, photons and π^0 which are associated, i.e. those tracks or particles which match a MC track or particle. When all the final states are associated, the event, or the decay, is called "associated". Analyzing

these events allows to determine the resolution of the apparatus. The true signal is then compared to the pre-selected $b\bar{b}$ inclusive events.

The pre-selection is divided into four distinct parts: the selection of the tracks, the reconstruction of the J/ψ, the η reconstruction and finally the reconstruction of the B_s^0. The pre-selection cuts are summarized in Tab. (4.1).

In this chapter, in order to ease the comparison between the signal and the background histograms, the different distributions have been re-normalized. The scale factor has been chosen to have the two distribution maxima at the same height.

4.2.1 Reconstruction of the primary vertex

In the event reconstruction, the primary vertex search and fit is performed using the iterative procedure described hereafter.

An histogram of the z-coordinate of the point of the closest approach to the beam line for all tracks (long, upstream and VELO) measured in the VELO is constructed with a bin width of 1 mm. The most populated bin of this histogram is used, together with its 4 neighbors on each side, to define a cluster of tracks. The mean z-value is taken as the z of a primary vertex coordinate (located on the beam axis). Tracks with a large χ^2 contribution to the vertex (> 225 for the first iteration and > 9 afterwards) are eliminated from the cluster, and the remaining tracks in the cluster are fitted to a new common vertex. This step is iterated until no further tracks are rejected.

If at least six tracks were used in the last iteration, the vertex is kept as a primary vertex; these tracks are then removed from the overall set of tracks, and the whole search procedure is started again to find additional primary vertices. If less than six tracks were used then the vertex is discarded and the search is stopped. In the case where no primary vertex has been found, the original vertex obtained from the histogram peak is kept as the sole primary vertex of the event.
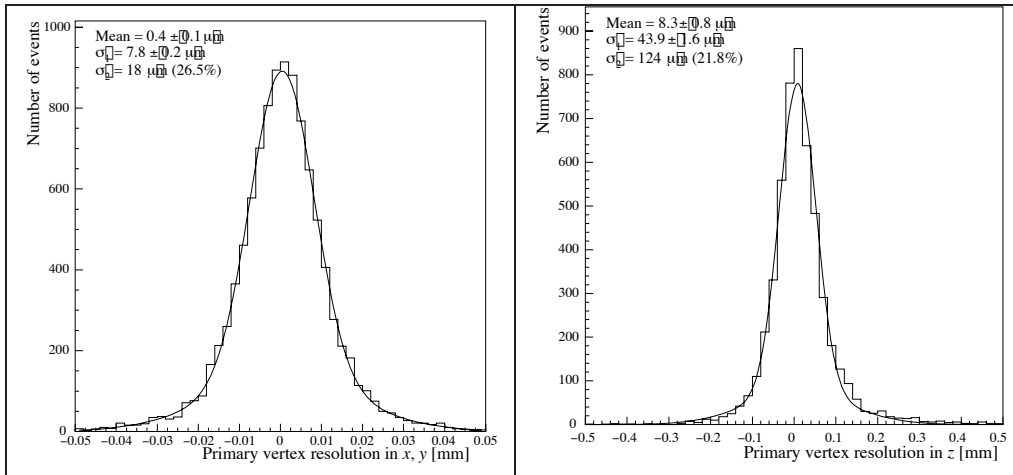
Figure 4.1: *Resolution of the $b\bar{b}$ vertex position, for x and y on the left and z on the right. These distributions were obtained from $b\bar{b}$ events passing the Level-0 and Level-1 triggers. This figure comes from [33].*

This procedure was developed in order to optimize the efficiency to find the $b\bar{b}$ pro-

duction vertex, which is on average 98%. The vertex position resolution[1], for b$\bar{\text{b}}$ pairs, are presented on Fig. (4.1). The fit is performed with double Gaussian which have an identical mean value. The width of the principal Gaussian ($\sim$ 75%) is 44 μm in z and 7.8 μm for x and y. The z-resolution is better for events with a single interaction (41.7 μm). There is also a bias in the z-coordinate of 8 μm due to b- of c-decay products which are not excluded by the χ^2 cut. This bias is not present in minimum-bias event.

4.2.2 Pre-selection of particles

Before the reconstruction of an event, the different particles involved in the decays of interest have to be sorted out from the background. A set of loose cuts is applied on their PID and transverse momentum. The particles from B-meson decay have a high transverse momentum: the minimum P_T of all the π's, μ's and γ's is set to 200 MeV/c. In addition, for the muons a $\Delta \ln \mathcal{L}_{\mu\pi} > -50$ is required. This cut is very loose for the muon from J/ψ decays, as shown on Fig. (4.2). No DLL cuts are applied on the pions.

$$B_s^0 \rightarrow J/\psi(\mu^+\ \mu^-)\ \eta(\gamma\ \gamma) \qquad\qquad B_s^0 \rightarrow J/\psi(\mu^+\ \mu^-)\ \eta(\pi^+\ \pi^-\ \pi^0)$$

a) DLL distribution of the μ^-   *b) DLL distribution of the μ^-*
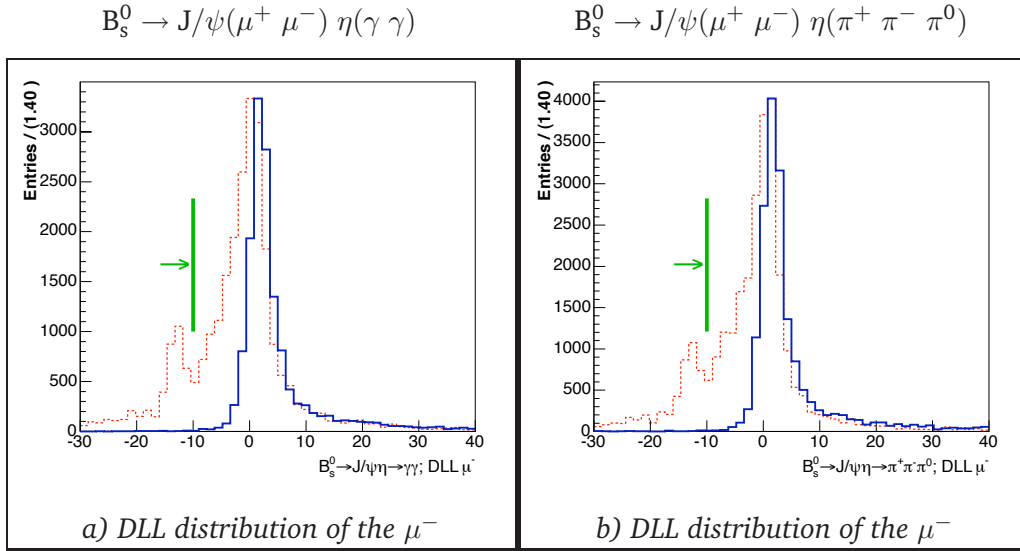
Figure 4.2: *(μ-π) DLL hypothesis of the μ^- after the pre-selection. The associated signal distribution is the blue line and the background the dashed red line. The final cuts are shown with the green lines.*

Photons candidates with $P_T > 200$ MeV/c are paired to reconstruct resolved π^0. Most of their combinations come from pairing of background clusters and γ's. The neutral pion mass resolution is $\sim$ 10 MeV/c^2. Therefore these particles must belong to the mass window $m(\pi^0)\ \epsilon\ [105, 165]$ MeV/c^2 (which represents a $\pm 3\sigma$ window). The merged π^0 can be distinguish from a single cluster: the energy of each cell of the cluster, provided its position does not coincide with a charged track, is shared between two virtual sub-clusters. Both of them are then reconstructed as isolated photons which can be paired in a π^0 candidate with an energy compatible with a pair of merged photons and with an invariant mass close to the neutral pion mass ($m(\pi^0)\ \epsilon\ [105, 165]$ MeV/c^2).

---

[1]The residual x_{res} of a reconstructed variable x_{rec} is defined as $x_{res} = x_{rec} - x_{MC}$, where x_{MC} is the MC generated value. The resolution can be estimated using the width of the Gaussian fit to x_{res}.

4.2.3   J/ψ reconstruction

The J/$\psi \to \mu^+ \mu^-$ pre-selection combines two muons with opposite charge. The candidate is accepted in this pre-selection if its invariant mass is compatible with the J/ψ one in a ± 200 MeV/c^2 mass window around the true mass[2] (m$_{\text{true}}$(J/ψ) = 3696.9 MeV/c^2).

Once this requirement has been met, an unconstrained vertex fit is performed with the two muons and its χ^2 has to be less than 50.

4.2.4 η reconstruction

Once a J/ψ has been found in the previous step, we perform the η candidate selection. This particle is reconstructed via its decays to $\gamma\gamma$ and $\pi^+\pi^-\pi^0$. The invariant mass of the two- or three-track combination must be within $\delta(m)(\eta) = \pm 200$ MeV/c^2 (m$_{\text{true}}$(η) = 547.75 MeV/c^2). At this point, the reconstruction differs strongly between the two studied decays.

For the pure radiative η decay mode, we have no information on the direction of the γ and, hence, cannot apply a vertex fit. For this reason, before reconstructing the η, the origin point of the two photon is moved to the J/ψ decay vertex [3]. Only η's with a high transverse momentum are accepted: for the pre-selection we ask $P_T(\eta) > 1500$ MeV/c.

For the $\eta \to \pi^+\pi^-\pi^0$ decay, an unconstrained vertex fit is performed with the two opposite charge pions. Then the π^0 decay products (γ γ) origin is set to the (π^+ π^-) vertex and their energy-momentum added to the two other tracks in order to form the resonance.

4.2.5   B$_s^0$ reconstruction

The pre-selection ends with the combination of the reconstructed J/ψ and η particles into a B$_s^0$ candidate. Several candidates are allowed per event. The four charged tracks, when present, must fit to a single vertex with a χ^2 of less than 50. For both decay channels, the mass window is chosen to be very loose $\delta(m)($B$_s^0) = \pm 600$ MeV/c^2 (m$_{\text{true}}$(B$_s^0) = 5369.6$ MeV/c^2), in order to study the signal-over-background ratio (Section (4.8)).

Three other pre-selection cuts are imposed to the surviving candidates. First, thanks to the large boost in this experiment, the B-mesons will have a large momentum in the z-direction and will fly for a while before decaying to their final states. This leads to the requirement that the Flight Distance (FD) of the B$_s^0$ should be larger than 0, i.e. that the reconstructed B$_s^0$ move forward.

The "Impact Parameter" (IP) of a track with respect to a point is the shortest distance of the point to the track. We can calculate the B$_s^0$ impact parameter with respect to the PV's. As many primary vertices can be constructed, the PV from which the B$_s^0$ originates is the one for which the B's IP is the smallest. The IP significance[4] (IPS) of the B$_s^0$ candidates must also be less than 10.

Finally, the B$_s^0$ should have its momentum pointing back to the primary vertex. Defining the angle θ_{Lp} between the vector from the B candidate origin vertex and its decay vertex

---

[2]The "true" mass of a particle is the mass used for the generation, which in most of the cases corresponds to the mass found in the PDG [14].

[3]This is a good approximation, because the J/ψ and the η are very short lived particles which will not fly more than a few femtometers. Then at LHCb's precision, their decay vertex can be identified as their creation vertex.

[4]The significance S$_x$ of a variable x is defined by the ratio S$_x = x/\sigma_x$, σ_x being the error on x.

$$B_s^0 \to J/\psi(\mu^+\ \mu^-)\ \eta(\gamma\ \gamma) \qquad\qquad B_s^0 \to J/\psi(\mu^+\ \mu^-)\ \eta(\pi^+\ \pi^-\ \pi^0)$$

a) Mass distribution of the B_s^0   *b) Mass distribution of the B_s^0*

Figure 4.3: *Mass spectrum after the pre-selection. The associated signal distribution is the blue line and the background the dashed red line. The final cuts are shown with the green lines.*

$\overrightarrow{\mathrm{L}}_{\text{vertices}} = (\overrightarrow{\text{Decay Vertex}} - \overrightarrow{\text{Origin Vertex}})$ and the particle's momentum $\overrightarrow{\mathrm{P}}_{B_s^0}$. The cosine

$$\cos\left(\theta_{Lp}\right) = \frac{\overrightarrow{\mathrm{L}}_{\text{vertices}} \cdot \overrightarrow{\mathrm{P}}_{B_s^0}}{|\overrightarrow{\mathrm{L}}_{\text{vertices}}||\overrightarrow{\mathrm{P}}_{B_s^0}|} \tag{4.2}$$

should be close to one (i.e. $\theta_{Lp} \sim 0$). The requirement on this parameter for the pre-selection is to have $\cos\left(\theta_{Lp}\right) > 0$. The result of the pre-selected B_s^0 mass can be seen on Fig. (4.3).

4.2.6 Pre-selection results

The pre-selection detailed above reduces the original data samples (see Section (3.7)) to a more manageable number of candidates and events for the fine tuning of the cuts. They are summarized in the following table. The background is estimated with the "v1" sample only.

Pre-selection	$B_s^0 \to J/\psi(\mu^+\ \mu^-)\ \eta(\gamma\ \gamma)$		$B_s^0 \to J/\psi(\mu^+\ \mu^-)\ \eta(\pi^+\ \pi^-\ \pi^0)$	
	Signal	Background	Signal	Background
Candidates	96'101	59'702	542'034	569'976
Associated Cand.	14'482	0	4'386	0
Events	23'950	8'929	29'781	15'012
Associated Events	1'391	0	3'766	0

The average number of reconstructed photons, neutral and charged pions in an event is very large (22, 11 and 28 candidates respectively) on contrary to the muons (2.1 candidates). Therefore the statistics of pre-selected candidates compared to the number of events results from different combinations of γ or π. This is particularly visible for the $B_s^0 \to J/\psi(\mu^+\ \mu^-)\ \eta(\pi^+\ \pi^-\ \pi^0)$ decay where twenty times more candidates than events

Cuts		$B_s^0 \to J/\psi\ \eta$ $\eta \to \gamma\gamma$	$B_s^0 \to J/\psi\ \eta$ $\eta \to \pi^+\pi^-\pi^0$
$\Delta\ln L_{\mu\pi}\ (\mu^+, \mu^-)$	$>$	-50	-50
$P_T\ (\mu^+, \mu^-)$ [MeV/c^2]	$>$	200	200
$\chi^2\ (J/\psi)$	$<$	50	50
$\delta(m)\ (J/\psi)$ [MeV/c^2]	$\pm$	200	200
$P_T\ (\gamma)$ [MeV/c]	$>$	200	
$P_T\ (\pi^\pm)$ [MeV/c]	$>$		200
$P_T\ (\pi^0)$ [MeV/c]	$>$		200
$\delta(m)\ (\pi^0)$ [MeV/c^2]	$\pm$		30
$P_T\ (\eta)$ [MeV/c]	$>$	1500	
$\delta(m)\ (\eta)$ [MeV/c^2]	$\pm$	200	200
$\chi^2\ (B_s^0)$	$<$		50
IPS (B_s^0)	$<$	10	10
FD (B_s^0) [mm]	$>$	0	0
$\cos\theta_{Lp}$	$>$	0	0
$\delta(m)\ (B_s^0)$ [MeV/c^2]	$\pm$	600	600

Table 4.1: *Pre-selection cuts used for $B_s^0 \to J/\psi(\mu^+\ \mu^-)\ \eta(\gamma\ \gamma)$ and $B_s^0 \to J/\psi(\mu^+\ \mu^-)\ \eta(\pi^+\ \pi^-\ \pi^0)$ decay channels.*

are preselected. The main goal of the selection will then be remove the wrong η candidates.

4.3 Fine tuning the cuts

Using all the events passing the pre-selection, a tighter set of cuts must be found to obtain a background-over-signal ratio as low as possible for the highest selection efficiency. This is done by tightening the pre-selection cuts described in Section (4.2) and by adding new criteria. The tuning was done by studying the distributions of the relevant parameters both for the signal and the background pre-selected candidates.

To avoid any bias in the selection, particularly for the background analyzes, the cuts have been tuned on $\sim 18M$ of inclusive b$\bar{\text{b}}$ events of which only ~ 10.5 millions were estimated to be independent (see Section (3.7.2)). The background distributions of this section are realized with these reduced data ("v1" b$\bar{\text{b}}$ sample). The background rejection studies of Section (4.8) were then performed on an additional sample of $\sim 20M$ events. The final selection cuts are summarized in the Tab. (4.2).

The distribution of the various parameters used in the selection are shown in the following figures. The signal and the background are normalized to the same highest bin. The histograms are filled with those events which pass the pre-selections cuts; the position of the tuned cuts for the final selection is indicated with a bold green vertical line. In the plots, the blue line represents the signal candidates while the red dashed line stands for the background. When the same distribution is shown for the two channel of interest, i.e. $B_s^0 \to J/\psi(\mu^+\ \mu^-)\ \eta(\gamma\ \gamma)$ and $B_s^0 \to J/\psi(\mu^+\ \mu^-)\ \eta(\pi^+\ \pi^-\ \pi^0)$, the first decay is plotted on the left and the second on the right and they are separated by a bold black line.

$$B_s^0 \rightarrow J/\psi(\mu^+ \ \mu^-) \ \eta(\gamma \ \gamma) \qquad\qquad B_s^0 \rightarrow J/\psi(\mu^+ \ \mu^-) \ \eta(\pi^+ \ \pi^- \ \pi^0)$$

a) P_T distribution of the μ^-   *b) P_T distribution of the μ^-*

c) IPS of the μ^-   *d) IPS of the μ^-*

Figure 4.4: *μ^- selection cuts. The associated signal distribution is the blue line and the background the dashed red line. The final cuts are shown with the green lines.*

4.3.1 Selection of the muons

The identification of the charged tracks is not exclusive, this means that they can be identified as more than one type of particle. The identification of the muons is achieved using loose cuts on the DLL difference with respect to the pion hypothesis. The cuts have been set to $\Delta \ln L_{\mu\pi} > -10$ (see Fig. (4.2 *a)* and *b)*)) and are applied to all muon candidates.

The muon P_T distributions are plotted on Fig. (4.4). The cut is $P_T > 300$ MeV/c for the "photon channel" and $P_T > 500$ MeV/c for the "pion channel". The looser cut on the muons' transverse momentum in the $B_s^0 \rightarrow J/\psi \ \eta(\gamma \ \gamma)$ will be "compensated" by a tighter cut on the η mass because of the high combinatorial background of the photons (see Section (4.3.5)). Fig. (4.2) shows that these cuts remove the very first bins, where few signal candidates are present.

As the particles originating from the decay of the J/ψ should not point back to the PV, they will have a significant IP. For the selection, the muons are asked to have their IPS

greater than 2. The IPS of the μ^- are plotted on Fig. (4.4 *c)* and *d)*).

4.3.2 Selection of the photons for $\eta \to \gamma\gamma$

The photons are required to have their minimum transverse momentum larger than 500 MeV/c. The plot of the P_T is shown on Fig. (4.5). The two photons are classified by their energy, the most energetic γ is called γ_1, and the less energetic γ_2. The cut on the γ's P_T is aimed to remove soft photons which in general do not originate from B-mesons but rather from the interaction point, radiative decays or other secondary interactions.

$$B_s^0 \to J/\psi(\mu^+\ \mu^-)\ \eta(\gamma\ \gamma)$$

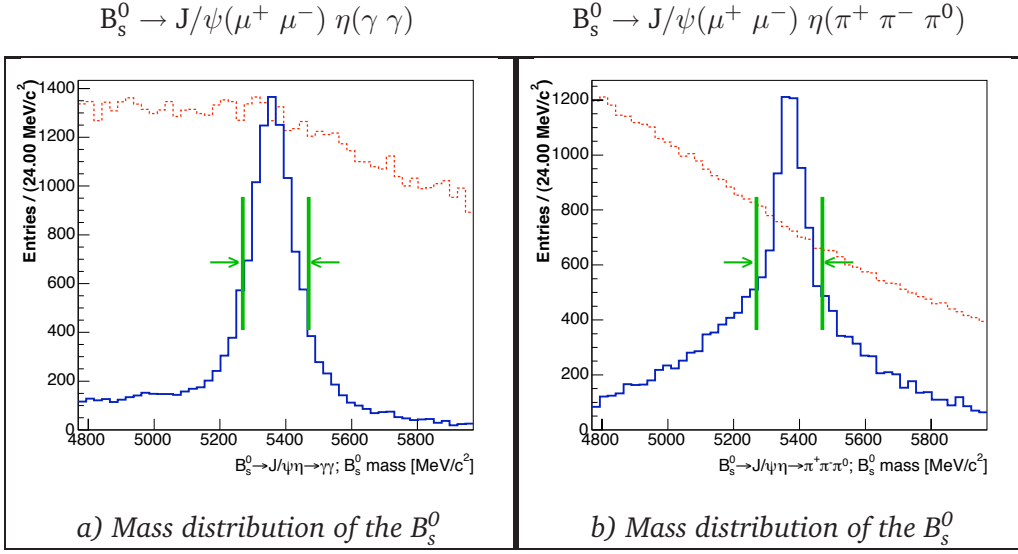*a) P_T distribution of γ_1* *b) P_T distribution of γ_2*

Figure 4.5: *Photon selection cuts. The associated signal distribution is the blue line and the background the dashed red line. The final cuts are shown with the green lines.*

4.3.3 Selection of the pions

The π from the $B_s^0 \to J/\psi\ \eta(\pi^+\ \pi^-\ \pi^0)$ are also not supposed to point to the PV, and this allow to set a cut on IPS > 2. This is shown on Fig. (4.6 *a)*). They are also from a B-decay and therefore have a high P_T. The requirement on the transverse momentum for the pions is $P_T > 500$ MeV/c Fig (4.6 *b)*). This selection allows a high rejection of the background pions.

The selection of the π^0 is quite different as it a composition of two photons. The selection cuts used, on the momentum, on P_T and on the mass distribution, can be seen on Fig. (4.6 *c)* and *d)*). The transverse momentum is asked to be larger than 700 MeV/c. This cut strongly reduces the combinatorial background in the $b\bar{b}$ data but also rejects about half of the signal data. The mass window is the same as for the pre-selection $m(\pi^0) \pm 30$ MeV/c^2 (3σ cut).

4.3.4 Selection of the J/ψ

The cuts on the J/ψ are quite loose, as shown on Fig. (4.7). The first requirement is based on the maximum χ^2 of the unconstrained vertex fit, which is fixed to 10. The transverse

$$B_s^0 \to J/\psi(\mu^+\ \mu^-)\ \eta(\pi^+\ \pi^-\ \pi^0)$$

a) IPS distribution of the π^-

b) P_T distribution of the π^-

c) P_T distribution of the π^0

d) Mass distribution of the π^0
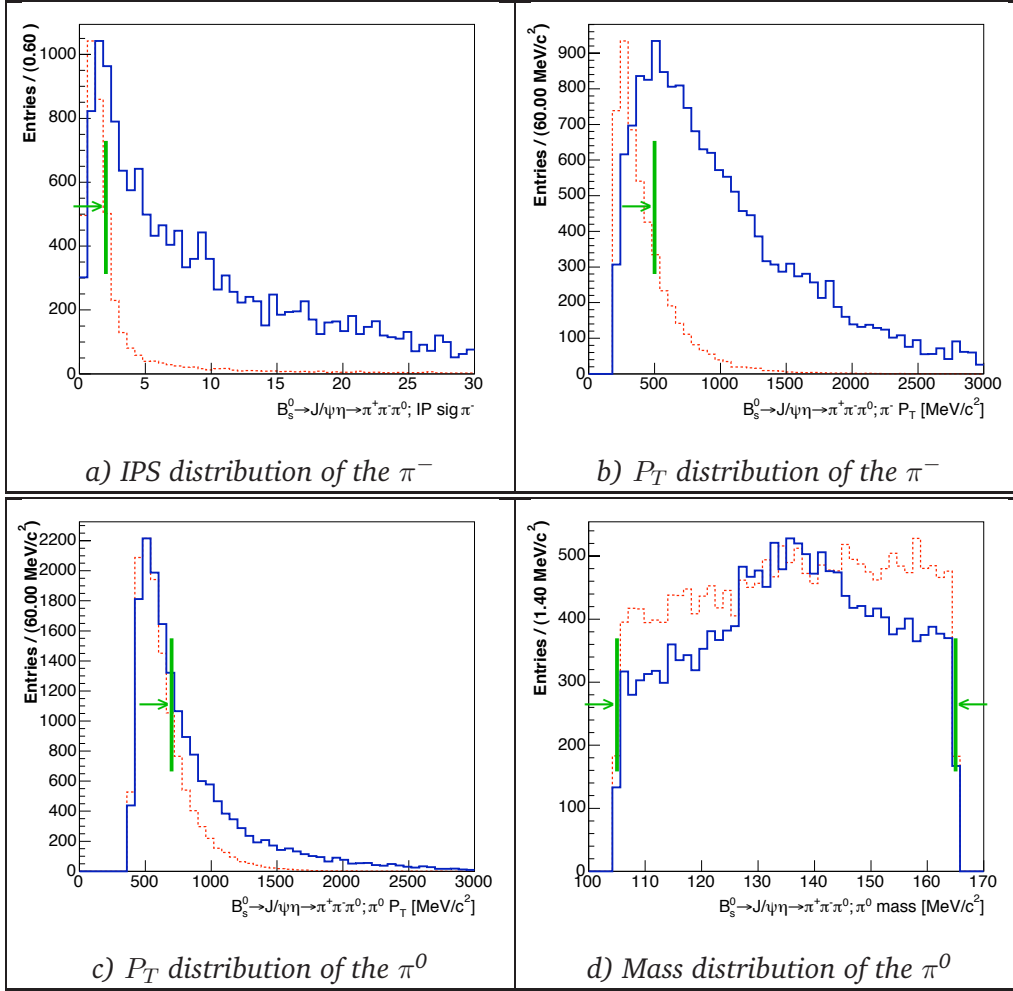
Figure 4.6: *Pion selection cuts for π^- (a) and b)) and for π^0 (c and d). The associated signal distribution is the blue line and the background the dashed red line. The final cuts are shown with the green lines.*

momentum of the J/ψ must be larger than 1000 MeV/c for the "photon channel" and larger than 500 MeV/c^2 for the pion decay mode. A third cut is applied on the IPS of the J/ψ which must be higher than 2. Finally the remaining candidates are asked to have a mass within a window of 100 MeV/c^2 around the nominal J/ψ mass.

4.3.5 Selection of the η

The η selection is the most difficult for the two decays of interest. In both cases, the large number of photons allows a lot of combinations for the η and the π^0 which are usually not the correct ones. Therefore the cuts on these light particles are kept very tight. The selection is shown on Fig. (4.8).

- $\underline{B_s^0 \to J/\psi(\mu^+\ \mu^-)\ \eta(\gamma\ \gamma)}$: This is the most difficult case, as there are no charged tracks involved in the η decay. The only possible requirements concern the P_T and

$$B_s^0 \rightarrow J/\psi(\mu^+ \ \mu^-) \ \eta(\gamma \ \gamma) \qquad\qquad B_s^0 \rightarrow J/\psi(\mu^+ \ \mu^-) \ \eta(\pi^+ \ \pi^- \ \pi^0)$$

a) P_T distribution of the J/ψ b) P_T distribution of the J/ψ

c) IPS distribution of the J/ψ d) IPS distribution of the J/ψ

e) Mass distribution of the J/ψ f) Mass distribution of the J/ψ

Figure 4.7: J/ψ selection cuts. The associated signal distribution is the blue line and the background the dashed red line. The final cuts are shown with the green lines.

$$B_s^0 \to J/\psi(\mu^+ \; \mu^-) \, \eta(\gamma \; \gamma) \qquad\qquad B_s^0 \to J/\psi(\mu^+ \; \mu^-) \, \eta(\pi^+ \; \pi^- \; \pi^0)$$

a) P_T distribution of the η b) P_T distribution of the η

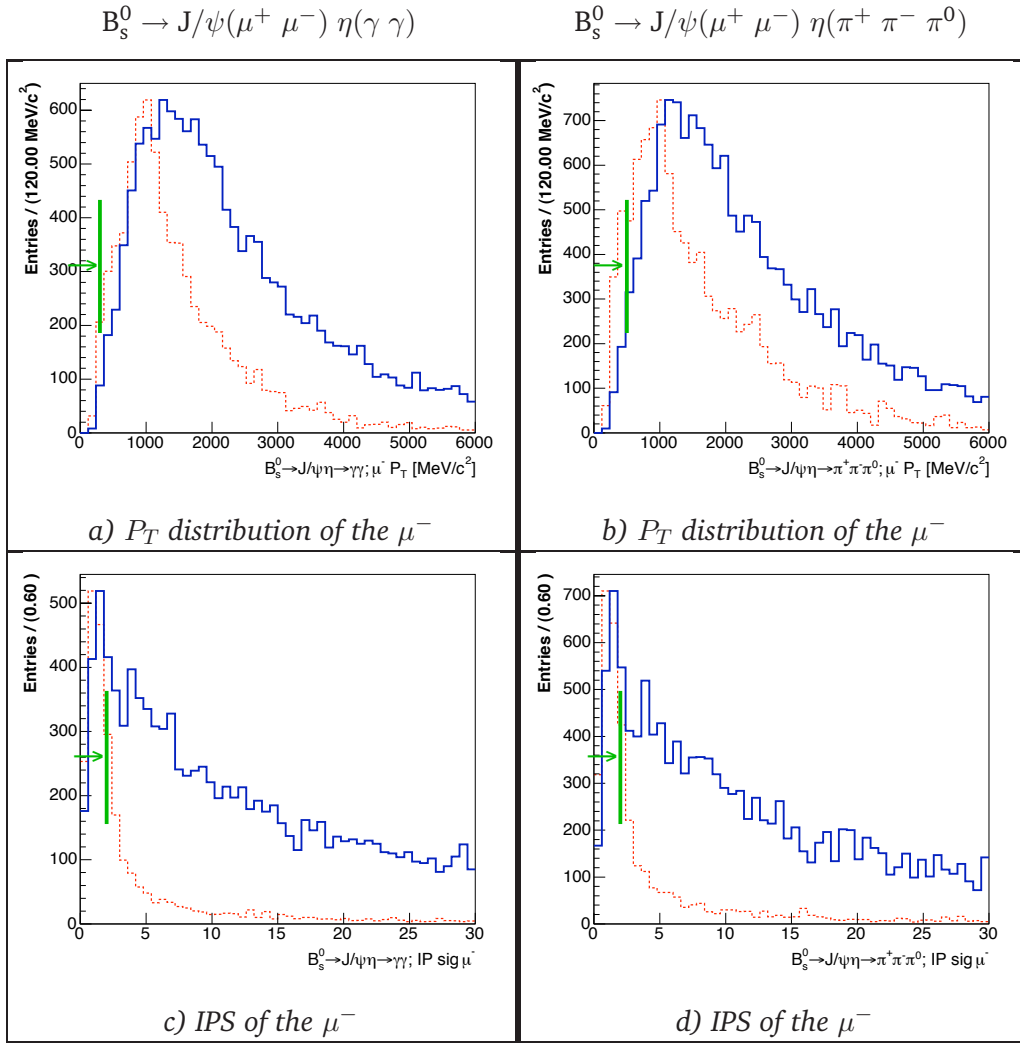c) Mass distribution of the η d) Mass distribution of the η

Figure 4.8: η selection cuts. The associated signal distribution is the blue line and the background the dashed red line. The final cuts are shown with the green lines.

the mass of the η candidates. The η transverse momentum must be higher than 2.8 GeV/c. This large cut remove some good signal events, but is necessary to remove a large part of the combinatorial background. The mass window is very small, to reject wrong combinations. The reconstructed η mass has to be within the mass window of ± 40 MeV/c^2 ($\sim 2.5\sigma$) around the nominal mass.

- $B_s^0 \to J/\psi(\mu^+ \; \mu^-) \, \eta(\pi^+ \; \pi^- \; \pi^0)$: For this decay mode of the η, there is no need to be as tight as previously. A minimum transverse momentum of 1000 MeV/c is enough as well as a mass window of ± 50 MeV/c^2 ($\sim 3\sigma$). There are no other requirements on the track parameters of the fitted charged pions.

4.3.6 Selection of the B_s^0

First we give the requirements on the B_s^0 candidates which are common to both the studied decay modes. The reconstructed B_s^0 candidates are supposed to point to the PV. Thus its

IPS is supposed to be small and the selection requires that IPS < 3. Moreover, it is required that $\cos(\theta_{Lp}) > 0.999$ (Eq. (4.2)). Then, the FD should be significant, i.e. FDS(B_s^0) > 5 where:

$$FDS = \frac{\|\overrightarrow{L}_{\text{vertices}}\|}{\sqrt{\sigma^2_{L_{\text{vertices}}}}},$$

to avoid background due to prompt J/ψ.

$$B_s^0 \rightarrow J/\psi(\mu^+ \; \mu^-) \; \eta(\gamma \; \gamma) \qquad\qquad B_s^0 \rightarrow J/\psi(\mu^+ \; \mu^-) \; \eta(\pi^+ \; \pi^- \; \pi^0)$$

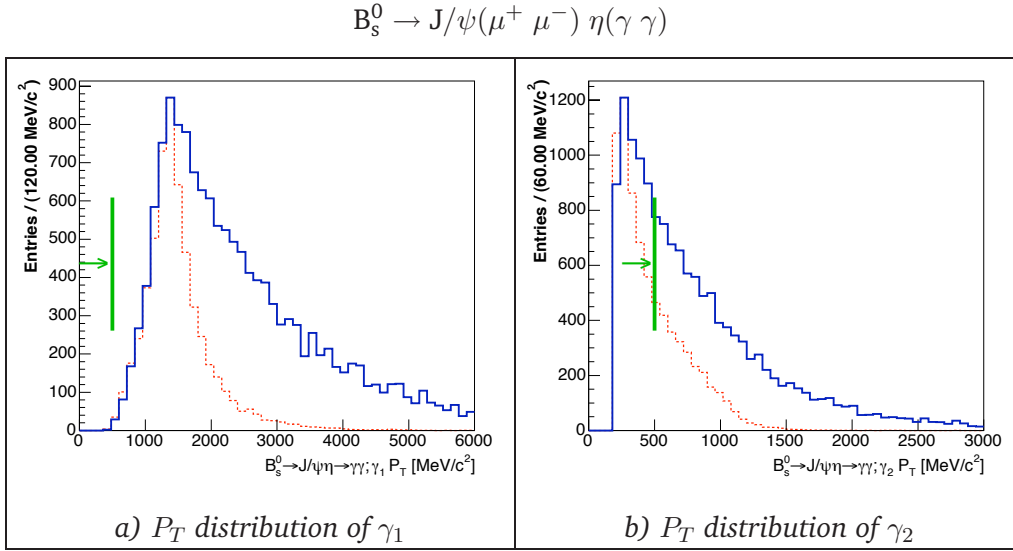*a) θ_{Lp} distribution*   *b) θ_{Lp} distribution*
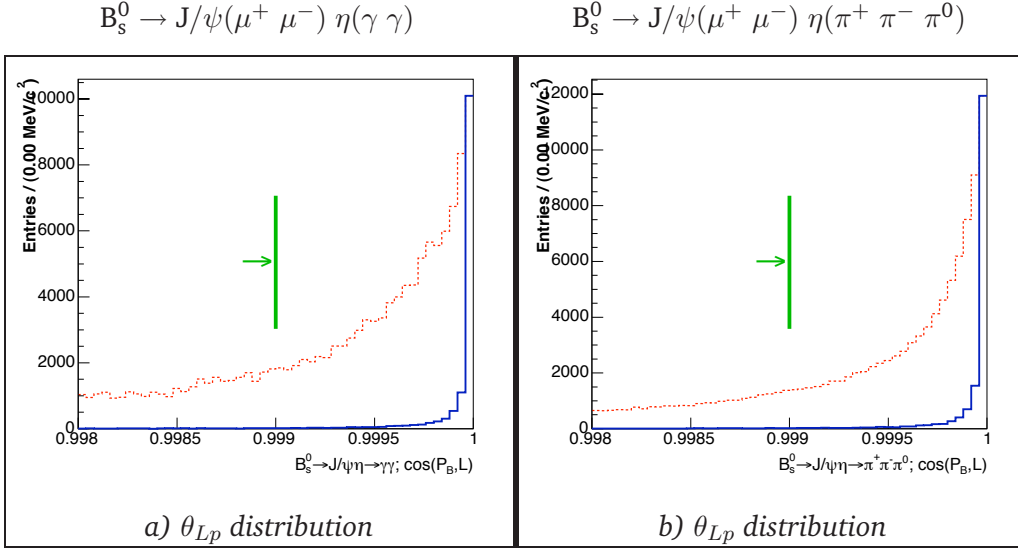
Figure 4.9: *θ_{Lp} selection cut. The associated signal distribution is the blue line and the background the dashed red line. The final cuts are shown with the green lines.*

Finally, the mass of the reconstructed B-meson should be close to its true mass. The requirement here is that the reconstructed mass falls within a ± 100 MeV/c^2 window around the true mass. This wide mass window is due to the large mass resolution for the B_s^0. This is essentially the consequence of the poor photon reconstruction of the ECAL. The background mass window is kept much larger than for the signal: ± 600 MeV/c^2. This will be explained in Section (4.8).

- $\underline{B_s^0 \rightarrow J/\psi(\mu^+ \; \mu^-) \; \eta(\gamma \; \gamma)}$: As previously for the η, the most important requirement for this channel is the transverse momentum cut. The P_T of the B-candidates have to be larger than 5 GeV/c. In addition, the FD must be larger than 2 mm.

- $\underline{B_s^0 \rightarrow J/\psi(\mu^+ \; \mu^-) \; \eta(\pi^+ \; \pi^- \; \pi^0)}$: For this decay mode, no P_T cuts are asked, but the Flight Distance requirements are tightened to FD > 3 mm.

$$B_s^0 \rightarrow J/\psi(\mu^+\ \mu^-)\ \eta(\gamma\ \gamma) \qquad\qquad B_s^0 \rightarrow J/\psi(\mu^+\ \mu^-)\ \eta(\pi^+\ \pi^-\ \pi^0)$$

a) P_T distribution of the B_s^0 candidates

b) χ^2 distribution of the B_s^0 candidates

c) FDS distribution of the B_s^0 candidates

d) FDS distribution of the B_s^0 candidates

e) IPS distribution of the B_s^0 candidates

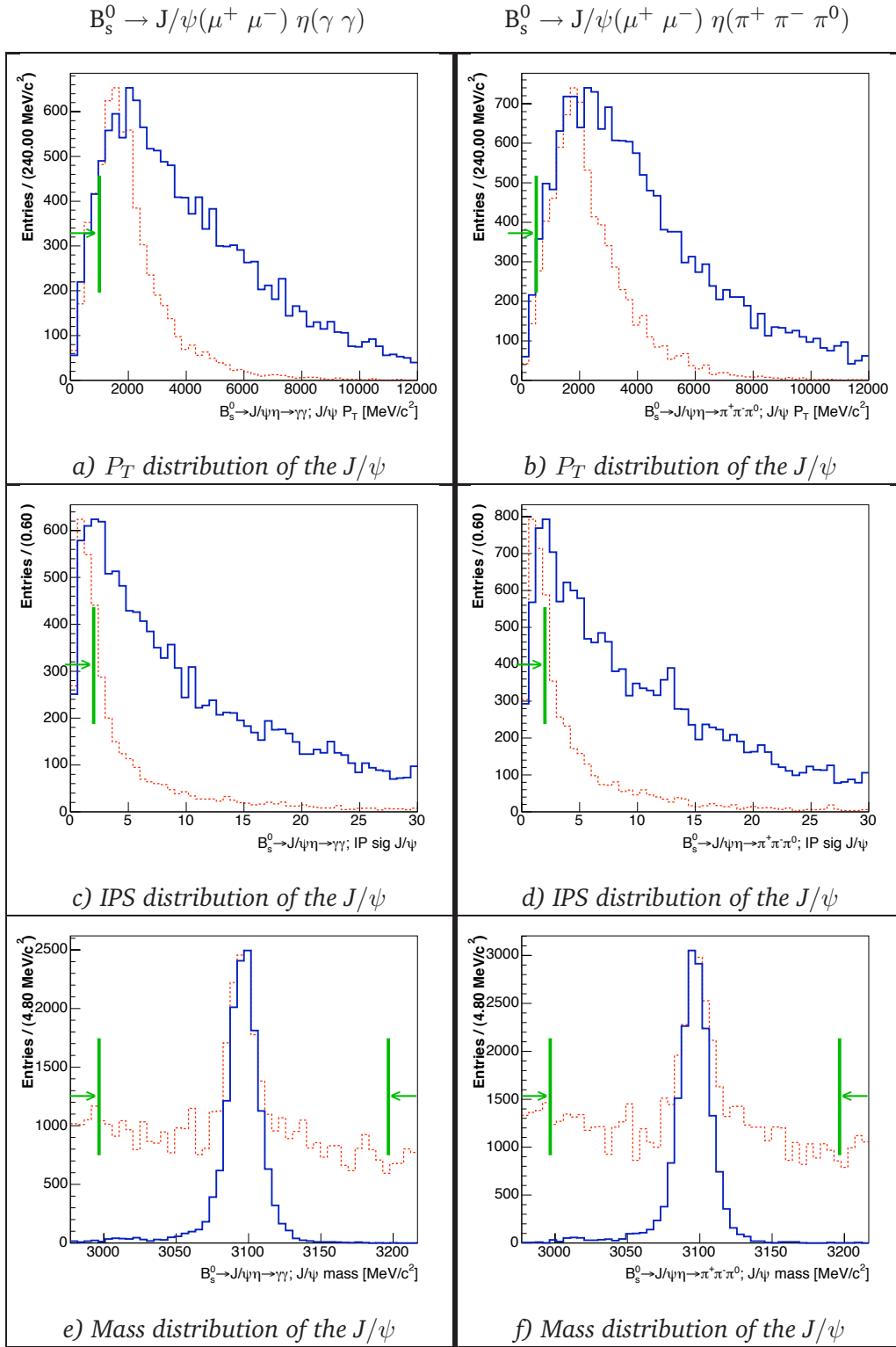f) IPS distribution of the B_s^0 candidates
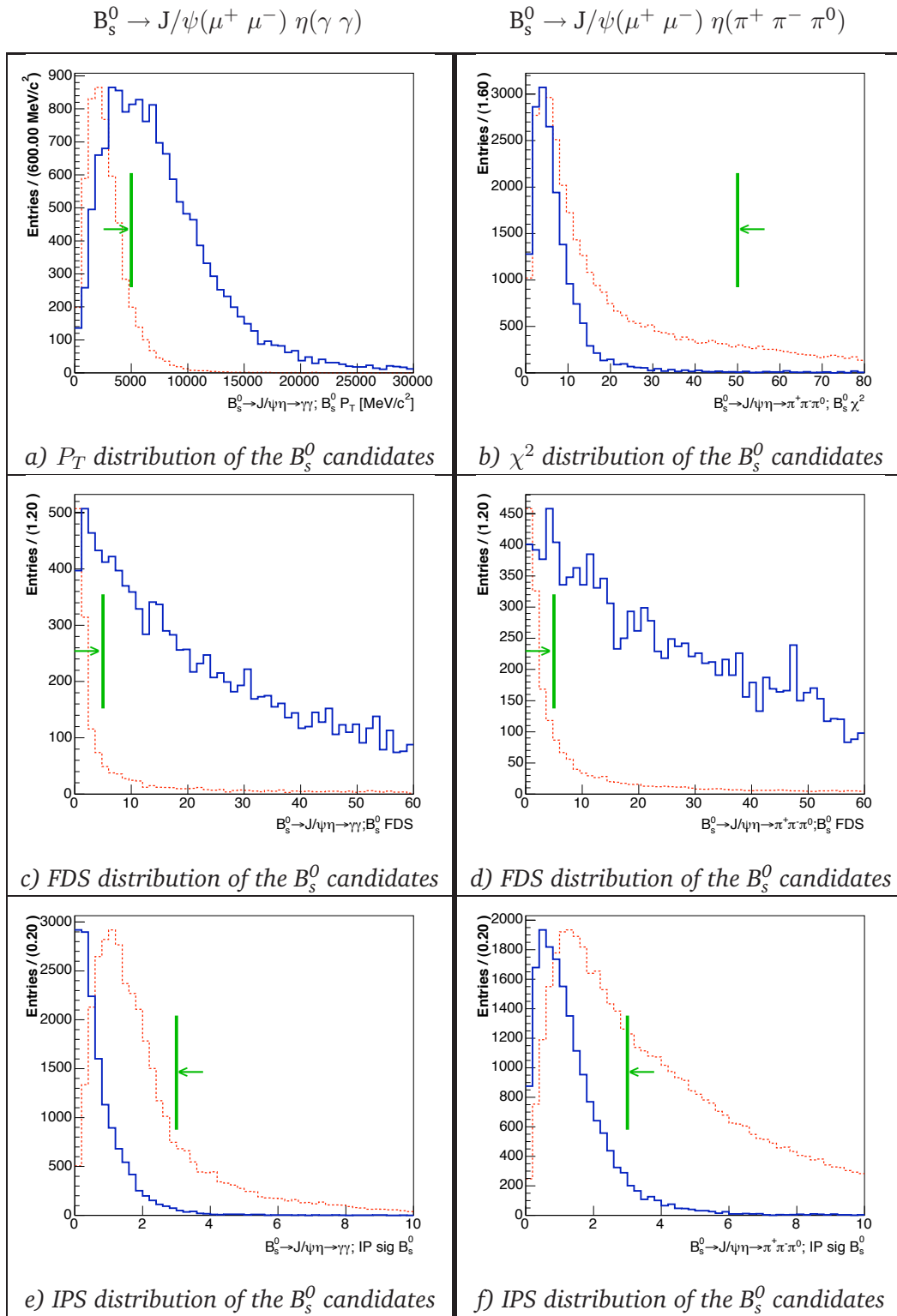
Figure 4.10: B_s^0 selection cuts. The associated signal distribution is the blue line and the background the dashed red line. The final cuts are shown with the green lines.
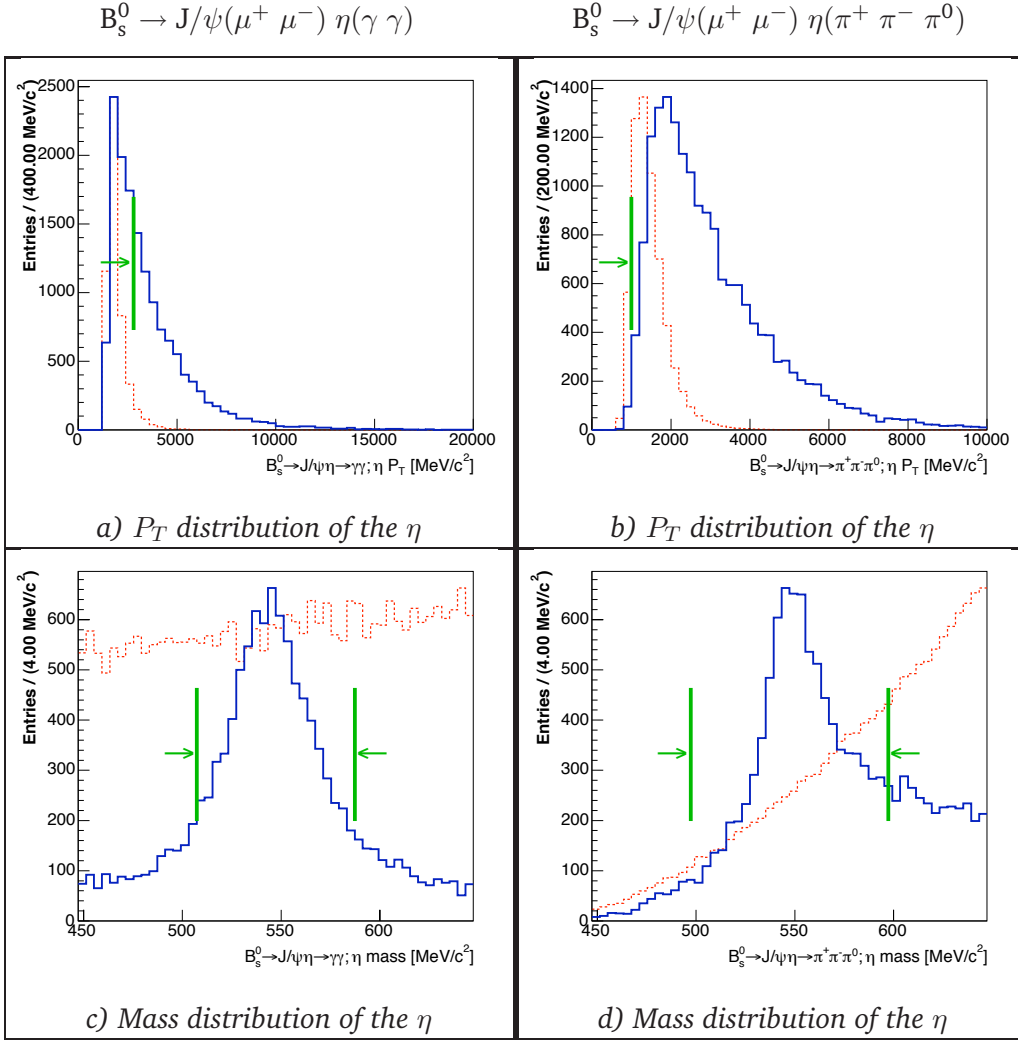
Cuts		$B_s^0 \to J/\psi\,\eta$ $\eta \to \gamma\gamma$	$B_s^0 \to J/\psi\,\eta$ $\eta \to \pi^+\pi^-\pi^0$
$\Delta \ln L_{\mu\pi}\ (\mu^+, \mu^-)$	>	-10	-10
$P_T\ (\mu^+, \mu^-)$ [MeV/c^2]	>	300	500
$IP/\sigma_{IP}\ (\mu^+, \mu^-)$	>	2	2
χ^2 (J/ψ)	<	10	10
P_T (J/ψ) [MeV/c]	>	1000	500
IP/σ_{IP} (J/ψ)	>	2	2
$\delta(m)$ (J/ψ) [MeV/c^2]	$\pm$	100	100
$P_T\ (\gamma)$ [MeV/c]	>	500	
$P_T\ (\pi^{\pm})$ [MeV/c]	>		500
$IP/\sigma_{IP}\ (\pi^{\pm})$	>		2
$P_T\ (\pi^0)$ [MeV/c]	>		700
$\delta(m)\ (\pi^0)$ [MeV/c^2]	$\pm$		30
$P_T\ (\eta)$ [MeV/c]	>	2800	1000
$\delta(m)\ (\eta)$ [MeV/c^2]	$\pm$	40	50
χ^2 (B$_s^0$)	<		50
p (B$_s^0$) [MeV/c^2]	>	5000	
IPS (B$_s^0$)	<	3	3
FDS (B$_s^0$)	>	5	5
FD (B$_s^0$) [mm]	>	2	3
$\cos\theta_{Lp}$	>	0.999	0.999
$\delta(m)$ (B$_s^0$) [MeV/c^2]	$\pm$	100	100

Table 4.2: *Selection cuts used for $B_s^0 \to J/\psi(\mu^+\ \mu^-)\ \eta(\gamma\ \gamma)$ and $B_s^0 \to J/\psi(\mu^+\ \mu^-)\ \eta(\pi^+\ \pi^-\ \pi^0)$ decay channels.*

4.4 Final selection

We will give in this section the resolutions which are obtained with the MC associated candidates surviving the tight selection cuts. This will allow an estimation of the physics performances of the LHCb reconstruction and analysis algorithms.

4.4.1 Selected events

The selection detailed in Section (4.3) reduced the pre-selected events to a sample containing essentially those with the decays of interest. The number of candidates, associated candidates and events passing these severe cuts are summarized in Tab. (4.3). We can conclude, for the "photon decay", that the selection is powerful on the $b\bar{b}$ "v1" sample, keeping not a single background event. The number of candidates is very close to the number of events, which means that there are very few multiple candidates[5] for one event.

The results are different for the channels with pions. There are no "v1" background candidates but the multiplicity of selected B$_s^0$ per event is often larger than one. This is

---

[5]By multiple we mean that several B$_s^0$ candidates can be reconstructed in a single event if a fake particle passes all the selection cuts. For example, two similar reconstructed η, one being issued from the generated decay and the other from combinatorial background, can be added to a J/ψ which results in two reconstructed B-mesons.

Selection	$B_s^0 \rightarrow J/\psi(\mu^+\ \mu^-)\ \eta(\gamma\ \gamma)$		$B_s^0 \rightarrow J/\psi(\mu^+\ \mu^-)\ \eta(\pi^+\ \pi^-\ \pi^0)$	
	Signal	$b\bar{b}$ bkg	Signal	$b\bar{b}$ bkg
Candidates	2′104	0	1′626	0
Events	2′084	0	1′486	0
Associated events	2′072	0	1′269	0

Table 4.3: *Number of selected candidates, events and associated events for the two studied decay modes, for the signal and the $b\bar{b}$ "v1" background.*

essentially due to the large number of π^0's which can be combined to the other particles to form the B-meson. To find a criterion to remove the non-associated candidates, we will rely on the simulation and track down the associated candidates. The criterion which was found to select the right $B_s^0 \rightarrow J/\psi\ \eta(\pi^+\ \pi^-\ \pi^0)$ is the reconstructed η mass which has the smallest difference with the "true" generated mass. This means that we expect the good neutral pion to have a better momentum and mass reconstruction than the fake ones. In this case, $\sim 70\%$ of the good combinations can be selected.

The purity, which is the ratio N_{asso}/N_{sel} is much better for the $B_s^0 \rightarrow J/\psi(\mu^+\ \mu^-)\ \eta(\gamma\ \gamma)$ channel and is close to $\sim 100\%$. The pion decay mode suffers from a less efficient π^0 association and the ratio N_{asso}/N_{sel} falls to $\sim 85\%$. Indeed, when we request only the four charged tracks to be selected, this ratio increases to $\sim 100\%$.

4.4.2   Mass resolutions

The invariant masses of the η, J/ψ and B_s^0 mesons are presented in Fig. (4.11). The distributions are shown for events with a selected B-meson, where all the cuts discussed in Section (4.3) have been applied before any trigger. The J/ψ mass distributions are very similar for the two channels. The mean value is very close to the generated true mass and the resolution are $\sigma_{m(J/\psi)} = (11.3 \pm 0.3)$ MeV/c^2 for $B_s^0 \rightarrow J/\psi(\mu^+\ \mu^-)\ \eta(\gamma\ \gamma)$, Fig. (4.11 *a)*) and $\sigma_{m(J/\psi)} = (11.2 \pm 0.3)$ MeV/c^2 for $B_s^0 \rightarrow J/\psi(\mu^+\ \mu^-)\ \eta(\pi^+\ \pi^-\ \pi^0)$, Fig. (4.11 *b)*). The tail on the left can be explained by the 10% of $J/\psi \rightarrow \mu^+\ \mu^-\ \gamma$ radiative decays as introduced in Section (3.6.1).

The mass distributions of the η are also fitted with a single Gaussian. The distribution are wider and the windows very tight around the true value. The mean values are close to the generated true mass, 3σ and 5σ for the $\eta \rightarrow \gamma\gamma$ and the $\eta \rightarrow \pi^+\pi^-\pi^0$ decays respectively, but the Gaussian fit does not seem to be a good approximation. The mass resolution are $\sigma_{m(\eta)} = (16.0 \pm 0.3)$ MeV/c^2 for the "photon channel", Fig. (4.11 *c)*), and $\sigma_{m(\eta)} = (12.7 \pm 0.4)$ MeV/c^2 for the other decay mode, Fig. (4.11 *d)*). The second distribution is narrower because of the charged pions contribution. In both cases, the mass resolution of the η suffers from the poor resolution of the ECAL, which does not allow to measure properly the momentum of the photons. This will be discussed in Section (4.5.2).

The B_s^0 mass for the "photon channel" can be fitted with a Gaussian having a resolution of $\sigma_{m(B_s^0)} = (52.6 \pm 1.3)$ MeV/c^2, but a bias is present for its mean value which is situated 7σ lower than the true mass, Fig. (4.11 *e)*). This bias is certainly due to photon energy loss or calibration problem. This can already be seen in the η mass. For the "pion decay", we get a resolution for the B-meson of $\sigma_{m(B_s^0)} = (44.3 \pm 1.3)$ MeV/c^2 and a good mean value, Fig. (4.11 *f)*).

$$B_s^0 \rightarrow J/\psi(\mu^+ \ \mu^-) \ \eta(\gamma \ \gamma)$$ $$B_s^0 \rightarrow J/\psi(\mu^+ \ \mu^-) \ \eta(\pi^+ \ \pi^- \ \pi^0)$$

a) Mass distribution of the J/ψ   *b) Mass distribution of the J/ψ*

c) Mass distribution of the η   *d) Mass distribution of the η*

e) Mass distribution of the B_s^0   *f) Mass distribution of the B_s^0*
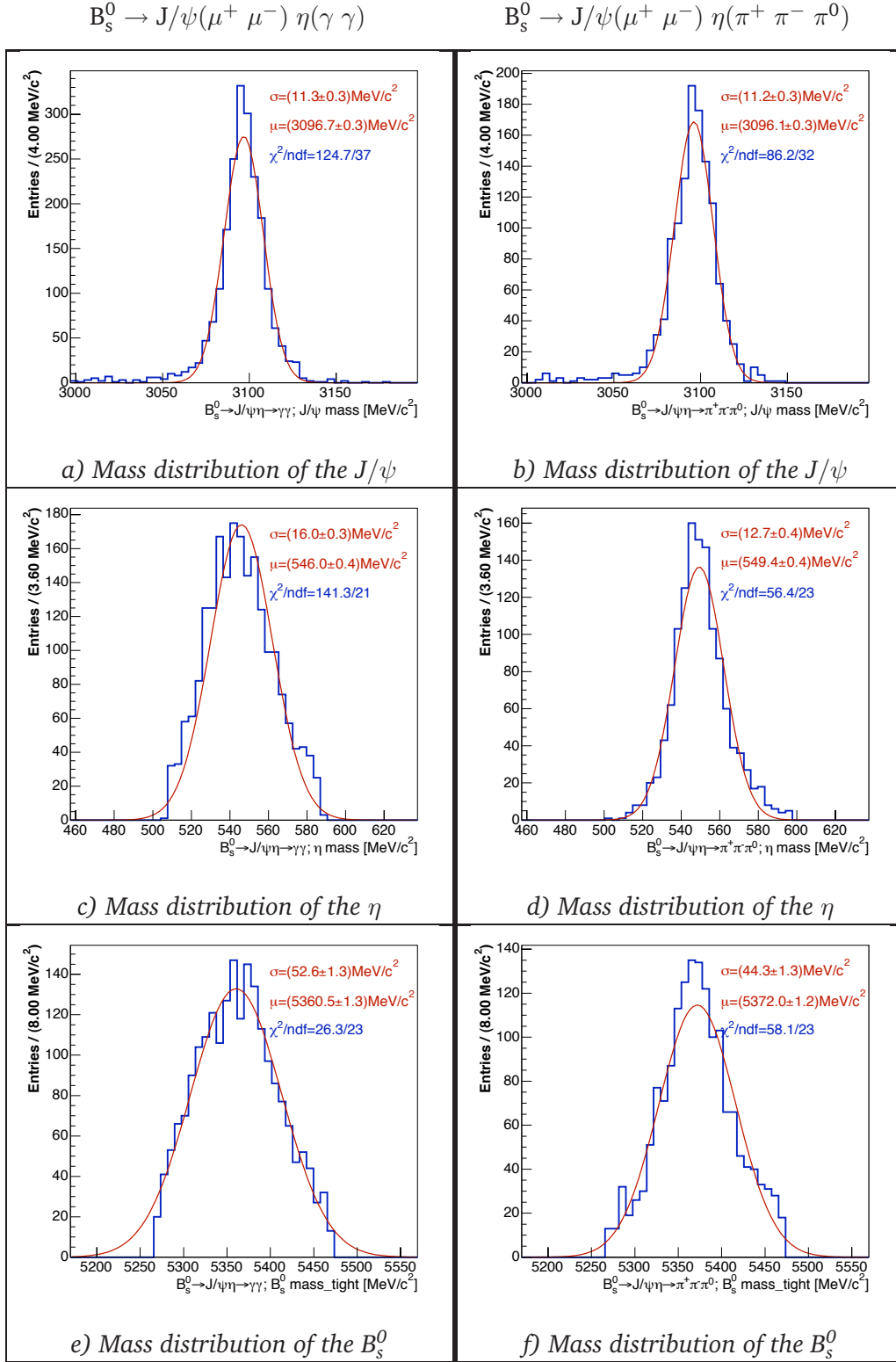
Figure 4.11: *J/ψ, η and B_s^0 mass distribution and Gaussian fit.*

4.4.3   Vertex resolutions

Unlike primary vertices which are reconstructed prior to the analysis presented here and about which information can be retrieved, secondary vertices have to be reconstructed for each candidate. Fig. (4.12) shows the resolution on the B_s^0 vertex in transverse (x, y) and longitudinal (z) directions with respect to the beam. Each distribution is fitted with a single Gaussian. The resolutions are ~ 20 μm in x, y and ~ 230 μm in z for the $B_s^0 \to J/\psi(\mu^+\ \mu^-)\ \eta(\gamma\ \gamma)$ and ~ 15 μm in x, y and ~ 180 μm in z for the other channel. The second set of resolutions is better, as more charged tracks are used to reconstruct the B_s^0 decay vertex.

4.5   Proper time studies

In the determination of the CP-violating asymmetry $A_{CP}(t)$, the error on the proper time measurement is one of the parameters to be included in a parameterization of the experimentally observed decay rates for each channel (see Section (1.4.4)). This error must be small enough to resolve the fast B_s^0 oscillations.

The proper time t satisfies the time dilatation formula $t = t^{lab}/\gamma$, where t^{lab} is the B-meson lifetime in the laboratory and γ is the relativistic factor. The decay length of the B_s^0, $\vec{L}_{vertices}$, is given by:

$$\vec{L}_{vertices} = \vec{x}_{DV} - \vec{x}_{PV} = c \cdot \vec{\beta} \cdot t,$$

where $\vec{\beta}$ is the relative velocity of the particle with respect to the speed of light c and $\vec{x}_{PV}$ and $\vec{x}_{DV}$ are the B-meson production vertex and its decay vertex coordinates respectively. The reconstructed B_s^0 proper time t is calculated as:

$$t = m(B_s^0) \cdot \frac{\vec{p}_{B_s^0} \cdot \vec{L}_{vertices}}{|\vec{p}_{B_s^0}|^2}, \tag{4.3}$$

with $\vec{p}_{B_s^0}$ the B-candidate momentum and $m(B_s^0)$ the B_s^0 mass. A method has been implemented in the analysis software to determine the proper time. Given a reconstructed particle (with its momentum and decay vertex) and a production vertex, its proper time can be derived by a χ^2 fit and the errors are given by the second derivative of this χ^2. This method is described in more detail in Ref. [93].

The proper time distributions are shown on Fig. (4.13). One can estimate the average proper time by multiplying a decaying exponential and an acceptance function (described in Section (4.5.3)) as it is shown on Fig. (4.13). This implementation describes well the proper time behavior:

- The exponential fits properly the tail of the distribution, which consists only of the proper time of the B_s^0 candidate.

- The acceptance function provide a good scheme of the cutoff at small proper time. This reduced efficiency is due to the trigger and the selection cuts, as explained in Section (4.5.3).

The proper time's slope that we obtained with this fit are $\tau = (1.45 \pm 0.04)$ ps for the "photon channel" decay and $\tau = (1.56 \pm 0.06)$ ps for the other channel. The first result is consistent with the true proper time used in the generation ($\tau_{true} = 1.472$ ps) and the second over-estimated.

$$B_s^0 \to J/\psi(\mu^+ \; \mu^-) \; \eta(\gamma \; \gamma) \qquad\qquad B_s^0 \to J/\psi(\mu^+ \; \mu^-) \; \eta(\pi^+ \; \pi^- \; \pi^0)$$

a) Resolution in x of the B_s^0 decay vertex

b) Resolution in x of the B_s^0 decay vertex

c) Resolution in y of the B_s^0 decay vertex

d) Resolution in y of the B_s^0 decay vertex

e) Resolution in z of the B_s^0 decay vertex

f) Resolution in z of the B_s^0 decay vertex
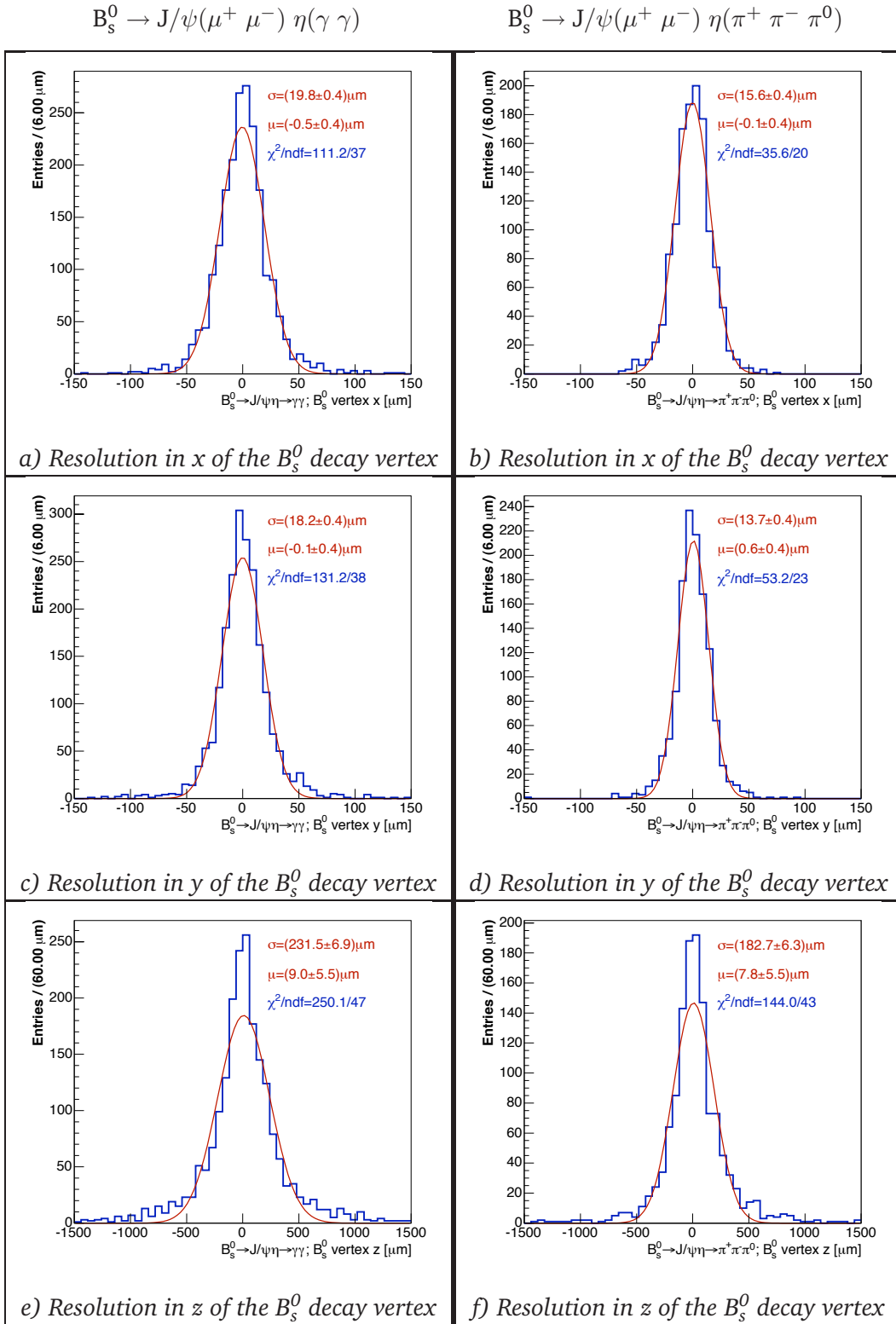
Figure 4.12: B_s^0 vertex position resolutions and Gaussian fits.

$B_s^0 \to J/\psi(\mu^+\ \mu^-)\ \eta(\gamma\ \gamma)$ $B_s^0 \to J/\psi(\mu^+\ \mu^-)\ \eta(\pi^+\ \pi^-\ \pi^0)$

a) B_s^0 proper time   b) B_s^0 proper time
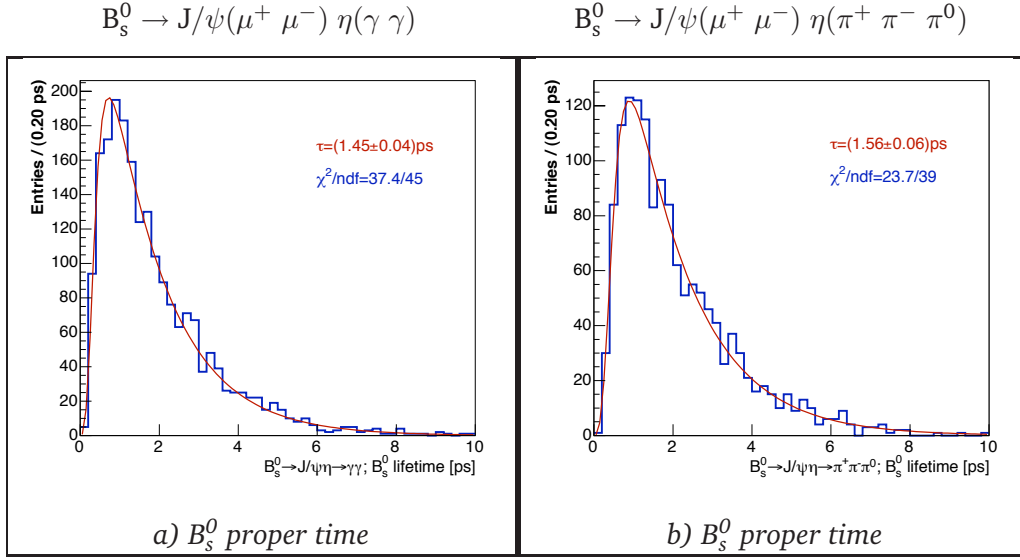
Figure 4.13: B_s^0 proper time fitted with an acceptance function multiplying an exponential.

4.5.1 Proper time resolution

The proper time resolution distributions are plotted on Fig. (4.14). The fits are performed with a single Gaussian. The resolutions for the channel with photons is not as good as the other decay mode: $\sigma_t = (120.8 \pm 3.2)$ fs. The fit with a single Gaussian does not seem adequate. The situation is better for the other decay mode: $\sigma_t = (68.3 \pm 2.0)$ fs. There is no bias in the mean position for any channels. Again, the difficulty in reconstructing the γ is the origin of the bad resolutions on the proper time. These results will be improved with a constrain on the mass during the vertex fitting, see Section (4.6.1) or using a Kalman Filter fit, see Section (4.6.2).

4.5.2 Contributions to the proper time resolution

Eq. (4.3) shows that the proper time depends on four parameters, the production vertex position, the decay vertex position, the momentum of the studied particle and its mass (10 parameters in total). The resolution on each of these measurements has an influence on the lifetime. Using the MC truth, one can determine the contribution of each of these parameters fixing it to the true MC value, except the mass. Their contributions to the proper time can be seen on Fig. (4.15). An estimation of the resolutions can be performed with Gaussian fits, even if they are rather bad for the last four distributions.

Fig. (4.15) a) and b) show the B_s^0 proper time resolution when the B-momentum ($P_{B_s^0}$) is fixed to its generated value. For the distributions c) and d), the primary vertex contribution has been removed, using instead the MC truth. Finally the secondary vertex position has been fixed for the two last plots, e) and f).

The tight and nice Gaussian fit when $P_{B_s^0}$ is not contributing to the resolution is a clear evidence that the momentum resolution is the disturbing parameter. The width obtained in this situation, $\sigma_t = (33.6 \pm 0.7)$ fs for the "photon channel" and $\sigma_t = (29.1 \pm 0.8)$ fs for the "pion channel", corresponds to the expected proper time resolutions for B-decays with only charged tracks. The non-Gaussian distribution shape of the other plots is another

$B_s^0 \to J/\psi(\mu^+ \ \mu^-) \ \eta(\gamma \ \gamma)$

$B_s^0 \to J/\psi(\mu^+ \ \mu^-) \ \eta(\pi^+ \ \pi^- \ \pi^0)$

a) Resolution of the B_s^0 proper time

b) Resolution of the B_s^0 proper time
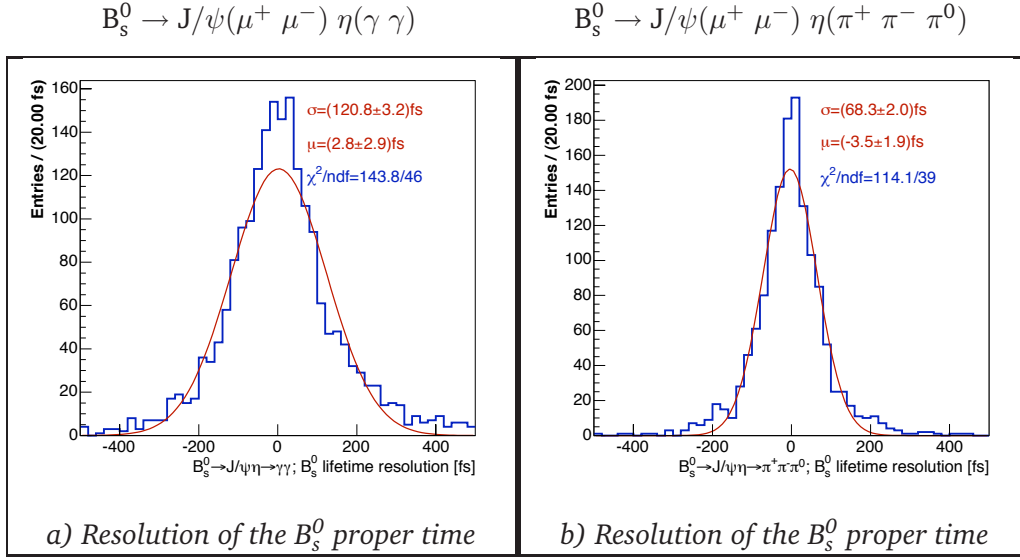
Figure 4.14: *B_s^0 proper time resolution with a Gaussian fit. A single Gaussian is fitted on the data to give an estimation of the distribution width.*

consequence of the $P_{B_s^0}$ resolution. The confirmation of the poor performances of the ECAL can be seen on Fig. (4.16). The B_s^0 momentum resolution is quite nice for the decays with four or six charged tracks: $B_s^0 \to J/\psi \ \phi$ and $B_s^0 \to \eta_c \ \phi$. For those decays, the B_s^0 relative momentum resolution is $(0.277 \pm 0.001)\%$ and $(0.223 \pm 0.004)\%$ respectively. We estimate that a resolution $\leq 0.4\%$ is needed to have a good proper time resolution, i.e. $\sigma_t \leq 40$ fs. Unfortunately, this is not the case for decays where photons are involved. The relative momentum resolution for the two studied decays are $\delta P/P = (1.13 \pm 0.02)\%$ for the decay with photons and $\delta P/P = (0.86 \pm 0.02)\%$ for the "pion channel".

The second cause of the poor lifetime resolution is due to the decay vertex position. This effect is only present in the $B_s^0 \to J/\psi(\mu^+ \ \mu^-) \ \eta(\gamma \ \gamma)$ channel and is visible comparing $c)$ to $e)$ distributions. The width of the proper time resolution is 1.5 times larger when the primary vertex is kept at its "true position" than when the decay vertex is fixed at its generated point: this shows that reconstructing the decay vertex with only two charged particles (the $\mu^{\pm}$ for the J/ψ decay) does not give a high precision (see also Fig. (4.12)).

4.5.3 Proper time acceptance

The selection criteria that we have used are based on the specific topology of the B-decays and require a detached secondary vertex. Thus the tight cuts defined in Section (4.3) biases the proper time distribution, removing the short lived B_s^0 mesons. This is clearly visible on Fig. (4.13). The probability to select signal events is no longer uniform but depends on the proper time. The acceptance which describes this probability is a time-dependent bin-to-bin selection efficiency. It compares the true proper time distribution of the signal after the selection to the same distribution without any cut (we only require the charged particles to be reconstructed as long tracks and the neutral ones to have appropriate clusters in the ECAL). The acceptance function for the two channels, before and after L0, L1 and HLT triggers, are shown on Fig. (4.17).

$B_s^0 \to J/\psi(\mu^+\ \mu^-)\ \eta(\gamma\ \gamma)$ $B_s^0 \to J/\psi(\mu^+\ \mu^-)\ \eta(\pi^+\ \pi^-\ \pi^0)$

a) Lifetime resolution - MC $P_{B_s^0}$ *b) Lifetime resolution - MC $P_{B_s^0}$*

c) Lifetime resolution - MC PV   *d) Lifetime resolution - MC PV*

e) Lifetime resolution - MC DV   *f) Lifetime resolution - MC DV*
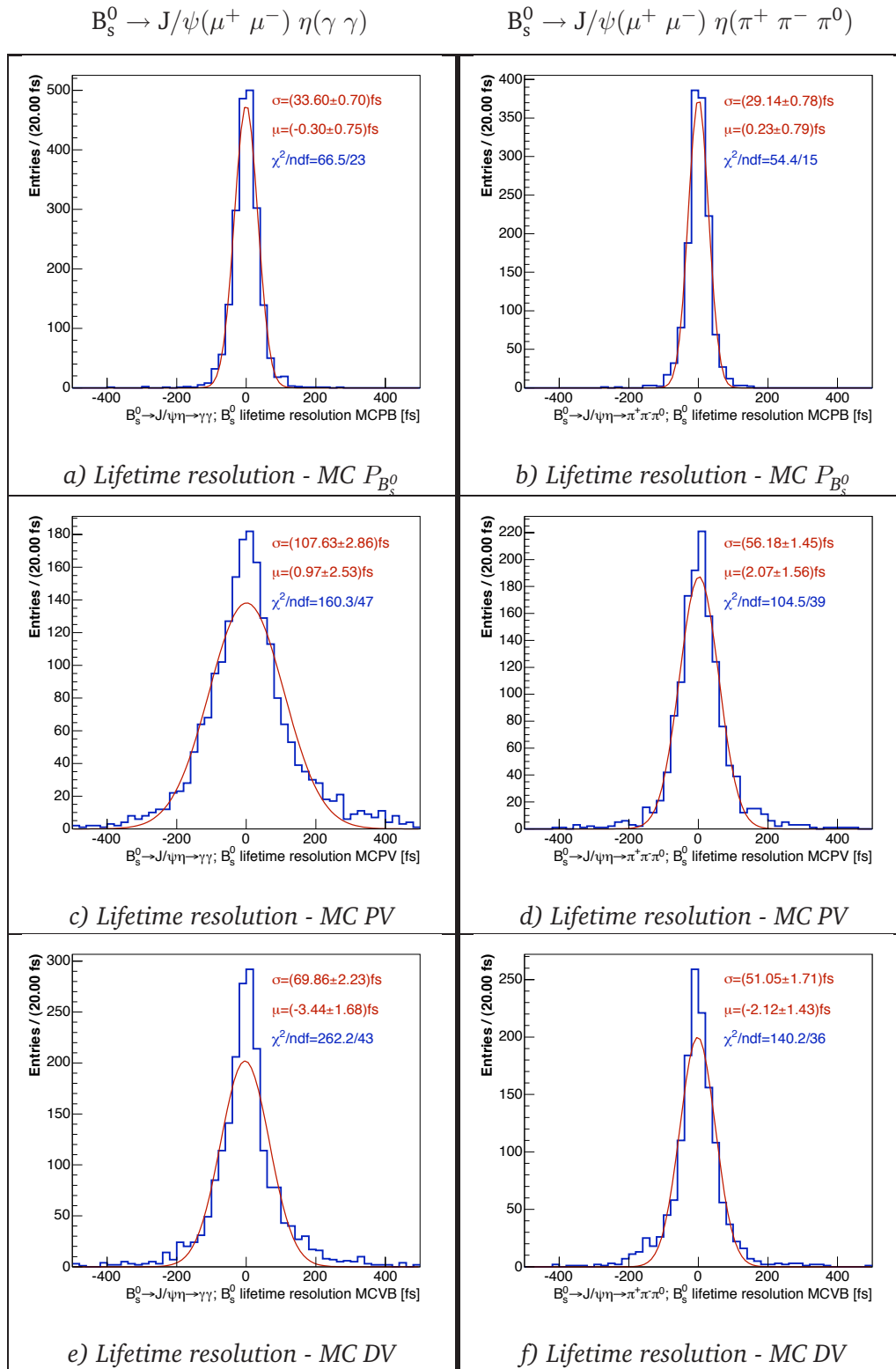
Figure 4.15: *Proper time resolution contributions. Single Gaussian have been fitted on the distribution to facilitate the comparison of their widths.*

$$B_s^0 \rightarrow J/\psi(\mu^+ \; \mu^-) \; \eta(\gamma \; \gamma)$$

$\sigma = (1.13 \pm 0.02)\%$

$\mu = (-0.18 \pm 0.02)\%$

$\chi^2/ndf = 22.6/12$

a) B_s^0 momentum resolution

$$B_s^0 \rightarrow J/\psi(\mu^+ \; \mu^-) \; \eta(\pi^+ \; \pi^- \; \pi^0)$$

$\sigma = (0.86 \pm 0.02)\%$

$\mu = (0.05 \pm 0.02)\%$

$\chi^2/ndf = 39.2/11$

b) B_s^0 momentum resolution

$$B_s^0 \rightarrow D_s \; \pi$$

$\sigma = (0.277 \pm 0.001)\%$

$\mu = (0.006 \pm 0.001)\%$

$\chi^2/ndf = 3026.5/41$

c) B_s^0 momentum resolution

$$B_s^0 \rightarrow \eta_c \; \phi$$

$\sigma = (0.223 \pm 0.004)\%$

$\mu = (-0.004 \pm 0.004)\%$

$\chi^2/ndf = 115.7/24$

d) B_s^0 momentum resolution
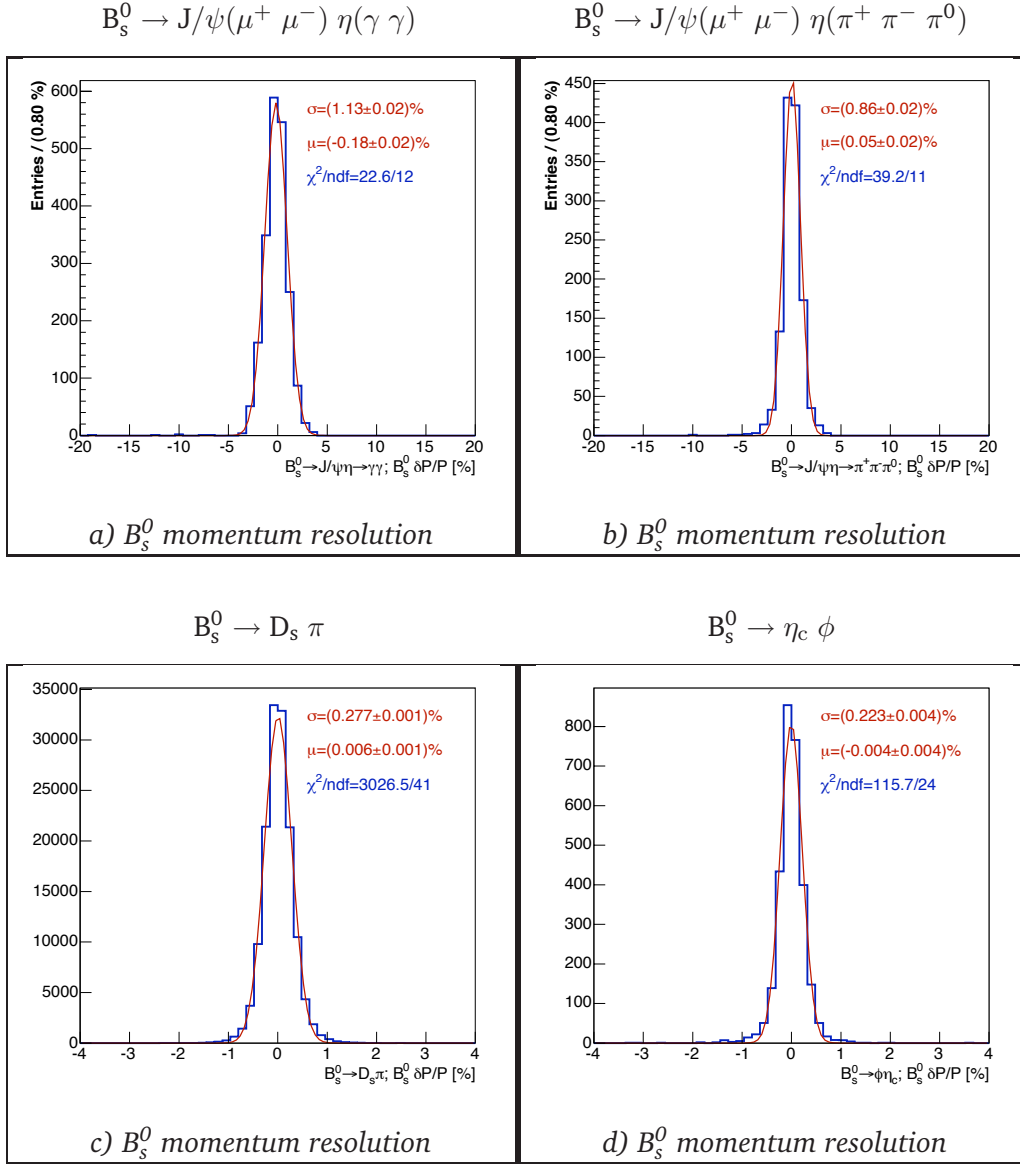
Figure 4.16: B_s^0 *relative momentum resolution and Gaussian fit of the B_s^0 for two studied channels above and for the $B_s^0 \rightarrow D_s \; \pi$ (left) and the $B_s^0 \rightarrow \eta_c \; \phi$ (right) below. The results are better for the last channel, thanks to its six charged decay products.*

The behavior of these acceptances can be fitted by a time-dependent efficiency function $\varepsilon_t(t)$ of the true proper time t:

$$\varepsilon_t(t) = acc_a \cdot \frac{(acc_s \cdot t)^3}{1 + (acc_s \cdot t)^3},\tag{4.4}$$

where acc_a is a normalization factor, acc_s parameterizes the slope of the rising part of the function. Fitting this distribution to the plots of Fig. (4.17), the results are $acc_s = (1.93 \pm 0.06)$ ps^{-1} for the "photon channel" and $acc_s = (1.58 \pm 0.05)$ ps^{-1} for the second decay mode, before L0, L1 and HLT triggers. Since the normalization is arbitrary, acc_a is also an arbitrary number.

$$B_s^0 \to J/\psi(\mu^+ \ \mu^-) \ \eta(\gamma \ \gamma) \qquad\qquad B_s^0 \to J/\psi(\mu^+ \ \mu^-) \ \eta(\pi^+ \ \pi^- \ \pi^0)$$

a) Acceptance function before triggers   b) Acceptance function before triggers

c) Acceptance function after HLT   d) Acceptance function after HLT
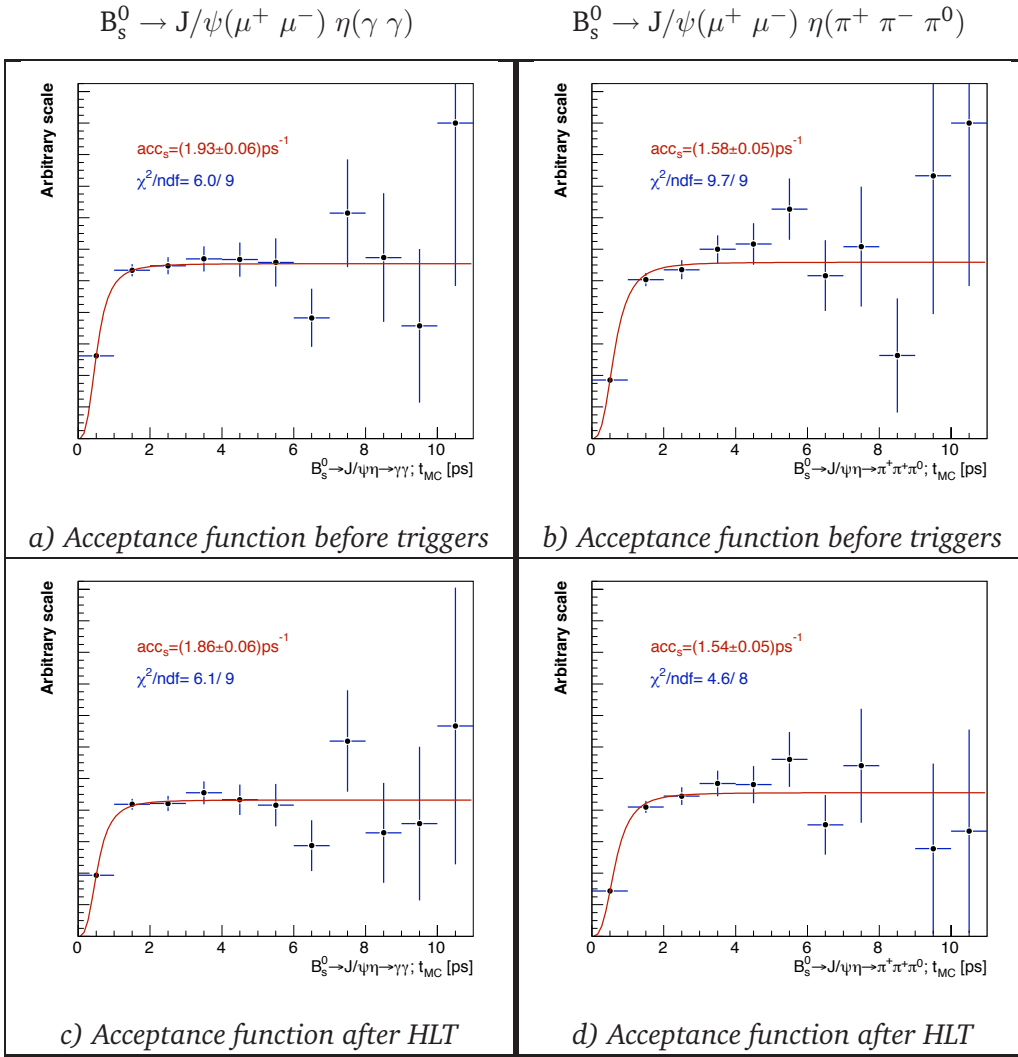
Figure 4.17: *Acceptance function fitted on the data ratio (biased over unbiased) before and after triggers (L0, L1 and HLT).*

The three levels of triggering slightly decrease the slope of the acceptance function, this means that the short live times are more strongly removed. However, the acc_s parameter remains almost unchanged within 1σ. The results are then $acc_s = (1.86 \pm 0.06)$ ps^{-1} for the decay in which the η radiatively decays, and $acc_s = (1.54 \pm 0.05)$ ps^{-1} for the other channel.

The difference in the acceptance for the two decay mode can be explained by the cuts on the flight distance FD, which are higher for the $B_s^0 \to J/\psi(\mu^+ \ \mu^-) \ \eta(\pi^+ \ \pi^- \ \pi^0)$ (see Tab. (4.2)).

4.5.4   Proper time errors and pulls

The errors on the proper time measurements and the corresponding pull[6] distributions are shown on Fig. (4.18). These errors are used in the sensitivity studies.

$$B_s^0 \rightarrow J/\psi(\mu^+ \ \mu^-) \ \eta(\gamma \ \gamma) \qquad\qquad B_s^0 \rightarrow J/\psi(\mu^+ \ \mu^-) \ \eta(\pi^+ \ \pi^- \ \pi^0)$$

a) Proper time measurement error σ_t

b) Proper time measurement error σ_t

c) Proper time pull distribution

d) Proper time pull distribution
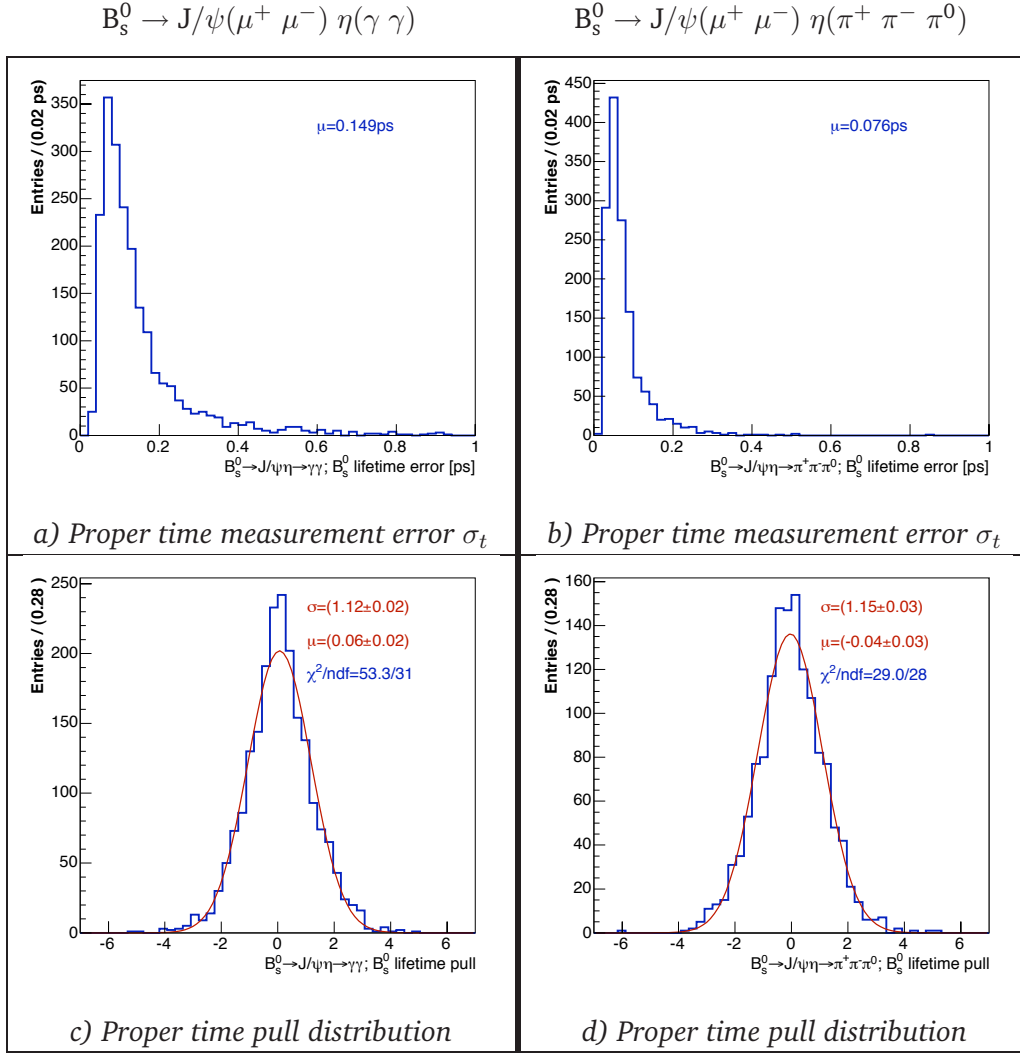
Figure 4.18: *Calculated error on the proper time and its pull distribution. The pull is fitted by a single Gaussian.*

The pull distributions are fitted with a single Gaussian and the results are $\sigma_{pull} = 1.12 \pm 0.02$ for the decay with photons and $\sigma_{pull} = 1.15 \pm 0.03$ for the "pion channel". Their means are both compatible with zero within 3σ. σ_{pull} are slightly larger than 1: this indicates that the errors on the proper time are under-estimated.

---

[6]The pull distribution of a variable x is the residual divided by its error: $(x_{rec} - x_{true})/\sigma_x$. It is used to check if the errors are estimated correctly. In this case, the result should be a Gaussian of mean zero and width unity.

4.6   Improvement of proper time resolution

The resolutions that we obtained for the B_s^0 proper time are not as good as channels in which the B_s^0 decays into charged particles. Two different methods have been applied trying to improve the proper time resolution: the first uses a mass constrained vertex fit on the η and the second a Kalman Filter fit.

4.6.1   Using a vertex mass constrained fit

To improve the mass resolution, we have performed a new vertex fit, constraining the η mass to its true value. As the mass is maintained fixed, the fitter will modify the momentum of the daughters particles (γ or π) to match the new requirements. The results on the mass, the proper time error and proper time resolution are shown on Fig. (4.19).

The η mass constrained vertex fit improves largely the mass and lifetime resolution of the $B_s^0 \to J/\psi(\mu^+\ \mu^-)\ \eta(\gamma\ \gamma)$ channel. The mass width decreases from $\sigma_{m(\eta)} = (52.6 \pm 1.3)$ MeV/c^2 to $\sigma_{m(\eta)} = (43.3 \pm 0.8)$ MeV/c^2 and the proper time resolution is improved from $\sigma_t = (120.8 \pm 3.2)$ fs to $\sigma_t = (47.1 \pm 1.2)$ fs. The pull distribution for the proper time has now a σ which is shrunk to $\sigma_{pull} = 1.05 \pm 0.02$.

There is no visible improvements on the B$_s^0$ mass for the "pion decay mode" with the constraint on the η mass. The lifetime resolution does improve, however, from $\sigma_t = (68.3 \pm 2.0)$ fs to $\sigma_t = (55.8 \pm 1.7)$ fs with the same pull distribution.

The same procedure has been repeated with a mass constrained vertex fit on the J/ψ candidates. In this case, there are no significant improvements: the mass resolution, for the $B_s^0 \to J/\psi(\mu^+\ \mu^-)\ \eta(\gamma\ \gamma)$, increases by ~ 3 MeV/c^2 but the proper time resolution decreases by ~ 3 ps. Therefore this second constraint on the J/ψ mass will not be applied to the selected data.

4.6.2   Using a Kalman Filter fit

The second way to improve the selection performances is based on a Kalman Filter method[7]. This tool refits the trajectories of charged particles to form vertices and then applies a mass constrained vertex fit to the decaying particles with a mass width less than 2 MeV/c^2 (which is the case of the J/ψ). The photon's parameters are then recovered from the calorimeter clusters and their four-momenta are inferred from the assumed produced vertex (the one of the other particles) and therefore will be correlated to this vertex position. The photon momenta are finally paired and added to the vertex. The final vertex position and momentum covariance matrices are calculated. A mass constrained vertex fit is also applied on the photon pair.

The results obtained with the Kalman Filter fit are by far the best obtained for these channels as shows Fig. (4.20). This method is the only one which takes advantages of the photons in the reconstruction of the B$_s^0$ candidates. The mass resolutions are $\sigma_{m(\eta)} = (33.6 \pm 0.7)$ MeV/c^2 for the $B_s^0 \to J/\psi\ \eta(\gamma\ \gamma)$ and $\sigma_{m(\eta)} = (20.0 \pm 0.7)$ MeV/c^2 for the channel with $\eta \to \pi^+\pi^-\pi^0$. No more biases are present in the mean value of the mass distribution which is a direct consequence of the η and the J/ψ mass constrained vertex fits.

---

[7]The Kalman Filter is an efficient recursive filter which estimates the state of a dynamic system from a series of incomplete and noisy measurements. An example of an application would be to provide accurate continuously-updated information about the position and velocity of an object given only a sequence of observations about its position, each of which includes some error.

$$B_s^0 \rightarrow J/\psi(\mu^+ \ \mu^-) \ \eta(\gamma \ \gamma) \qquad\qquad B_s^0 \rightarrow J/\psi(\mu^+ \ \mu^-) \ \eta(\pi^+ \ \pi^- \ \pi^0)$$

a) B_s^0 mass distribution b) B_s^0 mass distribution

c) B_s^0 proper time error d) B_s^0 proper time error

e) B_s^0 proper time resolution f) B_s^0 proper time resolution
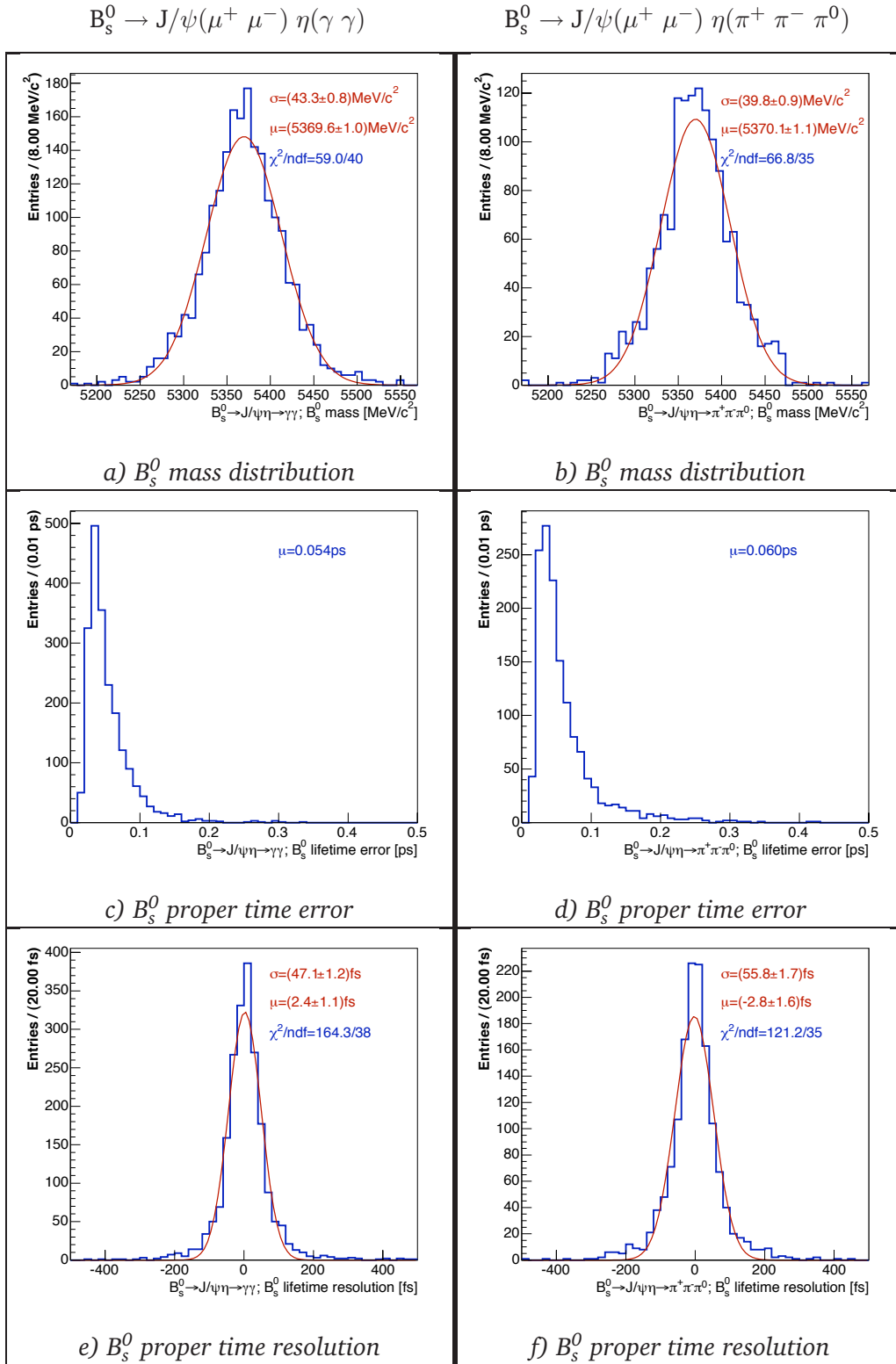
Figure 4.19: B_s^0 mass, proper time and lifetime resolution after η mass constrained vertex fit. The fits use single Gaussians.

$B_s^0 \rightarrow J/\psi(\mu^+\ \mu^-)\ \eta(\gamma\ \gamma)$ $B_s^0 \rightarrow J/\psi(\mu^+\ \mu^-)\ \eta(\pi^+\ \pi^-\ \pi^0)$

a) B_s^0 mass distribution

b) B_s^0 mass distribution

c) B_s^0 proper time error

d) B_s^0 proper time error

e) B_s^0 proper time resolution

f) B_s^0 proper time resolution
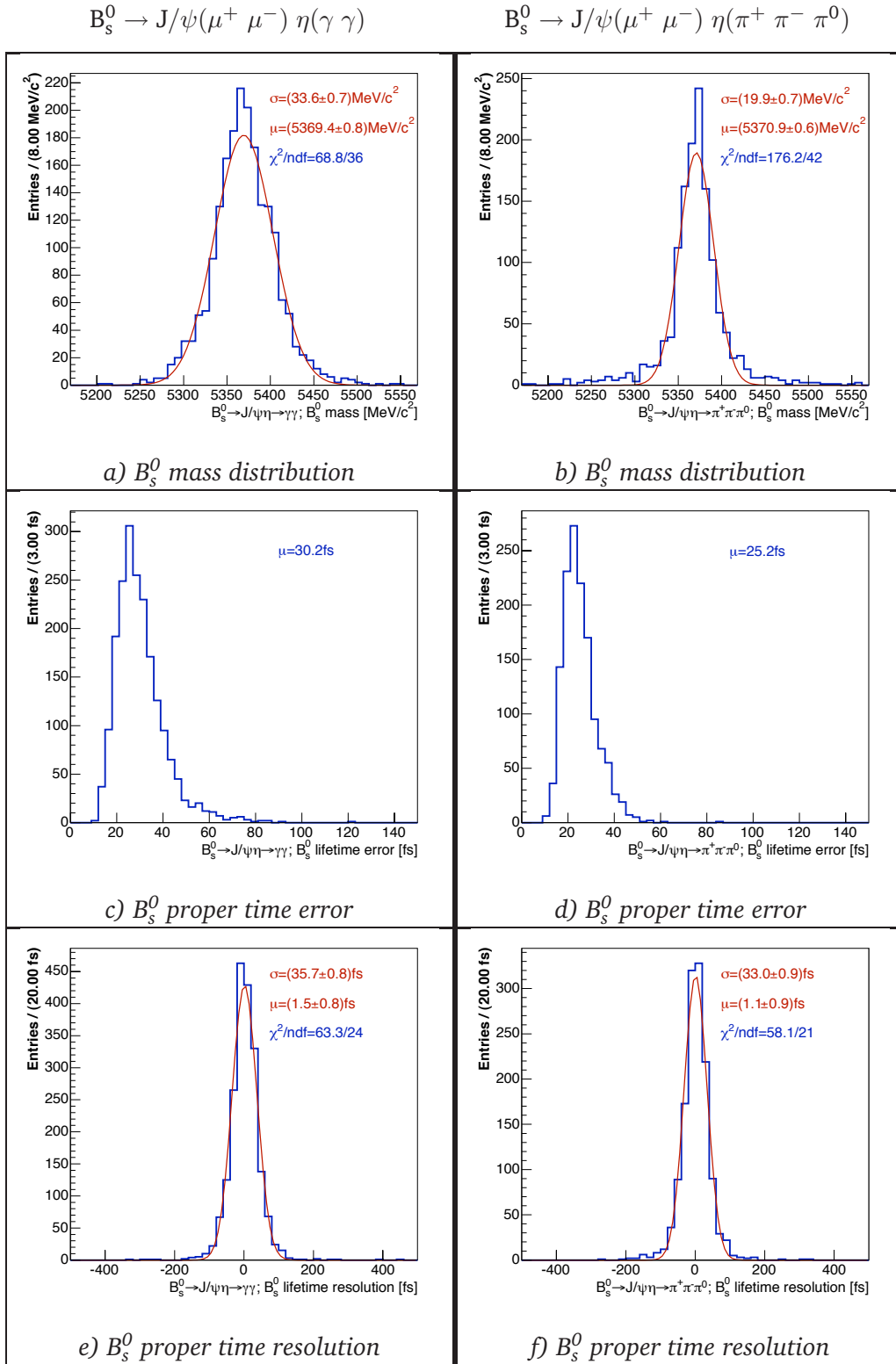
Figure 4.20: *B_s^0 mass, proper time and lifetime resolution after a Kalman Filter fit. The fits use single Gaussians.*

The errors on the B_s^0 proper time are much smaller than previously, as can be seen on Fig. (4.19) c) and d). These errors are small enough to resolve the fast $B_s^0 - \overline{B}_s^0$ oscillations.

The proper time resolution also is much lower: with this method we get $\sigma_t = (35.7 \pm 0.8)$fs for the "photon channel" and $\sigma_t = (32.9 \pm 0.9)$fs for the $B_s^0 \rightarrow J/\psi \; \eta(\pi^+ \; \pi^- \; \pi^0)$ decay mode. These large improvements are essentially due to the better estimation of the η or π^0 momenta which were the main source of proper time resolution degradation.

4.6.3 Comparison of the two methods

The pull distributions of the two fits described above are shown on Fig. (4.21). The width of the Gaussian fits are larger for the Kalman Filter fit (KF) than for the η mass constrained fit (EMC): $\sigma_{pull}^{KF} = 1.22 \pm 0.02$ compared to for $\sigma_{pull}^{EMC} = 1.05 \pm 0.02$ $\eta \rightarrow \gamma\gamma$ decay mode and $\sigma_{pull} = 1.32 \pm 0.03$ compared to $\sigma_{pull}^{EMC} = 1.15 \pm 0.03$ for $\eta \rightarrow \gamma\gamma$ channel.
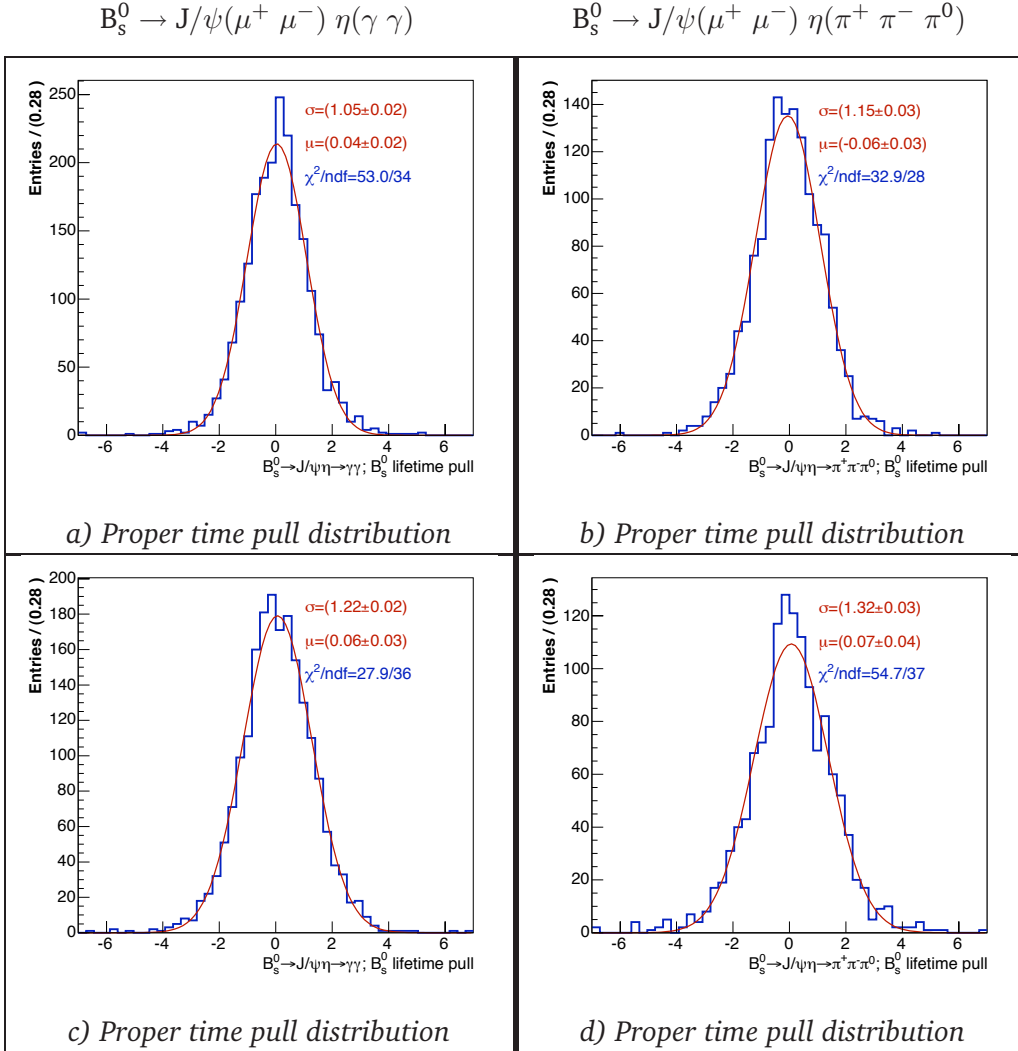
Figure 4.21: *Proper time pull distributions for the η mass vertex constrained fit above and the Kalman Filter fit below. The pulls are fitted by single Gaussians.*

The proper time resolution improvement of the KF fit for the $B_s^0 \rightarrow J/\psi \; \eta(\gamma \; \gamma)$ with

respect to the EMC fit is $\sim 24\%$. Nevertheless its errors given by the proper time pull width increases by $\sim 17\%$ when compared to the EMC fit. This cuts down drastically the benefit of the Kalman Filter. This effect is less important for the $\eta \to \pi^+\pi^-\pi^0$ channel where the enhancement of $\sim 41\%$ for the proper time resolution is reduced by 18%.

However these two fits show large improvements in the mass resolution, proper time error distribution and lifetime resolution. The KF fit gives better results but the pull distributions need to be understood. For the study of the physics performances of the LHCb experiment to the weak mixing phase ϕ_s, the Kalman Filter fit results will be used with a correction factor taking the pull width into account (see Chapter (5)).

4.7 Efficiencies and annual signal yields

In this section are presented the selection and rejection efficiencies as well as the annual signal yield at $2\,\mathrm{fb}^{-1}$ and the background-over-signal ratio. All these studies are performed after the tight selection. The errors on the efficiencies have been calculated with the assumption that the numerator is a subset of the denominator. Also, as discussed in Section (3.7.2), these estimations are performed with the numbers of independent events.

4.7.1 Efficiencies

The final numbers for the reconstruction and the offline selection of the $B_s^0 \to J/\psi\,\eta$ decay channels are listed in Tab. (4.4). The following definitions apply to the generated events:

 - N_{gen}: total number of generated MC signal events (i.e. the number of events on tape) used for the analysis;

 - $N_{'ible}$: number of reconstructible events with long tracks and neutrals (see Section (3.2.4));

 - $N_{'ed}$: number of reconstructed events (see Section (3.2.4));

 - $N_{'ible\&'ed}$: number of events that are both reconstructible and reconstructed;

while the definitions concerning the off-line selected events are:

 - N_{sel}: number of events surviving the tight selection cuts;

 - N_{trg}: number of off-line selected events passing the L0, L1 and HLT triggers;

 - N_{tag}: number of off-line selected tagged events passing L0, L1 and HLT.

$B_s^0 \to J/\psi\,\eta$	N_{gen}	$N_{'ible}$	$N_{'ed}$	$N_{'ible\&'ed}$	N_{sel}	N_{trg}	N_{tag}
$\eta \to \gamma\gamma$	139'500	25'590	34'484	21'907	2'084	1'595	995
$\eta \to \pi^+\pi^-\pi^0$	171'000	26'109	27'635	19'718	1'486	1'183	728

Table 4.4: *Reconstruction and offline-selection numbers for the studied decays.*

The total signal efficiency, ε_{tot}, is the fraction of generated MC signal events containing a signal B decay that are triggered, reconstructed and selected with the offline tight cuts for physics analysis. ε_{tot} can be written as the product of several contributions:

$$\varepsilon_{tot} = \varepsilon_{det} \times \varepsilon_{rec/det} \times \varepsilon_{sel/rec} \times \varepsilon_{trg/sel},$$

where:

- $\varepsilon_{det} = \dfrac{\varepsilon_{off}}{\varepsilon_{rec/det}\varepsilon_{sel/rec}}$ is the detection efficiency which includes the result of a cut of 400 mrad on the polar angle of the b-hadron done at the generator level and the selection of reconstructible events;

- $\varepsilon_{off} = \dfrac{N_{sel}}{N_{gen}}\varepsilon_{gen}^{signal}$ is the total offline selection efficiency on the detected events;

- $\varepsilon_{gen}^{signal}$ is the 400 mrad cut efficiency defined in Section (3.7.1);

- $\varepsilon_{rec/det} = \dfrac{N_{,ible\&'ed}}{N_{,ible}}$ is the reconstruction efficiency on the detected events;

- $\varepsilon_{sel/rec} = \dfrac{N_{sel}}{N_{,ed}}$ is the efficiency on the off-line selection of the reconstructed events;

- $\varepsilon_{trg/sel} = \dfrac{N_{trg}}{N_{sel}}$ is the combined L0, L1 and HLT trigger efficiency on the off-line selected events.

All the above efficiencies are shown in Tab. (4.5). The total efficiency is ~ 1.7 larger for the channel with photons. This can be explained by the better detection and reconstruction efficiency of this channel. When the final state multiplicity is larger as for $B_s^0 \to J/\psi(\mu^+\,\mu^-)\,\eta(\pi^+\,\pi^-\,\pi^0)$, the probability to have all the particles in the acceptance and reconstructed is lower. The selection efficiency for $\eta \to \pi^+\pi^-\pi^0$ is lower compared to $\eta \to \gamma\gamma$ because of the larger number of final states and the additional cuts on the charged pions from the η. On the other hand, the selected $\eta \to \pi^+\pi^-\pi^0$ events are cleaner and have a better trigger efficiency (especially the L1-trigger efficiency).

$B_s^0 \to J/\psi\,\eta$	Factors (in %) forming ε_{tot} (in %)				
	$\varepsilon_{tot} = \varepsilon_{det} \times \varepsilon_{rec/det} \times \varepsilon_{sel/rec} \times \varepsilon_{trg/sel}$				
	ε_{det}	$\varepsilon_{rec/det}$	$\varepsilon_{sel/rec}$	$\varepsilon_{trg/sel}$	ε_{tot}
$\eta \to \gamma\gamma$	10.02 ± 0.30	85.6 ± 0.2	6.04 ± 0.13	76.5 ± 0.9	0.396 ± 0.013
$\eta \to \pi^+\pi^-\pi^0$	7.41 ± 0.26	75.5 ± 0.3	5.38 ± 0.14	79.6 ± 1.0	0.240 ± 0.009

Table 4.5: *Summary of the signal efficiencies for the DC04 $B_s^0 \to J/\psi\,\eta$ data.*

4.7.2 Trigger performances

For completeness, we separate in Tab. (4.6) the L0, L1 and HLT contributions to the N_{trg} and $\varepsilon_{trg/sel}$, where:

- N_{L0}: Number of off-line selected events passing the L0 trigger;

- N_{L1}: Number of off-line selected events passing the L0 and L1 trigger;

- N_{HLT}: Number of off-line selected events passing the L0, L1 and HLT trigger;

- $\varepsilon_{L0/sel}$ is the L0 efficiency on the off-line selected events;

- $\varepsilon_{L1/L0}$ is the L1 efficiency on the off-line selected events surviving L0;

$B_s^0 \to J/\psi \, \eta$	N_{sel}	N_{L0}	N_{L1}	N_{HLT}	$\varepsilon_{L0/sel}$	$\varepsilon_{L1/L0}$	$\varepsilon_{HLT/L1}$
$\eta \to \gamma\gamma$	2'084	2'022	1'749	1'595	97.0 ± 0.4	86.5 ± 0.8	91.2 ± 0.7
$\eta \to \pi^+\pi^-\pi^0$	1'486	1'403	1'312	1'183	94.4 ± 0.6	93.5 ± 0.7	90.2 ± 0.8

Table 4.6: *Trigger contributions and efficiencies for the studied decays.*

  − $\varepsilon_{HLT/L1}$ is the HLT efficiency on the off-line selected events surviving L0 and L1.

In Tab. (4.7) can be found the number of L1 selected events, with respect to the six trigger lines (see Section (2.5.3)). There is an overlap in the total sum of the lines as several lines can be confirmed for the same event.

In Tab. (4.8) is summarized the results for the four streams of the High Level Trigger (see Section (2.5.4)). Overlap is also present in this scheme.

L1 line	$B_s^0 \to J/\psi \, \eta$	
	$\eta \to \gamma\gamma$	$\eta \to \pi^+\pi^-\pi^0$
Generic (P_T)	1403	1193
Single-muon	1084	753
Dimuon general	411	256
Dimuon J/ψ	921	675
Electron	250	54
Photon	423	39
L1-Decision	1749	1312

Table 4.7: *L1 trigger lines selection.*

HLT Stream	$B_s^0 \to J/\psi \, \eta$	
	$\eta \to \gamma\gamma$	$\eta \to \pi^+\pi^-\pi^0$
HLT-Generic	1692	1284
Inclusive B	1117	813
Exclusive B	1244	1012
Dimuon	1365	1009
D*	4	16
HLT-Decision	1595	1183

Table 4.8: *HLT streams selection.*

4.7.3 Tagging performances

In the Tab. (4.10) are shown the tagging performances for both decay modes. The tagging efficiency, the wrong tag fraction and the effective combined tagging efficiency (see Section (3.3)) are given before any trigger, after L0 and after L0 and L1.

The performances calculated after triggers are $\varepsilon_{tag} = (62.7\pm1.2)\%$, $\omega_{tag} = (35.2\pm1.5)\%$ and $\varepsilon_{eff} = (5.5 \pm 1.4)\%$ for the "photon decay" and $\varepsilon_{tag} = (62.1 \pm 1.4)\%$, $\omega_{tag} = (30.4 \pm 1.7)\%$ and $\varepsilon_{eff} = (9.5\pm2.1)\%$ for the other decay mode. The wrong tag fraction is smaller for the "pion channel" which can be explained by the low selection and reconstruction efficiency of this channel: only very clean events are reconstructed and selected, which are certainly easier to tag.

The tagging performances for the B_s^0 candidates, after triggers, are detailed in Tab. (4.10), with respect to four tagging categories: the lepton charge, the opposite sign kaon, the same sign kaon and the vertex charge. More than one tag can be set for one event and this explains the possible overlaps.

4.7.4 Untagged signal yields

The 2 fb^{-1} untagged signal yield ($N_{phys}^{2\text{fb}^{-1}}$) is the number of selected, reconstructed and triggered events (without tagging). It can be calculated with the number of event pro-

		$B_s^0 \to J/\psi(\mu^+ \mu^-) \eta(\gamma \gamma)$			
		Before triggers	After L0	After L0&L1	After L0&L1&HLT
ε_{tag}	[%]	59.6 ± 1.1	60.4 ± 1.1	62.6 ± 1.2	62.7 ± 1.2
ω_{tag}	[%]	34.5 ± 1.4	34.7 ± 1.4	35.0 ± 1.5	35.2 ± 1.5
ε_{eff}	[%]	5.7 ± 1.3	5.6 ± 1.3	5.7 ± 1.4	5.5 ± 1.4

		$B_s^0 \to J/\psi(\mu^+ \mu^-) \eta(\pi^+ \pi^- \pi^0)$			
		Before triggers	After L0	After L0&L1	After L0&L1&HLT
ε_{tag}	[%]	60.8 ± 1.2	61.1 ± 1.3	61.1 ± 1.3	62.1 ± 1.4
ω_{tag}	[%]	31.3 ± 1.5	31.4 ± 1.6	31.3 ± 1.6	30.4 ± 1.7
ε_{eff}	[%]	8.5 ± 1.8	8.5 ± 1.9	8.6 ± 1.9	9.5 ± 2.1

Table 4.9: *Tagging efficiency, wrong tag fraction and effective combined tagging efficiency before triggers, after L0 and after L0 and L1.*

Tagging categories	$B_s^0 \to J/\psi \eta$					
	$\eta \to \gamma\gamma$			$\eta \to \pi^+\pi^-\pi^0$		
	ε_{tag} [%]	ω_{tag} [%]	ε_{eff} [%]	ε_{tag} [%]	ω_{tag} [%]	ε_{eff} [%]
Lepton charge	10.4 ± 0.8	49.1 ± 3.9	0.0 ± 0.0	8.7 ± 0.8	32.1 ± 4.4	1.1 ± 0.6
Opposite sign K	29.7 ± 1.1	42.9 ± 2.3	0.6 ± 0.4	28.0 ± 1.3	36.8 ± 2.5	2.0 ± 0.8
Same sign K	31.2 ± 1.2	33.5 ± 2.1	3.4 ± 0.9	32.6 ± 1.3	31.0 ± 2.3	4.7 ± 1.1
Vertex charge	23.6 ± 1.1	46.2 ± 2.6	0.1 ± 0.2	26.2 ± 1.2	41.4 ± 2.7	0.8 ± 0.5
Total	62.7 ± 1.2	35.2 ± 1.5	5.5 ± 1.4	62.1 ± 1.4	30.4 ± 1.7	9.5 ± 2.1

Table 4.10: *Tagging performances for the four categories, after triggers.*

duced per 2 fb^{-1} (see Tab. (3.5)) multiplied by the total efficiency (ε_{tot}): $N_{phys}^{2\text{fb}^{-1}} = N_{B_s^0 \to J/\psi \ \eta}^{2\text{fb}^{-1}} \times \varepsilon_{tot}$. The yields are given in Tab. (4.11).

Decay	$N_{phys}^{2\text{fb}^{-1}}$ [10^3]	
	$\theta_p = -20°$	$\theta_p = -10°$
$B_s^0 \to J/\psi(\mu^+ \mu^-) \eta(\gamma \gamma)$	7.1 ± 3.2	10.7 ± 4.8
$B_s^0 \to J/\psi(\mu^+ \mu^-) \eta(\pi^+ \pi^- \pi^0)$	2.4 ± 1.1	3.8 ± 1.7

Table 4.11: *Untagged signal yields for 2 fb^{-1}.*

The expected yields for the two decay modes, after one year of data taking at 2 fb^{-1}, is in the interval [7.1k, 10.7k] for the "photon channel" and [2.4k, 3.8k] for the $B_s^0 \to J/\psi(\mu^+ \mu^-) \eta(\pi^+ \pi^- \pi^0)$ channel, depending on the mixing angle of η.

4.8 Background contributions

The three different backgrounds which can deteriorate the selected signal (see Section (3.6.3)) have been passed through the selection criteria used for the two channels under study. Tab. (4.12) summarizes the number of the processed events as well as the number

of events which pass the selection criteria, before and after all the triggers. One important fact to mention is that all the events selected here belongs to the same category, i.e. $H_b \to J/\psi$ X. Every time a non-signal event is selected, it has at least a J/ψ which comes directly from a b-hadron and which is correctly reconstructed (with respect to the MC "truth").

$B_s^0 \to J/\psi\,\eta$	$\eta \to \gamma\gamma$			$\eta \to \pi^+\pi^-\pi^0$		
	N_{gen}	N_{sel}	N_{HLT}	N_{gen}	N_{sel}	N_{HLT}
inclusive $b\bar{b}$	30'500'000	16	14	27'500'00	3	3
$\to$ inclusive $b\bar{b}$ v1	10'500'000	0	0	10'500'00	0	0
$\to$ inclusive $b\bar{b}$ v2	20'000'000	16	14	17'000'00	3	3
$B_d^0 \to J/\psi(\mu^+\,\mu^-)\,K^*(K^+\,\pi^-)$	641'000	25	19	633'000	23	17
$B_d^0 \to J/\psi(\mu^+\,\mu^-)\,K_S^0(\pi^+\,\pi^-)$	89'000	3	3	89'000	0	0
$B^+ \to J/\psi(\mu^+\,\mu^-)\,K^+$	200'000	3	3	200'000	0	0
$B_s^0 \to J/\psi(\mu^+\,\mu^-)\,\phi(K^+\,K^-)$	366'000	10	8	394'000	121	100
$B_s^0 \to J/\psi(\mu^+\,\mu^-)\,\eta'(\pi^+\,\pi^-\,\eta)$	100'000	2	2	100'000	6	6
$\Lambda_b^0 \to J/\psi\,\Lambda$	100'000	6	0	100'000	0	0
inclusive J/ψ	1'800'000	6	3	1'700'000	1	0
$\to H_b \to J/\psi$ X	128'000	6	3	121'000	1	0
$\to$ prompt J/ψ	1'672'000	0	0	1'579'000	0	0

Table 4.12: *Number of events surviving the tight selection for the three types of background events (see Section (3.6.3)). The mass window has been increased by a factor six for the selection on $b\bar{b}$ events.*

An important point to notice is that in the $b\bar{b}$ "v1" sample, not a single event passes the tight selection cuts which is not the case for the "v2" data sample. This is a consequence of the fine tuning of the selection criteria on the $b\bar{b}$ "v1" data which introduces biases while the second sample is unbiased.

4.8.1 Inclusive $b\bar{b}$ background levels

The inclusive $b\bar{b}$ background contribution can be estimated with the following formula:

$$\left(\frac{B}{S}\right)_{signal}^{b\bar{b}} = \frac{\varepsilon_{gen}^{b\bar{b}}}{\varepsilon_{gen}^{signal}} \frac{1}{2 \cdot f_{B_s^0} \cdot \mathcal{BR}_{vis}^{signal}} \frac{N_{sel}^{b\bar{b}}/N_{gen}^{b\bar{b}}}{N_{sel}^{signal}/N_{gen}^{signal}}, \qquad (4.5)$$

where:

- $\varepsilon_{gen}^{b\bar{b}} = 43.21\%$ is the 400 mrad acceptance cut for the $b\bar{b}$ events (Section (3.7.1));

- $\varepsilon_{gen}^{signal} = 34.71\%$ is the 400 mrad acceptance cut for the signal events (Section (3.7.1));

- $f_{B_s^0}$ is the $b\bar{b}$ hadronization factor for B_s^0 production (see Tab. (3.3)),

- $\mathcal{BR}_{vis}^{signal}$ are the $B_s^0 \to J/\psi\,\eta$ visible branching ratios as given in Tab. (3.4);

- $N_{sel}^{b\bar{b}}$ is the number of background events passing the tight cuts but in the loose B_s^0 mass window of ± 600 MeV/c^2 (Tab. (4.12));

- $N_{gen}^{b\overline{b}}$ is the number of background events analyzed, "v1"+"v2" (Tab. (4.12));

- N_{sel}^{signal} is the number of signal events selected (Tab. (4.3));

- N_{gen}^{signal} is the number of signal events analyzed (Tab. (4.3)).

When the number of selected background event $N_{sel}^{b\overline{b}}$ is very small (less than 10), it is not possible to use the background-over-signal ratio of Eq. (4.5) to estimate the expected background level after the selection. This problem can be overcome by using the unified approach of Feldman and Cousins [94] which gives the unified confidence intervals $[\nu_1, \nu_2]$ for the mean of a Poisson variable given n observed events in the absence of background, for different confidence level values.

Because of the low statistics, the estimation of $N_{sel}^{b\overline{b}}$ is performed with the background events passing a B_s^0 wider mass window. Assuming that the $b\overline{b}$ background is uniformly distributed in this window, we simply multiply the 90% confidence level interval by the ratio of the two mass windows[8].

As the only background contribution comes from $H_b \rightarrow J/\psi$ X events, another correction factor has to be applied to account for an over-estimation of the $H_b \rightarrow J/\psi$ X production in the simulation [51] with respect to the experimental values [14]. This factor is $f_{prod}^{H_b \rightarrow J/\psi\ X} = 0.60 \pm 0.22$.

Decays	$\theta_p = -20°$		$\theta_p = -10°$	
	No trigger	HLT	No trigger	HLT
$B_s^0 \rightarrow J/\psi(\mu^+\ \mu^-)\ \eta(\gamma\ \gamma)$	2.6±1.3	3.0±1.5	1.7±0.9	2.0±1.0
$B_s^0 \rightarrow J/\psi(\mu^+\ \mu^-)\ \eta(\pi^+\ \pi^-\ \pi^0)$	[0.6, 3.9]	[0.7, 4.9]	[0.4, 2.6]	[0.5, 3.2]

Table 4.13: *Central value and 90% confidence level interval of the $b\overline{b}$ background to signal level, before and after all triggers.*

The B/S results for the inclusive $b\overline{b}$ are given in Tab. (4.13). The central values are 2.6 ± 1.3 before triggers and 3.0 ± 1.5 after triggers for $\theta_p = -20°$. These numbers are quite large and are due to the high multiplicity of the photons.

The "pion channel", with a smaller production yield, has a 90% CL upper limit of 3.9 before any triggers and 4.9 after the HLT for the same η mixing angle. For this decay mode, the background rejection is better thanks to the charged pions in the final state, but the low selection efficiency and its poor branching fraction render the selection difficult.

As the branching fractions are larger for $\theta_p = -10°$, the background levels are of course reduced.

The triggers should act in the same manner on the signal and on the background events, as they have the same topology due to the selection cuts. The triggers'effect is to reduce the statistics which reflects on the background-over-signal ratios. Therefore only the numbers quoted before triggers will be considered for the selection performances.

---

[8]The ratio of the two different mass windows is 1/6: 100 MeV/c^2 for the signal and 600 MeV/c^2 for the background.

4.8.2   Backgrounds from Specific b-hadron decays

The background contributions due to specific $H_b \to J/\psi$ X channels, detailed in Section (3.6.3), are calculated with:

$$\left(\frac{B}{S}\right)^{spec.}_{signal} = \frac{f_B}{f_{B_s^0}} \frac{\mathcal{BR}^{spec.}_{\text{vis}}}{\mathcal{BR}^{signal}_{\text{vis}}} \frac{N^{spec.}_{sel}/N^{spec.}_{gen}}{N^{signal}_{sel}/N^{signal}_{gen}}, \tag{4.6}$$

with the following definitions:

 - f_B is the b$\overline{\text{b}}$ hadronization factor for H_b production (see Tab. (3.3));

 - $\mathcal{BR}^{spec.}_{vis}$ are the $H_b \to J/\psi$ X visible branching ratios as given in Tab. (3.6);

 - $N^{spec.}_{sel}$ is the number of background events surviving the tight cuts (see Tab. (4.12));

 - $N^{spec.}_{gen}$ is the number of background events analyzed (Tab. (4.12)).

Most of these decays have a non negligible contribution to the background-over-signal ratio. For instance, the most dangerous channel for the $B_s^0 \to J/\psi\ \eta(\gamma\ \gamma)$ decay mode is the $B_d^0 \to J/\psi(\mu^+\ \mu^-)\ K^*(K^+\ \pi^-)$ which gives a B/S of 0.07±0.03 before triggers for the $\theta_p = -20°$. For the $B_s^0 \to J/\psi\ \eta(\pi^+\ \pi^-\ \pi^0)$ channel, the most polluting contribution is the $B_s^0 \to J/\psi(\mu^+\ \mu^-)\ \phi(K^+\ K^-)$: the B/S ratio is up to 0.23±0.13 before triggers and for $\theta_p = -20°$.

The detailed results of the background-over-signal ratios on these specific background channels can be found in Appendix (B).

4.8.3   Inclusive $H_b \to J/\psi$ X background studies

The previous sections show that this type of events can deteriorate our signal and, as already mentioned, is the only contribution to our background. Therefore, inclusive J/ψ events have been used to check our B/S estimations. In the inclusive J/ψ sample, $(7.1 \pm 2.5)\%$ of the events come from $H_b \to J/\psi$ X and the other $(92.9 \pm 2.5)\%$ are prompt J/ψ, which will be analyzed in next section. We have therefore used $128'000 \pm 45'000$ $H_b \to J/\psi$ X events with the $B_s^0 \to J/\psi\ \eta(\gamma\ \gamma)$ decay channel and $121'000 \pm 43'000$ $H_b \to J/\psi$ X events with the $B_s^0 \to J/\psi\ \eta(\pi^+\ \pi^-\ \pi^0)$ channel (see Tab. (4.12)). The B/S ratio can be estimated with:

$$\left(\frac{B}{S}\right)^{H_b \to J/\psi\ X}_{signal} = \frac{\varepsilon^{incl.\ J/\psi}_{gen}}{\varepsilon^{signal}_{gen}} \frac{f_{incl.\ J/\psi}}{f_{B_s^0}} \frac{\mathcal{BR}^{J/\psi \to \mu^+\ \mu^-}_{\text{vis}}}{\mathcal{BR}^{signal}_{\text{vis}}} \frac{N^{H_b \to J/\psi\ X}_{sel}/N^{H_b \to J/\psi\ X}_{gen}}{N^{signal}_{sel}/N^{signal}_{gen}}, \tag{4.7}$$

with the following definitions:

 - $\varepsilon^{incl.\ J/\psi}_{gen} = 39.9\%$ is the 400 mrad requirement acceptance for the inclusive J/ψ events (Section (3.7.1));

 - $f_{incl.\ J/\psi}$ is the fraction of b-hadrons decaying into a J/ψ and anything else (see Section (3.6.3));

 - $\mathcal{BR}^{J/\psi \to \mu^+\ \mu^-}_{vis}$ is the $J/\psi \to \mu^+\ \mu^-$ visible branching ratio as given in Tab. (3.4);

 - $N^{H_b \to J/\psi\ X}_{sel}$ is the number of background events surviving the tight selection cuts (see Tab. (4.12));

Decays	$\theta_p = -20°$		$\theta_p = -10°$	
	No trigger	HLT	No trigger	HLT
$B_s^0 \to J/\psi(\mu^+ \ \mu^-) \ \eta(\gamma \ \gamma)$	[1.2, 6.3]	[0.8, 5.4]	[0.8, 4.1]	[0.5, 3.5]
$B_s^0 \to J/\psi(\mu^+ \ \mu^-) \ \eta(\pi^+ \ \pi^- \ \pi^0)$	[0.2, 7.6]	[0, 5.3]	[0.1, 5.0]	[0, 3.5]

Table 4.14: *90% confidence level interval of the $H_b \to J/\psi$ X background level, before and after all triggers.*

$-$ $N_{gen}^{H_b \to J/\psi \ X}$ is the number of background events analyzed (Tab. (4.12)).

With our tight cuts, it is more likely that the only background events to survive are the ones from the $H_b \to J/\psi$ X decays. One cannot add the contributions of $b\overline{b}$ and $H_b \to J/\psi$ X, the latter being a sub-sample of the previous. The central values and 90% confidence level are in agreement. The $B_s^0 \to J/\psi \ \eta(\gamma \ \gamma)$ channel, is a noisy channel because of the γ. This is not the case of the $B_s^0 \to J/\psi \ \eta(\pi^+ \ \pi^- \ \pi^0)$ decay mode which calls for more statistics to refine the B/S estimations.

Further studies should be done to eventually remove a part of this background using adequate "vetoes", i.e. removing events which have been selected for another study as $B_d^0 \to J/\psi(\mu^+ \ \mu^-) \ K^*(K^+ \ \pi^-)$, which is the most polluting one.

The B/S estimations performed with the $b\overline{b}$ events are more precise than the ones with the $H_b \to J/\psi$ X due to higher statistics. As the second category belongs to the inclusive $b\overline{b}$ one, we will use the numbers of Tab. (4.13) to quote the background-to-noise ratio of this channel.

4.8.4 Prompt J/ψ contribution

The prompt J/ψ has a large production yield (see Section 3.6.3) and requires a high statistics study to have an accurate estimation of its B/S contribution. However, not a single event survives the selection cuts for both decay modes. In Appendix (B), a table summarizes the corresponding B/S 90% confidence level interval. We think that this background will not be a problem for the two channels of interest, thanks to the large flight distance and impact parameter cuts. Therefore we will not consider at this stage this improbable background contribution.

4.9   Selection summary

This chapter presents the reconstruction and selection of the $B_s^0 \rightarrow J/\psi(\mu^+\ \mu^-)\ \eta(\gamma\ \gamma)$ and the $B_s^0 \rightarrow J/\psi(\mu^+\ \mu^-)\ \eta(\pi^+\ \pi^-\ \pi^0)$ decay channels (preliminary results of the $B_s^0 \rightarrow J/\psi(e^+\ e^-)\ \eta(\gamma\ \gamma)$ decay are presented in Appendix (C)). The efficiencies, yields and B/S are summarized in Tab. (4.15). The different resolutions, acceptance and tagging efficiencies of this analysis are finally given.

$B_s^0 \rightarrow J/\psi\ \eta$	θ_P	Factors (in %) forming ε_{tot} (in %)					Assumed visible BR (in 10^{-6})	Annual signal yield	B/S ratio from incl. $b\bar{b}$ bkg
		ε_{det} ·	$\varepsilon_{rec/det}$ ·	$\varepsilon_{sel/rec}$ ·	$\varepsilon_{trg/sel}$ =	ε_{tot}			
		ε_{det}	$\varepsilon_{rec/det}$	$\varepsilon_{sel/rec}$	$\varepsilon_{trg/sel}$	ε_{tot}			
$\eta \rightarrow \gamma\gamma$	$(-20°)$ $(-10°)$	10.0	85.6	6.04	76.5	0.396	8.3 12.8	7.1 k 10.7 k	2.6 1.7
$\eta \rightarrow$ $\pi^+\pi^-\pi^0$	$(-20°)$ $(-10°)$	7.41	75.5	5.38	79.6	0.240	4.7 7.3	2.4 k 3.8 k	< 3.9 < 2.6

Table 4.15: *Results of the $B_s^0 \rightarrow J/\psi\ \eta$ reconstruction for both η decay modes into two photons and three pions.*

$B_s^0 \rightarrow J/\psi(\mu^+\ \mu^-)\ \eta(\gamma\ \gamma)$

- J/ψ mass resolution: $\sigma_{m(J/\psi)} = (11.3 \pm 0.3)$ MeV/c^2;

- η mass resolution: $\sigma_{m(\eta)} = (16.0 \pm 0.3)$ MeV/c^2;

- B_s^0 mass resolution after Kalman Filter fit: $\sigma_{m(B_s^0)} = (33.6 \pm 0.7)$ MeV/c^2;

- Proper time resolution after Kalman Filter fit: $\sigma_t = (35.7 \pm 0.8)$ fs;

- Acceptance slope after triggers: $acc_s = (1.86 \pm 0.06)$ ps^{-1};

- Tagging efficiencies after triggers: $\varepsilon_{tag} = (62.7 \pm 1.2)\%, \quad \omega_{tag} = (35.2 \pm 1.5)\%$.

$B_s^0 \rightarrow J/\psi(\mu^+\ \mu^-)\ \eta(\pi^+\ \pi^-\ \pi^0)$

- J/ψ mass resolution: $\sigma_{m(J/\psi)} = (11.2 \pm 0.3)$ MeV/c^2;

- η mass resolution: $\sigma_{m(\eta)} = (12.7 \pm 0.4)$ MeV/c^2;

- B_s^0 mass resolution after Kalman Filter fit: $\sigma_{m(B_s^0)} = (20.0 \pm 0.7)$ MeV/c^2;

- Proper time resolution after Kalman Filter fit: $\sigma_t = (32.9 \pm 0.9)$ fs;

- Acceptance slope after triggers: $acc_s = (1.54 \pm 0.05)$ ps^{-1};

- Tagging efficiencies after triggers: $\varepsilon_{tag} = (62.1 \pm 1.4)\%, \quad \omega_{tag} = (30.4 \pm 1.7)\%$.

The selection efficiency $\varepsilon_{sel/rec}$ is low but acceptable given the high background rejection that is required. The dominant background contributions should come from $b\bar{b}$ events and more specifically from $H_b \rightarrow J/\psi$ X. This channel suffers also from the bad momentum resolutions of the neutral particles which results in a wide mass and a large lifetime resolution.

Could the $B_s^0 \rightarrow J/\psi\ \eta$ channels contribute to the sensitivity studies of ϕ_s as a pure CP eigenstate ? This question will be answered in the next chapter.

Chapter 5

LHCb sensitivity to the B_s^0 physics parameters
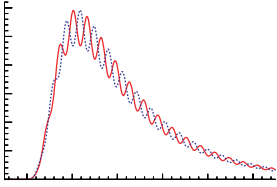
In this chapter we discuss how to extract the relevant CP violation parameters from CP eigenstates $\bar{b} \to \bar{c}c\bar{s}$ quark transition decays and to determine the sensitivity that can be achieved. The performances are then estimated with toy Monte Carlo. Finally the contribution of the pure CP eigenstates channels are compared to the $B_s^0 \to J/\psi\,\phi$ channel.

$\mathcal{I}$N this section, we will present the method to determine the sensitivity of our experiment to the B_s^0 mixing phase ϕ_s. As stated in Chapter (1), the decay $B_s^0 \to J/\psi\,\eta$ proceeds through a tree diagram with $\bar{b} \to \bar{c}c\bar{s}$ quark transition and a CP asymmetry results from the interference between the $B_s^0 - \overline{B}_s^0$ mixing and their decay. In our case where the final state ($J/\psi\,\eta$) is a pure CP eigenstate, one has direct access to the mixing phase via:

$$A_{\mathrm{CP}}(t) = \frac{-\eta_{f_{\mathrm{CP}}}\sin\left(\phi_s\right)\sin\left(\Delta \mathrm{m}_s t\right)}{\cosh\left(\frac{\Delta \Gamma_s t}{2}\right) - \eta_{f_{\mathrm{CP}}}\cos\left(\phi_s\right)\sinh\left(\frac{\Delta \Gamma_s t}{2}\right)}.$$

The channel that we have presented in the previous chapters will be used for this study together with $B_s^0 \to \eta_c\,\phi$, which is a pure CP eigenstate as well. The "golden channel" $B_s^0 \to J/\psi\,\phi$ which is an admixture of CP eigenstates is also studied. In addition, a control channel for which no CP asymmetry is expected must be used and the result of the analysis on this channel be checked; we will use the $B_s^0 \to D_s\,\pi$ decay.

5.1   Outline of the method to extract ϕ_s

The number of events that one can generate in a full Monte Carlo simulation is quite low (due to CPU and storage limitations) and will not allow to determine the sensitivity of the experiment to the physics parameters we are looking for. We therefore use a *toy*

---

[1]This chapter as well as the toys extracting the sensitivities to the physics parameters are inspired by [84] and are the product of a fruitful collaboration with L. Fernández.

Monte Carlo[2] which simulates the results of around 250 "experiments" with a statistics corresponding to 2 fb^{-1} per experiment. The resolutions, purity (i.e. Background/Signal ratio) and acceptance of LHCb are deduced from the full simulation.

For each of the events, the mass of the B_s^0, its proper time and the "transversity angle" for the channel $B_s^0 \rightarrow J/\psi \ \phi$ are generated. The event is fitted according to a likelihood function which includes the physical parameters that we want to determine as free parameters. The events are grouped in so-called "experiments" which correspond to a statistics of 2 fb^{-1}, i.e. one year of data taking at the nominal luminosity $\mathcal{L}_{\text{LHCb}}^{av} = 2 \cdot 10^{32}$ cm^{-2}s^{-1}. For each of these "experiments", we obtain the mean values and the errors on the physical parameters. The distributions of the errors have a mean value which correspond to the sensitivity of the experiment: the sensitivity to a parameter is defined as the average value of the errors distributions when repeating the same experiment a large number of times. Indeed according to the Central Limit Theorem, the mean error of a distribution tends to the average of the central values of the errors for the individual experiments.

5.2   Simulation of signal events and likelihood description

In order to study the sensitivity to the B_s^0 physics parameters in LHCb, the following approach has been applied. Events are generated with a toy Monte Carlo for different channels and settings. The studied decay modes are the $B_s^0 \rightarrow J/\psi \ \eta(\gamma \ \gamma)$, the $B_s^0 \rightarrow J/\psi \ \eta(\pi^+ \ \pi^- \ \pi^0)$ and the $B_s^0 \rightarrow \eta_c \ \phi$ for the pure CP eigenstates and the $B_s^0 \rightarrow J/\psi \ \phi$ for the admixture of CP eigenstates. An uncertainty on the reconstructed decay time ($\delta \, t_{rec}$) is assigned to each generated event. The value for $\delta \, t_{rec}$ is obtained from an event with the same true decay time (t_{true}) as the toy event but one which was simulated with the full simulation (see Chapter (3)). The events are smeared according to the pull of the decay time as obtained from the full MC simulation. The error and the pull distributions for the $B_s^0 \rightarrow J/\psi \ \eta$ are shown in Section (4.5.4 and 4.6.3).

The background slopes have been estimated with the full simulation. Then the mass and the lifetime have been fitted with single decreasing exponentials for all the candidates in the sideband region defined as ($m_{sideband} < |m_{rec} - m_{true}| < m_{loose}$). The loose mass window, ($m_{true} \pm m_{loose}$), is the mass region in which all the events are generated and the sideband region, ($m_{true} \pm m_{sideband}$), is the limit from where it is assumed that there is no longer signal in the data.

5.2.1   Modeling the B_s^0 mass

The probability density function (PDF) that is used to fit and generate the mass distribution consists of the sum of two extended likelihoods [95], a Gaussian (G) for the signal (sig) and an exponential (E) for the background (bkg) [3]:

$$
\begin{aligned}
\mathcal{L}_m^{sig}(m_i; N_{sig}, m_{B_s^0}, \sigma_{B_s^0}) &\propto (N_{sig})^{N^{obs}} e^{-N_{sig}} G(m_i; m_{B_s^0}, \sigma_{B_s^0}), \\
\mathcal{L}_m^{bkg}(m_i; N_{bkg}, \kappa_{bkg}) &\propto (N_{bkg})^{N^{obs}} e^{-N_{bkg}} E(m_i; \kappa_{bkg}),
\end{aligned}
\tag{5.1}
$$

with the following definitions:

---

[2]The toys Monte Carlo have been developed in C++, using the ROOFIT v2.03 libraries and interfaced to ROOT v4.02.

[3]The Poisson distributions in front of the G and E functions insure to have the correct proportion of signal/background in the signal tight mass window.

- m_i is the mass generated/fitted for the experiment i;

- N_{sig} is the number of signal events in the tight mass window;

- N^{obs} is the total number of observed events in the data sample;

- $m_{B_s^0} = 5.3696$ GeV/c^2 represents the mass of the B$_s^0$;

- $\sigma_{B_s^0}$ stands for the B-mass resolution;

- $N_{bkg} = N_{sig} \times B/S$ is the number of background events in the tight mass window, ($m_{true} \pm m_{tight}$), with B/S the background-over-signal ratio in the same window (signal region);

- κ_{bkg} is the slope of the background exponential.

The nominal signal resolution parameters $\sigma_{B_s^0}$ are taken from the full Monte Carlo simulation of each channel, whereas the nominal background parameter is estimated to be $\kappa_{bkg} = -1.0$ (MeV/c^2)$^{-1}$ from a guess based on the full MC simulation.
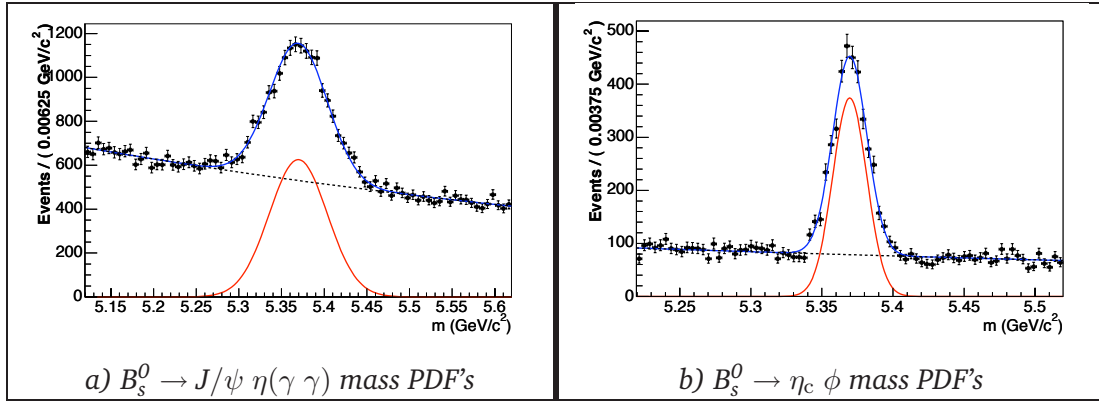
Figure 5.1: *Mass projection PDF's for the B$_s^0 \to J/\psi\ \eta(\gamma\ \gamma)$ and the B$_s^0 \to \eta_c\ \phi$ channels. The background is the dotted black line, the signal the red line and the sum of the two contributions in blue. The dots are the toy generated events.*

Two examples of mass projection PDF's are shown on Fig. (5.1). The B$_s^0 \to J/\psi\ \eta(\gamma\ \gamma)$ parameters come from the full selection detailed in Chapter (4):

- $\sigma_{B_s^0} = 34$ MeV/c^2, $N_{sig} = 8900$, $B/S = 2.0$ and $m_{tight}(B_s^0) = 100$ MeV/c^2.

Where $m_{tight}(B_s^0)$ is the tight mass window used for the selection. The second example shows the B$_s^0 \to \eta_c\ \phi$ mass PDF. Its mass resolution and B/S are better than the J/$\psi\ \eta(\gamma\gamma)$ decay mode, but with a smaller yield [96]:

- $\sigma_{B_s^0} = 12$ MeV/c^2, $N_{sig} = 3000$, $B/S = 0.7$ and $m_{tight}(B_s^0) = 50$ MeV/c^2.

5.2.2 $\bar{b} \to \bar{c}c\bar{s}$ quark transitions to pure CP eigenstates

Among the different B$_s^0$ decays studied at LHCb with pure CP eigenstates, three have been used for this analysis because of their high statistics or of their clean signature with

respect to the other channels and their availability: $B_s^0 \rightarrow J/\psi(\mu^+ \; \mu^-) \; \eta(\gamma \; \gamma)$, $B_s^0 \rightarrow J/\psi(\mu^+ \; \mu^-) \; \eta(\pi^+ \; \pi^- \; \pi^0)$ and $B_s^0 \rightarrow \eta_c(4h) \; \phi(K^+ \; K^-)$. All of them are CP-even eigenstates ($\eta_{f_{CP}} = +1$). The observed decay rates for these channels, assuming a perfect resolution, are defined as:

$$
\begin{aligned}
R\left(B_s^0(t) \rightarrow f\right) &= (1 - \omega_{tag}) \times \Gamma\left(B_s^0(t) \rightarrow f\right) + \omega_{tag} \times \Gamma\left(\overline{B}_s^0(t) \rightarrow f\right), \\
R\left(\overline{B}_s^0(t) \rightarrow f\right) &= (1 - \omega_{tag}) \times \Gamma\left(\overline{B}_s^0(t) \rightarrow f\right) + \omega_{tag} \times \Gamma\left(B_s^0(t) \rightarrow f\right), \quad (5.2)
\end{aligned}
$$

where the $\Gamma\left(B_s^0(t) \rightarrow f\right)$ and $\Gamma\left(\overline{B}_s^0(t) \rightarrow f\right)$ are the decay rates defined in Section (1.5.4) with the definition of Eq. (1.22) and ω_{tag} is the wrong tag fraction. These decay rates can be developed in terms of the physics parameters $\Delta\Gamma_s$, ϕ_s and Δm_s as:

$$
\begin{aligned}
R\left(B_s^0(t) \rightarrow f\right) &= |A_f(0)|^2 \cdot e^{-\Gamma_s t} \times \left[\cosh\left(\frac{\Delta\Gamma_s t}{2}\right) - \eta_{f_{CP}} \cos(\phi_s) \sinh\left(\frac{\Delta\Gamma_s t}{2}\right) \right. \\
&\qquad \left. + D\,\eta_{f_{CP}} \sin(\phi_s) \sin(\Delta m_s t) \right], \\
R\left(\overline{B}_s^0(t) \rightarrow f\right) &= |A_f(0)|^2 \cdot e^{-\Gamma_s t} \times \left[\cosh\left(\frac{\Delta\Gamma_s t}{2}\right) - \eta_{f_{CP}} \cos(\phi_s) \sinh\left(\frac{\Delta\Gamma_s t}{2}\right) \right. \\
&\qquad \left. - D\,\eta_{f_{CP}} \sin(\phi_s) \sin(\Delta m_s t) \right], \quad (5.3)
\end{aligned}
$$

where $D = (1 - 2 \cdot \omega_{tag})$ is the tagging dilution factor, already defined in Section (3.3). The corresponding analytical transition rates $\Gamma\left(B_s^0(t) \rightarrow f\right)$ and $\Gamma\left(\overline{B}_s^0(t) \rightarrow f\right)$ can be obtained again by setting $\omega_{tag} = 0$ in the observed decay rates R. For untagged events, $\omega_{tag} = 0.5$, which cancels the $\sin\phi_s$ term of Eq. (5.3) and renders the determination of ϕ_s much less accurate.

The rates R are drawn on Fig. (5.2) with the nominal parameter values, namely $\Delta m_s = 20$ ps^{-1} and $\Delta\Gamma_s/\Gamma_s = 10\%$. The wrong tag fraction is fixed to $\omega_{tag} = 30\%$ and the weak mixing phase has been increased by a factor ten with respect to the SM value to demonstrate the oscillations: $\phi_s = -0.4$ rad. The $y-$axis has an arbitrary scale.

The figure $a)$ represents the decay rates as expressed by Eq. (5.3). The red line represents the B_s^0 and the blue dashed line the $\overline{B}_s^0$. On figure $b)$ the lifetime resolution has been accounted for resolution curve with a Gaussian shape. The time dependent decay rate then extends to negative time values, which allows to determine the time resolution in this analysis. However, when introducing the time dependent acceptance (Fig. (5.2 c)) where $acc_s = 1.3$ ps^{-1}) the negative part of the decay rate distribution is completely suppressed. It will therefore be impossible to determine the proper time resolution from the negative part of time distribution.

5.2.3 $\bar{b} \rightarrow \bar{c}c\bar{s}$ quark transitions to an admixture of CP eigenstates

The most promising channel of the $\bar{b} \rightarrow \bar{c}c\bar{s}$ quark transitions to an admixture of CP eigenstates category is the $B_s^0 \rightarrow J/\psi \; \phi$ channel, often characterized as "gold plated" decay, because of its relatively large yield, the absence of penguin contribution and its nice experimental signature. The situation in the $B_s^0 \rightarrow J/\psi \; \phi$ decay is a bit more difficult than in the case of the vector-pseudoscalar modes ($J/\psi \; \eta$, $\eta_c \; \phi$ and $J/\psi \; \eta^{'}$) due to the different CP eigenstates which can however be disentangled with an angular analysis.

a) Decay rates,

b) with lifetime resolution,

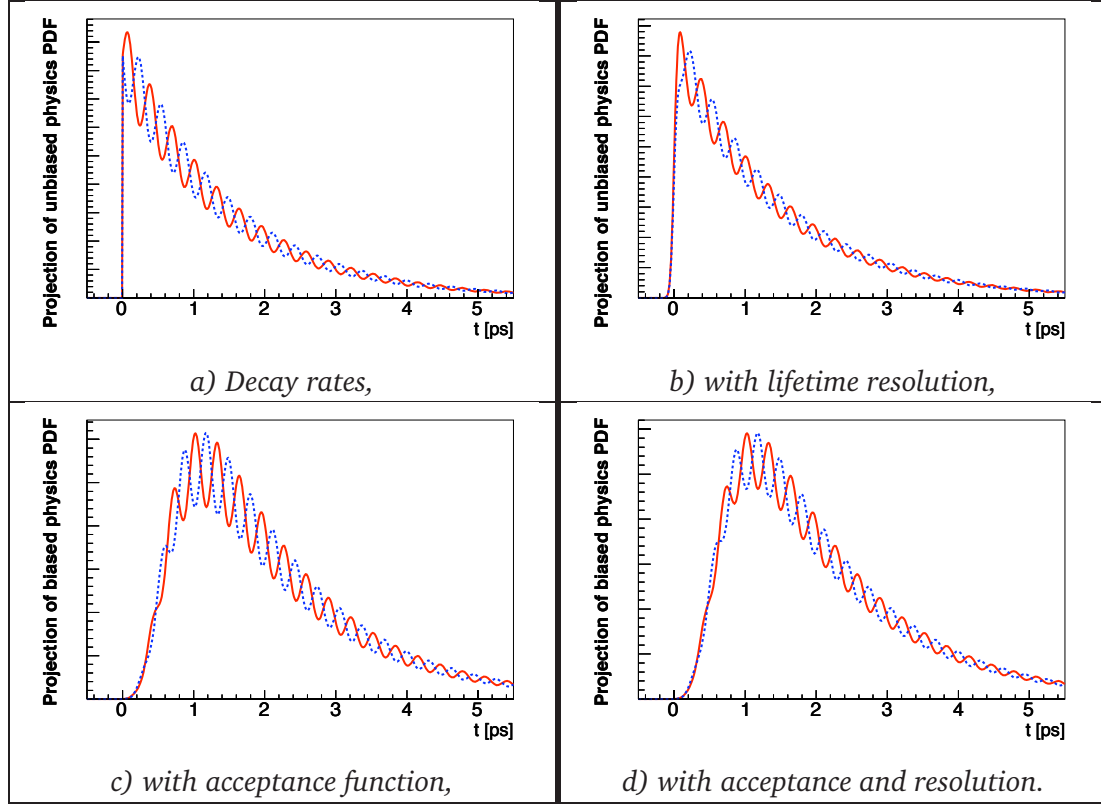*c) with acceptance function,*

d) with acceptance and resolution.

Figure 5.2: *Decay rates for a* $\bar{b} \to \bar{c}c\bar{s}$ *pure CP eigenstate. The red line represents the* B_s^0 *and the blue dashed line the* $\overline{B}_s^0$. *To be able to observe the oscillations in the figures, a* ϕ_s *value is used that is* $\phi_s = -0.4$ *which is ten times larger than the Standard Model expectations.*

It is convenient to introduce linear polarization amplitudes $A_0(t)$, $A_\parallel(t)$, $A_\perp(t)$ [97], where $A_\perp(t)$ describes a CP-odd final state configuration and both $A_0(t)$ and $A_\parallel(t)$ correspond to the CP-even final state configuration. The time evolution of these amplitudes, corresponding to the "ordinary" decay rates for a pure CP eigenstates $\bar{b} \to \bar{c}c\bar{s}$ decay, are with tagging and perfect resolution:

$$
\begin{aligned}
|A_0(t)|^2 &= |A_0(0)|^2 \cdot e^{-\Gamma_s t} \\
&\times \left[\cosh\left(\frac{\Delta\Gamma_s t}{2}\right) - \cos(\phi_s)\sinh\left(\frac{\Delta\Gamma_s t}{2}\right) + D\,\sin(\phi_s)\sin(\Delta m_s t) \right], \\
|A_\parallel(t)|^2 &= |A_\parallel(0)|^2 \cdot e^{-\Gamma_s t} \\
&\times \left[\cosh\left(\frac{\Delta\Gamma_s t}{2}\right) - \cos(\phi_s)\sinh\left(\frac{\Delta\Gamma_s t}{2}\right) + D\,\sin(\phi_s)\sin(\Delta m_s t) \right], \\
|A_\perp(t)|^2 &= |A_\perp(0)|^2 \cdot e^{-\Gamma_s t} \\
&\times \left[\cosh\left(\frac{\Delta\Gamma_s t}{2}\right) + \cos(\phi_s)\sinh\left(\frac{\Delta\Gamma_s t}{2}\right) - D\,\sin(\phi_s)\sin(\Delta m_s t) \right], \quad (5.4)
\end{aligned}
$$

Fortunately, one only needs to separate the contributions of the CP-even and CP-odd amplitudes, which can be done on the basis of a single observable θ_{Tr}, the so-called transversity angle. This angle is defined as the angle between the positive charged lepton and the normal to the ϕ decay plane, in the J/ψ rest frame, as shown on Fig. (5.3). The differential
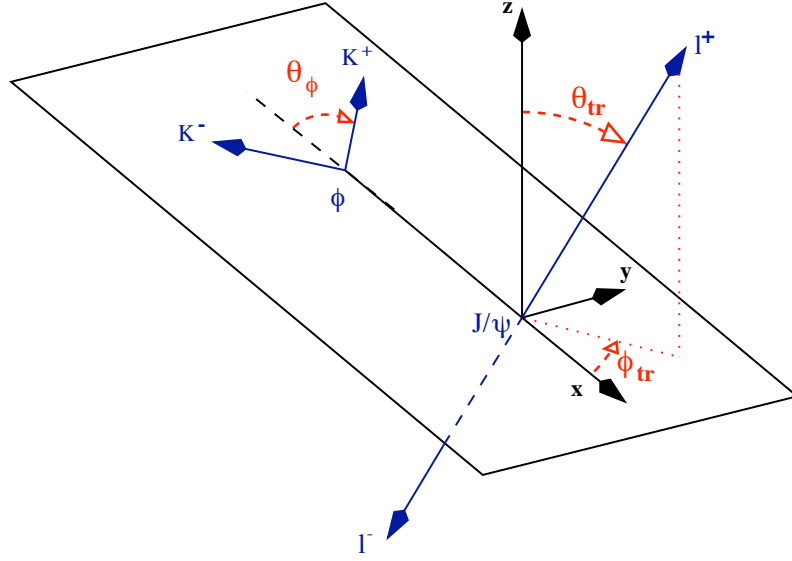
Figure 5.3: *Definition of the transversity angle θ_{Tr} in the rest frame of the J/ψ, in the $B_s^0 \rightarrow J/\psi(\ell^+ \ell^-)\,\phi(\mathrm{K}^+\,\mathrm{K}^-)$ decay.*

decay rate, with the one-angle distribution, then takes the following form [98, 99]:

$$\frac{d\Gamma(t)}{d(\cos(\theta_{\mathrm{Tr}}))} \propto \left[|A_0(t)|^2 + \left|A_\parallel(t)\right|^2\right]\frac{3}{8}(1 + \cos^2\theta_{\mathrm{Tr}}) + |A_\perp(t)|^2\,\frac{3}{4}\sin^2\theta_{\mathrm{Tr}}. \tag{5.5}$$

With the help of this one-angle distribution, the observables $|A_0(t)|^2$, $|A_\parallel(t)|^2$ and $|A_\perp(t)|^2$, as well as their CP conjugates, can be determined.

a) $\bar{b} \rightarrow \bar{c}c\bar{s}$ pure CP eigenstate   b) $J/\psi\,\phi$ CP eigenstate admixture

Figure 5.4: *Observed decay rates biased by an acceptance and convoluted with a lifetime resolution. Pure CP eigenstates are on the left and CP admixture on the right, with $R_T = 0.2$ and $\phi_s = -0.4$.*

It is also useful to introduce another parameter, the fraction of CP-odd decays R_T, defined as:

$$R_T \equiv \frac{|A_\perp(0)|^2}{\displaystyle\sum_{f=0,\parallel,\perp}|A_f(0)|^2}.$$

This fraction has been measured by the CDF collaboration to be $R_T = (0.2 \pm 0.1)$ [100]. It acts as a "kind of dilution term" in front of $\sin \phi_s$ similar to the one induced by the tagging. This is shown on Fig. (5.4) for the biased decay rates with Gaussian lifetime resolution, comparing $\bar{b} \rightarrow \bar{c}c\bar{s}$ pure CP decays to the $B_s^0 \rightarrow J/\psi \phi$ channel[4]. The amplitudes of the oscillations for the non pure CP final state are smaller.

5.2.4 $B_s^0 \rightarrow D_s \pi$ as a flavor specific control channel

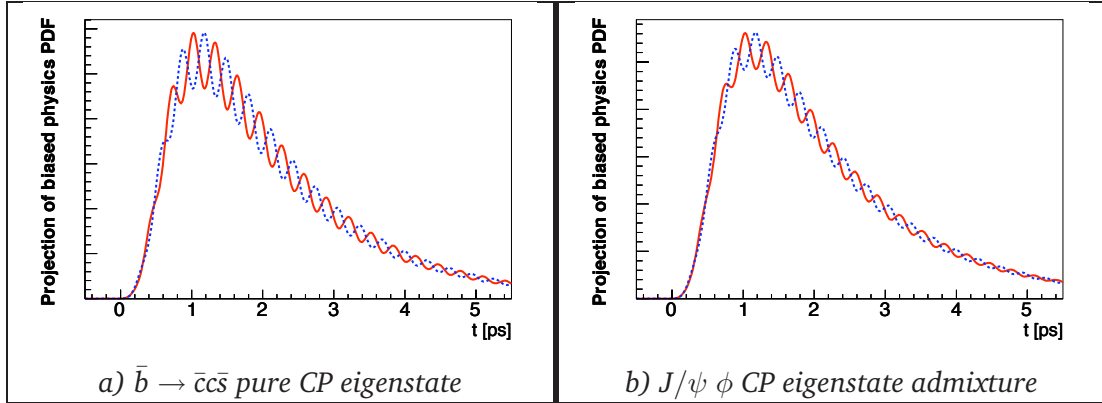The $B_s^0 \rightarrow D_s \pi$ decay is a flavor specific B-decay in which only a single tree diagram contributes. The B_s^0 decays directly to $f = D_s^- \pi^+$ and the $\overline{B}_s^0$ to $\overline{f} = D_s^+ \pi^-$. There is no CP violation expected. The analytical decay rates, with a possible mistag probability ω_{tag} and perfect resolution, are given by:

$$
\begin{aligned}
R\left(B_s^0(t) \rightarrow f\right) &= |A_f(0)|^2 \cdot e^{-\Gamma_s t} \times \left[\cosh\left(\frac{\Delta\Gamma_s t}{2}\right) + D \cos\left(\Delta m_s t\right) \right], \\
R\left(\overline{B}_s^0(t) \rightarrow \overline{f}\right) &= |\overline{A}_{\overline{f}}(0)|^2 \cdot e^{-\Gamma_s t} \times \left[\cosh\left(\frac{\Delta\Gamma_s t}{2}\right) - D \cos\left(\Delta m_s t\right) \right].
\end{aligned}
$$

From these decay rates the B_s^0 oscillation frequency Δm_s, the wrong tag fraction ω_{tag}, the B_s^0 proper time $\tau_{B_s^0} \equiv 1/\Gamma_s$ and the decay width difference $\Delta\Gamma_s$ can be determined.

a) Decay rates,

b) with lifetime resolution,

c) with acceptance function,

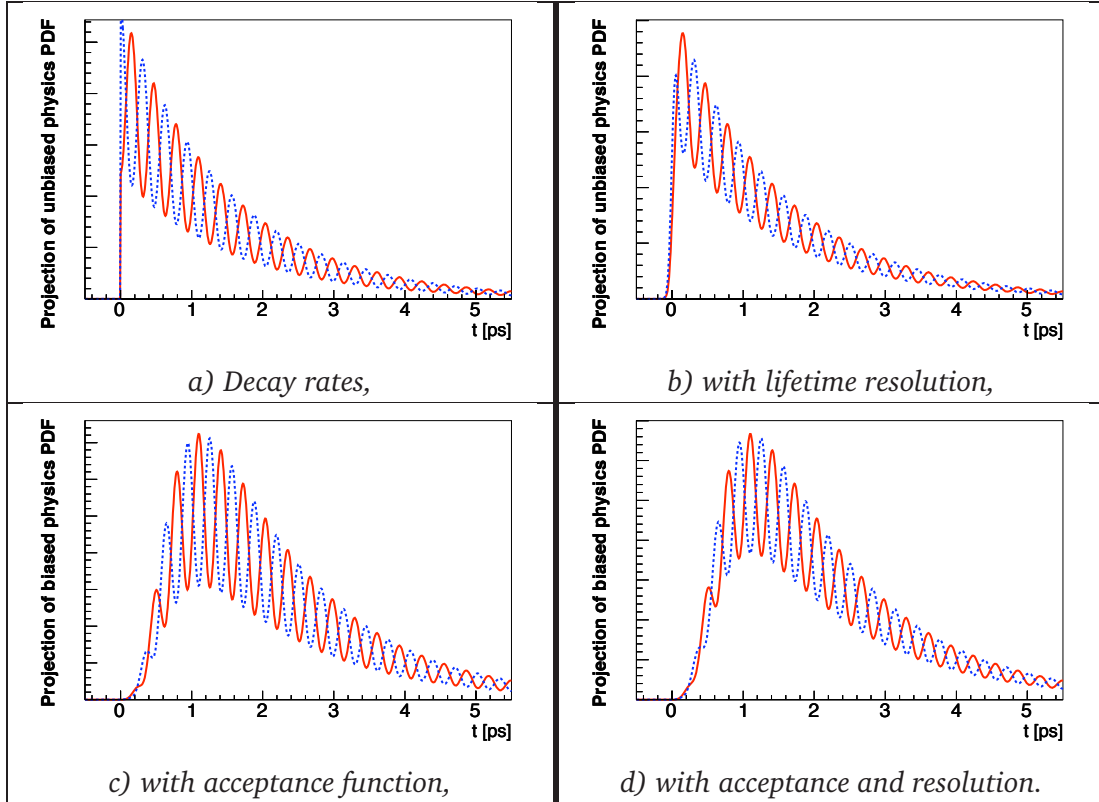d) with acceptance and resolution.

Figure 5.5: *Observed decay rates for a flavor specific B_s^0-decay.*

---

[4]For the plot on Fig. (5.4 *b*)), θ_{Tr} has been fixed to 0.5 instead of being integrated on its full range. It has been checked that the this simplification has negligible effects on the amplitudes of the oscillation.

Fig. (5.5 a)) shows the time dependent decay rates of the B$_s^0 \rightarrow$ D$_s$ π channel with the same input parameters as in Section (5.2.2). A Gaussian resolution is introduced in b), resolution is put in c) and both effects are present in d). The amplitude of the oscillations is clearly much larger than for the $\bar{b} \rightarrow \bar{c}c\bar{s}$ CP eigenstates transitions. Therefore this channel is used simultaneously with the CP eigenstates decays to help in the determination of the wrong tag fraction ω_{tag} as well as the mixing parameters Δm_s and $\Delta\Gamma_s/\Gamma_s$ and $\tau_{B_s^0}$.

5.2.5 Modeling the transversity angle

When the final state is not a pure CP eigenstate, an angular analysis is performed to distinguish the different CP contributions.

The resolution of θ_{Tr} is obtained with the RMS of the θ_{Tr} residual ($\theta_{Tr}{}^{rec} - \theta_{Tr}{}^{true}$) in the signal events of the B$_s^0 \rightarrow$ J$/\psi$ ϕ full MC simulation. The RMS obtained is 18.2 mrad [84]. This effect is introduced in the toy by smearing the θ_{Tr} distribution with a Gaussian of 20 mrad. One does not expect the resolution to have a large impact as θ_{Tr} distributions vary slowly on the scale of the resolution. Therefore this effect will not be included in the likelihood functions used for the fit. The signal and background are described by:

$$
\begin{aligned}
\mathcal{L}_{\theta_{Tr}}^{sig,even}(\theta_{Tr i}) &\propto (1 + \cos\theta_{Tr i}{}^2)/2, \\
\mathcal{L}_{\theta_{Tr}}^{sig,odd}(\theta_{Tr i}) &\propto (1 - \cos\theta_{Tr i}{}^2), \\
\mathcal{L}_{\theta_{Tr}}^{bkg}(\theta_{Tr i}) &\propto (1 + \alpha_{bkg}\cos\theta_{Tr i}{}^2).
\end{aligned}
\tag{5.6}
$$

The background is assumed to be flat which leads to a α_{bkg} nominal value of zero.

5.2.6 Modeling the B$_s^0$ proper time

The proper time model depends strongly on the tight selection which has a direct influence on the lifetime resolution. Therefore the physics model will be biased by a time-dependent efficiency, defined by Eq. (4.4) of Section (4.5.3). The likelihood must therefore be convoluted with the proper time resolution. A scale factor S is introduced in the likelihood which multiplies the event-by-event proper time error (it corresponds to the width of the proper time pull distribution).

The signal and background likelihoods, for CP-even and CP-odd eigenstates decay modes, are given by:

$$
\begin{aligned}
\mathcal{L}_{t,even}^{sig}(t_i^{rec}, \sigma_{t_i^{rec}}, q_i; \overrightarrow{\alpha}, \omega_{tag}, acc_s, S) &\propto \Big[\big[(1-\omega_{tag})\Gamma_{B_s^0 \rightarrow f}^{even}(t_i^{true}, q_i; \overrightarrow{\alpha}) + \omega_{tag}\Gamma_{\overline{B}_s^0 \rightarrow f}^{even}(t_i^{true}, q_i; \overrightarrow{\alpha})\big] \\
&\qquad \otimes R(t_i^{rec} - t_i^{true}, \sigma_{t_i^{rec}}; S)\Big] \times A(t_i^{rec}; acc_s), \\[2mm]
\mathcal{L}_{t,odd}^{sig}(t_i^{rec}, \sigma_{t_i^{rec}}, q_i; \overrightarrow{\alpha}, \omega_{tag}, acc_s, S) &\propto \Big[\big[(1-\omega_{tag})\Gamma_{B_s^0 \rightarrow f}^{odd}(t_i^{true}, q_i; \overrightarrow{\alpha}) + \omega_{tag}\Gamma_{\overline{B}_s^0 \rightarrow f}^{odd}(t_i^{true}, q_i; \overrightarrow{\alpha})\big] \\
&\qquad \otimes R(t_i^{rec} - t_i^{true}, \sigma_{t_i^{rec}}; S)\Big] \times A(t_i^{rec}; acc_s), \\[2mm]
\mathcal{L}_t^{bkg}(t_i^{true}; \tau_{bkg}, acc_s) &\propto \Big[E(t_i^{true}; \tau_{bkg}) \otimes \delta(t_i^{rec} - t_i^{true})\Big] \times A(t_i^{rec}; acc_s),
\end{aligned}
\tag{5.7}
$$

with the following definitions:

- t_i^{true} is the true proper time used for the generation;

- t_i^{rec} is the proper time generated;

- $q_i = \pm 1$ is the tagging category for the B-meson candidate, either B_s^0 or $\overline{B}_s^0$ respectively; $q_i = 0$ if the candidate is untagged;

- $A(t_i^{rec}; acc_s)$ is the time dependent efficiency;

- $\sigma_{t_i^{rec}}$ represents the reconstructed proper time per event error;

- $\overrightarrow{\alpha} = (\Delta\Gamma_s/\Gamma_s, \Delta m_s, \phi_s, \tau_{B_s^0})$ is for the vector of physics parameters (with R_T in addition for the $B_s^0 \to J/\psi\,\phi$ channel);

- $\Gamma_{B_s^0 \to f}^{even}$ is the analytical decay rates of the CP-even decays ($\Gamma_{B_s^0 \to f}$, $|A_0(t)|^2$ and $|A_\parallel(t)|^2$), and $\Gamma_{B_s^0 \to f}^{odd}$ the CP-odd decays ($|A_\perp(t)|^2$);

- $R(t_i^{rec} - t_i^{true}, \sigma_{t_i^{rec}}; S) = G(t_i^{rec} - t_i^{true}, S\sigma_{t_i^{rec}})$ is the Gaussian resolution function;

- $\tau_{bkg} = 1.0$ ps is the slope of the exponentially decaying background in the proper time distribution.

In the parameterization of the background, the computed per-event error is not used, as the majority of the background has a combinatorial origin and does not have a definite proper time. Therefore one does not expect the computed per-event proper time error to be an accurate measure of the resolution of the reconstructed candidate.

Fig. (5.6) shows the B_s^0 lifetime projection of the PDF's used for the generation of pure CP-even eigenstates, the signal is in red and the background in black and dotted. Figure a) shows the projection for $B_s^0 \to J/\psi\,\eta(\gamma\,\gamma)$, where the parameters are taken from the full MC simulation detailed in Chapter (4) and are:

- $< \sigma_{t_i^{rec}} > = 30.4$ fs, $\quad acc_s = 1.9$ ps^{-1}, $\quad S = 1.2$, $\quad \omega_{tag} = 35\%$ $\quad$ and $\quad \varepsilon_{tag} = 63\%$.

The figure b) represents the $B_s^0 \to \eta_c\,\phi$ lifetime projection of the PDF with:

- $< \sigma_{t_i^{rec}} > = 26.2$ fs, $\quad acc_s = 1.3$ ps^{-1}, $\quad S = 1$, $\quad \omega_{tag} = 31\%$ $\quad$ and $\quad \varepsilon_{tag} = 66\%$.

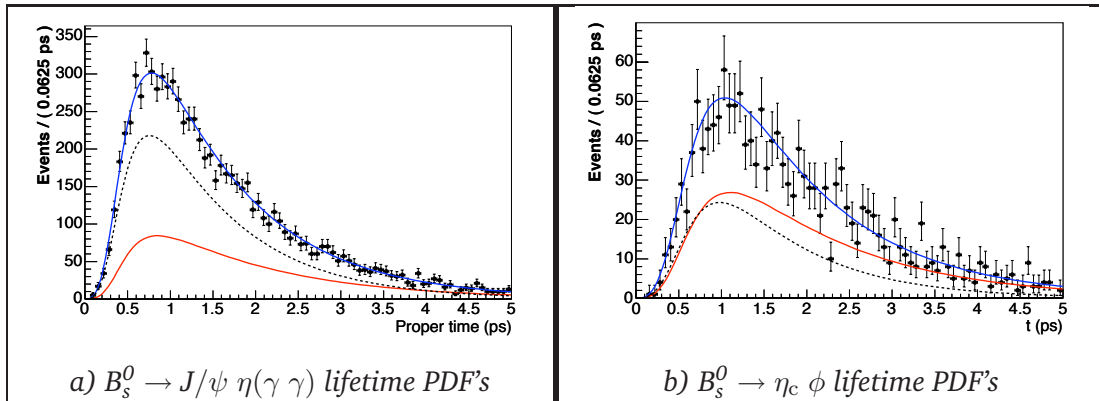a) $B_s^0 \to J/\psi\,\eta(\gamma\,\gamma)$ lifetime PDF's   b) $B_s^0 \to \eta_c\,\phi$ lifetime PDF's

Figure 5.6: *Lifetime projection of the B_s^0 PDF's for the $B_s^0 \to J/\psi\,\eta(\gamma\,\gamma)$ and the $B_s^0 \to \eta_c\,\phi$ channels in the signal region. The background is the dotted black line, the signal the red line and in blue the sum of the two contributions. The dots are the toy generated events.*

5.2.7   Total likelihood

The total likelihood which is used to generate and to fit the events is given by:

$$\mathcal{L}^{tot} = \prod_{i \in B_s^0 \to f} \mathcal{L}_i(m_i, \theta_{\mathrm{Tr}i}, t_i, \sigma_{t_i^{rec}}, q_i),$$

where $\mathcal{L}_i$ is the combination of mass terms (Eq. (5.1)), the angular terms (Eq. (5.6)) and the lifetime terms (Eq. (5.7)):

$$\begin{aligned}
\mathcal{L}_i(m_i, \theta_{\mathrm{Tr}i}, t_i, \sigma_{t_i^{rec}}, q_i) &= \mathcal{L}_m^{sig}(m_i) \Big[R_T \mathcal{L}_{\theta_{\mathrm{Tr}}}^{sig,odd}(\theta_{\mathrm{Tr}i}) \mathcal{L}_{t,odd}^{sig}(t_i^{rec}, \sigma_{t_i^{rec}}, q_i) \\
&\qquad + (1 - R_T) \mathcal{L}_{\theta_{\mathrm{Tr}}}^{sig,even}(\theta_{\mathrm{Tr}i}) \mathcal{L}_{t,even}^{sig}(t_i^{rec}, \sigma_{t_i^{rec}}, q_i) \Big] \cdot \\
&\quad \mathcal{L}_m^{bkg}(m_i) \mathcal{L}_{\theta_{\mathrm{Tr}}}^{bkg}(\theta_{\mathrm{Tr}i}) \mathcal{L}_t^{bkg}(t_i^{rec}).
\end{aligned} \qquad (5.8)$$

The likelihood function for the $B_s^0 \to D_s \pi$ channel (see Section (5.2.4)) is maximized simultaneously with the above likelihood. As we know the amplitudes of this flavor specific channel, we are able to determine the mistag fraction ω_{tag} which we assume to be the same for the two samples. The statistical error on this determination of ω_{tag} is due to the finite size of the control sample; moreover, as the triggering strategies will differ from channel to channel, the wrong tag fraction might also differ and, thus, introduce a systematic uncertainty. The size of this effect remains to be studied.

The present toy Monte Carlo does not allow two different event-by-event error sample to be input. This means that the $\sigma_{t_i^{rec}}$ are defined only by the $\bar{b} \to \bar{c}c\bar{s}$ decay lifetime errors, for the signal and for the control channel. In the situation of B-decays with only charged final products these values are very close to the $B_s^0 \to D_s \pi$. This is unfortunately not the case for the two $B_s^0 \to J/\psi \, \eta$ channels where the lifetime measurements are less accurate due to the presence of the larger than one scale factor. Therefore the sensitivities to the parameters which are determined by both the control and the signal channels might be worse.

5.2.8   Input to the toy Monte Carlo

In Tab. (5.1) are summarized all the inputs used in the toy Monte Carlo to extract the physics parameters[5]. The numbers used for the sensitivity studies of the $B_s^0 \to J/\psi \, \eta$ have been detailed in Chapter (4). The average value of the parameters at $\theta_P = -20°$ and at $\theta_P = -10°$ is chosen. This is a good approximation of a $\theta_P = -15°$ mixing angle as the branching fraction is almost linear in this interval (as shown by Fig. (1.9)). The large pull distribution widths observed after the Kalman Filter fit have been introduced through the scale factor S.

For $B_s^0 \to \eta_c \, \phi$, the latest results from [96] have been used. Most of the $B_s^0 \to J/\psi \, \phi$ parameters are from the reoptimized TDR [33], however the yield has been updated for the new trigger algorithms and is estimated to be 125k events[6] for 2 fb^{-1}. The tagging efficiencies are from the "cheated selection" as given in Section (3.3) for the "cheated"

---

[5]The definitions of the different mass windows are: the tight mass window = $(m_{true} \pm m_{tight})$, the loose mass window = $(m_{true} \pm m_{loose})$ and the sideband mass window = $(m_{sideband} < |m_{rec} - m_{true}| < m_{loose})$.

[6]For the TDR, the annual yield was estimated to 100k events, with a trigger efficiency of $\varepsilon_{trg}^{J/\psi \, \phi} = 0.64$ which was very close to the $B_s^0 \to J/\psi \, \eta$ one: $\varepsilon_{trg}^{J/\psi \, \eta(\gamma\gamma)} = 0.65$ [33]. Therefore the old yield has been corrected with the actual estimated trigger efficiency of $\varepsilon_{trg}^{J/\psi \, \phi} = 0.80$.

selection. Being conservative we take the upper bound of the 90% CL interval for the B/S ratio. The parameterization and nominal parameters used for the $B_s^0 \to D_s \pi$ sample are described in [92], except for ε_{tag} and ω_{tag} (see Section (3.3)) and the yield now takes into account the HLT [101].

Parameters	$J/\psi\,\eta(\gamma\gamma)$	$J/\psi\,\eta(\pi^+\pi^-\pi^0)$	$\eta_c\,\phi$	$J/\psi\,\phi$	$D_s^\mp\,\pi^\pm$
N_{sig} [k events]	8.9	3.1	3	125	69
B/S	2.0	3.0	0.7	0.3	0.8
m_{tight} [MeV/c^2]	100	100	50	50	50
$m_{sideband}$ [MeV/c^2]	150	150	75	75	75
m_{loose} [MeV/c^2]	250	250	150	150	150
$\sigma_{B_s^0}$ [MeV/c^2]	34	20	12	13	14
acc_s after triggers [ps^{-1}]	1.9	1.5	1.3	2.9	1.3
$<\sigma_{t_i^{rec}}>$ [fs]	30.4	25.5	26.2	35.8	33.5
S	1.2	1.3	1	1	1
ω_{tag} [%]	35	30	31	33	31
ε_{tag} [%]	63	62	66	60	65

Table 5.1: *Input used by the MC toys to extract the sensitivity to the physics parameters. The scale factor is not known for the last three channels and therefore set to 1.*

The nominal values for the physics parameters are listed in Tab. (5.2). The default value for $\Delta\Gamma_s/\Gamma_s$ is 10%, following the predictions of Beneke at al. [102] who gave the value of $\Delta\Gamma_s/\Gamma_s = (9.3^{+3.4}_{-4.6})\%$. The other parameters are also explored to test the sensitivity of the experiment to them. In the fit procedure, only one parameter can be varied at a time for a set of "experiments".

Physics Parameters	Lower values		**Nominal**	Higher values	
ϕ_s [rad]		-0.2	$-\mathbf{0.04}$	0.0	
Δm_s [ps^{-1}]		15	**20**	25	
$\Delta\Gamma_s/\Gamma_s$		0.0	**0.1**	0.2	
$\tau_{B_s^0}$ [ps]		$-$	**1.472**	$-$	
R_T	0.0	0.1	**0.2**	0.3	0.5

Table 5.2: *Physics parameter values used to explore the sensitivity of LHCb.*

5.2.9 Fit procedure

Given the large number of events involved (see Section (5.2.8)), the fit is performed in three steps on the three variables m_i, t_i and $\theta_{\mathrm{Tr}i}$. Only the proper time distribution is fitted using a unbinned maximum likelihood. As the resolution scale factor cannot be fitted together with the acceptance function, the scale factor S has been fixed.

1. **Mass fit:** First, the mass distribution alone is fitted in the loose mass window. Its parameters are then fixed. This is equivalent to determining the signal probability

for one event based on its reconstructed mass where the signal probability can be written:

$$P_m^{sig}(m_i) = \frac{\mathcal{L}_m^{sig}(m_i; m_{B_s^0}, \sigma_{B_s^0})}{\mathcal{L}_m^{sig}(m_i; m_{B_s^0}, \sigma_{B_s^0}) + \mathcal{L}_m^{bkg}(m_i; \kappa_{bkg})},$$

and replacing $\mathcal{L}_m^{sig}(m_i)$ by $P_m^{sig}(m_i)$ and $\mathcal{L}_m^{bkg}(m_i)$ by $(1 - P_m^{sig}(m_i))$ in the likelihood of Eq. (5.8).

2. **Sideband region fit:** The second step consists of determining the parameter of the acceptance function (acc_s) and the slope of the background time distribution (τ_{bkg}). For this, we used the events of the sideband regions. Our hypothesis is that these parameters do not depend on the reconstructed mass and that the acceptance function is the same for the background and for the signal. This hypothesis is correct for the present analysis but might be a source of systematic uncertainties when dealing with the real data.

   For the last stage of the fit, the above parameters are kept fixed.

3. **Signal parameters fit:** Finally the signal parameters are extracted from events belonging to the tight mass window around the nominal B_s^0-mass. The parameters left free in this last fit are: $\Delta\Gamma_s/\Gamma_s$, $\tau_{B_s^0}$, Δm_s, ω_{tag}, ϕ_s and R_T for the non-pure CP eigenstates. Only the two last parameters are completely determined by the $\bar{b} \to \bar{c}c\bar{s}$ decays whereas the other can benefit from the help of the control channel.

5.3 Likelihood fit results

In this section, we present the results of the likelihood fits used to extract the physics parameters from the data generated with the toy Monte Carlo. First tests have been performed on the correlations between the most sensitive parameters. Then the sensitivity to the physics parameters has been studied for the nominal SM values. Finally the sensitivities are determined for different values of the unknown physics variables. A particular emphasis will be carried on the weak mixing phase as it is the direct manifestation of CP violation.

5.3.1 Physics parameters correlation studies

The correlations between the most sensitive parameters, i.e. the non-diagonal terms of the covariance matrix[7], has to be known before running the full analysis. They will point to the parameters which cannot be measured simultaneously.

   The correlation studies have been performed with the $B_s^0 \to J/\psi\ \phi$ decay channel, as this latter is the most general one with both CP-even and CP-odd contributions. The fit

---

[7]The correlation coefficient ρ for two independent random variable X and Y is defined as:

$$\rho = \frac{Cov[X,Y]}{\sqrt{Var[X]Var[Y]}},$$

where $Cov[X,Y] = E[XY] - E[X]E[Y]$ is the covariance of X and Y, $E[X] = \sum_x xf(x)$ is the expectation, $f(x)$ is a probability function and $Var[X] = E[X^2] - E[X]^2$ is the variance. The diagonal elements of the correlation matrix are always 1 (as $Cov[X,X] = Var[X]$). Therefore we are interested in the off-diagonal terms which give prominence to the parameters that cannot be determined simultaneously.
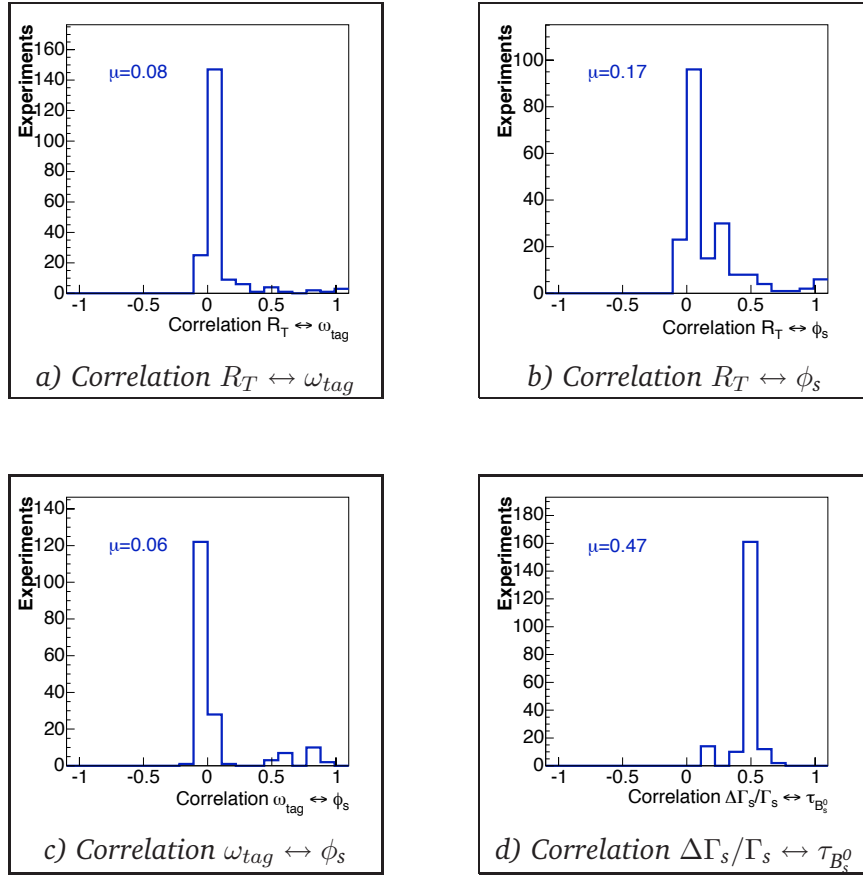
a) Correlation $R_T \leftrightarrow \omega_{tag}$

b) Correlation $R_T \leftrightarrow \phi_s$

c) Correlation $\omega_{tag} \leftrightarrow \phi_s$

d) Correlation $\Delta\Gamma_s/\Gamma_s \leftrightarrow \tau_{B_s^0}$

Figure 5.7: *Correlations plots for the $B_s^0 \to J/\psi\,\phi$ channel. All the parameters not involved in the correlation are fixed to the nominal values. μ is the average value of the different experiment correlations.*

procedure is the one explained in Section (5.2.9) with the input values defined in Section (5.2.8), except that in the signal parameters fitting, only the two studied physics parameters are let free, all the others being set to their nominal values. About 200 experiments have been simulated for each pair of the following variables:

- $R_T \leftrightarrow \omega_{tag}$, $R_T \leftrightarrow \phi_s$, $\omega_{tag} \leftrightarrow \phi_s$, $\tau_{B_s^0} \leftrightarrow \Delta\Gamma_s/\Gamma_s$ and $\phi_s \leftrightarrow \Delta\Gamma_s/\Gamma_s$.

As one can deduce from the decay rates, Eq. (5.4) and (5.5), the three parameters ω_{tag}, ϕ_s and R_T act similarly on the distribution and change the amplitude of its oscillations. The correlation study shows that, even if one could *a priori* suspect some difficulties to disentangle the contributions of these three variables, they are fortunately mostly uncorrelated (Fig. (5.7 a), b) and c)). On these figures, most of the experiments show no correlations, but for a few experiments the fit experiences difficulties to converge to the nominal values and this increases the correlations between the free parameters.

Two observations can be made from these figures:

- There is almost no correlation between ω_{tag} and ϕ_s or R_T;

- A larger correlation appears for the couple $\phi_s \leftrightarrow R_T$.

This can be explained by the fact that ω_{tag} is obtained with the help of the control channel which is not the case for ϕ_s or R_T, only determined by B$_s^0 \to$ J$/\psi\ \eta$, B$_s^0 \to \eta_c\ \phi$ and B$_s^0 \to$ J$/\psi\ \phi$.

$\Delta\Gamma_s/\Gamma_s$ and $\tau_{B_s^0}$ are strongly correlated, which is clear from the definition $\tau_{B_s^0} \equiv 1/\Gamma_s$. This leads to biases in their mean values (see Fig. (5.7 d))).

The last three correlation studies focus on the weak mixing phase ϕ_s and the relative B$_s^0$ lifetime difference $\Delta\Gamma_s/\Gamma_s$. Three cases are taken into account:

1. Standard decay rates where both $\sin\phi_s$ and $\cos\phi_s$ contribute;

2. Only first order terms in ϕ_s are present as the B$_s^0$ mixing phase is very small, which means $\cos\phi_s = 1$;

3. The contribution of the $\sin\phi_s$ term is set to zero. This can happen when the dilution factor is zero, i.e. when an "untagged" experiment is performed (Eq. (5.3)).
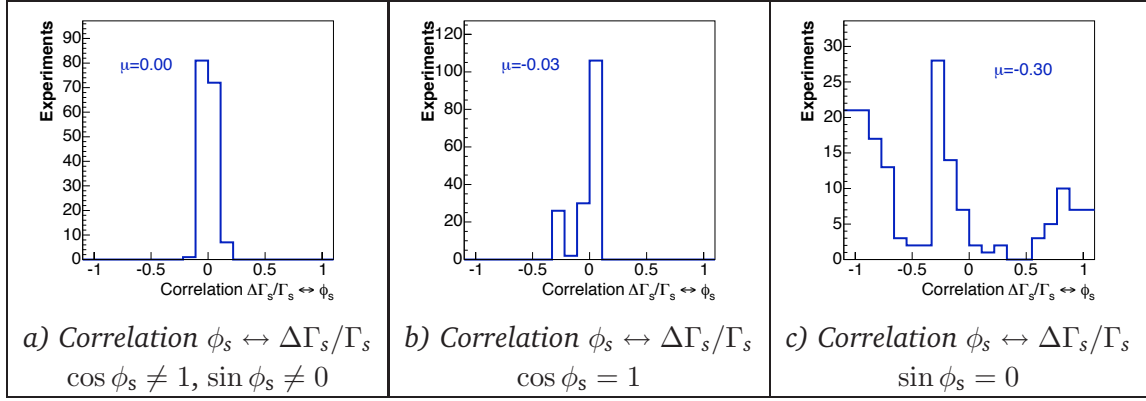

Figure 5.8: Correlations plots for the B$_s^0 \to$ J$/\psi\ \phi$ channel varying the contribution of ϕ_s to the decay rates. All the parameters not involved in the correlation are fixed to the nominal values. μ is the average value of the correlation.

There is not any noticeable correlation between ϕ_s and $\Delta\Gamma_s/\Gamma_s$ in the two first cases. However, a correlation is observed between these two parameters when $\sin\phi_s$ is set to zero: this can be explained by the fact that the weak mixing phase is small and that the contribution of ϕ_s is quite poor with only the $\cos\phi_s$ term (see Eq. (5.3)) compared to $\Delta\Gamma_s/\Gamma_s$ in the $\sinh(\Delta\Gamma_s t/2)$ term.

5.3.2 Resolution measurements with real data

The negative tail in the proper time distribution, as shown on Fig. (5.2 b)), will enable the lifetime resolution to be measured directly. This can be done only for unbiased samples with a flat acceptance function. This condition is practically impossible to reach with B-meson decays as the most powerful selection cuts are based on the impact parameter or on the B$_s^0$ distance of flight, especially for channels with neutral particles.

It is also possible to extract the resolution scale factor and the wrong tag fraction if the event-by-event proper time errors are known, looking at the Δm_s oscillation amplitudes. Unfortunately the correlation coefficient of the scale factor is very large. This renders the

results hard to believe. Another method is therefore needed to determine the proper time resolution.

The best way would be to study prompt J/ψ. These particles have a negligible decay length and they are only triggered with mass cuts. This means they should not be biased in proper time and peak at zero in proper time. Therefore their lifetime resolution could be measured directly. This resolution has then to be propagated to the different B-decay channels, containing generally more tracks and with larger P_T.

5.3.3 Sensitivities to the physics parameters

The mean values, the errors and the pull distribution from a set of ~ 250 experiments, each representing one year of data taking at $\mathcal{L}_{\mathrm{LHCb}}^{av} = 2 \cdot 10^{32}$ cm^{-2}s^{-1} and simulated with nominal values of the input physics parameters (see Tab. (5.1)) are shown in the following plots:

- Fig. (5.9) for the weak mixing phase ϕ_{s};

- Fig. (5.10) for the mass difference $\Delta \mathrm{m}_{\mathrm{s}}$;

- Fig. (5.11) for the relative width difference $\Delta\Gamma_{\mathrm{s}}/\Gamma_{\mathrm{s}}$;

- Fig. (5.12) for the B_{s}^0 proper time $\tau_{B_{\mathrm{s}}^0}$;

- Fig. (5.13) for the wrong tag fraction ω_{tag};

- Fig. (5.14) for the CP-odd fraction R_T, only for the $B_{\mathrm{s}}^0 \to J/\psi\,\phi$ decay mode.

The expected sensitivities are estimated by the mean of the error distribution and are summarized in Tab. (5.3)

Sensitivity	$J/\psi\,\eta(\gamma\gamma)$	$J/\psi\,\eta(\pi^+\pi^-\pi^0)$	$\eta_{\mathrm{c}}\,\phi$	$J/\psi\,\phi$	Nominal
$\boldsymbol{\sigma(\phi_{\mathrm{s}})}$ **[rad]**	0.112	0.148	0.106	0.031	-0.04
$\boldsymbol{\sigma(\Delta \mathrm{m}_{\mathrm{s}})}$ **[ps^{-1}]**	0.0122	0.0084	0.0084	0.0113	20
$\boldsymbol{\sigma(\Delta\Gamma_{\mathrm{s}}/\Gamma_{\mathrm{s}})}$	0.019	0.024	0.025	0.011	0.1
$\boldsymbol{\sigma(\tau_{B_{\mathrm{s}}^0})}$ **[ps]**	0.0057	0.0059	0.0062	0.0041	1.472
$\boldsymbol{\sigma(\omega_{tag})}$	0.0049	0.0046	0.0046	0.0056	$0.30 - 0.35$
$\boldsymbol{\sigma(R_T)}$	$-$	$-$	$-$	0.0047	0.2

Table 5.3: *Sensitivity of LHCb to the physics parameters for the nominal values defined in Section (5.2.8).*

The sensitivity on ϕ_{s} specially depends on both the statistics and the proper time resolution. It is evident looking at Fig. (5.9) that the huge yield of the "golden decay mode" renders its sensitivity to the weak mixing phase much more accurate than all the other pure CP eigenstates channels. On the other hand, even with 3 times less events per 2 fb^{-1}, the $B_{\mathrm{s}}^0 \to \eta_{\mathrm{c}}\,\phi$ channel measures ϕ_{s} with slightly better accuracy than the $B_{\mathrm{s}}^0 \to J/\psi\,\eta(\gamma\,\gamma)$. This is a direct consequence of the importance of the lifetime resolution, tagging and mass windows in the determination of the B_{s}^0 mixing parameters.

$\tau_{B_{\mathrm{s}}^0}$ and ω_{tag} are determined essentially by the $B_{\mathrm{s}}^0 \to D_{\mathrm{s}}\,\pi$ in all the pure CP eigenstates B_{s}^0 decay modes and have similar results. For the $B_{\mathrm{s}}^0 \to J/\psi\,\phi$ channel, the sensitivity is significantly better for $\tau_{B_{\mathrm{s}}^0}$ due to its high statistics, but curiously ω_{tag} is less precisely

estimated with this channel. This can be explained by the correlation between ω_{tag}, ϕ_s and R_T in the signal sample. This can worsen the determination of the wrong tag fraction.

Δm_s cannot be directly compared between the different channel as it is essentially determined by the $B_s^0 \to D_s \pi$ and depends strongly on the proper time resolution. The problem is that the resolution used for the $B_s^0 \to D_s \pi$ decay is the one of the studied $\bar{b} \to \bar{c}c\bar{s}$ signal channels. Therefore it is normal that the $B_s^0 \to \eta_c \phi$ and the $B_s^0 \to J/\psi \, \eta(\pi^+ \, \pi^- \, \pi^0)$, which have the best lifetime resolution, are the most sensitive to the B_s^0 mass difference parameter.

The pull distributions for the ϕ_s, Δm_s, ω_{tag} and R_T parameters determined by the fits show that the errors estimated by the likelihood fits does represent the variance of the results. Nevertheless small biases can be present for R_T and ω_{tag}.

This is not the case for $\Delta\Gamma_s/\Gamma_s$ and $\tau_{B_s^0}$, as expected by the correlation between these two parameters seen in Section (5.3.1), which are strongly biased and have over-estimated errors for $\Delta\Gamma_s/\Gamma_s$ and under-estimated errors for $\tau_{B_s^0}$. One can note that the biases of $\Delta\Gamma_s/\Gamma_s$ seem to disappear when the statistics increases. A more detailed study on the likelihood terms depending on $1/\tau_{B_s^0} = \Delta\Gamma_s$ would be necessary to check if the extremum is well defined.
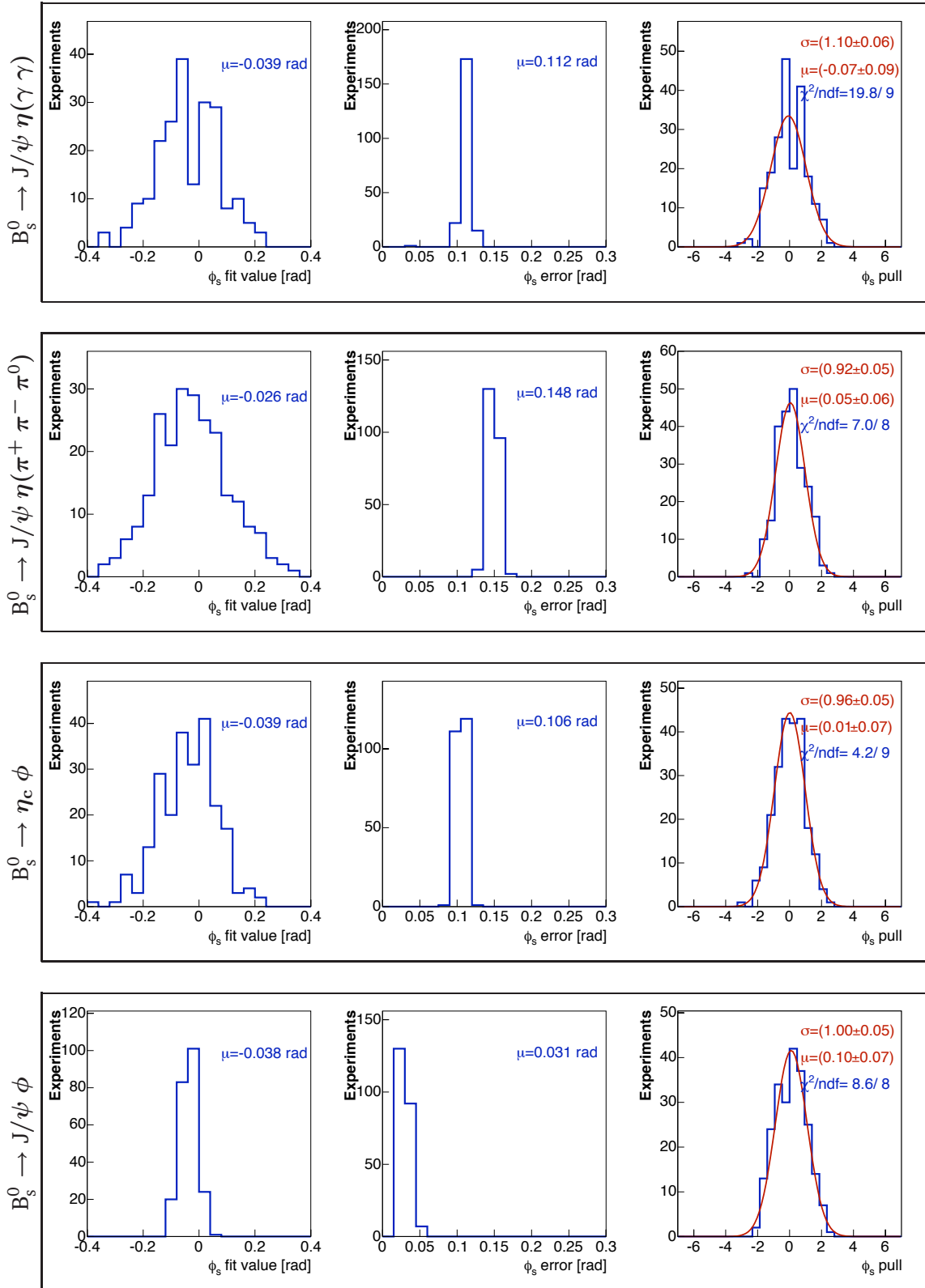
Figure 5.9: ϕ_s likelihood fit output, error and pull distributions for the nominal parameters.

Figure 5.10: Δm_s likelihood fit output, error and pull distributions for the nominal parameters.

Figure 5.11: $\Delta\Gamma_s/\Gamma_s$ likelihood fit output, error and pull distributions for the nominal parameters.

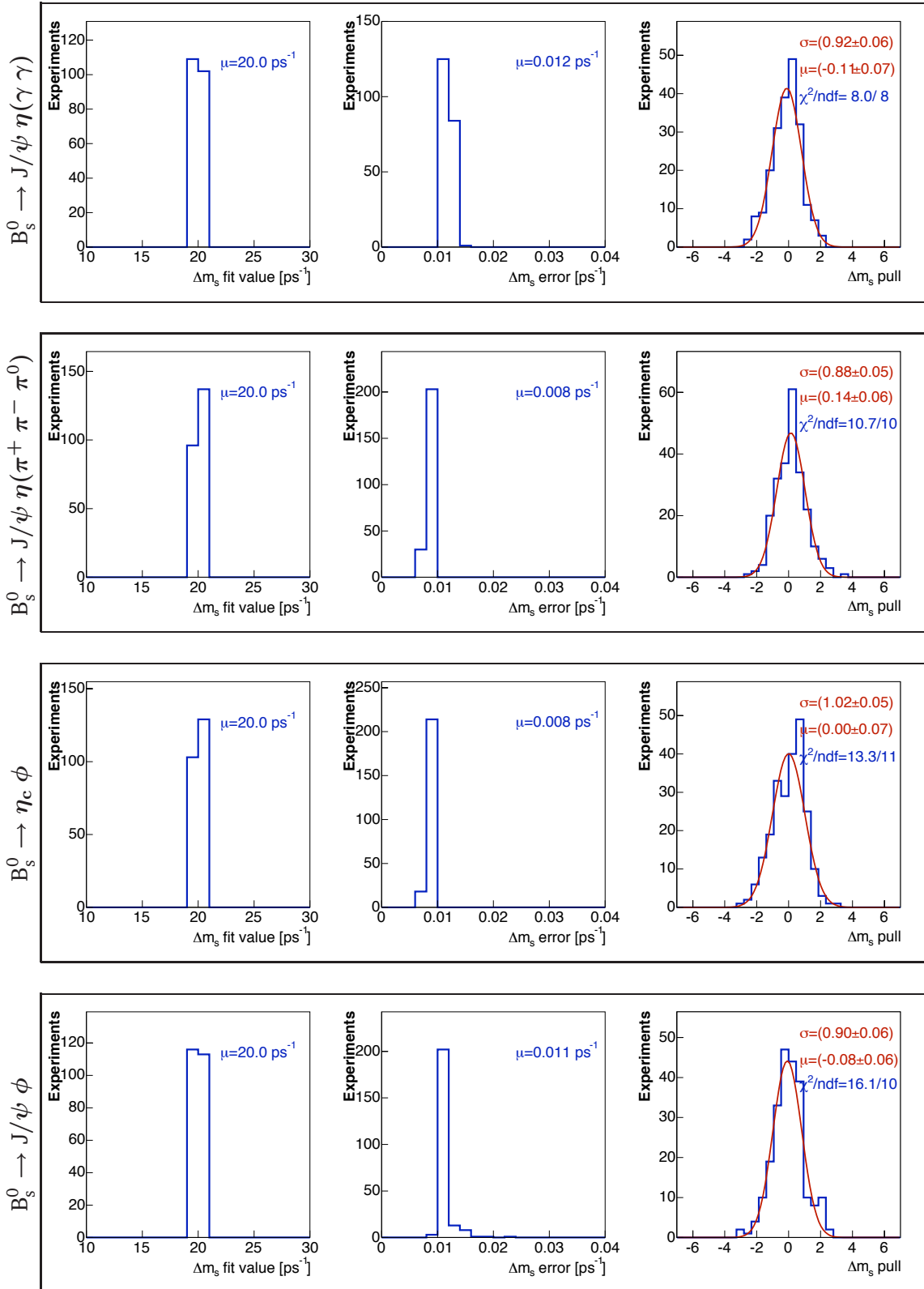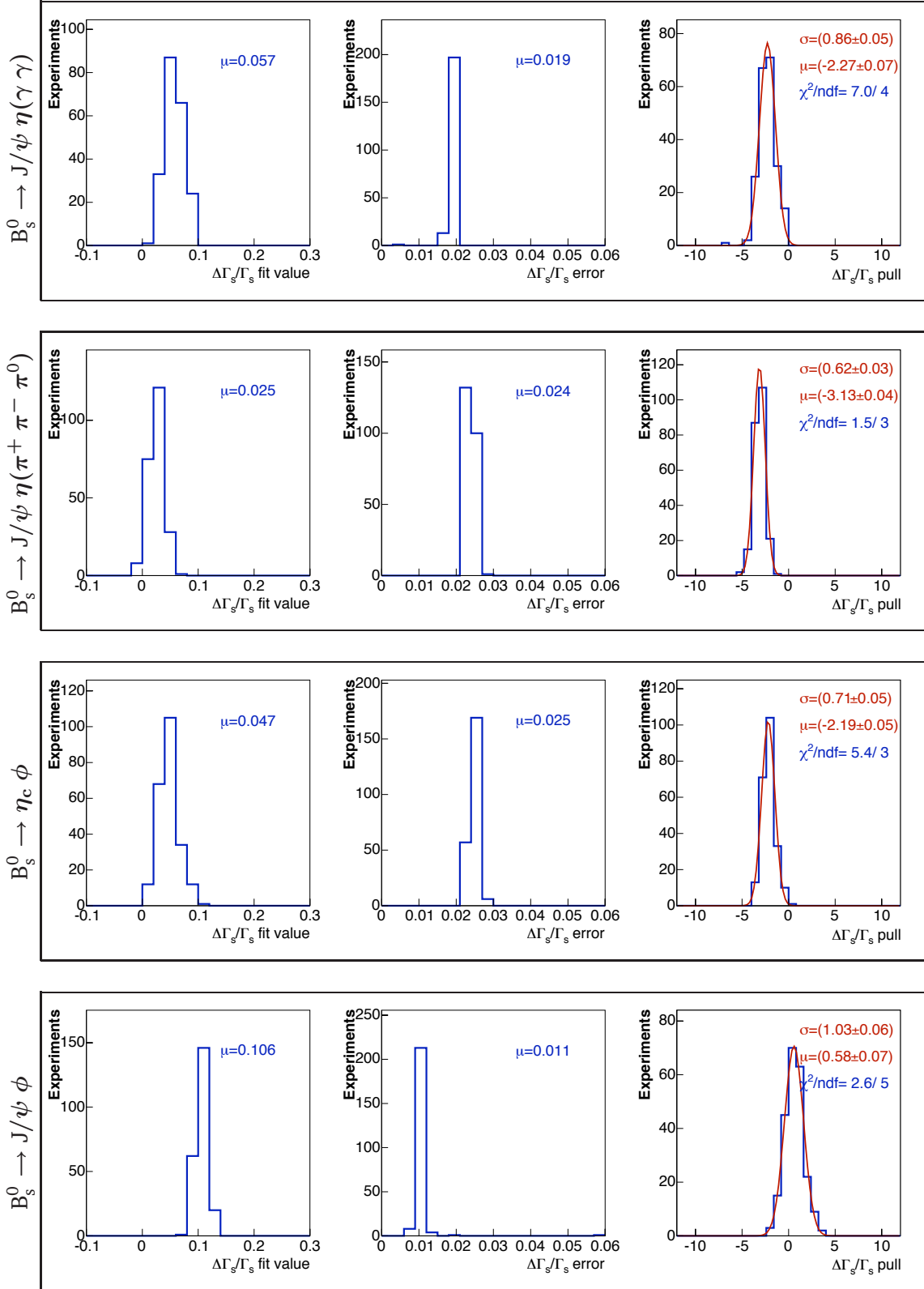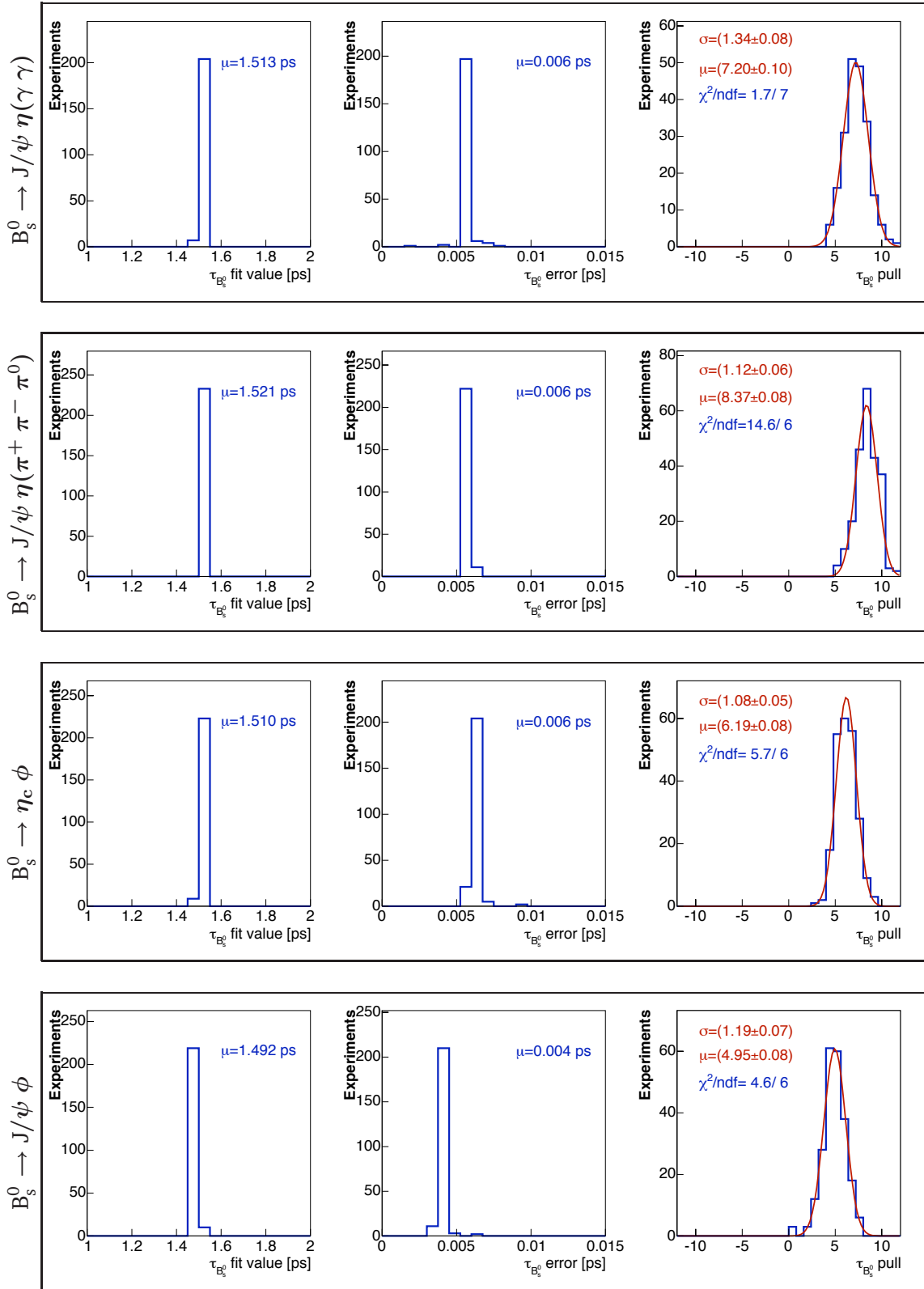Figure 5.12: $\tau_{B_s^0}$ likelihood fit output, error and pull distributions for the nominal parameters.
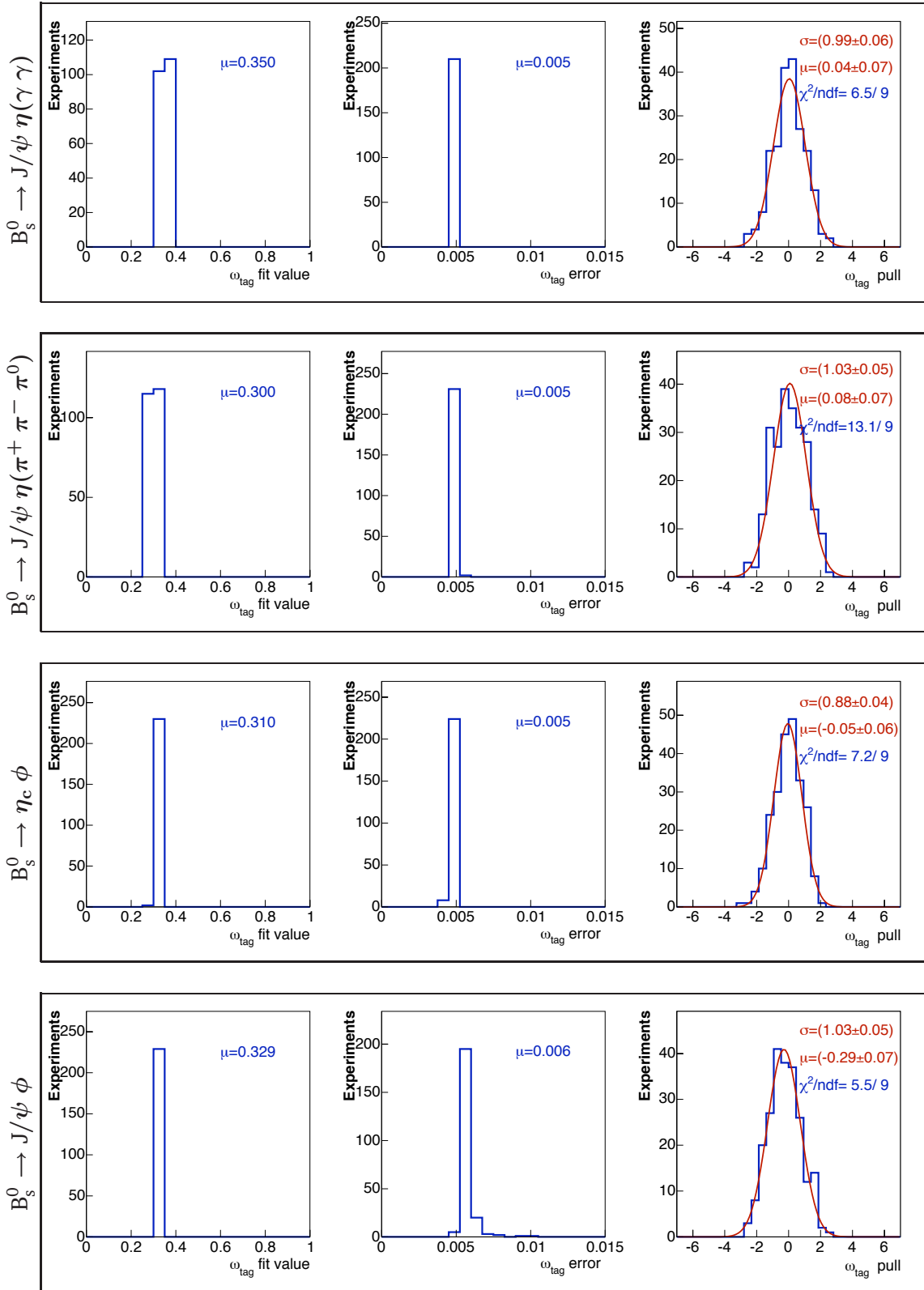
Figure 5.13: ω_{tag} *likelihood fit output, error and pull distributions for the nominal parameters.*
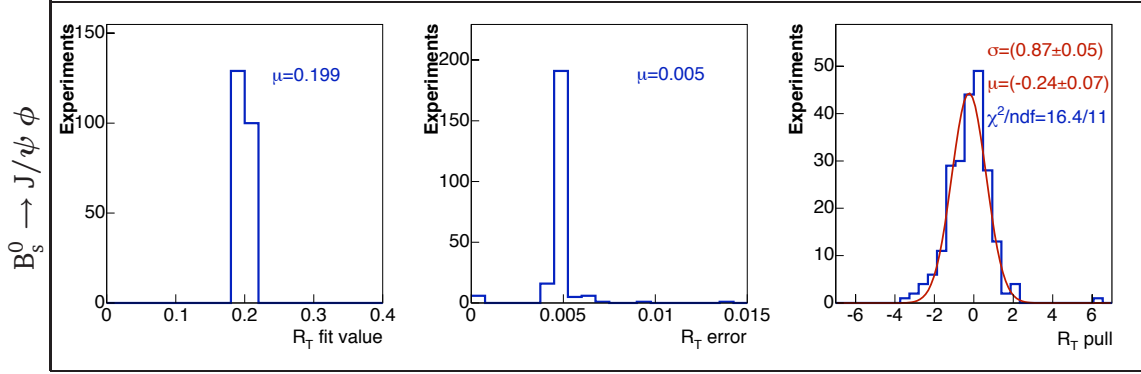
Figure 5.14: *R_T likelihood fit output, error and pull distributions for the nominal parameters.*

5.3.4   Sensitivities with scanned parameters

The sensitivity to the physics parameters is explored for different values of ϕ_s, $\Delta\Gamma_s/\Gamma_s$, ω_{tag} and R_T. These parameters are varied one at a time while the other ones are kept to their assumed nominal values but they are still floated. The results are summarized in Tab. (5.4) for the weak mixing phase ϕ_s, in Tab. (5.5) for the mass difference Δm_s, in Tab. (5.6) for the relative proper time difference $\Delta\Gamma_s/\Gamma_s$, in Tab. (5.7) for B_s^0 proper time $\tau_{B_s^0}$, in Tab. (5.8) for wrong tag fraction ω_{tag} and in Tab. (5.9) for the CP-odd fraction R_T.

The different parameter set-ups are defined as:

A   Nominal parameters defined in Section (5.2.8);

B   **A** with $\Delta m_s = 15$ [ps^{-1}];

C   **A** with $\Delta m_s = 25$ [ps^{-1}];

D   **A** with $\phi_s = -0.2$ [rad];

E   **A** with $\phi_s = 0.0$ [rad];

F   **A** with $\Delta\Gamma_s/\Gamma_s = 0.0$;

G   **A** with $\Delta\Gamma_s/\Gamma_s = 0.2$;

H   **A** with $R_T = 0.0$;

 I   **A** with $R_T = 0.1$;

J   **A** with $R_T = 0.3$;

K   **A** with $R_T = 0.5$.

The four last categories, **H, I , J** and **K**, only make sense for the $B_s^0 \rightarrow J/\psi\ \phi$ channel, where an admixture of CP eigenstates is present. Therefore the results when R_T varies are presented in a stand alone table, Tab. (5.10).

$\sigma(\phi_s)$ [rad]	A	B	C	D	E	F	G
$B_s^0 \to J/\psi\,\eta(\gamma\,\gamma)$	**0.112**	0.102	0.126	0.112	0.114	0.120	0.099
$B_s^0 \to J/\psi\,\eta(\pi^+\,\pi^-\,\pi^0)$	**0.148**	0.136	0.161	0.149	0.151	0.152	0.139
$B_s^0 \to \eta_c\,\phi$	**0.106**	0.100	0.113	0.108	0.105	0.109	0.097
$B_s^0 \to J/\psi\,\phi$	**0.031**	0.028	0.034	0.032	0.030	0.033	0.030

Table 5.4: *Sensitivity of LHCb to ϕ_s after one year of data taking when varying the different parameters.*

$\sigma(\Delta m_s)$ [ps^{-1}]	A	B	C	D	E	F	G
$B_s^0 \to J/\psi\,\eta(\gamma\,\gamma)$	**0.0122**	0.0106	0.0133	0.0121	0.0117	0.0117	0.0120
$B_s^0 \to J/\psi\,\eta(\pi^+\,\pi^-\,\pi^0)$	**0.0084**	0.0076	0.0093	0.0084	0.0084	0.0083	0.0085
$B_s^0 \to \eta_c\,\phi$	**0.0084**	0.0079	0.0093	0.0084	0.0084	0.0083	0.0086
$B_s^0 \to J/\psi\,\phi$	**0.0113**	0.0106	0.0126	0.0111	0.0115	0.0112	0.0117

Table 5.5: *Sensitivity of LHCb to Δm_s after one year of data taking when varying the different parameters.*

$\sigma(\Delta\Gamma_s/\Gamma_s)$	A	B	C	D	E	F	G
$B_s^0 \to J/\psi\,\eta(\gamma\,\gamma)$	**0.019**	0.019	0.019	0.019	0.019	0.019	0.018
$B_s^0 \to J/\psi\,\eta(\pi^+\,\pi^-\,\pi^0)$	**0.024**	0.024	0.024	0.024	0.024	0.023	0.025
$B_s^0 \to \eta_c\,\phi$	**0.025**	0.025	0.025	0.025	0.024	0.024	0.024
$B_s^0 \to J/\psi\,\phi$	**0.011**	0.011	0.010	0.011	0.011	0.012	0.009

Table 5.6: *Sensitivity of LHCb to $\Delta\Gamma_s/\Gamma_s$ after one year of data taking when varying the different parameters.*

$\sigma(\tau_{B_s^0})$ [ps]	A	B	C	D	E	F	G
$B_s^0 \to J/\psi\,\eta(\gamma\,\gamma)$	**0.0057**	0.0057	0.0057	0.0057	0.0057	0.0058	0.0065
$B_s^0 \to J/\psi\,\eta(\pi^+\,\pi^-\,\pi^0)$	**0.0059**	0.0058	0.0059	0.0059	0.0058	0.0058	0.0066
$B_s^0 \to \eta_c\,\phi$	**0.0062**	0.0062	0.0062	0.0062	0.0062	0.0061	0.0075
$B_s^0 \to J/\psi\,\phi$	**0.0041**	0.0045	0.0041	0.0041	0.0041	0.0048	0.0039

Table 5.7: *Sensitivity of LHCb to $\tau_{B_s^0}$ after one year of data taking when varying the different parameters.*

$\sigma(\omega_{tag})$	A	B	C	D	E	F	G
$B_s^0 \to J/\psi\,\eta(\gamma\,\gamma)$	**0.0049**	0.0044	0.0056	0.0049	0.0049	0.0049	0.0050
$B_s^0 \to J/\psi\,\eta(\pi^+\,\pi^-\,\pi^0)$	**0.0046**	0.0042	0.0052	0.0046	0.0046	0.0046	0.0046
$B_s^0 \to \eta_c\,\phi$	**0.0046**	0.0043	0.0049	0.0046	0.0046	0.0046	0.0046
$B_s^0 \to J/\psi\,\phi$	**0.0056**	0.0050	0.0062	0.0055	0.0055	0.0055	0.0059

Table 5.8: *Sensitivity of LHCb to ω_{tag} after one year of data taking when varying the different parameters.*

$\sigma(R_T)$	A	B	C	D	E	F	G
$B_s^0 \to J/\psi\,\phi$	**0.0047**	0.0047	0.0046	0.0047	0.0046	0.0048	0.0047

Table 5.9: *Sensitivity of LHCb to R_T after one year of data taking when varying the different parameters.*

$B_s^0 \to J/\psi\ \phi$	**H**	**I**	**A**	**J**	**K**
$\sigma(\phi_s)$ [rad]	0.021	0.025	**0.031**	0.039	0.062
$\sigma(\Delta m_s)$ [ps^{-1}]	0.0118	0.0117	**0.0113**	0.0114	0.0115
$\sigma(\Delta\Gamma_s/\Gamma_s)$	0.0087	0.0097	**0.0107**	0.0117	0.0140
$\sigma(\tau_{B_s^0})$ [ps]	0.0048	0.0047	**0.0041**	0.0037	0.0037
$\sigma(\omega_{tag})$	0.0058	0.0056	**0.0056**	0.0055	0.0055
$\sigma(R_T)$	0.0047	0.0047	**0.0047**	0.0047	0.0044

Table 5.10: *Sensitivity of LHCb to the physics parameters after one year of data taking when varying the different parameters, for the $B_s^0 \to J/\psi\ \phi$ channel.*

This scan allows to underline the dependencies of the physics parameters to different input values. The most remarkable behaviors are:

ϕ_s The weak mixing phase sensitivity decreases with increasing Δm_s and R_T and with decreasing $\Delta\Gamma_s/\Gamma_s$;

Δm_s The sensitivity to Δm_s decreases with increasing Δm_s and $\Delta\Gamma_s/\Gamma_s$;

ω_{tag} The wrong tag fraction sensitivity also decreases with increasing Δm_s.

The behavior of $\tau_{B_s^0}$ and $\Delta\Gamma_s/\Gamma_s$ sensitivities are more difficult to assess since these parameters are strongly correlated.

For the measurement of the mixing phase ϕ_s, one can only say that this parameter will be better determined when $\Delta\Gamma_s/\Gamma_s$ is large and Δm_s and R_T are small.

5.3.5   Combined sensitivities to ϕ_s

One can now combine the different decay mode results obtained for the different decay channels in order to estimate the expected statistical precision on the B_s^0 physics parameters for 2 fb^{-1}. This is done using the formula:

$$\frac{1}{\sigma_{b \to \bar{c}c\bar{s}}^k} = \sqrt{\sum_i \left(\frac{1}{\sigma_i^k}\right)^2},$$

where the σ_i^k represents the sensitivity of the channel i to the physics variable k. The contribution of each channel to the sensitivity can be estimated with Weight $= (\sigma_{b \to \bar{c}c\bar{s}}^k/\sigma_i^k)^2$. The results are summarized in Tab. (5.11). The relative contribution of the pure decays in the estimation of $\sigma(\phi_s)$ is $\sim 17.1\%$.

For 10 fb^{-1}, i.e. 5 years of LHCb data taking at the actual nominal luminosity $\mathcal{L}_{\text{LHCb}}^{av} = 2 \cdot 10^{32}$ cm^{-2}s^{-1}, the estimated sensitivity on ϕ_s is $\sigma_{b \to \bar{c}c\bar{s}}^{\phi_s} \approx 0.013$ rad.

5.4   Discussion

The contribution of B_s^0 decaying to pure CP eigenstates to the determination of the B_s^0 physics parameters is limited. The fact that the decay does not contain both an even and a odd part is not significant compared to the huge difference in the available statistics. One can however note that the admixture of CP eigenstates degrades the sensitivity on the weak mixing phase ϕ_s from 0.021 mrad to 0.031 mrad (cf. Tab. (5.10)).

Channels	$\sigma(\phi_s)$ [rad]	Weight [%]
$B_s^0 \rightarrow J/\psi \, \eta(\gamma \, \gamma)$	0.112	6.4
$B_s^0 \rightarrow J/\psi \, \eta(\pi^+ \, \pi^- \, \pi^0)$	0.148	3.6
$B_s^0 \rightarrow \eta_c \, \phi$	0.106	7.1
Combined three pure CP eigenstates channels	**0.068**	17.1
$B_s^0 \rightarrow J/\psi \, \phi$	0.031	82.9
Combined all four CP eigenstates channels	**0.028**	100.0

Table 5.11: *Combined ϕ_s sensitivity for the $\bar{b} \rightarrow \bar{c}c\bar{s}$ decays into CP eigenstates with and without the $B_s^0 \rightarrow J/\psi \, \phi$.*

This study has been performed with the three pure CP eigenstate channels described in this chapter. Of course, several other decay modes could be added. They are under investigation at the present time, such as for example, the $B_s^0 \rightarrow J/\psi(e^+ \, e^-) \, \eta(\gamma \, \gamma)$ (briefly presented in Appendix (C)), the $B_s^0 \rightarrow J/\psi(\mu^+ \, \mu^-) \, \eta'(\pi^+ \, \pi^- \, \eta)$ and the $B_s^0 \rightarrow J/\psi(\mu^+ \, \mu^-) \, \eta'(\rho^0 \, \gamma)$ decay modes. All of them, however, contain photons in their final state and will suffer from the poor resolution both in energy and in position of the calorimeter. In addition their yields will be lower than for $B_s^0 \rightarrow J/\psi \, \eta(\gamma \, \gamma)$. Therefore, it is reasonable to think that their contribution to the determination of ϕ_s, Δm_s and $\Delta \Gamma_s/\Gamma_s$ will be marginal.

One major increase in statistics will be the $B_s^0 \rightarrow J/\psi(e^+ \, e^-) \, \phi$ channel which can add more than 25'000 events to the $B_s^0 \rightarrow J/\psi \, \phi$ decays.

With a better electromagnetic calorimeter, we could improve the energy and the momentum resolutions on the photons. One could then relax the cuts on the η parameters and therefore, the selection efficiency would scale up. This improvement will benefit to all the decays in which photons are present.

The toy Monte Carlo suffers from a limitation in the proper time event-by-event error model. Only one contribution can be input in the simulation as well as only one scale factor. For the channels with a scale factor larger than 1, the determination of the physics parameters performed by the control channel will be worsened, especially the wrong tag fraction which has direct consequences in the estimation of ϕ_s. Future developments of the analysis tools could enhance the quoted sensitivities for the $B_s^0 \rightarrow J/\psi \, \eta$ channels.

Although the contribution of the decay channels into pure CP eigenstates is low, they can be used to cross-check the results obtained with the $B_s^0 \rightarrow J/\psi \, \phi$ "golden decay mode". And if New Physics is present, ϕ_s will be larger and these low statistics channels will be able to bring to light its effect.

Conclusion

$\mathfrak{T}$HE study presented in this dissertation demonstrates the ability of the LHCb experiment to reconstruct the $B_s^0 \to J/\psi\, \eta$ decay channel, offering an access to the $\sin(\phi_s)$ measurement. The present work also points out that the pure CP eigenstates $\bar{b} \to \bar{c}c\bar{s}$ quark transitions contribute substantially to the determination of the B_s^0 weak mixing phase.

The selection of the $B_s^0 \to J/\psi(\mu^+\ \mu^-)\ \eta(\gamma\ \gamma)$ and the $B_s^0 \to J/\psi(\mu^+\ \mu^-)\ \eta(\pi^+\ \pi^-\ \pi^0)$ channels developed in the present work is based on the topological and kinetic characteristics of the B-meson decays which are its impact parameters, its transverse momentum and its flight distance. This selection has been optimized to keep the highest selection efficiency for the signal while reducing at maximum the contribution of background events composed of inclusive $b\bar{b}$, specific $H_b \to J/\psi\, X$ channels and inclusive J/ψ events. The analysis shows that the $H_b \to J/\psi\, X$ is the only background contribution to the background-to-signal ratio. The B/S for the $\eta \to \gamma\gamma$ channel is between 2.6 ± 1.3 and 1.7 ± 0.9 before trigger for a η mixing angle running from $\theta_P = -20°$ to $\theta_P = -10°$. The statistics available for the $\eta \to \pi^+\pi^-\pi^0$ decay mode were not sufficient to determine precisely the B/S ratio. However a 90% CL interval has been estimated for this B/S ratio to [0.6, 3.9] for $\theta_p = -20°$ and [0.4, 2.6] for $\theta_p = -10°$.

The branching fraction of the $B_s^0 \to J/\psi\, \eta$ channel has been estimated to be in the range $[3.12 \cdot 10^{-4}; 4.76 \cdot 10^{-4}]$ depending on the η mixing angle. Thanks to the high luminosity of LHCb, between 8'000 and 10'000 events can be reconstructed and selected in one year with satisfactory performances. After applying a Kalman Filter fit, the mass resolutions are 33.6 ± 0.7 MeV/c^2 for the $\eta \to \gamma\gamma$ channel and 20.0 ± 0.7 MeV/c^2 for the $\eta \to \pi^+\pi^-\pi^0$ decay mode. The proper time resolutions are both around 35 fs. Nevertheless the pull distributions after the Kalman Filter fit show an under-estimation of the errors of $\sim 22\%$ for the "photon channel" and $\sim 32\%$ for the "pion decay mode". The important parameter for the sensitivity studies is not the resolution but the error on the proper time. The Kalman Filter fit does not allow for the moment to obtain the correct lifetime errors: corrections have been applied to account for this.

The general feeling is that this analysis deserves a continuation. Especially, improvements in the photon reconstruction and proper time fitting strategies can still be performed.

These results have been then used in a toy Monte Carlo to assess the sensitivity of the LHCb experiment to the B_s^0 physics parameters using pure CP eigenstates $\bar{b} \to \bar{c}c\bar{s}$ channels. In addition to $B_s^0 \to J/\psi\, \eta(\gamma\ \gamma)$ and $B_s^0 \to J/\psi\, \eta(\pi^+\ \pi^-\ \pi^0)$, the decay to a pure CP eigenstate $B_s^0 \to \eta_c\, \phi$ has been added. These three decay modes are finally compared to the $B_s^0 \to J/\psi(\mu^+\ \mu^-)\ \phi(K^+\ K^-)$ which has a much larger statistics but suffers from being a non-pure CP eigenstate. An angular analysis is therefore required to distinguish

between the different CP contributions, an operation which can worsen its sensitivity to ϕ_s.

This simulation takes into account the proper time error measurements, the B/S ratios and the selection efficiencies of the signal with respect to the B_s^0 proper time. The tagging efficiencies are also included in the toy Monte Carlo. Reproducing several times the simulation for one year of LHCb data taking, we obtain the statistical error on the B_s^0 weak mixing phase. This error allows to estimate the sensitivity of the LHCb experiment to ϕ_s which varies from 0.10 rad to 0.15 rad for the pure CP eigenstates channels and depends on the values of ω_{tag}, $\Delta\Gamma_s/\Gamma_s$ and ϕ_s. They contribute up to 17% of the total sensitivity on the B_s^0 weak mixing phase while the other 83% are covered by the $B_s^0 \to J/\psi \, \phi$ channel with a sensitivity to this parameter of 0.031 rad.

As the B_s^0 system is poorly known for the time being, the first year of LHCb data taking will provide the first measurements with high statistics to determine the weak mixing phase ϕ_s. Any value of ϕ_s substantially larger than the SM prediction ($\phi_s \simeq -0.04$ rad) will be an evidence for New Physics. Therefore all the channels which can contribute to its measurement and which can help to improve the accuracy of its determination will be required.

Appendix A

Phase convention

Calculation of the ratio q/p. In both the B_d^0 and B_s^0 systems, it can be argued that $|\Gamma_{12}| \ll |M_{12}|$ and that CP is conserved in $B_q^0 - \overline{B}_q^0$ mixing. As a result:

$$\frac{q}{p} = -\eta_B e^{i\xi}, \tag{A.1}$$

$$= -\sqrt{\frac{M_{12}^*}{M_{12}}}, \tag{A.2}$$

where ξ is the arbitrary CP transformation phase in

$$(\mathcal{CP})\,|B_q^0\rangle = e^{2i\xi}|\overline{B}_q^0\rangle, \quad (\mathcal{CP})\,|\overline{B}_q^0\rangle = e^{-2i\xi}|B_q^0\rangle.$$

The parameter $\eta_B = \pm 1$ appears in $(\mathcal{CP})\,|B_H\rangle = \eta_B|B_H\rangle$, consistently with the fact that, if there is CP conservation in the mixing, then the eigenstates of the Hamiltonian must also be CP eigenstates.

Let us use Eq. (A.2) to calculate the ratio q/p. M_{12} is obtained from an effective Hamiltonian having a weak (CP odd) phase $-\phi_M$ and a $\Delta_B = 2$ operator $\mathcal{O}$:

$$M_{12} = e^{-i\phi_M}\langle B_q^0|\mathcal{O}|\overline{B}_q^0\rangle, \quad M_{12}^* = e^{i\phi_M}\langle \overline{B}_q^0|\mathcal{O}^\dagger|B_q^0\rangle.$$

Using the relation $(\mathcal{CP})\,\mathcal{O}^\dagger\,(\mathcal{CP})^\dagger = e^{2i\xi_M}\mathcal{O}$ and the unitarity of $(\mathcal{CP})$, the ratio becomes:

$$\frac{q}{p} = -\eta_B e^{i(\phi_M+\xi+\xi_M)}. \tag{A.3}$$

This should be equal to $-\eta_B e^{i\xi}$, as in Eq. (A.1). The CP transformation phase ξ_M must therefore be chosen such that $\phi_M + \xi_M = 0$.

Calculation of λ_f. Let us consider the decays of B_q^0 and $\overline{B}_q^0$ into a CP eigenstate f_{cp}:

$$(\mathcal{CP})\,|f_{cp}\rangle = \eta_f|f_{cp}\rangle,$$

with $\eta_f = \pm 1$. We assume that the decay amplitudes have only one weak phase ϕ_D, with an operator $\mathcal{O}'$ controlling the decay,

$$A_f = e^{i\phi_D}\langle f_{cp}|\mathcal{O}'|B_q^0\rangle, \quad \overline{A}_f = e^{-i\phi_D}\langle f_{cp}|\mathcal{O}'^\dagger|\overline{B}_q^0\rangle.$$

Using the relation $(\mathcal{CP})\,\mathcal{O}'^{\dagger}\,(\mathcal{CP})^{\dagger} = e^{2i\xi_D}\mathcal{O}'$ and the unitarity of $(\mathcal{CP})$, the ratio of the amplitudes becomes:

$$\frac{\overline{A}_f}{A_f} = -\eta_f e^{-i(2\phi_D + \xi + \xi_D)}. \tag{A.4}$$

While both (q/p) and $(\overline{A}_f/A_f)$ acquire overall phase redefinitions when phase rotations are made, the quantity:

$$\lambda_f = \frac{q}{p}\frac{\overline{A}_f}{A_f} \tag{A.5}$$

has a convention independent phase that has physical significance and will be used to differentiate the CP violations. Combining Eq. (A.3) and Eq. (A.4), one gets:

$$\lambda_f \equiv \frac{q_B}{p_B}\frac{\overline{A}_f}{A_f} = -\eta_{\mathrm{B}}\eta_f e^{i(\phi_M - 2\phi_D)}e^{i(\xi_M - \xi_D)}.$$

As ξ_M and ξ_D arise in the CP transformations of the mixing and the decay operators, they are equal and cancel out, which leads to:

$$\lambda_f \equiv \frac{q_B}{p_B}\frac{\overline{A}_f}{A_f} = -\eta_{\mathrm{B}}\eta_f e^{i(\phi_M - 2\phi_D)}.$$

For decays dominated by a single diagram, we obtain:

$$\lambda_f = -\eta_{\mathrm{B}}\eta_f e^{-i\phi_{\mathrm{CKM}}}, \quad \text{with} \quad \phi_{\mathrm{CKM}} = \phi_M - 2\phi_D.$$

As direct consequences of this result, and from the fact that in the Standard Model, when neglecting CP violation, one obtains $\eta_{\mathrm{B}} = -1$, meaning that the heavier state is CP odd in that limit, we can rewrite Eqs. (1.21):

$$|\lambda_f| = 1, \quad C_f = 0, \quad S_f = -\eta_f \sin\phi_{\mathrm{CKM}}, \quad D_f = \eta_f \cos\phi_{\mathrm{CKM}}.$$

Appendix B

Background contributions

𝕿ʜᴇ three different background contribution ($b\bar{b}$ events, $H_b \to J/\psi$ X candidates and prompt J/ψ) are detailed in the following tables. Tab. (B.1) summarizes the channels investigated, the number of events used for the analysis and the tight cuts surviving events (identical to Tab. (4.12)). All the results given in this appendix are based on these numbers.

The $b\bar{b}$ contribution to the B/S ratio, already given in Tab. (4.13), is shown again in Tab. (B.2), in order to have a complete survey of the background contributions to B/S in this appendix.

The details of the specific background contributions, for the six specific decays under study (see Sec. (3.6.3)), can be found in this appendix tables, before and after all triggers. They represent the 90% confidence level interval of the background level when there are less than 10 events selected:

- $B_d^0 \to J/\psi(\mu^+ \; \mu^-) \; K^*(K^+ \; \pi^-)$ in Tab. (B.3);

- $B_d^0 \to J/\psi(\mu^+ \; \mu^-) \; K_S^0(\pi^+ \; \pi^-)$ in Tab. (B.4);

- $B^+ \to J/\psi(\mu^+ \; \mu^-) \; K^+$ in Tab. (B.5);

- $B_s^0 \to J/\psi(\mu^+ \; \mu^-) \; \phi(K^+ \; K^-)$ in Tab. (B.6);

- $B_s^0 \to J/\psi(\mu^+ \; \mu^-) \; \eta^{'}(\pi^+ \; \pi^- \; \eta)$ in Tab. (B.7);

- $\Lambda_b^0 \to J/\psi \; \Lambda$ Tab. (B.8).

Tab. (B.9) shows the B/S results of the selection on the $H_b \to J/\psi$ X events. Prompt J/ψ analysis is also shown on Tab. (B.10).

133

$B_s^0 \to J/\psi\ \eta$	$\eta \to \gamma\gamma$			$\eta \to \pi^+\pi^-\pi^0$		
	N_{gen}	N_{sel}	N_{HLT}	N_{gen}	N_{sel}	N_{HLT}
inclusive $b\bar{b}$	30'500'000	16	14	27'500'00	3	3
$\to$ inclusive $b\bar{b}$ v1	10'500'000	0	0	10'500'00	0	0
$\to$ inclusive $b\bar{b}$ v2	20'000'000	16	14	17'000'00	3	3
$B_d^0 \to J/\psi(\mu^+\ \mu^-)\ K^*(K^+\ \pi^-)$	641'000	25	19	633'000	23	17
$B_d^0 \to J/\psi(\mu^+\ \mu^-)\ K_S^0(\pi^+\ \pi^-)$	89'000	3	3	89'000	0	0
$B^+ \to J/\psi(\mu^+\ \mu^-)\ K^+$	200'000	3	3	200'000	0	0
$B_s^0 \to J/\psi(\mu^+\ \mu^-)\ \phi(K^+\ K^-)$	366'000	10	8	394'000	121	100
$B_s^0 \to J/\psi(\mu^+\ \mu^-)\ \eta'(\pi^+\ \pi^-\ \eta)$	100'000	2	2	100'000	6	6
$\Lambda_b^0 \to J/\psi\ \Lambda$	100'000	6	0	100'000	0	0
inclusive J/ψ	1'800'000	6	3	1'700'000	1	0
$\to H_b \to J/\psi\ X$	128'000	6	3	121'000	1	0
$\to$ prompt J/ψ	1'672'000	0	0	1'579'000	0	0

Table B.1: *Number of events surviving the tight selection for the three types of background events (see Section (3.6.3)). The mass window has been increased by a factor six for the selection on $b\bar{b}$ events.*

Decays	$\theta_p = -20°$		$\theta_p = -10°$	
	No trigger	HLT	No trigger	HLT
$B_s^0 \to J/\psi(\mu^+\ \mu^-)\ \eta(\gamma\ \gamma)$	2.6±1.3	3.0±1.5	1.7±0.9	2.0±1.0
$B_s^0 \to J/\psi(\mu^+\ \mu^-)\ \eta(\pi^+\ \pi^-\ \pi^0)$	[0.6, 3.9]	[0.7, 4.9]	[0.4, 2.6]	[0.5, 3.2]

Table B.2: *Central value and 90% confidence level interval of the $b\bar{b}$ background level, before and after all triggers.*

Decays	$\theta_p = -20°$		$\theta_p = -10°$	
	No trigger	HLT	No trigger	HLT
$B_s^0 \to J/\psi(\mu^+\ \mu^-)\ \eta(\gamma\ \gamma)$	0.07±0.03	0.07±0.03	0.05±0.02	0.05±0.02
$B_s^0 \to J/\psi(\mu^+\ \mu^-)\ \eta(\pi^+\ \pi^-\ \pi^0)$	0.20±0.10	0.19±0.09	0.13±0.06	0.12±0.06

Table B.3: *Central value of the $B_d^0 \to J/\psi(\mu^+\ \mu^-)\ K^*(K^+\ \pi^-)$ background level, before and after all triggers.*

Decays	$\theta_p = -20°$		$\theta_p = -10°$	
	No trigger	HLT	No trigger	HLT
$B_s^0 \to J/\psi(\mu^+\ \mu^-)\ \eta(\gamma\ \gamma)$	[0.01, 0.07]	[0.01, 0.07]	[0.01, 0.05]	[0.01, 0.04]
$B_s^0 \to J/\psi(\mu^+\ \mu^-)\ \eta(\pi^+\ \pi^-\ \pi^0)$	[0, 0.05]	[0, 0.06]	[0, 0.03]	[0, 0.04]

Table B.4: *90% confidence level interval of the $B_d^0 \to J/\psi(\mu^+\ \mu^-)\ K_S^0(\pi^+\ \pi^-)$ background level, before and after all triggers.*

Decays	$\theta_p = -20°$		$\theta_p = -10°$	
	No trigger	HLT	No trigger	HLT
$B_s^0 \to J/\psi(\mu^+ \ \mu^-) \ \eta(\gamma \ \gamma)$	[0, 0.05]	[0.01, 0.06]	[0, 0.03]	[0, 0.04]
$B_s^0 \to J/\psi(\mu^+ \ \mu^-) \ \eta(\pi^+ \ \pi^- \ \pi^0)$	[0, 0.08]	[0, 0.10]	[0, 0.05]	[0, 0.06]

Table B.5: *90% confidence level interval of the* $B^+ \to J/\psi(\mu^+ \ \mu^-) \ K^+$ *background level, before and after all triggers.*

Decays	$\theta_p = -20°$		$\theta_p = -10°$	
	No trigger	HLT	No trigger	HLT
$B_s^0 \to J/\psi(\mu^+ \ \mu^-) \ \eta(\gamma \ \gamma)$	[0, 0.01]	[0, 0.01]	[0, 0.01]	[0, 0.01]
$B_s^0 \to J/\psi(\mu^+ \ \mu^-) \ \eta(\pi^+ \ \pi^- \ \pi^0)$	0.23±0.13	0.24±0.13	0.15±0.08	0.16±0.09

Table B.6: *90% confidence level interval and central value of the* $B_s^0 \to J/\psi(\mu^+ \ \mu^-) \ \phi(K^+ \ K^-)$ *background level, before and after all triggers.*

Decays	$\theta_p = -20°$		$\theta_p = -10°$	
	No trigger	HLT	No trigger	HLT
$B_s^0 \to J/\psi(\mu^+ \ \mu^-) \ \eta(\gamma \ \gamma)$	[0,0]	[0,0]	[0,0]	[0,0]
$B_s^0 \to J/\psi(\mu^+ \ \mu^-) \ \eta(\pi^+ \ \pi^- \ \pi^0)$	[0, 0.01]	[0, 0.01]	[0, 0.01]	[0, 0.01]

Table B.7: *90% confidence level interval of the* $B_s^0 \to J/\psi(\mu^+ \ \mu^-) \ \eta'(\pi^+ \ \pi^- \ \eta)$ *background level, before and after all triggers.*

Decays	$\theta_p = -20°$		$\theta_p = -10°$	
	No trigger	HLT	No trigger	HLT
$B_s^0 \to J/\psi(\mu^+ \ \mu^-) \ \eta(\gamma \ \gamma)$	[0, 0.02]	[0, 0.01]	[0, 0.01]	0
$B_s^0 \to J/\psi(\mu^+ \ \mu^-) \ \eta(\pi^+ \ \pi^- \ \pi^0)$	[0, 0.01]	[0, 0.02]	[0, 0.01]	[0, 0.01]

Table B.8: *90% confidence level interval of the* $\Lambda_b^0 \to J/\psi \ \Lambda$ *background level, before and after all triggers.*

Decays	$\theta_p = -20°$		$\theta_p = -10°$	
	No trigger	HLT	No trigger	HLT
$B_s^0 \to J/\psi(\mu^+ \ \mu^-) \ \eta(\gamma \ \gamma)$	[1.2, 6.3]	[0.8, 5.4]	[0.8, 4.1]	[0.5, 3.5]
$B_s^0 \to J/\psi(\mu^+ \ \mu^-) \ \eta(\pi^+ \ \pi^- \ \pi^0)$	[0.2, 7.6]	[0, 5.3]	[0.1, 5.0]	[0, 3.5]

Table B.9: *90% confidence level interval of the* $H_b \to J/\psi \ X$ *background level, before and after all triggers.*

Decays	$\theta_p = -20°$		$\theta_p = -10°$	
	No trigger	HLT	No trigger	HLT
$B_s^0 \to J/\psi(\mu^+ \ \mu^-) \ \eta(\gamma \ \gamma)$	[0, 1.6]	[0, 2.1]	[0, 1.1]	[0, 1.4]
$B_s^0 \to J/\psi(\mu^+ \ \mu^-) \ \eta(\pi^+ \ \pi^- \ \pi^0)$	[0,5.2]	[0, 6.5]	[0, 3.4]	[0, 4.3]

Table B.10: *90% confidence level interval of the prompt* J/ψ *background level, before and after all triggers.*

Appendix C

$B_s^0 \rightarrow J/\psi(e^+ \, e^-) \, \eta(\gamma \, \gamma)$ selection at LHCb

---

𝕿HE determination of the weak mixing phase ϕ_s with pure CP transitions requires as many contributions as possible. Therefore an analysis has been performed on the $B_s^0 \rightarrow J/\psi(e^+ \, e^-) \, \eta(\gamma \, \gamma)$ channel which could be a candidate to an improvement in the determination of the B_s^0 mixing phase. This mode is expected to have less statistics than the $B_s^0 \rightarrow J/\psi(\mu^+ \, \mu^-) \, \eta(\gamma \, \gamma)$. This is caused by the difficulty to reconstruct the electrons momentum. These latter have about 12 meters to travel before reaching the ECAL. All along this trajectory, they will cross the magnetic field, interact with matter and radiate photons via Bremsstrahlung. This impairs the J/ψ momentum reconstruction and leads to a less efficient selection.

The J/ψ ($e^+ \, e^-$) selection starts by making an electron PID requirement of $\Delta \ln L_{e\pi} > 2$. The electron candidates must have a transverse momentum greater than 300 MeV/c. A procedure to add the energy lost by Bremsstrahlung is applied [33]. Taking pairs of oppositely charged electrons, an unconstrained vertex fit is performed and its χ^2 must be less than 10. The momentum of the J/ψ candidate is asked to be larger than $P(J/\psi) = 20$ GeV/c and its minimum P_T is 1000 MeV/c. The impact parameter of the candidate must be larger than 2 with respect to any primary vertices. Finally its mass must be in the range 2.9969 GeV/c^2 < m(J/ψ) < 3.1969 GeV/c^2.

The other cuts of this selection are almost the same as for the $B_s^0 \rightarrow J/\psi(\mu^+ \, \mu^-) \, \eta(\gamma \, \gamma)$ and can be found in Tab. (4.2). Only one cut of the η has been tightened to reduced the combinatorial background as this J/ψ is less clean than the muonic one: $P_T(\eta) = 3'000$ MeV/c. The results of this analysis are summarized in Tab. (C.1). The mass and proper time resolution are given after the η mass constrained fit.

The trigger efficiency of the $B_s^0 \rightarrow J/\psi(e^+ \, e^-) \, \eta(\gamma \, \gamma)$ is much lower than the channels with muons. The electron signature is less clean and their multiplicity too high. Moreover, as no specific channels containing electrons has been yet implemented to the HLT, the triggering efficiency of the High Level Trigger is close to zero. The numbers of Tab. (C.1) are quoted after L1, before HLT.

Fortunately this tight triggering selection benefits to the tagging, performances of which are much better than for the $B_s^0 \rightarrow J/\psi(\mu^+ \, \mu^-) \, \eta(\gamma \, \gamma)$ channel. The wrong tag fraction is particularly low.

This channel has a total selection efficiency 6 times smaller than the "muon one". This means that the expected untagged 2 fb^{-1} yield will be between $\sim$ 1k and $\sim$ 1.5k. The

Parameters	$B_s^0 \to J/\psi(e^+\ e^-)\ \eta(\gamma\ \gamma)$
N_{gen}	197'000
$N_{'ible}$	29'838
N_{ted}	39'636
$N_{'ible\&'ed}$	23'615
N_{sel}	695
N_{L0}	498
N_{L1}	338
N_{HLT}	10
ε_{det} [%]	8.86 ± 0.50
$\varepsilon_{rec/det}$ [%]	59.6 ± 0.2
$\varepsilon_{sel/rec}$ [%]	2.33 ± 0.09
$\varepsilon_{trg/sel}$ [%] (after L1 and before HLT)	48.5 ± 1.9
ε_{tot} [%]	0.060 ± 0.004
2 fb^{-1} untagged yield ($\Theta_P = -10°$) (after L1)	1020 ± 425
2 fb^{-1} untagged yield ($\Theta_P = -20°$) (after L1)	1560 ± 651
B/S ($\Theta_P = -10°$) before triggers (90% CL)	[0; 4.8]
B/S ($\Theta_P = -20°$) before triggers (90% CL)	[0; 3.1]
$\sigma(m_{B_s^0})$ [MeV/c^2]	63.1 ± 2.3
acc_s [ps^{-1}] after L1	1.86 ± 0.15
$\sigma(\tau_{B_s^0})$ [fs]	48.4 ± 2.0
$< \sigma_{t_i^{rec}} >$ [fs]	55
ω_{tag} [%] (after L1)	28.5 ± 3.3
ε_{tag} [%] (after L1)	60.4 ± 2.7
ε_{eff} [%] (after L1)	11.2 ± 4.8

Table C.1: *Summary of the $B_s^0 \to J/\psi(e^+\ e^-)\ \eta(\gamma\ \gamma)$ selection results.*

results can only be worse than the ones obtained with the $B_s^0 \to J/\psi(\mu^+\ \mu^-)\ \eta(\pi^+\ \pi^-\ \pi^0)$ even with a better tagging. Moreover the HLT will not be as good as the dimuon one. This will not allow this contribution to improve very much the pure CP eigenstates sensitivity to ϕ_s.

Bibliography

[1] A. D. SAKHAROV. Violation of CP invariance, C asymmetry, and baryon asymmetry of the Universe. *Pisma Zh. Eksp. Teor. Fiz.*, 5:32–35, 1967.

[2] M. B. GAVELA, P. HERNANDEZ, J. ORLOFF, AND O. PENE. Standard model CP violation and baryon asymmetry. *Mod. Phys. Lett.*, A9:795–810, 1994, hep-ph/9312215.

[3] J. H. CHRISTENSON, J. W. CRONIN, V. L. FITCH, AND R. TURLAY. Evidence for the 2π decay of the K_2^0 meson. *Phys. Rev. Lett.*, 13:138–140, 1964.

[4] BaBar, B. AUBERT ET AL. Measurement of CP violating asymmetries in B^0 decays to CP eigenstates. *Phys. Rev. Lett.*, 86:2515–2522, 2001, hep-ex/0102030.

[5] Belle, K. ABE ET AL. Observation of large CP violation in the neutral B meson system. *Phys. Rev. Lett.*, 87:091802, 2001, hep-ex/0107061.

[6] ELLIOT LEADER AND ENRICO PREDAZZI. *An introduction to gauge theories and modern particle physics*, volume 13. Cambridge University Press, 1996.

[7] ROBERT FLEISCHER. Flavour physics and CP violation. 2004, hep-ph/0405091.

[8] ANDRZEJ J. BURAS AND ROBERT FLEISCHER. Quark mixing, CP violation and rare decays after the top quark discovery. *Adv. Ser. Direct. High Energy Phys.*, 15:65–238, 1998, hep-ph/9704376.

[9] JOAO P. SILVA. Phenomenological aspects of CP violation. 2004, hep-ph/0410351.

[10] P. BALL ET AL. B decays at the LHC. 2000, hep-ph/0003238.

[11] SHELDON L. GLASHOW. Partial Symmmeries of weak interactions. *Nucl. Phys.*, 22:579–588, 1961.

[12] STEVEN WEINBERG. A model of lepton. *Phys. Rev. Lett.*, 19:1264–1266, 1967.

[13] ABDUS SALAM. Weak and electromagnetic interactions. 1968. Originally printed in *Svartholm: Elementary Particle Theory, Proceedings Of The Nobel Symposium Held 1968 At Lerum, Sweden*, Stockholm 1968, 367-377.

[14] S. EIDELMAN ET AL. Review of Particle Physics. *Physics Letters B*, 592:1+, 2004.

[15] Belle, A. ABASHIAN ET AL. Measurement of the CP violation parameter $\sin 2\phi_1$ in B^0 meson decays. *Phys. Rev. Lett.*, 86:2509–2514, 2001, hep-ex/0102018.

[16] E. NOETHER. Invariante Variationsprobleme. *Nachr. D. Koenig. Gesellsch. D. Wiss. Zu Goettingen*, 2:235–237, 1918.

[17] W. PAULI. *Niels Bohr and the Development of Physics*. McGraw-Hill Book Company, Inc, New York, 1955.

[18] PETER W. HIGGS. Spontaneous symmetry breakdown without massless bosons. *Phys. Rev.*, 145:1156–1163, 1966.

[19] M. KOBAYASHI AND T. MASKAWA. CP violation in the renormalizable theory of weak interaction. *Prog. Theor. Phys.*, 49:652–657, 1973.

[20] N. CABIBBO. Unitary symmetry and leptonic decays. *Phys. Rev. Lett.*, 10:531–532, 1963.

[21] S. L. GLASHOW, J. ILIOPOULOS, AND L. MAIANI. Weak interactions with lepton − hadron symmetry. *Phys. Rev.*, D2:1285–1292, 1970.

[22] LING-LIE CHAU AND WAI-YEE KEUNG. Comments on the parametrization of the Kobayashi-Maskawa matrix. *Phys. Rev. Lett.*, 53:1802, 1984.

[23] LINCOLN WOLFENSTEIN. Parametrization of the Kobayashi-Maskawa matrix. *Phys. Rev. Lett.*, 51:1945, 1983.

[24] CECILIA JARLSKOG AND RAYMOND STORA. Unitarity polygons and CP violation areas and phases in the Standard Electroweak Model. *Phys. Lett.*, B208:268, 1988.

[25] R. ALEKSAN, B. KAYSER, AND D. LONDON. Determining the quark mixing matrix from CP violating asymmetries. *Phys. Rev. Lett.*, 73:18–20, 1994, hep-ph/9403341.

[26] GUSTAVO C. BRANCO, LUIS LAVOURA, AND JOAO P. SILVA. *CP violation*. Oxford University Press, 1999.

[27] C. JARLSKOG. A Basis independent formulation of the connection between quark mass matrices, CP violation and experiment. *Z. Phys.*, C29:491–497, 1985.

[28] SuperKEKB Physics Working Group, A. G. AKEROYD ET AL. Physics at super B factory. 2004, hep-ex/0406071.

[29] L. J. SPENCER ET AL. Measurement of B meson semileptonic decay. *Phys. Rev. Lett.*, 47:771–774, 1981.

[30] C. BEBEK ET AL. Evidence for new flavor production at the upsilon (4S). *Phys. Rev. Lett.*, 46:84, 1981.

[31] CLEO, K. CHADWICK ET AL. Decay of b flavored hadrons to single muon and dimuon final states. *Phys. Rev. Lett.*, 46:88–91, 1981.

[32] HEAVY FLAVOR AVERAGING GROUP(HFAG). Averages of b-hadron properties as of winter 2005. 2005, hep-ex/0505100.

[33] LHCb. LHCb technical design report: Reoptimized detector design and performance. 2003. CERN-LHCC-2003-030.

[34] V. WEISSKOPF AND EUGENE P. WIGNER. Calculation of the natural brightness of spectral lines on the basis of Dirac's theory. *Z. Phys.*, 63:54–73, 1930.

[35] V. WEISSKOPF AND E. WIGNER. Over the natural line width in the radiation of the harmonius oscillator. *Z. Phys.*, 65:18–29, 1930.

[36] OLIVIER SCHNEIDER. $B^0 - \overline{B}^0$ mixing. 2004, hep-ex/0405012.

[37] BaBar, B. AUBERT ET AL. Observation of direct CP violation in $B_d^0 \to K^+ \pi^-$ decays. *Phys. Rev. Lett.*, 93:131801, 2004, hep-ex/0407057.

[38] Belle, Y. CHAO ET AL. Evidence for direct CP violation in $B_d^0 \to K^+ \pi^-$ decays. *Phys. Rev. Lett.*, 93:191802, 2004, hep-ex/0408100.

[39] CDF II. Branching fraction and CP asymmetries in $B_{d,s}^0 \to h^+ h'^-$. 2000.

[40] CLEO, S. CHEN ET AL. Measurement of charge asymmetries in charmless hadronic B meson decays. *Phys. Rev. Lett.*, 85:525–529, 2000, hep-ex/0001009.

[41] ZOLTAN LIGETI. The CKM matrix and CP violation. 2004, hep-ph/0408267.

[42] ALEPH, D. BUSKULIC ET AL. First measurement of the B(S) meson mass. *Phys. Lett.*, B311:425–430, 1993.

[43] CDF, F. ABE ET AL. Observation of the decay $B_s^0 \to J/\psi \ \phi$ in $\overline{p} - p$ collisions at $\sqrt{s} = 1.8$ TeV. *Phys. Rev. Lett.*, 71:1685–1689, 1993.

[44] P. Z. SKANDS. Branching ratios for $B_{d,s}^0 \to J/\psi \ \eta$ and $B_{d,s}^0 \to \eta \ \ell^+ \ell^-$, extracting gamma from $B_{d,s}^0 \to J/\psi \ \eta$, and possibilities for constraining C(10A) in semileptonic B decays. *JHEP*, 01:008, 2001, hep-ph/0010115.

[45] TS-CE. Civil engineering LHC Project. `http://ts-dep.web.cern.ch/ts-dep/groups/ce/lhc/LHC_HOME.htm`.

[46] P. IGO-KEMENES. Review of Particle Physics. *The European Physical Journal*, C(15):274, 2004.

[47] LHC Study Group. The Large Hadron Collider: Conceptual design. CERN-AC-95-05-LHC.

[48] 2004. See for instance `http://user.web.cern.ch/user/Index/LHC.html` or `http://lhcb-elec.web.cern.ch/lhcb-elec/html/key_parameters.htm`.

[49] LHCb, S. AMATO ET AL. LHCb technical proposal. CERN-LHCC-98-4.

[50] P. NASON ET AL. Bottom production. In G. ALTARELLI AND M.L. MANGANO, editors, *Proceedings of the 1999 Workshop on Standard Model Physics (and more) at the LHC*, volume CERN 2000-004. CERN Organisation européenne pour la recherche nucléaire, 1999, hep-ph/0003142.

[51] LHCb, P. ROBBE. Parameters of DC04 Monte Carlo productions. `https://uimon.cern.ch/twiki/bin/view/LHCb/SettingsDc04`.

[52] LHCb. LHCb magnet: Technical design report. CERN-LHCC-2000-007.

[53] LHCb. LHCb VELO TDR: Vertex locator. Technical design report. CERN-LHCC-2001-011.

[54] P238, J. ELLET ET AL. Development and test of a large silicon strip system for a hadron collider Beauty trigger. *Nucl. Instr. and Meth.*, A317:28–46, 1992.

[55] LHCb. LHCb : Inner tracker technical design report. 2002. CERN-LHCC-2002-029.

[56] LHCb Outer Tracker, L. B. A. HOMMELS. The LHCb outer tracker detector design and production. CERN-THESIS-2005-035.

[57] LHC-B. LHCb : RICH technical design report. CERN-LHCC-2000-037.

[58] P.A. CHERENKOV. Visible light from clear liquid under the action of gamma radiation. *CR Acc. Sci. USSR*, 8:451, 1934.

[59] LHCb. LHCb RICH detectors Home Page. `http://lhcb-rich.web.cern.ch/lhcb-rich/`.

[60] LHCb. LHCb calorimeters: Technical design report. 2000. CERN-LHCC-2000-036.

[61] LHCb. LHCb muon system technical design report. CERN-LHCC-2001-010.

[62] LHCb. LHCb trigger system technical design report. 2002. CERN-LHCC-2003-031.

[63] LHCb, P. KOPPENBURG AND L. FERNÁNDEZ. HLT exclusive selections design and implementation. 2005. CERN-LHCb-2005-015.

[64] LHCb, P. R. BARBOSA-MARINHO ET AL. LHCb online system technical design report: Data acquisition and experiment control. CERN-LHCC-2001-040.

[65] G. BARRAND ET AL. GAUDI — The software architecture and framework for building LHCb data processing applications. Published in CHEP 2000, Computing in high energy and nuclear physics 92-95, 2000.

[66] M. CATTANEO ET AL. The GAUDI project. `http://proj-gaudi.web.cern.ch/proj-gaudi/`, 2001.

[67] W. POKORSKI ET AL. GAUSS. `http://lhcb-comp.web.cern.ch/lhcb-comp/Simulation/`, 2002.

[68] TORBJÖRN SJÖSTRAND ET AL. High-energy-physics event generation with PYTHIA 6.1. *Comput. Phys. Commun.*, 135:238–259, 2001, hep-ph/0010017.

[69] BABAR. The EVTGEN package home page. `http://www.slac.stanford.edu/~lange/EvtGen/`.

[70] CERN. GEANT— Detector description and Simulation Tool. CERN Program Library Long Writeup W5013.

[71] M. CATTANEO ET AL. BOOLE. `http://lhcb-comp.web.cern.ch/lhcb-comp/Digitization/`, 2003.

[72] M. CATTANEO ET AL. BRUNEL. `http://lhcb-comp.web.cern.ch/lhcb-comp/Reconstruction/`, 2000.

[73] G. CORTI ET AL. DAVINCI. `http://lhcb-comp.web.cern.ch/lhcb-comp/Analysis/`, 2001.

[74] LHCb, M. BENAYOUN AND O. CALLOT. The forward tracking, an optical model method. 2002.

[75] LHCb, X. XIE. Short track reconstruction with VELO and TT. 2003. CERN-LHCb-2003-100.

[76] LHCb, R. HIERCK. Track following in LHCb. 2001. CERN-LHCb-2001-112.

[77] LHCb, R. HIERCK ET AL. Performance of the LHCb OO track-fitting software. 2000. CERN-LHCb-2000-086.

[78] LHCb, FLAVOUR TAGGING WORKING GROUP. v5r5 Performances on a few channels. https://uimon.cern.ch/twiki/bin/view/LHCb/FlavourTagging.

[79] LHCb, J.R.T. DE MELLO NETO S. AMATO AND C. NUNES. The LHCb sensitivity to $\sin(2\beta)$ from $B_d^0 \rightarrow J/\psi(\mu^+ \mu^-) K_S^0$ asymmetry. 2003. CERN-LHCb-2003-107.

[80] LHCb, H. TERRIER AND B. PIETRZYK. $B_d^0 \rightarrow J/\psi(e^+ e^-) K_S^0$ selection. 2003. CERN-LHCb-2003-125.

[81] L. ALLEBONE AND U. EGEDE. Exclusive selection of $B_d^0 \rightarrow D^{(*)} \pi$. 2003. CERN-LHCb-2003-126.

[82] LHCb, J. VAN HUNEN M. PROKUDIN A. GOLUTVIN, R. HIERCK AND R. WHITE. $B_s^0 \rightarrow D_s K$ and $B_s^0 \rightarrow D_s \pi$ event selection. 2003. CERN-LHCb-2003-127.

[83] LHCb, V. VAGNONI ET AL. CP sensitivity with $B_d^0 \rightarrow$ hh decays at LHCb. CERN-LHCb-2003-124.

[84] LHCb, G. RAVEN. Sensitivity studies of χ and $\Delta\Gamma_s$ with $B_s^0 \rightarrow J/\psi(\mu^+ \mu^-) \phi(K^+ K^-)$. 2003. CERN-LHCb-2003-119.

[85] LHCb, J. VAN HUNEN R. HIERCK AND M. MERK. The sensitivity for Δm_s and $\gamma + \chi$ from $B_s^0 \rightarrow D_s \pi$ and $B_s^0 \rightarrow D_s K$ decays. 2003. CERN-LHCb-2003-103.

[86] P. KOPPENBURG. Contribution to the development of the LHCb Vertex Locator and study of rare semeleptonic decays. *Thèse de doctorat*, published at the *Université de Lausanne*, 2002.

[87] The CKMfitter Group. Updated results on the CKM matrix and the unitarity triangle. Results presented at HEP 2005, Europhyiscs Conference, Lisboa, Portugal, http://ckmfitter.in2p3.fr, 2005.

[88] LHCb, S. JIMENEZ. Analysis of $B_s^0 \rightarrow J/\psi \eta^{'}$. Talk presented at the CP measurements Working Group, CERN, Geneva, August 11th 2005, http://agenda.cern.ch/fullAgenda.php?ida=a053649#2005-08-11.

[89] LHCb, E. CONTE. Analysis of the channel $\Lambda_b^0 \rightarrow J/\psi \Lambda$. http://agenda.cern.ch/fullAgenda.php?ida=a053434#2005-06-16, 2005.

[90] LHCb, H. TERRIER. Etude de la violation de CP dans le canal $B_d^0 \rightarrow J/\psi(e^+ e^-) K_S^0$, identification et reconstruction des électrons dans l'expérience LHCb. 2005. CERN-THESIS-2005-031.

[91] LHCb. LHCb bookkeeping facility. `http://lhcbdata.home.cern.ch/lhcbdata/bkk/`.

[92] LHCb, L. NICOLAS. Selection and study of the $B_s^0 \to D_s^- \pi^+$ decay at LHCb. 2005. CERN-THESIS-2005-035.

[93] LHCb, G. RAVEN. Selection of $B_s^0 \to J/\psi \phi$ and $B^+ \to J/\psi K^+$. 2003. CERN-LHCb-2003-118.

[94] GARY J. FELDMAN AND ROBERT D. COUSINS. A Unified approach to the classical statistical analysis of small signals. *Phys. Rev.*, D57:3873–3889, 1998, physics/9711021.

[95] G. COWAN. Statistical data analysis. 1998. Oxford, UK: Clarendon (1998) 197 p.

[96] L. FERNÁNDEZ. $B_s^0 \to \eta_c \phi$ selection with DC04. Talk presented at the CP measurements Working Group, CERN, Geneva, August 11th 2005, `http://agenda.cern.ch/fullAgenda.php?ida=a053649#2005-08-11`.

[97] JONATHAN L. ROSNER. Determination of pseudoscalar charmed meson decay constants from B meson decays. *Phys. Rev.*, D42:3732–3740, 1990.

[98] AMOL S. DIGHE, ISARD DUNIETZ, HARRY J. LIPKIN, AND JONATHAN L. ROSNER. Angular distributions and lifetime differences in $B_s^0 \to J/\psi \phi$ decays. *Phys. Lett.*, B369:144–150, 1996, hep-ph/9511363.

[99] AMOL S. DIGHE, ISARD DUNIETZ, AND ROBERT FLEISCHER. Extracting CKM phases and $B_s^0 - \overline{B}_s^0$ mixing parameters from angular distributions of non-leptonic B decays. *Eur. Phys. J.*, C6:647–662, 1999, hep-ph/9804253.

[100] CDF, D. ACOSTA ET AL. Analysis of decay-time dependence of angular distributions in $B_s^0 \to J/\psi \phi$ and $B_d^0 \to J/\psi K^*$ decays and measurement of the lifetime difference between B_s^0 mass eigenstates. *Phys. Rev. Lett.*, 94:101803, 2005, hep-ex/0412057.

[101] P. KOPPENBURG. Status of specific HLT. Talk presented at the LHCC Comprehensive review for LHCb, CERN, Geneva, January 31st 2005, `http://agenda.cern.ch/fullAgenda.php?ida=a045908#2005-01-31`.

[102] MARTIN BENEKE AND ALEXANDER LENZ. Lifetime difference of B_s^0 mesons: Theory status. *J. Phys.*, G27:1219–1224, 2001, hep-ph/0012222.

Benjamin Carron

High Energy Physics Laboratory (LPHE)
Swiss Federal Institute of Technology (EPFL)
CH-1015 Lausanne-Dorigny

Born on January 14th 1976,
in Fully (VS), Switzerland
Single, no children

EDUCATION

2005 (expected)	PhD thesis in high energy physics on *$B_s^0 \rightarrow J/\psi\,\eta$ decays and sensitivity to the B_s^0 mixing phase at LHCb*, at LPHE, EPFL Supervisor: Dr. Minh-Tâm TRAN
2003	1er Séminaire Transalpin de Physique on *Living matter: a new challenge to physicists*, Les Diablerets
2001	*2001 European School of High-Energy Physics*, Beatenberg
2000	Physics diploma thesis on *Study of the b-jets flavor tagging in the LHCb experiment*, EPFL Supervisor: Prof. Aurelio BAY (IPHE LAUSANNE) - MARK: 9/10
1995	Swiss federal Maturity and Latin-English Baccalaureate, Sion

PREVIOUS WORK EXPERIENCE

2000–2005	PhD thesis work in high energy physics on the LHCb experiment at CERN, Geneva
2005	Collaboration in the "CP measurements" Working Group of the LHCb experiment at CERN
2002-2005	Collaboration in the physics group of the LHCb experiment at CERN
2000-2004	Teaching assistant (practical training and laboratories for senior undergraduate physics students; supervision of graduating student projects), University of Lausanne
2000–2003	LHCb Inner Tracker web-master at IPHE, University of Lausanne
2000-2002	Research and development of the silicon inner tracker of the LHCb experiment at CERN
1998–2000	Teaching assistant at the Physics Department (practical training and laboratories for senior undergraduate physics students), EPFL
1999-2000	Collaboration in the "b-jets flavor tagging" working group of the LHCb experiment at CERN
1999	Graduation project in High Energy Physics, on a Van der Graaff accelerator, EPFL